Advanced catalytic materials and technologies in biomass conversion

Edited by
Xianxiang Liu, Pau Loke Show, Haian Xia and Jun Yue

About Frontiers

Frontiers is more than just an open access publisher of scholarly articles: it is a pioneering approach to the world of academia, radically improving the way scholarly research is managed. The grand vision of Frontiers is a world where all people have an equal opportunity to seek, share and generate knowledge. Frontiers provides immediate and permanent online open access to all its publications, but this alone is not enough to realize our grand goals.

Frontiers journal series

The Frontiers journal series is a multi-tier and interdisciplinary set of open-access, online journals, promising a paradigm shift from the current review, selection and dissemination processes in academic publishing. All Frontiers journals are driven by researchers for researchers; therefore, they constitute a service to the scholarly community. At the same time, the *Frontiers journal series* operates on a revolutionary invention, the tiered publishing system, initially addressing specific communities of scholars, and gradually climbing up to broader public understanding, thus serving the interests of the lay society, too.

Dedication to quality

Each Frontiers article is a landmark of the highest quality, thanks to genuinely collaborative interactions between authors and review editors, who include some of the world's best academicians. Research must be certified by peers before entering a stream of knowledge that may eventually reach the public - and shape society; therefore, Frontiers only applies the most rigorous and unbiased reviews. Frontiers revolutionizes research publishing by freely delivering the most outstanding research, evaluated with no bias from both the academic and social point of view. By applying the most advanced information technologies, Frontiers is catapulting scholarly publishing into a new generation.

What are Frontiers Research Topics?

Frontiers Research Topics are very popular trademarks of the *Frontiers journals series*: they are collections of at least ten articles, all centered on a particular subject. With their unique mix of varied contributions from Original Research to Review Articles, Frontiers Research Topics unify the most influential researchers, the latest key findings and historical advances in a hot research area.

Find out more on how to host your own Frontiers Research Topic or contribute to one as an author by contacting the Frontiers editorial office: frontiersin.org/about/contact

Advanced catalytic materials and technologies in biomass conversion

Table of contents

Production of the 2,5-Furandicarboxylic Acid Bio-Monomer From 5-Hydroxymethylfurfural Over a Molybdenum-Vanadium Oxide Catalyst

Jian Liu, Sha Wen, Fei Wang, Xiaoting Zhu, Zhijuan Zeng and Dulin Yin*

National and Local Joint Engineering Laboratory for New Petro-chemical Materials and Fine Utilization of Resources, Key Laboratory of the Assembly and Application of Organic Functional Molecules of Hunan Province, Hunan Normal University, Changsha, China

2, 5-Furandicarboxylic acid (FDCA) is an important bio-monomer that can potentially replace terephthalic acid to synthesize degradable polyesters. Efficient selective oxidation of biomass-based 5-hydroxymethylfurfural (HMF) to FDCA has been a significant but challenging work in the past decades. In this study, a novel molybdenum-vanadium oxide (Mo-V-O) catalyst was prepared by a simple method and showed excellent catalytic activity for converting HMF to FDCA. A high FDCA selectivity of 94.5 and 98.2% conversion of HMF were achieved under the optimal conditions with tert-butyl hydroperoxide as the oxidant. FT-IR, SEM, XRD and TG were applied to investigate the properties of Mo-V-O catalyst. After fitting experimental data with the first-order kinetics equation, the evaluated apparent activation energies of HMF oxidation were obtained. The experimental design and study were carried out by response surface methodology (RSM) to test the effects of reaction conditions on the catalytic process.

Keywords: biomass, 5-hydroxymethylfurfural, 2, 5-furandicarboxylic acid, selective oxidation, no-noble metal catalyst

1 INTRODUCTION

Owing to the exhaustion of fossil resources and the aggravation of environmental problems, many efforts have been made to exploit sustainable and environmentally friendly alternatives (Gao et al., 2018; Pal and Saravanamurugan, 2020). As such, the excavation of renewable resources that can be used to produce extensive commodity chemicals is of great significance (Zhao et al., 2020). In this context, biomass is the most abundant renewable resource, and is considered a potential material for industrial production (Guo et al., 2020). Hence, the exploitation of biomass represents a significant step towards the goal of sustainable development of natural resources (Lin et al., 2021). In addition, through their depolymerization, biopolymers derived from biomass can be further converted into high-value-added platform chemical compounds for use in subsequent applications.

5-Hydroxymethylfurfural (HMF) which originates from cellulose or cellulose-derived carbohydrates, has been identified as a platform compound that can be intensively processed

FIGURE 1 | FT-IR spectra of the samples: **(A)** V_2O_5, **(B)** MoO_3, and **(C)** Mo-V-O.

FIGURE 2 | XRD patterns of the samples.
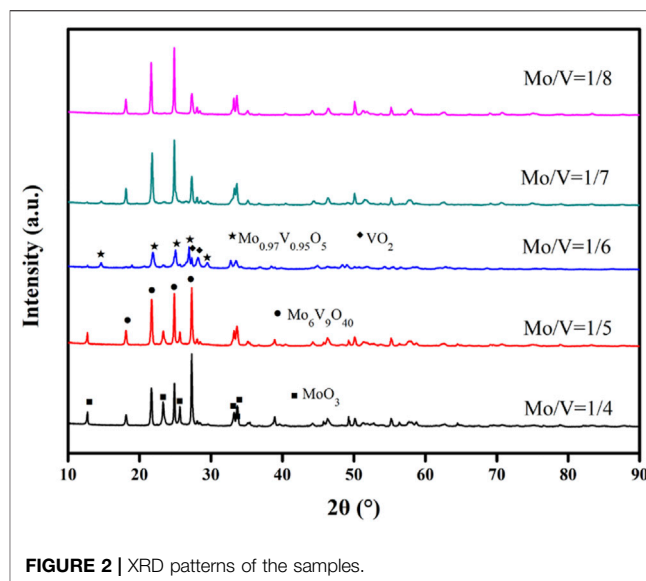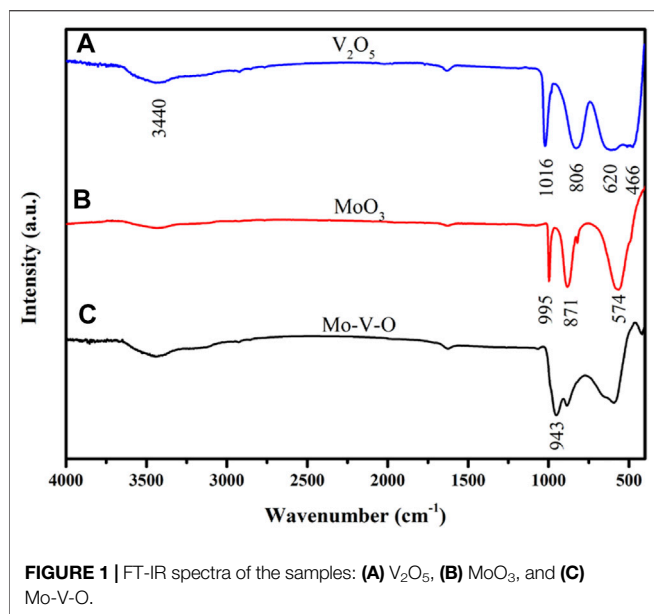
into 2,5-diformylfuran (DFF), 5-hydroxymethyl-2-furancarboxylic acid (HFCA), 5-formyl-2-furancarboxylic acid (FFCA), and 2,5-furandicarboxylic acid (FDCA) (Pal and Saravanamurugan, 2020; Hong et al., 2019a; Hong et al., 2019b). More specifically, the oxidative transformations of HMF are key routes toward a wide variety of chemicals and biofuels (Gao et al., 2020; Hong et al., 2021). In particular, FDCA, which is derived from the successive oxidation of HMF, is a substitute for petroleum-derived terephthalic acid, which can be employed in the preparation of polyethylene furanoate (PEF) to ultimately alleviate the shortage of resources and relieve environmental stress (Tirsoaga et al., 2020).

The most common preparation of FDCA is carried out under basic conditions, which complicates downstream separation, increases the number of added reagents, and generates inorganic salts (Hayashi et al., 2019). Therefore, the development of a basic-free system is considered of particular importance. Furthermore, the high costs of noble metals renders these catalysts less attractive, and hinders scale-up industrialization (Zhou et al., 2018). Alternatively, the advantages of transition metals are well known; however, vanadium, which is commonly used in the oxidation of HMF, undergoes a loss of its active components during the reaction, and so tends to be employed in combination with other elements. (Navarro et al., 2009; Rodikova and Zhizhina, 2020). In this context, Zhao et al. synthesized a catalyst based on vanadium dioxide (VO_2)-embedded mesoporous carbon spheres (V-CS) using a facile hydrothermal method, which produced DFF in a yield of 99.0% (Zhao et al., 2018). In addition, Lai et al. prepared a new type of magnetic vanadium-based catalyst, namely $NH_4 \cdot V_3O_8/Fe_3O_4$ (M-V-O), which gave a 95.5% conversion of HMF and a 82.9% selectivity toward DFF (Lai et al., 2020). More recently, Wang et al. used a novel crystalline Mo-V-O oxide as a heterogeneous catalyst in the liquid phase with molecular oxygen for the selective oxidation of alcohols (Wang and Ueda, 2009),

FIGURE 3 | TG pattern of Mo-V-O.
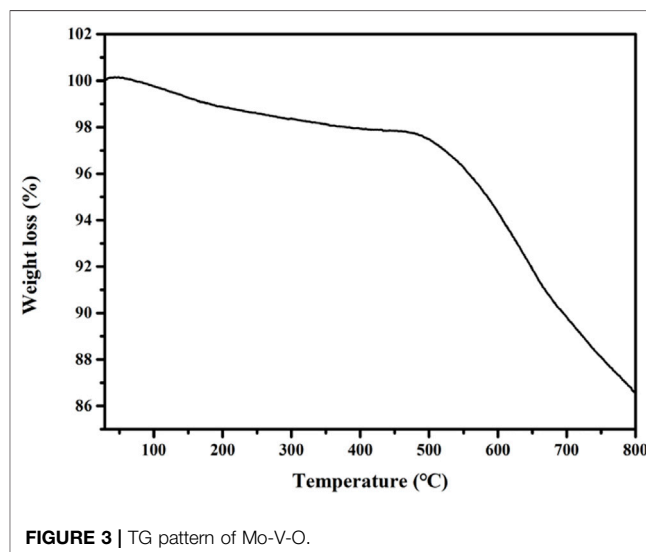
while Rasteiro et al. investigated the one-step oxydehydration of glycerol to acrylic acid over molybdenum and vanadium mixed oxides, achieving a selectivity of 33.5% towards acrylic acid and a 100% conversion of glycerol (Rasteiro et al., 2017). Therefore, Mo-V-O, which contains non-noble metals, appears to be suitable for use as a catalyst for the oxidation of HMF to FDCA without the requirement for a base.

Thus, we herein report the development of a simple and feasible method for preparing a catalyst for the oxidation of HMF to FDCA in the absence of base. During this study, a range of reaction parameters, such as the temperature, reaction time, HMF/TBHP molar ratio, and catalyst amount, are examined and optimized. A series of characterization methods are then applied to investigate the catalyst, and a kinetic study and response surface methodology (RSM) are also carried out.
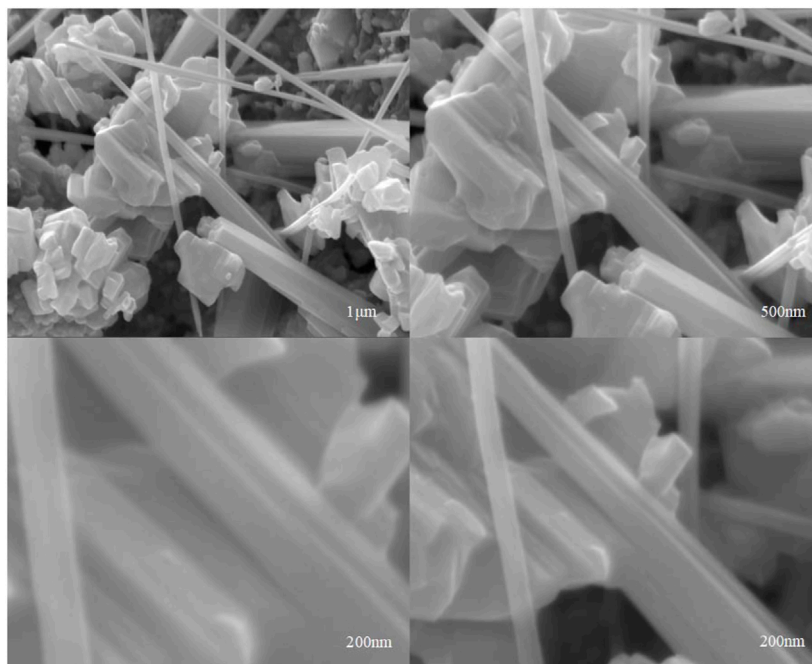
FIGURE 4 | SEM images of Mo-V-O.
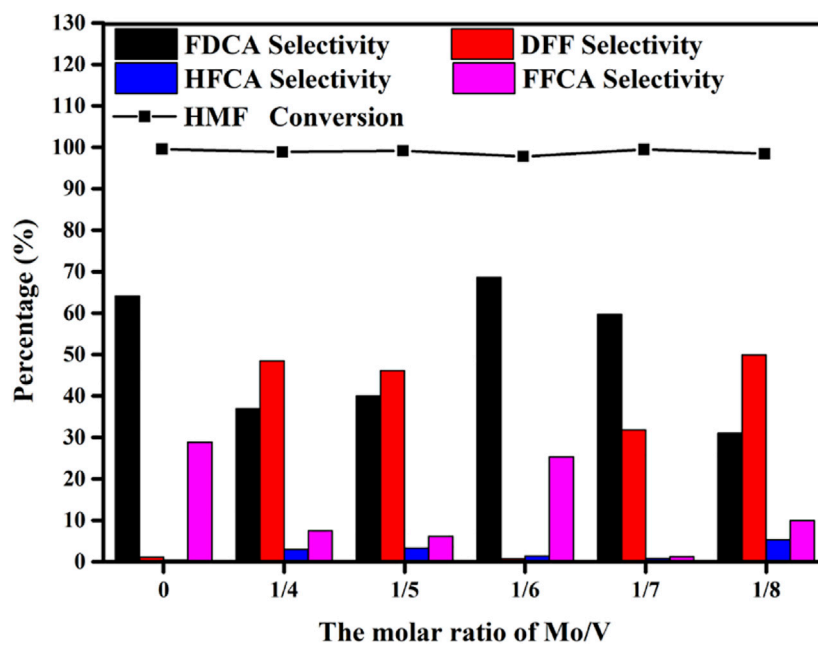
FIGURE 5 | Effects of the Mo/V molar ratios on the catalytic oxidation of HMF. Reaction conditions:0.5 mmol HMF, 5 mmol TBHP, 30 mg Mo-V-O catalyst, 5 ml TBA, 10 h, 80°C.
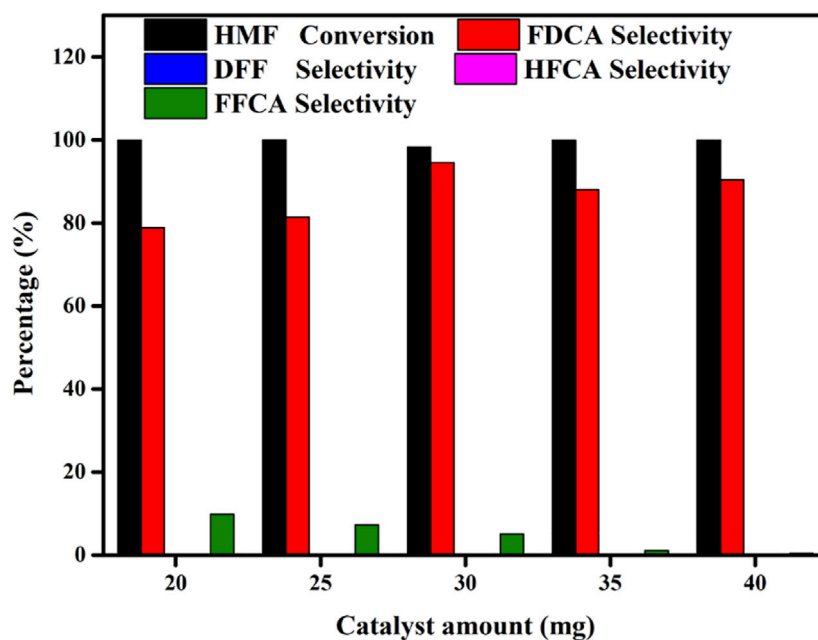
FIGURE 6 | Effects of the amount of Mo-V-O catalyst on the oxidation of HMF. Reaction conditions:0.5 mmol HMF, 10 mmol TBHP, 5 ml TBA, 80°C, 10 h.
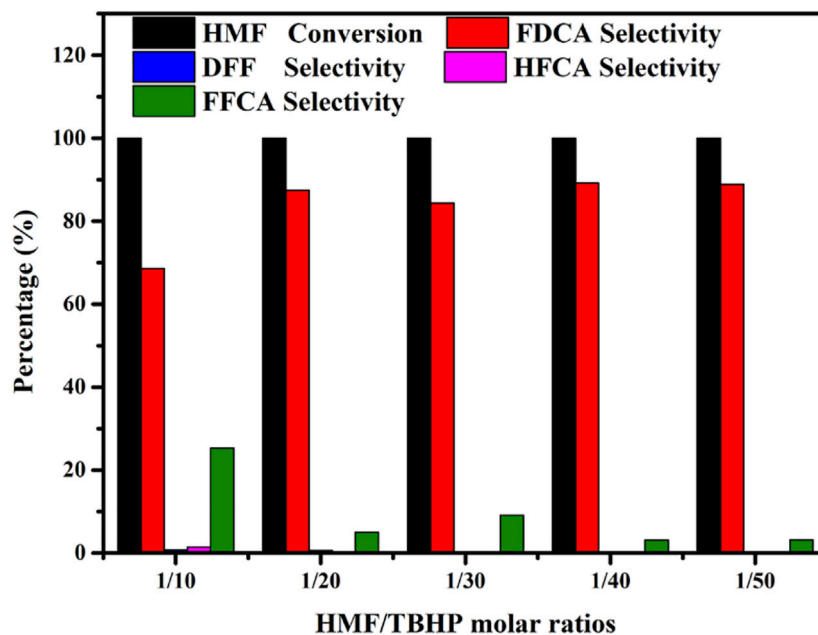
FIGURE 7 | Effects of the HMF/TBHP molar ratio on the reaction selectivity. Reaction conditions:0.5 mmol HMF, 30 mg catalyst, 5 ml TBA, 4 h, 80°C.

2 MATERIALS AND METHODS

2.1 Materials

5-Hydroxymethylfurfural (97.0%) and *tert*-butyl hydroperoxide (TBHP) (70.0%) were purchased from Shanghai Macklin Biochemical Co., Ltd (Shanghai, China). 2,5-Dimethylfuran (≥98.0%) was purchased from Shanghai D&B Biological Science and Technology Co., Ltd (Shanghai, China) $(NH_4)_6Mo_7O_{24} \cdot 4H_2O$, $C_6H_8O_7 \cdot H_2O$, and *tert*-butanol (TBA) (≥99.0%) were purchased from Sinopharm Chemical Reagent Co., Ltd (Shanghai, China). NH_4VO_3 (≥99.0%) was purchased from Tianjin Guangfu Technology Development Co., Ltd (Tianjin, China). V_2O_5 was
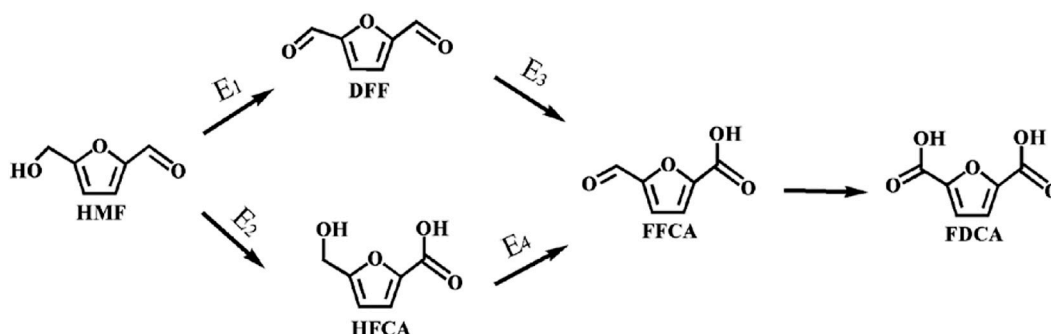
SCHEME 1 | Reaction pathway of the aerobic oxidation of HMF to FDCA over Mo-V-O.
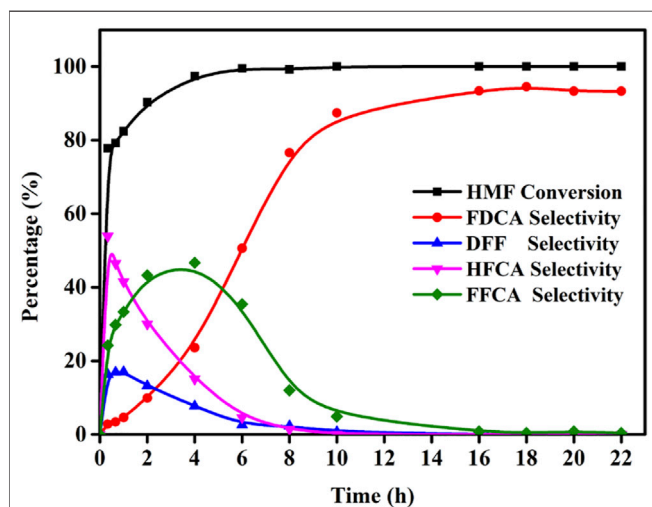
FIGURE 8 | Effects of the reaction time for the oxidation of HMF over Mo-V-O. Reaction conditions: 0.5 mmol HMF, 10 mmol TBHP, 30 mg catalyst, 5 ml TBA, 80°C.

TABLE 1 | The activation energy of the reaction.

Entry	Ea (kJ/mol)
E_1	18.17
E_2	4.58
E_3	39.7
E_4	60.7

TABLE 2 | Experimental design of the independent variables.

Independent variables	Factors	Ranges and levels		
		−1	0	1
Time(h)	A	13	10	16
Catalyst dosage (mg)	B	25	30	35
TBHP/HMF	C	20	30	40

range of 400–4,000 cm^{-1}. Thermogravimetry-differential thermal analysis (TG-DTG, Germany) curves were recorded under a N_2 flow on a Netzsch Model STA 409 PC instrument (Mark, American) using α-Al$_2$O$_3$ as the standard material. Data were recorded from room temperature to 800°C at a heating rate of 10°C/min. X-ray diffraction (XRD) studies were performed using a Bruker diffractometer with Cu Kα radiation to survey the crystal structure over a 2θ range of 10–80°. Scanning electron microscopy (SEM) images were collected using a Zeiss Sigma 300 microscope (Carl Zeiss, Germany).

2.4 The Oxidation of HMF

HMF (0.5 mmol) was dissolved in 5 ml TBA while Mo-V-O (30 mg) was added. In the case of adding oxidant TBHP (5 mmol), the reaction carried out at 80 °C in round-bottom flask. The reactor was cooled to room temperature. The reaction mixture was analyzed by Agilent 1260 HPLC system, equipped with Venusil XBP C18 chromatographic column (4.6 × 250 mm, 5 μm, Phenomenex, United States) and a UV–Vis (280 nm) detector was used to analysis product. The quantification was carried out using the external standard method. The mobile phase was constituted of acetic acid solution (0.1 wt%) and acetonitrile in a volume ratio of 95: 5,

purchased from Tianjin Guangfu Technology Development Co., Ltd. MoO$_3$ was purchased from Tianjin Guangfu Technology Development Co., Ltd.

2.2 Catalyst Preparation

Mo-V-O was synthesized according to the following procedure (NH$_4$)$_6$Mo$_7$O$_{24}$·4H$_2$O (0.003 mol) and NH$_4$VO$_3$ (0.018 mol) were mixed in deionized water (50 ml) and heated for 30 min at 80°C. Subsequently, C$_6$H$_8$O$_7$·H$_2$O was slowly added and after stirring for 12 h, the reaction mixture was dried for 12 h in an oven. The mixture was then ground and calcined at 500°C in a muffle furnace for 5 h. The prepared samples are denoted as Mo-V-O.

2.3 Characterization

The synthesized samples were characterized using Fourier transform infrared spectroscopy (FT-IR). The spectra of the catalysts were collected using the KBr pellet technique on a Nicolet 370 (Thermo Nicolet, American) infrared spectrophotometer in the wavenumber

TABLE 3 | Box-Behnken design of experiments.

Entry	Factor			FDCA selectivity (%)
	Time(h)	Catalyst dosage (mg)	TBHP/HMF	
1	13 (-1)	25 (-1)	20 (-1)	77.5
2	13 (-1)	30 (0)	30 (0)	87.0
3	13 (-1)	35 (+1)	40 (+1)	88.3
4	13 (-1)	30 (0)	30 (0)	85.7
5	13 (-1)	30 (0)	30 (0)	82.9
6	10 (0)	25 (-1)	30 (0)	87.5
7	13 (-1)	30 (0)	30 (0)	89.6
8	13 (-1)	30 (0)	30 (0)	82.3
9	16 (+1)	35 (+1)	30 (0)	86.4
10	10 (0)	30 (0)	40 (+1)	87.6
11	10 (0)	30 (0)	20 (-1)	78.2
12	16 (+1)	25 (-1)	30 (0)	84.9
13	13 (-1)	35 (+1)	20 (-1)	80.4
14	16 (+1)	30 (0)	20 (-1)	85.6
15	16 (+1)	30 (0)	40 (+1)	88.9
16	13 (-1)	25 (-1)	40 (+1)	85.5
17	10 (0)	35 (+1)	30 (0)	88.2

TABLE 4 | ANOVA results of the quadratic model.

Source	Sum of squares	Df	Mean square	F-value	p-value prob > F	
Model	112.36	3	37.45	5.27	0.0134	significant
A-Time	2.31	1	2.31	0.33	0.5782	
B-Catalyst Amount	7.80	1	7.80	1.10	0.3138	
C-TBHP/HMF	102.24	1	102.24	14.39	0.0022	
Residual	92.36	13	7.10			
Lack of fit	68.77	9	7.64	1.3	0.4299	not significant
Pure error	23.59	4	5.90			
Cor total	204.72	16				

and the samples were identified at a rate of 0.7 ml/min at 30°C. The equations were as follows:

HMF conversion (%)=(1- moles of HMF/moles of HMF added) × 100

FDCA selectivity (%) = moles of FDCA/(moles of HMF added - moles of HMF) ×100

3 RESULTS AND DISCUSSION

3.1 Catalyst Characterization
3.1.1 Infrared Spectra of Mo-V-O
The FTIR spectra of the samples are shown in **Figure 1**, where the broad peak at 3,440 cm^{-1} corresponds to the H-OH bending vibration of physically adsorbed water. In addition, the characteristic peaks of V_2O_5 at 1,016 and 806 cm^{-1} originate from the symmetric stretching vibrations of V-O and V=O, while the peaks at 620 and 466 cm^{-1} could be attributed to the symmetric stretching vibration and asymmetric stretching vibration of V-O-V, respectively (Zhang et al., 2016). Furthermore, strong peaks at 995, 871, and 574 cm^{-1} can also be seen in the FT-IR spectra, which could be associated with MoO_3, wherein the peak at 943 cm^{-1} arises from Mo-O-V,

thereby confirming the formation of Mo-V-O (Guan et al., 2008).

3.1.2 XRD Patterns of Mo-V-O Containing Various Mo/V Molar Ratios
XRD analysis was performed to determine the crystal structure of the catalyst. Thus, the XRD spectra of the samples are presented in **Figure 2**, and show the characteristic reflections of MoO_3 (JCPDF 05-0508), $Mo_6V_9O_{40}$ (JCPDF 34-0527), VO_2 (JCPDF 33-1,440), and $Mo_{0.97}V_{0.95}O_5$ (JCPDF 50-0535), as indicated in the figure. It can be seen that upon increasing the Mo/V molar ratio, the characteristic peak intensities for MoO_3 at $2\theta = 12.7, 23.3$, and $25.5°$ decreased. The molar ratio that gave the optimal catalytic effect was determined to be 1/6, in which the characteristic peaks at $2\theta = 14.6, 21.8, 25.0$, and $26.9°$ were assigned to $Mo_{0.97}V_{0.95}O_5$. Moreover, the characteristic peaks at $2\theta = 27.3$ and $28.2°$ were attributed to VO_2, which were also visible at a Mo/V molar ratio of 1/6.

3.1.3 TG Curve of Mo-V-O
The stability of a catalyst is a key performance parameter, and so we investigated the thermal stability, which is an indicator of the catalyst stability, using the TG approach. As shown in **Figure 3**, the TG thermogram shows that the catalyst
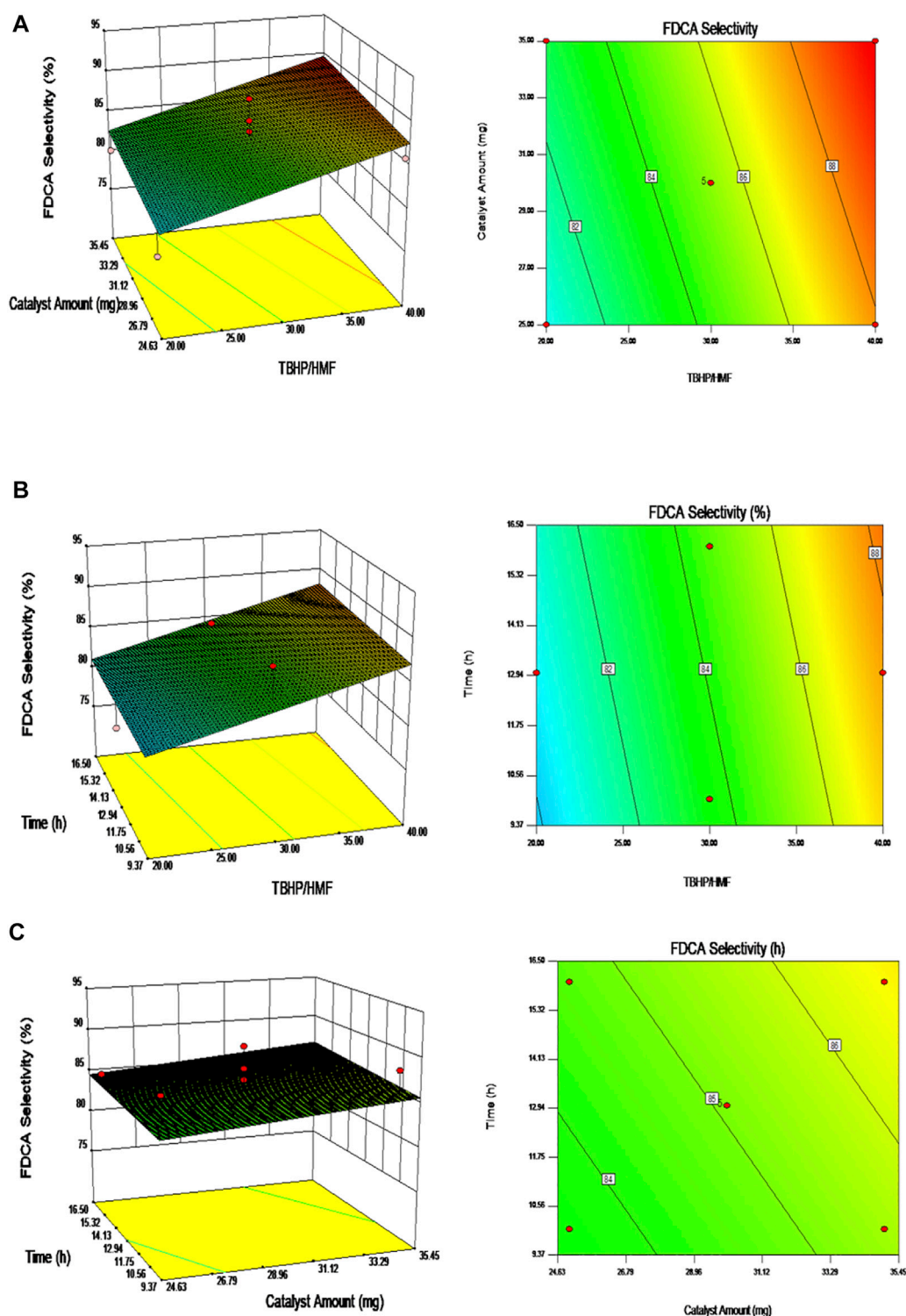
FIGURE 9 | The surface-response plots on the FDCA selectivity: **(A)** Fixed Time; **(B)** Fixed catalyst amount; **(C)** Fixed TBHP/HMF molar ratio.

underwent two major mass loss stages. The first mass loss stage at ~190°C was attributed to the thermal dehydration of the catalyst, while the second and main mass-loss stage was ascribed to the decomposition of metal oxides at ~660°C.

3.1.4 SEM Images of Mo-V-O

In order to obtain morphology information of the catalyst, the SEM was applied and shown in **Figure 4**. It can be seen that the catalyst appear nanorods morphology, and bulk-like

morphology which formed by stacking of flake crystals. Most of Mo-V-O showed bulk-like structure which exhibited an irregular size, and the flake-like structure is observed clearly. Furthermore, the dimensions of nanorods were less consistent and comprised of different sizes showing that Mo-V-O material possessed different compositions, which is consistent with XRD.

3.2 Effects of Different Mo/V Molar Ratio on the Oxidation of HMF by Mo-V-O

Figure 5 displayed the products distribution of HMF converting to FDCA by pure V_2O_5 and the different molar ratio of Mo/V. In the presence of TBHP, V_2O_5 exhibits the ability of HMF oxidation to FDCA. However, there was only liquid without any catalyst after reaction indicating the instability of vanadium. Moreover, the composition of catalyst is an important factor affecting the performance of catalyst. As the changed Mo/V molar ratio from 1/4 to 1/6, FDCA selectivity varied from 36.9 to 68.6% at the same condition. Further adjusted the Mo/V molar ratio, a selective decline appeared. The above different catalytic effects indicate that the composition of different catalysts may be different, which is consistent with the XRD results.

3.3 Influence of the Mo-V-O Amount on the Oxidation of HMF

Generally, the number of active sites directly affects the catalytic performance. Thus, to optimize the catalytic performance, we examined the effect of the catalyst dosage at values ranging from 20 to 40 mg, and the results are presented in **Figure 6**. Upon increasing the catalyst loading, the number of active sites and the contact area between the catalyst and the substrate also increased, thereby influencing the reaction outcome. Interestingly, the HMF conversion did not change significantly with an increase in the catalyst dosage, indicating that even at a low catalyst dosage, the HMF conversion was adequate. However, the relationship between the catalyst dosage and the number of active sites was found to affect the selectivity toward FDCA. More specifically, as the catalyst dosage was initially increased from 20 to 30 mg, the selectivity toward FDCA increased from 87.6 to 94.5%. However, upon further increasing the amount of catalyst to 40 mg, the selectivity toward FDCA decreased, likely due to the fact than an excess of catalyst decreased the probability of effective contact between the catalyst and the substrate. This suggests that a 30 mg catalyst loading was sufficient for the conversion of HMF to FDCA.

3.4 Influence of the HMF/TBHP Molar Ratio on the Oxidation of HMF

Since TBHP is employed as an oxidant in the HMF-to-FDCA pathway, different amounts of TBHP can also produce diverse catalytic performances, and thus the amount of TBHP is a crucial parameter. Hence, to gain further insight into the effect of TBHP on the oxidation of HMF into FDCA over Mo-V-O, different HMF/TBHP molar ratios were investigated. As shown in **Figure 7**,

the conversion of HMF and the corresponding selectivity towards different oxidation products were found to vary under different HMF: TBHP ratios. More specifically, the selectivity toward FDCA increased substantially from 5.9 to 62.7% as the HMF/TBHP molar ratio was increased from 1/10 to 1/50, thereby indicating that TBHP was required for the selective oxidation of HMF. However, upon increasing this ratio to 1/20, the conversion of HMF to FDCA reached 97.4%, beyond which point, only minor increases were observed. Based on the products detected following this reaction, it was apparent that the aldehyde and hydroxyl groups present on the furan ring of HMF were oxidized to their corresponding intermediates, which further afforded FDCA from FFCA, as outlined in **Scheme 1**. Thus, from both economic and environmental perspectives, an HMF/TBHP molar ratio of 1/20 was considered optimal for the conversion of HMF, and so was selected for further experiments.

3.5 Influence of the Reaction Time on Oxidation of HMF

Using the reaction conditions optimized above, the influence of the reaction time was then investigated (i.e., 0–22 h) to study the product distribution and selectivity changes over time. As shown in **Figure 8**, five oxidation products were formed, which indicates that the conversion of HMF to FDCA does not only involve the oxidation of aldehyde or hydroxyl groups individually, but also the combined oxidation of both functional groups. As a result, HMF can produce FDCA via two path ways. It was found that the HMF conversion rapidly reached 77.8% after 20 min, and then increased to almost 100.0% by 4 h. In addition, the FDCA selectivity gradually increased to 94.5% over 18 h, although variations in the DFF, HFCA, and FFCA contents were observed according to the different HMF oxidation pathways that were followed, although in these cases, an initial increase was followed by a subsequent decrease as the FDCA selectivity increased.

4 REACTION KINETICS OF HMF OXIDATION OVER THE MO-V-O CATALYST

As described above, the conversion of HMF to FDCA involves both sequential and parallel reactions, which renders it difficult to estimate the intrinsic reactivity of the Mo-V-O-catalyzed process (Hayashi et al., 2019). Examination of the reaction kinetics is therefore an effective means to provide additional insight into the reaction and evaluate the catalyst performance (Davis et al., 2014; Ren et al., 2015). Initially, it was assumed that the HMF oxidation reactions were all first order reactions, and so the aforementioned activation energy was calculated using the following formulae:

$$\frac{d[HMF]}{dt} = -(k_1 + k_2)[HMF] \tag{1}$$

$$\frac{d[DFF]}{dt} = k_1.[HMF] - k_3.[DFF] \tag{2}$$

$$\frac{d[HFCA]}{dt} = k_1 \cdot [HMF] - k_4 \cdot [HFCA] \tag{3}$$

$$[HMF] = C_1 \cdot e^{-(k_1+k_2)t} \tag{4}$$

$$[DEF] = \frac{k_1 C_1}{(k_3 - (k_1 + k_2))} \cdot \left(e^{-(k_1+k_2)t} - e^{-k_3 \cdot t}\right) \tag{5}$$

$$[HFCA] = \frac{k_2 C_1}{(k_4 - (k_1 + k_2))} \cdot \left(e^{-(k_1+k_2)t} - e^{-k_4 \cdot t}\right) \tag{6}$$

Due to the particularity of the reaction process, the activation energy was only partially calculated. More specifically, the data calculated at different temperatures were fit to obtain the Arrhenius plot shown in **Supplementary Figure S1** (Ma et al., 2019), and the apparent activation energies (E_a) for the oxidation of HMF to DFF and HFCA were determined to be 18.17 and 4.58 kJ mol^{-1}, respectively, illustrating the preference toward oxidation of the aldehyde group by Mo-V-O. Subsequently, the further oxidation reaction of DFF and HFCA were investigated (see **Supplementary Figure S2),** and were calculated to be 39.7 and 60.7 kJ mol^{-1}, demonstrating the preferential oxidation of the alcohol group by Mo-V-O. The E_a results are shown in **Table 1**, $E_1 > E_2$ and $E_3 > E_4$ indicated DFF was more susceptible to further oxidation which was consistent with **Figure 8** where the HFCA selectivity was higher than the DFF selectivity at the same time.

5 RESPONSE SURFACE METHODOLOGY (RSM)

Response surface methodology (RSM) is a statistical method for solving multivariable problems by using a reasonable experimental design method and obtaining certain data through experiments. For this purpose, a multiple quadratic regression equation is used to fit the functional relationship between the factors and response values, and the optimal process parameters are determined through analysis of the regression equation (Bezerra et al., 2008; Yemi and Mazza, 2012; Gaidoumi et al., 2019; Yabalak et al., 2018). The Box-Behnken design (BBD) software, which is a quadratic response surface, has been applied to approximate a response function for experimental data that cannot be described by linear functions (Seo and Han, 2014). Hence, the optimal conditions were confirmed by the BBD using RSM which exhibited the FDCA selectivity. The BBD requires three levels of each experimental factor, which are coded as −1, 0, and +1. Thus, the FDCA selectivity was predicted using different combinations of three independent variables, as summarized in **Table 2**. The quadratic model that illustrates the interaction between the dependent and independent variables is as follows:

$$Y = \beta_0 + \beta_A A + \beta_B B + \beta_C C + \beta_{AB} AB + \beta_{AC} AC + \beta_{BC} BC + \beta_{AA} A^2$$
$$+ \beta_{BB} B^2 + \beta_{CC} C^2 + \varepsilon$$
$$\tag{7}$$

where Y is the predicted response; A, B, and C represent the three independent variables; β_i is the linear effect; β_{ii} is the squared

effect; and β_{ij} is the interaction effect. β_0 represents the constant and random errors.

For the purpose of this study, three factors were considered, namely the time (A), the catalyst dosage (B), and the TBHP: HMF molar ratio (C). The tested conditions included reaction times of 10–16 h, catalyst dosages of 25–35 mg, and TBHP:HMF molar ratios of 1:20–1:40. A total of 17 experimental runs were included, as outlined in **Table 3**. Data analysis was performed using Design Expert 8.0.6.1(Stat-Ease., Inc., MN, United States) (Sahoo and Gupta, 2013).

In the quadratic model, analysis of variance (ANOVA) was used to analyze the adequacy of the developed model, and the results are presented in **Table 4**. Generally, the suitability of the model is confirmed by a higher Fisher's value (F value) with a probability value (p value) that is as low as possible. More specifically, values of "Prob > F″" lower than 0.0500 indicating the model terms are significant. In this case, TBHP: HMF is a significant model term. In addition, the "Lack of Fit F-value" of 1.30 implies that the Lack of Fit is not significant relative to the pure error, which means the model has good predictability. Thus, the second order polynomial equation that describes the HMF yield in terms of the actual parameters is given here:

$$FDCA\ Selectivity = +66.30907 + 0.17917 * A + 0.19750 * B + 0.35750 * C \tag{8}$$

As shown in **Figure 9**, the experimental results can be presented in the form of three-dimensional response-surface plots and contour plots under fixed conditions. These plots clearly show the integrated effects of the two random variables, wherein all plots confirmed that the FDCA selectivity increased with an increase in any individual variable. Thus, according to the RSM, the selectivity toward FDCA changes upon variation in the reaction factors.

6 CONCLUSION

We herein reported the development of a simple and feasible method for preparing a catalyst for the oxidation of 5-hydroxymethylfurfural (HMF) to 2,5-furandicarboxylic acid (FDCA) in the absence of base. More specifically, a Mo-V-O catalyst was successfully prepared and was found to exhibit an excellent catalytic performance when *tert*-butyl hydroperoxide (TBHP) was employed as the sole oxidant. Under the optimized conditions determined during the course of our study, HMF was converted to FDCA with 98.2% conversion and 94.5% selectivity. Furthermore, the apparent activation energy was calculated to determine the oxidation sequence of the hydroxyl and aldehyde groups of the reactant and the intermediates. Moreover, response surface methodology was used to investigate the relationship between the catalyst loading, the TBHP/HMF molar ratio, and the reaction time. It was found that these three parameters positively affected the HMF oxidation efficiency. These results are of particular interest due to the ongoing necessity to utilize renewable resources to produce extensive commodity chemicals. Finally, considering

the cost advantages of non-noble metal catalysts, further research is desirable in the oxidation of HMF to FDCA under the base-free conditions established herein.

DATA AVAILABILITY STATEMENT

The original contributions presented in the study are included in the article/**Supplementary Material**, further inquiries can be directed to the corresponding author.

AUTHOR CONTRIBUTIONS

JL:Investigation, Methodology, Writing—Original draft preparation. SW:Data curation, Formal analysis, Writing—review and editing. FW: Validation. XZ:Methodology. ZZ: Visualization. DY:

Conceptualization, Project administration, Funding acquisition, Supervision.

FUNDING

SUPPLEMENTARY MATERIAL

The Supplementary Material for this article can be found online at: https://www.frontiersin.org/articles/10.3389/fchem.2022.853112/full#supplementary-material

REFERENCES

Bezerra, M. A., Santelli, R. E., Oliveira, E. P., Villar, L. S., and Escaleira, L. A. (2008). Response Surface Methodology (RSM) as a Tool for Optimization in Analytical Chemistry. *Talanta* 76, 965–977. doi:10.1016/j.talanta.2008.05.019

Davis, S. E., Benavidez, A. D., Gosselink, R. W., Bitter, J. H., de Jong, K. P., and Davis, R. J. (2014). Kinetics and Mechanism of 5-hydroxymethylfurfural Oxidation and Their Implications for Catalyst Development. *J. Mol. Catal. A: Chem.* 388-389, 123–132. doi:10.1016/j.molcata.2013.09.013

Gaidoumi, A. E., Loqman, A., Benadallah, A. C., Bali, B. E., and Kherbeche, A. (2019). Co(II)-pyrophyllite as Catalyst for Phenol Oxidative Degradation: Optimization Study Using Response Surface Methodology. *Waste Biomass Valori.* 10, 1043–1051. doi:10.1007/s12649-017-0117-5

Gao, T., Yin, Y., Zhu, G., Cao, Q., and Fang, W. (2020). Co₃O₄ NPs Decorated Mn-Co-O Solid Solution as Highly Selective Catalyst for Aerobic Base-free Oxidation of 5-HMF to 2,5-FDCA in Water. *Catal. Today* 355, 252–262. doi:10.1016/j.cattod.2019.03.065

Gao, Z., Li, C., Fan, G., Yang, L., and Li, F. (2018). Nitrogen-doped Carbon-Decorated Copper Catalyst for Highly Efficient Transfer Hydrogenolysis of 5-hydroxymethylfurfural to Convertibly Produce 2,5-dimethylfuran or 2,5-dimethyltetrahydrofuran. *Appl. Catal. B: Environ.* 226, 523–533. doi:10.1016/j.apcatb.2018.01.006

Guan, J., Yang, Y., Liu, B., Ma, Y., Yu, X., Liu, J., et al. (2008). Oxidation of Isobutane over Hydrothermally Synthesized Mo-V-Te-Nb-O Mixed Oxide Catalysts. *React. Kinet Catal. Lett.* 95, 313–320. doi:10.1007/s11144-008-5387-2

Guo, D., Liu, X., Cheng, F., Zhao, W., Wen, S., Xiang, Y., et al. (2020). Selective Hydrogenolysis of 5-hydroxymethylfurfural to Produce Biofuel 2, 5-dimethylfuran over Ni/ZSM-5 Catalysts. *Fuel* 274, 117853. doi:10.1016/j.fuel.2020.117853

Hayashi, E., Yamaguchi, Y., Kamata, K., Tsunoda, N., Kumagai, Y., Oba, F., et al. (2019). Effect of MnO2 Crystal Structure on Aerobic Oxidation of 5-Hydroxymethylfurfural to 2,5-Furandicarboxylic Acid. *J. Am. Chem. Soc.* 141, 890–900. doi:10.1021/jacs.8b09917

Hong, M., Min, J., Wu, S., Cui, H., Zhao, Y., Li, J., et al. (2019a). Metal Nitrate Catalysis for Selective Oxidation of 5-Hydroxymethylfurfural into 2,5-Diformylfuran under Oxygen Atmosphere. *ACS Omega* 4, 7054–7060. doi:10.1021/acsomega.9b00391

Hong, M., Wu, S., Jena, H. S., Li, J., Ding, L., Wang, J., et al. (2021). Bio-based green Solvent for Metal-free Aerobic Oxidation of 5-hydroxymethylfurfural to 2,5-diformylfural over Nitric Acid-Modified Starch. *Catal. Commun.* 149, 106196. doi:10.1016/j.catcom.2020.106196

Hong, M., Wu, S., Li, J. T., Wang, J., Wei, L. F., and Li, K. (2019b). Aerobic Oxidation of 5-(hydroxymethyl)furfural into 2,5-diformylfuran Catalyzed by

Starch Supported Aluminum Nitrate. *Catal. Commun.* 136, 105909. doi:10.1016/j.catcom.2019.105909

Lai, J., Zhou, S., Cheng, F., Guo, D., Liu, X., Xu, Q., et al. (2020). Efficient and Selective Oxidation of 5-hydroxymethylfurfural into 2, 5-diformylfuran Catalyzed by Magnetic Vanadium-Based Catalysts with Air as Oxidant. *Catal. Lett.* 150, 1301–1308. doi:10.1007/s10562-019-03041-w

Lin, K.-Y. A., Oh, W.-D., Zheng, M.-W., Kwon, E., Lee, J., Lin, J.-Y., et al. (2021). Aerobic Oxidation of 5-hydroxymethylfurfural into 2,5-diformylfuran Using Manganese Dioxide with Different crystal Structures: A Comparative Study. *J. Colloid Interf. Sci.* 592, 416–429. doi:10.1016/j.jcis.2021.02.030

Ma, Y., Zhang, T., Chen, L., Cheng, H., and Qi, Z. (2019). Self-developed Fabrication of Manganese Oxides Microtubes with Efficient Catalytic Performance for the Selective Oxidation of 5-hydroxymethylfurfural. *Ind. Eng. Chem. Res.* 58, 13122–13132. doi:10.1021/acs.iecr.9b02650

Navarro, O. C., Canós, A. C., and Chornet, S. I. (2009). Chemicals from Biomass: Aerobic Oxidation of 5-Hydroxymethyl-2-Furaldehyde into Diformylfurane Catalyzed by Immobilized Vanadyl-Pyridine Complexes on Polymeric and Organofunctionalized Mesoporous Supports. *Top. Catal.* 52, 304–314. doi:10.1007/s11244-008-9153-5

Pal, P., Kumar, S., Devi, M. M., and Saravanamurugan, S. (2020). Oxidation of 5-hydroxymethylfurfural to 5-formyl Furan-2-Carboxylic Acid by Non-precious Transition Metal Oxide-Based Catalyst. *J. Supercrit. Fluids* 160, 104812. doi:10.1016/j.supflu.2020.104812

Pal, P., and Saravanamurugan, S. (2020). Recent Advances in the Development of 5-Hydroxymethylfurfural Oxidation with Base (Nonprecious)-Metal-Containing Catalysts. *ChemSusChem* 12, 145–163. doi:10.1002/cssc.201801744

Rasteiro, L. F., Vieira, L. H., Possato, L. G., Pulcinelli, S. H., Santilli, C. V., and Martins, L. (2017). Hydrothermal Synthesis of Mo-V Mixed Oxides Possessing Several Crystalline Phases and Their Performance in the Catalytic Oxydehydration of Glycerol to Acrylic Acid. *Catal. Today* 296, 10–18. doi:10.1016/j.cattod.2017.04.006

Ren, F., Zheng, Y.-F., Liu, X.-M., Yang, Q.-Q., Zhang, Q., and Shen, F. (2015). Thermal Oxidation Reaction Process and Oxidation Kinetics of Abietic Acid. *RSC Adv.* 5, 17123–17130. doi:10.1039/C4RA16791K

Rodikova, Y., and Zhizhina, E. (2020). Catalytic Oxidation of 5-hydroxymethylfurfural into 2, 5-diformylfuran Using V-Containing Heteropoly Acid Catalysts. *React. Kinet. Mech. Cat.* 130, 403–415. doi:10.1007/s11144-020-01782-z

Sahoo, C., and Gupta, A. K. (2013). KApplication of Statistical Experimental Design to Optimize the Photocatalytic Degradation of a Thiazin Dye Using Silver Ion-Doped Titanium Dioxide. *J. Environ. Sci. Health A* 48, 694–705. doi:10.1080/10934529.2013.744598

Seo, Y. H., and Han, J.-I. (2014). Direct Conversion from Jerusalem Artichoke to Hydroxymethylfurfural (HMF) Using the Fenton Reaction. *Food Chem.* 151, 207–211. doi:10.1016/j.foodchem.2013.11.067

Tirsoaga, A., El Fergani, M., Nuns, N., Simon, P., Granger, P., Parvulescu, V. I., et al. (2020). Multifunctional Nanocomposites with Non-precious Metals and Magnetic Core for 5-HMF Oxidation to FDCA. *Appl. Catal. B: Environ.* 278, 119309. doi:10.1016/j.apcatb.2020.119309

Wang, F., and Ueda, W. (2009). Selective Oxidation of Alcohols Using Novel Crystalline Mo-V-O Oxide as Heterogeneous Catalyst in Liquid Phase with Molecular Oxygen. *Catal. Today* 144, 358–361. doi:10.1016/j.cattod.2008.12.034

Yabalak, E., Görmez, Ö., and Gizir, A. M. (2018). Subcritical Water Oxidation of Propham by H2O2 Using Response Surface Methodology (RSM). *J. Environ. Sci. Health B* 53, 334–339. doi:10.1080/03601234.2018.1431468

Yemiş, O., and Mazza, G. (2012). Optimization of Furfural and 5-hydroxymethylfurfural Production from Wheat Straw by a Microwave-Assisted Process. *Bioresour. Technol.* 109, 215–223. doi:10.1016/j.biortech.2012.01.031

Zhang, Y. F., Zheng, J. Q., Zhao, Y. F., Hu, T., Gao, Z. M., and Meng, C. G. (2016). Fabrication of V$_2$O$_5$ with Various Morphologies for High-Performance Electrochemical Capacitor. *Appl. Surf. Sci.* 377, 385–393. doi:10.1016/j.apsusc.2016.03.180

Zhao, D., Su, T., Wang, Y., Varma, R. S., and Len, C. (2020). Recent Advances in Catalytic Oxidation of 5-hydroxymethylfurfural. *Mol. Catal.* 495, 111133. doi:10.1016/j.mcat.2020.111133

Zhao, J., Chen, X., Du, Y., Yang, Y., and Lee, J.-M. (2018). Vanadium-embedded Mesoporous Carbon Microspheres as Effective Catalysts for Selective Aerobic Oxidation of 5-Hydroxymethyl-2-Furfural into 2, 5-diformylfuran. *Appl. Catal. A: Gen.* 568, 16–22. doi:10.1016/j.apcata.2018.09.015

Zhou, H., Xu, H. H., and Liu, Y. (2018). Aerobic Oxidation of 5-hydroxymethylfurfural to 2, 5-furandicarboxylic Acid over Co/Mn-Lignin Coordination Complexes-Derived Catalysts. *Appl. Catal. B-environ* 244, 965–973. doi:10.1016/j.apcatb.2018.12.046

Reductive Upgrading of Biomass-Based Levulinic Acid to γ-Valerolactone Over Ru-Based Single-Atom Catalysts

Ye Meng, Yumei Jian, Dandan Chen, Jinshu Huang, Heng Zhang* and Hu Li*

State Key Laboratory Breeding Base of Green Pesticide and Agricultural Bioengineering, Key Laboratory of Green Pesticide and Agricultural Bioengineering, Ministry of Education, State-Local Joint Laboratory for Comprehensive Utilization of Biomass, Center for R&D of Fine Chemicals, Guizhou University, Guiyang, China

With the great adjustment of world industrialization and the continuous improvement of energy consumption requirements, the selective conversion of biomass-based platform molecules to high-value chemicals and biofuels has become one of the most important topics of current research. Catalysis is an essential approach to achieve energy-chemical conversion through the "bond breaking-bond formation" principle, which opens a broad world for the energy sector. Single-atom catalysts (SACs) are a new frontier in the field of catalysis in recent years, and exciting achievements have been made in biomass energy chemistry. This mini-review focuses on catalytic conversion of biomass-based levulinic acid (LA) to γ-valerolactone (GVL) over SACs. The current challenges and future development directions of SACs-mediated catalytic upgrading of biomass-based LA to produce value-added GVL, and the preparation and characterization of SACs are analyzed and summarized, aiming to provide theoretical guidance for further development of this emerging field.

Keywords: biomass, value-added chemicals, γ-Valerolactone, single-atom catalysts (SACs), levulinic acid (LA)

INTRODUCTION

With advances in research and industrial technology, biomass is now increasingly deemed as one of the most valuable renewable resources that can be converted into a variety of platform molecules, fine chemicals, biofuels, and solid biochars (Li et al., 2015; Liu et al., 2015; Li et al., 2017; Li H et al., 2019; Li H et al., 2020; Meng and Li, 2021; Meng et al., 2022). γ-Valerolactone (GVL) is an important platform molecule and green solvent, which can be used to produce liquid fuels, polymers, intermediates for fine chemicals synthesis, and seasonings (Wright and Palkovits, 2012; Zhang, 2016; Ye et al., 2020). Catalytic hydrogenation of biomass-based levulinic acid (LA) is one of the most effective methods to produce GVL, which has attracted increasing attention in recent years. Homogeneous catalysts can be uniformly dispersed in the catalytic system, which can effectively promote LA hydrogenation to produce GVL. However, due to the high boiling point of GVL (207–208°C), the product/catalyst separated by distillation is not economical, resulting in a homogeneous system not suitable for the target production of GVL (Zhang, 2016). Therefore, the large-scale production of GVL almost certainly depends on heterogeneous catalysts, because heterogeneous catalysts are easier to be separated from nonvolatile GVL (Zhang, 2016; Zhang et al., 2019).
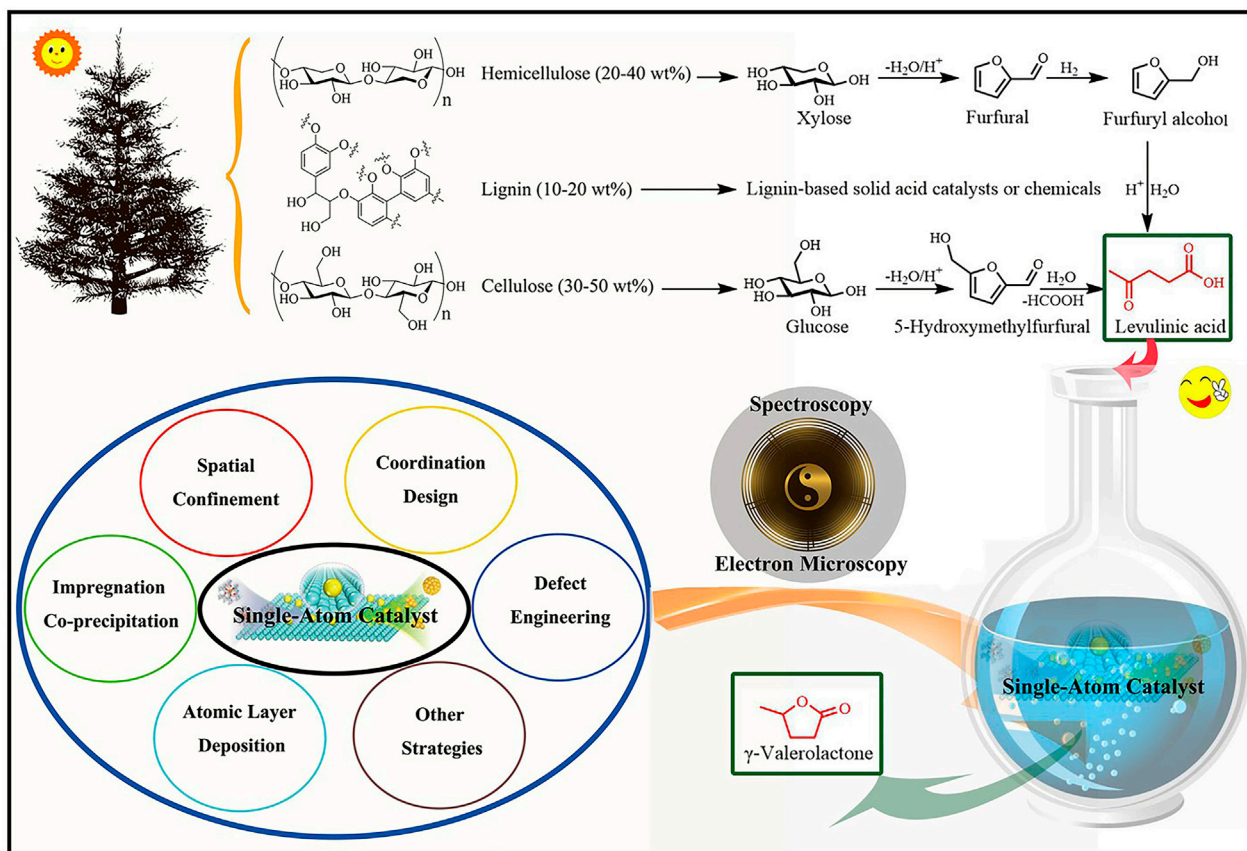
FIGURE 1 | The schematic of reductive upgrading of biomass-based LA (levulinic acid) to GVL (γ-valerolactone) over single-atom catalysts.

Metal sites play an important role in the hydrogenation, intramolecular (trans) esterification or dehydration of LA to obtain GVL (Dutta et al., 2019). Therefore, improving the utilization rate of metal atoms is the key step to reduce the production cost and obtain high efficiency in the whole catalytic process. Single-atom catalysts (SACs) are supported catalysts containing only isolated active centers (Chen et al., 2018; Ji et al., 2020), in which a strong interaction or considerable charge transfer between highly dispersed single metal atoms and solid supports. This unique structure allows single-metal atoms of the SACs to have a desired electronic structure and carry specific electrical charges different from those of conventional metal nanoparticles (Ding et al., 2019; Xue et al., 2022). It seems one of the most promising materials for rational utilization of metal resources and atomic economy. In theory, all the involved metal atoms could behave as homogeneously as homogeneous catalysts, with an atomic efficiency of 100% (Ding et al., 2019). SACs have shown excellent catalytic performance, with respect to activity, selectivity, and stability, in catalytic conversion of various biomass-derived feedstocks into target value-added chemicals (De et al., 2022).

Some excellent reviews have depicted the catalytic production of GVL from biomass-based platform molecule LA in different perspectives (Wright and Palkovits, 2012; Zhang, 2016; Ye et al.,

2020), while SACs applied in this field have not been comprehensively discussed till now. This mini-review focuses on the preparation and characterization of SACs and their application in the conversion of LA to GVL. The advantages and disadvantages of SACs, and the catalytic activity of LA over SACs are introduced emphatically.

CATALYTIC CONVERSION OF LA TO GVL

LA is an important platform molecule, which can be easily and economically produced from lignocellulose *via* a simple and high-yield acid-catalyzed hydrolysis process (**Figure 1**) (Rackemann and Doherty, 2011; Ruppert et al., 2012; Khan et al., 2018). The condensation ability of LA is related to hydrogenation, and the generation of GVL may be realized through the hydrogenation of unsaturated carbon-carbon or carbon-oxygen bonds. Therefore, GVL can be synthesized by hydrogenation of LA through following two reaction mechanisms. *1*) Hydrogenation of ketone group of LA to produce unstable intermediate 4-hydroxy-pentanoic acid (HPA), and subsequent dehydration followed by an intramolecular esterification, resulting in the ring closure to yield GVL. *2*) LA is directly dehydrated to produce α-angelica lactone and then hydrogenated to produce

GVL (Zhang, 2016; Dutta et al., 2019; Ye et al., 2020). In these two pathways, the hydrogenation step depends on the metal active sites of the catalyst, and the dehydration and cyclization steps are affected by the acidic conditions of the reaction system (Galletti et al., 2012; Lin et al., 2018; Cai et al., 2019). In this regard, improving the utilization rate of metal atoms is a key step to reducing the cost and obtaining high efficiency for the overall catalytic process.

In recent years, SACs have opened up a vast field of catalysis because of their advantages of high atomic utilization rate, high activity, high stability, and high selectivity. Many different active phases, including noble and non-noble metals, have been tested to catalyze the conversion of LA to GVL (Yan et al., 2013; Yuan et al., 2013; Mai et al., 2014). Ruthenium-based catalysts remain preferred because they are usually the most active and selective catalysts. Using metal-organic framework (MOF) NH_2-MIL-125 as the precursor, Zhang et al. prepared Ru single-atom catalyst ($Ru/TiO_2@CN$) by loading anatase and rutile mixed-phase TiO_2 on nitrogen-doped amorphous carbon through high-temperature calcination (Zhang et al., 2021). At room temperature, the conversion of LA and selectivity of GVL could reach 100% through hydrogenation and dehydration reactions. The turnover frequency (TOF) of the catalyst was about 35 times higher than that of the industrial Ru/C catalyst, also with superior selectivity toward GVL. In addition, the mechanism study showed that LA is first converted to HPA through the hydrogenation process, and then HPA is rapidly dehydrated to GVL. The stability of 0.85 wt% $Ru/ZrO_2@C$ catalyst prepared by wet impregnation method for the conversion of LA to GVL was significantly improved (Cao et al., 2017). $ZrO_2@C$ support, with a nano t-ZrO_2 (3.3 nm) structure embedded in amorphous carbon, was obtained by thermal decomposition of UiO-66 material (Zr-MOF). The catalytic performance of $Ru/ZrO_2@C$ in LA-to-GVL conversion was tested under 10 bar H_2 at 150°C in an aqueous solution, and compared with that of commercial 5 wt% Ru/C. Both catalysts could achieve the full conversion of LA and the quantitative yield of GVL, while 5 wt% Ru/C exhibited poor deactivation resistance after the first operation. Inductively coupled plasma optical emission spectroscopy (ICP), X-ray photoelectron spectroscopy (XPS), high-resolution transmission electron microscopy (HR-TEM), aberration-corrected scanning transmission electron microscopy (AC-STEM), temperature-programmed reduction (TPR), and physical adsorption data showed that the rapid deactivation of Ru/C was mainly due to the leaching of Ru and the loss of surface area caused by carbon deposition in micropores (Cao et al., 2017). In contrast, the self-made $Ru/ZrO_2@C$ catalyst could be repeatedly recycled in water and high proton aqueous solution, with no significant decrease in catalytic performance. Yang et al. reported a single-atom catalyst (SAC) with a core-shell structure synthesized by core-shell bistability strategy using amine-modified Ru_1/Fe_3O_4 as the core and periodic mesoporous organic silicon (PMO) as the shell (Yang et al., 2021). The Ru atom (0.76 wt%) was inserted into the oxygen vacancy of Fe_3O_4 spheres and stabilized by the amine group of 1,6-hexanediamine. Hollow PMO spheres are hydrophobic, which provides a strong barrier for the core of internal Ru_1/

Fe_3O_4, while the mesopores of the shell (4.2 nm) together with the cavity enhance the porosity of the catalyst. The conversion rate of LA was up to 99% with the GVL selectivity of up to 98.9%, while the high catalyst stability was still maintained after seven cycles. Regulating the electronic structure of metal catalysts can improve the catalyst performance, but it is very challenging work to regulate the electronic structure of atom-level catalysts. Fortunately, a RuCo single-atom alloy (SAA) catalyst was recently reported, in which precisely tailored electron-rich Ru atoms were confined to Co lattices, and ZIF-67 containing Ru was prepared by pyrolysis (Shao et al., 2021). The experimental study and calculation simulation showed that its activity was derived from the intrinsic active site of RuCo SAA. It was further illustrated that the electron-rich Ru single atom promoted the adsorption of C=O/H_2 and the dissociation of H_2 to H atom, especially beneficial to hydrogenation of the unsaturated γ-C of LA, which is the rate-determining step of LA hydrogenation. The more Ru content, the better the reaction activity of RuCo is for LA-to-GVL, and the TOF value could reach 3500 h^{-1}, which is 27 times higher than that of commercial 5 wt% Ru/C catalyst. Han et al. also reported a strategy using notched polyoxomtalate (N-POM) to immobilize Ru atoms, which could prevent the aggregation of Ru during pyrolysis and obtain atom-dispersed Ru catalysts anchored onto uniform subsupporter WO_x clusters on carbon-nitrogen ($Ru_1@WO_x$/CN) (Han et al., 2021). The synthesized $Ru_1@WO_x$/CN catalyst had good catalytic activity for the hydrogenation of LA to GVL under solvent-free conditions (99% conversion, and 100% selectivity). Properly regulating the active center of the Ru electronic structure can promote the formation and dehydration of HPA intermediates to form GVL. The N-POM strategy is also excellent in preparing a series of atom-dispersed noble metal atoms, which provides an opportunity to find SACs. The stability of the catalyst in polar solvents is also a very important indicator in the catalytic upgrading of the biomass platform molecules. The activity, selectivity, and stability of Ru-based catalysts supported on TiO_2, ZrO_2, and C in the conversion of GVL from LA at 30 bar H_2 and 150°C were investigated (Ftouni et al., 2016). All the tested catalysts showed good GVL yield in fresh use, but only Ru/ZrO_2 catalyst could maintain high yield in multiple cycles. Surprisingly, the widely used Ru/TiO_2 catalyst showed rapid deactivation after the first catalytic test. The characterization structure showed that the partial deactivation of Ru was attributed to the reduction of Ti support and the coating of Ru nanoparticles, namely the interaction of harmful strong metal supports, rather than the sintering or coking of Ru. In contrast, the Zr support showed no signs of activity reduction after five cycles and had high morphological and structural stability. It is worth noting that in the fresh Ru/ZrO_2 catalyst, even if the Ru loading is 1 wt%, Ru can still be completely dispersed on the fresh catalyst, and some Ru nanoparticles can be observed after recycling. Further studies on Ru/ZrO_2 catalysts showed that the dioxane was easily replaced by milder solvents, including GVL itself. Recently, in addition to the SACs constructed with Ru as the active center, which shows excellent catalytic performance in the research system of LA-to-GVL conversion, Ir-based SACs have also come into the vision

of researchers. Cao et al. first reported an ultra-stable Ir-based SAC (0.6 wt% Ir@ZrO$_2$@C) (Cao et al., 2019). In polar and proton reaction media (pH = 3 and pH = 1) under harsh conditions (T = 155°C, P$_{H2}$ = 40 bar), 2.7 wt% Ir/C and 0.6 wt % Ir/ZrO$_2$ nanocatalysts showed significant deactivation in recycling experiments, mainly due to the leaching of Ir into acidic reaction media. In contrast, Ir@ZrO$_2$@C SAC catalyst showed advantages in selectivity and unprecedented stability toward GVL, which could be recycled continuously seven times (pH = 3) and six times (pH = 1) in aqueous solution without deactivation and metal sintering or leaching. It is thus can be observed that the *in-situ* synthesis process that limits the entry of a single atom into the metal-organic framework by space proves to be an effective method for preparing acid-resistant solid catalysts.

PREPARATION AND CHARACTERIZATION

The catalytic performance of SACs with a good structure and coordination environment is greatly improved, which is helpful for the identification of active sites and the study of catalytic mechanisms at an atomic level. Although SACs have made proud achievements in various catalytic fields such as thermal catalysis, photo-catalysis, electro-catalysis, and photoelectron-catalysis, the preparation of highly dispersed SACs still presents some challenges (Ji et al., 2020). Here, the synthesis strategies of SACs are summarized for a better understanding of the construction process of SACs to promote the application of SACs for LA-to-GVL (e.g., impregnation, co-precipitation, spatial confinement, coordination, and defect strategy) (**Figure 1**). As a typical preparation method, the impregnation and co-precipitation methods are of great significance for the preparation of SACs by controlling metal loadings and selecting suitable high surface area supports (Wei et al., 2014; Zhang X et al., 2018; Ye et al., 2019). For example, Ftouni et al. prepared two 1 wt% Ru catalysts supported on TiO$_2$ and monoclinic ZrO$_2$ by wet impregnation method (Ftouni et al., 2016). The spatial confinement strategy is to disperse single atoms in space using porous materials such as zeolites (Masoumifard et al., 2018; Liu L et al., 2020), metal-organic frameworks (MOFs) (Jiao and Jiang, 2019), and covalent organic frameworks (COFs) (Yi et al., 2018; Zhong et al., 2019). N-POM was used to confine Ru atoms to prepare highly dispersed Ru1@WO$_x$/CN catalysts for producing GVL (Han et al., 2021). The coordination usually takes the target single atom as the coordination center, which then coordinates with the ligand containing lone pair electrons to form highly dispersed SACs. Ligands commonly used are polymers and polymer-derived materials with abundant heteroatoms (Pan et al., 2018; He et al., 2019), MOFs and their derivatives (Zhang et al., 2016; Yang et al., 2019), carbon-based materials (Li X et al., 2020), and C$_3$N$_4$ and graphdiyne (Tan et al., 2017). The defect strategy is to prepare materials with dispersed defect sites from relatively intact materials, followed by introducing single atoms into the defect sites to form highly dispersed SACs (Beniya and Higashi, 2019). These materials usually include oxides, hydroxides (Dvorak et al., 2016; Sun et al., 2019),

graphene, and other deficiency-rich materials (Fei et al., 2019). The strategy of direct conversion of metal nanoparticles into SACs is to create suitable synthesis conditions to break the metal bond of nanoparticles and form a new bond between the single metal atom and the anchor chain of the support (Moliner et al., 2016). The "top-down" strategy is to directly convert metal block materials and metal oxide powers materials into SACs (Qu et al., 2018). Single-atom alloy strategy is dependent on the dispersion of metal single-atom sites into another metal nanomaterial (Greiner et al., 2018; Li M et al., 2019; Shao et al., 2021). Chemical etching strategies include direct etching of bulk metals and nanoparticles (Qiu et al., 2015), and indirect template-assisted etching into SACs (Han et al., 2017; Sun et al., 2018). Atomic layer deposition (ALD) technology has a good ability to control the deposition of single atom or cluster on the support, so it is one of the powerful methods to accurately prepare ideal single-atom materials (Sun et al., 2013; Zhang L et al., 2018). In addition, other preparation strategies that are not commonly used include photochemistry method (Karkas et al., 2016), electrochemistry method (Zhang et al., 2017), freezing-assisted method (Wei et al., 2017), microwave-assisted method (Bilecka and Niederberger, 2010), ball-milling method (Cui et al., 2016), ionic-liquid-assisted method (Xi and Sun, 2019), and so on.

With continuous efforts in recent years, researchers have developed a variety of effective synthesis strategies, as discussed above. In connection to this, how to reveal the isolated reactive centers and overall structural information of SACs is also a very important link. In this mini-review paper, the structural characterization of isolated reactive centers in SACs (especially the Ru-based SACs for LA-to-GVL conversion) was disclosed by using advanced technologies such as electron microscopy and spectroscopy (**Figure 1**) (Xue et al., 2022). Transmission electron microscopy (TEM) with the atomic resolution has been developed as an effective method to study the detailed structural information of isolated reaction centers and their interactions with supports. The additional energy dispersive X-ray (EDX) detector of scanning transmission electron microscopy (STEM) can further provide element mappings, clarify the atomic dispersion of metal atoms on supports, and further evaluate the dispersion degree of single atoms. In addition, aberration-corrected high-angle annular dark-field scanning transmission electron microscopy (AC-HAADF-STEM) can easily confirm the existence of isolated reaction centers on the supports, as long as the metal atoms exhibit a much higher atomic number than the supporting elements (Lee et al., 2019; Chen et al., 2020). Although electron microscope images provide effective information to identify the structural information of the catalysts, it should be noted that there are some limitations in its application in structural characterization. Due to the limited electron penetration ability of microscopic technology, it is difficult to observe the isolated metal atoms modified in the bulk phase or cavities, rather than the surface structure. In addition, the electron microscope can only image the local structure, and cannot provide the overall structure information of the SACs (Liu J et al., 2020). Therefore, some additional spectral methods are

needed to provide supplementary data and support the existence of isolated metal sites in SACs. For example, X-ray photoelectron spectroscopy (XPS) is widely used to reveal the surface valence structure of SACs. Compared with pure metal, the obvious change of binding energy may explain the oxidation state of isolated metal atoms and exclude the existence of nanoparticles (Han et al., 2021; Shao et al., 2021). In addition, X-ray absorption spectroscopy (XAS) is one of the most commonly used and powerful tools to characterize SACs, including X-ray absorption near-edge structure (XANES) spectroscopy and the extended X-ray absorption fine structure (EXAFS) (Pan et al., 2019; Qiao et al., 2022). XANES can provide local electronic state information of the detected elements, while EXAFS can provide a high-resolution coordination environment and local geometry details of isolated metal sites. As site-specific characterization techniques, Fourier transform infrared spectroscopy (FTIR) and Raman spectroscopy are also widely used to evaluate the existence of isolated metal sites (Li et al., 2016; Fang et al., 2018), because they have obvious displacement relative to clusters or nanoparticles. The theoretical calculation also is one of the most important research methods (Han et al., 2021), state density, wave function $|\Psi|^2$, and modeling can verify each other with electron microscopy and spectroscopy. Taking together, the above characterization methods are conducive to revealing the role of SACs in the LA-to-GVL conversion system, which provides an effective basis for the visualization of the system in the future.

CONCLUSION AND PERSPECTIVES

The over-exploitation of fossil resources has caused serious social and environmental problems, and the high-value conversion of renewable resources has gradually become a global research upsurge. This mini-review focuses on the conversion of LA to GVL over SACs, and also extends to the involved reaction mechanism (e.g., hydrogenation, cyclization, and dehydration), synthesis methods (e.g., impregnation, co-precipitation, spatial

confinement, self-assembling, and defect sites), and structural characterization methods (e.g., electron microscopy, and spectroscopy) of SACs. Both SACs and traditional heterogeneous catalysts show high activity and selectivity in the catalytic conversion of LA to GVL. However, traditional heterogeneous catalysts tend to lose activity after reaction, while SACs show excellent stability. At present, the SACs in this field mainly use Ru species as the active sites. Therefore, the development of SCAs with cheap transition metals as the active sites is one of the major tasks for LA-to-GVL, which is conducive to reducing the catalyst cost and promoting the commercialization of this field. In addition, the development of cleaner and more sustainable catalytic systems for LA-to-GVL is also a hot topic for future research, such as single-atom electro- and photocatalytic systems. In conclusion, SACs have great potential in large-scale catalytic production of GVL from LA. Further development of facile preparation methods of SACs and eco-friendly catalytic processes, as well as elucidation of the single-atom active center is challenging but an unprecedented opportunity to promote the industrialization of SACs for biomass valorization.

AUTHOR CONTRIBUTIONS

YM organized and prepared this manuscript; YJ made preliminary revisions to the manuscript; DC and JH participated in literature collection and collation; HZ and HL supervised and contributed to reviewing the manuscript.

FUNDING

REFERENCES

Beniya, A., and Higashi, S. (2019). Towards Dense Single-Atom Catalysts for Future Automotive Applications. *Nat. Catal.* 2, 590–602. doi:10.1038/s41929-019-0282-y

Bilecka, I., and Niederberger, M. (2010). Microwave Chemistry for Inorganic Nanomaterials Synthesis. *Nanoscale* 2, 1358–1374. doi:10.1039/b9nr00377k

Cai, X., Xu, Q., Tu, G., Fu, Y., Zhang, F., and Zhu, W. (2019). Synergistic Catalysis of Ruthenium Nanoparticles and Polyoxometalate Integrated within Single UiO−66 Microcrystals for Boosting the Efficiency of Methyl Levulinate to γ-Valerolactone. *Front. Chem.* 7, 42. doi:10.3389/fchem.2019.00042

Cao, W., Lin, L., Qi, H., He, Q., Wu, Z., Wang, A., et al. (2019). In-situ Synthesis of Single-Atom Ir by Utilizing Metal-Organic Frameworks: An Acid-Resistant Catalyst for Hydrogenation of Levulinic Acid to γ-valerolactone. *J. Catal.* 373, 161–172. doi:10.1016/j.jcat.2019.03.035

Cao, W., Luo, W., Ge, H., Su, Y., Wang, A., and Zhang, T. (2017). UiO-66 Derived Ru/ZrO₂@C as a Highly Stable Catalyst for Hydrogenation of Levulinic Acid to γ-valerolactone. *Green. Chem.* 19, 2201–2211. doi:10.1039/c7gc00512a

Chen, Y., Ji, S., Chen, C., Peng, Q., Wang, D., and Li, Y. (2018). Single-Atom Catalysts: Synthetic Strategies and Electrochemical Applications. *Joule* 2, 1242–1264. doi:10.1016/j.joule.2018.06.019

Chen, Y., Ji, S., Sun, W., Lei, Y., Wang, Q., Li, A., et al. (2020). Engineering the Atomic Interface with Single Platinum Atoms for Enhanced Photocatalytic Hydrogen Production. *Angew. Chem. Int. Ed.* 59, 1295–1301. doi:10.1002/anie.201912439

Cui, X., Xiao, J., Wu, Y., Du, P., Si, R., Yang, H., et al. (2016). A Graphene Composite Material with Single Cobalt Active Sites: A Highly Efficient Counter Electrode for Dye-Sensitized Solar Cells. *Angew. Chem. Int. Ed.* 55, 6708–6712. doi:10.1002/anie.201602097

De, S., Burange, A. S., and Luque, R. (2022). Conversion of Biomass-Derived Feedstocks into Value-Added Chemicals over Single-Atom Catalysts. *Green. Chem.* 24, 2267–2286. doi:10.1039/d1gc04285h

Ding, S., Hülsey, M. J., Pérez-Ramírez, J., and Yan, N. (2019). Transforming Energy with Single-Atom Catalysts. *Joule* 3, 2897–2929. doi:10.1016/j.joule.2019.09.015

Dutta, S., Yu, I. K. M., Tsang, D. C. W., Ng, Y. H., Ok, Y. S., Sherwood, J., et al. (2019). Green Synthesis of Gamma-Valerolactone (GVL) through Hydrogenation of Biomass-Derived Levulinic Acid Using Non-noble Metal

Catalysts: A Critical Review. *Chem. Eng. J.* 372, 992–1006. doi:10.1016/j.cej.2019.04.199

Dvořák, F., Farnesi Camellone, M., Tovt, A., Tran, N.-D., Negreiros, F. R., Vorokhta, M., et al. (2016). Creating Single-Atom Pt-Ceria Catalysts by Surface Step Decoration. *Nat. Commun.* 7, 10801. doi:10.1038/ncomms10801

Fang, X., Shang, Q., Wang, Y., Jiao, L., Yao, T., Li, Y., et al. (2018). Single Pt Atoms Confined into a Metal-Organic Framework for Efficient Photocatalysis. *Adv. Mater.* 30, 1705112. doi:10.1002/adma.201705112

Fei, H., Dong, J., Chen, D., Hu, T., Duan, X., Shakir, I., et al. (2019). Single Atom Electrocatalysts Supported on Graphene or Graphene-like Carbons. *Chem. Soc. Rev.* 48, 5207–5241. doi:10.1039/c9cs00422j

Ftouni, J., Muñoz-Murillo, A., Goryachev, A., Hofmann, J. P., Hensen, E. J. M., Lu, L., et al. (2016). ZrO$_2$ Is Preferred over TiO2 as Support for the Ru-Catalyzed Hydrogenation of Levulinic Acid to γ-Valerolactone. *ACS Catal.* 6, 5462–5472. doi:10.1021/acscatal.6b00730

Galletti, A. M. R., Antonetti, C., De Luise, V., and Martinelli, M. (2012). A Sustainable Process for the Production of γ-valerolactone by Hydrogenation of Biomass-Derived Levulinic Acid. *Green. Chem.* 14, 688. doi:10.1039/c2gc15872h

Greiner, M. T., Jones, T. E., Beeg, S., Zwiener, L., Scherzer, M., Girgsdies, F., et al. (2018). Free-atom-like D States in Single-Atom alloy Catalysts. *Nat. Chem* 10, 1008–1015. doi:10.1038/s41557-018-0125-5

Han, Y., Dai, J., Xu, R., Ai, W., Zheng, L., Wang, Y., et al. (2021). Notched-Polyoxometalate Strategy to Fabricate Atomically Dispersed Ru Catalysts for Biomass Conversion. *ACS Catal.* 11, 2669–2675. doi:10.1021/acscatal.0c04006

Han, Y., Wang, Y.-G., Chen, W., Xu, R., Zheng, L., Zhang, J., et al. (2017). Hollow N-Doped Carbon Spheres with Isolated Cobalt Single Atomic Sites: Superior Electrocatalysts for Oxygen Reduction. *J. Am. Chem. Soc.* 139, 17269–17272. doi:10.1021/jacs.7b10194

He, X., He, Q., Deng, Y., Peng, M., Chen, H., Zhang, Y., et al. (2019). A Versatile Route to Fabricate Single Atom Catalysts with High Chemoselectivity and Regioselectivity in Hydrogenation. *Nat. Commun.* 10, 3663. doi:10.1038/s41467-019-11619-6

Ji, S., Chen, Y., Wang, X., Zhang, Z., Wang, D., and Li, Y. (2020). Chemical Synthesis of Single Atomic Site Catalysts. *Chem. Rev.* 120, 11900–11955. doi:10.1021/acs.chemrev.9b00818

Jiao, L., and Jiang, H.-L. (2019). Metal-Organic-Framework-Based Single-Atom Catalysts for Energy Applications. *Chem* 5, 786–804. doi:10.1016/j.chempr.2018.12.011

Kärkäs, M. D., Porco, J. A., Jr., and Stephenson, C. R. J. (2016). Photochemical Approaches to Complex Chemotypes: Applications in Natural Product Synthesis. *Chem. Rev.* 116, 9683–9747. doi:10.1021/acs.chemrev.5b00760

Khan, A. S., Man, Z., Bustam, M. A., Nasrullah, A., Ullah, Z., Sarwono, A., et al. (2018). Efficient Conversion of Lignocellulosic Biomass to Levulinic Acid Using Acidic Ionic Liquids. *Carbohydr. Polym.* 181, 208–214. doi:10.1016/j.carbpol.2017.10.064

Lee, B.-H., Park, S., Kim, M., Sinha, A. K., Lee, S. C., Jung, E., et al. (2019). Reversible and Cooperative Photoactivation of Single-Atom Cu/TiO$_2$ Photocatalysts. *Nat. Mater.* 18, 620–626. doi:10.1038/s41563-019-0344-1

Li, H., Guo, H., Fang, Z., Aida, T. M., and Smith, R. L. (2020). Cycloamination Strategies for Renewable N-Heterocycles. *Green. Chem.* 22, 582–611. doi:10.1039/c9gc03655e

Li, H., Li, Y., Fang, Z., and Smith, R. L. (2019). Efficient Catalytic Transfer Hydrogenation of Biomass-Based Furfural to Furfuryl Alcohol with Recyclable Hf-Phenylphosphonate Nanohybrids. *Catal. Today* 319, 84–92. doi:10.1016/j.cattod.2018.04.056

Li, H., Saravanamurugan, S., Yang, S., and Riisager, A. (2015). Catalytic Alkylation of 2-Methylfuran with Formalin Using Supported Acidic Ionic Liquids. *ACS Sustain. Chem. Eng.* 3, 3274–3280. doi:10.1021/acssuschemeng.5b00850

Li, H., Zhao, W., and Fang, Z. (2017). Hydrophobic Pd Nanocatalysts for One-Pot and High-Yield Production of Liquid Furanic Biofuels at Low Temperatures. *Appl. Catal. B: Environ.* 215, 18–27. doi:10.1016/j.apcatb.2017.05.039

Li, M., Duanmu, K., Wan, C., Cheng, T., Zhang, L., Dai, S., et al. (2019). Single-atom Tailoring of Platinum Nanocatalysts for High-Performance Multifunctional Electrocatalysis. *Nat. Catal.* 2, 495–503. doi:10.1038/s41929-019-0279-6

Li, X., Rong, H., Zhang, J., Wang, D., and Li, Y. (2020). Modulating the Local Coordination Environment of Single-Atom Catalysts for Enhanced Catalytic Performance. *Nano Res.* 13, 1842–1855. doi:10.1007/s12274-020-2755-3

Li, Y., Wang, Z., Xia, T., Ju, H., Zhang, K., Long, R., et al. (2016). Implementing Metal-To-Ligand Charge Transfer in Organic Semiconductor for Improved Visible-Near-Infrared Photocatalysis. *Adv. Mater.* 28, 6959–6965. doi:10.1002/adma.201601960

Lin, Z., Luo, M., Zhang, Y., Wu, X., Fu, Y., Zhang, F., et al. (2018). Coupling Ru Nanoparticles and Sulfonic Acid Moieties on Single MIL-101 Microcrystals for Upgrading Methyl Levulinate into γ-valerolactone. *Appl. Catal. A: Gen.* 563, 54–63. doi:10.1016/j.apcata.2018.06.027

Liu, J., Li, H., Liu, Y.-C., Lu, Y.-M., He, J., Liu, X.-F., et al. (2015). Catalytic Conversion of Glucose to 5-hydroxymethylfurfural over Nano-Sized Mesoporous Al2O3-B2o3 Solid Acids. *Catal. Commun.* 62, 19–23. doi:10.1016/j.catcom.2015.01.008

Liu, J., Wu, H., Li, F., Feng, X., Zhang, P., and Gao, L. (2020). Recent Progress in Non-Precious Metal Single Atomic Catalysts for Solar and Non-Solar Driven Hydrogen Evolution Reaction. *Adv. Sustain. Syst.* 4, 2000151. doi:10.1002/adsu.202000151

Liu, L., Wang, N., Zhu, C., Liu, X., Zhu, Y., Guo, P., et al. (2020). Direct Imaging of Atomically Dispersed Molybdenum that Enables Location of Aluminum in the Framework of Zeolite ZSM-5. *Angew. Chem. Int. Ed.* 59, 819–825. doi:10.1002/anie.201909834

Mai, E. F., Machado, M. A., Davies, T. E., Lopez-Sanchez, J. A., and Teixeira da Silva, V. (2014). Molybdenum Carbide Nanoparticles within Carbon Nanotubes as superior Catalysts for γ-valerolactone Production via Levulinic Acid Hydrogenation. *Green. Chem.* 16, 4092–4097. doi:10.1039/c4gc00920g

Masoumifard, N., Guillet-Nicolas, R., and Kleitz, F. (2018). Synthesis of Engineered Zeolitic Materials: From Classical Zeolites to Hierarchical Core-Shell Materials. *Adv. Mater.* 30, 1704439. doi:10.1002/adma.201704439

Meng, Y., and Li, H. (2021). Electrocatalytic Oxidation of Biomass-Derived 5-Hydroxymethylfurfural to 2,5-Furandicarboxylic Acid Coupled with H$_2$ Evolution. *Curr. Org. Chem.* 25, 2810–2814. doi:10.2174/1385272825666210927101643

Meng, Y., Yang, S., and Li, H. (2022). Electro- and Photocatalytic Oxidative Upgrading of Bio-based 5-Hydroxymethylfurfural. *ChemSusChem* e202102581. doi:10.1002/cssc.202102581

Moliner, M., Gabay, J. E., Kliewer, C. E., Carr, R. T., Guzman, J., Casty, G. L., et al. (2016). Reversible Transformation of Pt Nanoparticles into Single Atoms inside High-Silica Chabazite Zeolite. *J. Am. Chem. Soc.* 138, 15743–15750. doi:10.1021/jacs.6b10169

Pan, Y., Chen, Y., Wu, K., Chen, Z., Liu, S., Cao, X., et al. (2019). Regulating the Coordination Structure of Single-Atom Fe-NxCy Catalytic Sites for Benzene Oxidation. *Nat. Commun.* 10, 4290. doi:10.1038/s41467-019-12362-8

Pan, Y., Liu, S., Sun, K., Chen, X., Wang, B., Wu, K., et al. (2018). A Bimetallic Zn/Fe Polyphthalocyanine-Derived Single-Atom Fe-N 4 Catalytic Site:A Superior Trifunctional Catalyst for Overall Water Splitting and Zn-Air Batteries. *Angew. Chem. Int. Ed.* 57, 8614–8618. doi:10.1002/anie.201804349

Qiao, S., He, Q., Zhang, P., Zhou, Y., Chen, S., Song, L., et al. (2022). Synchrotron-radiation Spectroscopic Identification towards Diverse Local Environments of Single-Atom Catalysts. *J. Mater. Chem. A.* 10, 5771–5791. doi:10.1039/d1ta08254j

Qiu, H.-J., Ito, Y., Cong, W., Tan, Y., Liu, P., Hirata, A., et al. (2015). Nanoporous Graphene with Single-Atom Nickel Dopants: An Efficient and Stable Catalyst for Electrochemical Hydrogen Production. *Angew. Chem. Int. Ed.* 54, 14031–14035. doi:10.1002/anie.201507381

Qu, Y., Li, Z., Chen, W., Lin, Y., Yuan, T., Yang, Z., et al. (2018). Direct Transformation of Bulk Copper into Copper Single Sites via Emitting and Trapping of Atoms. *Nat. Catal.* 1, 781–786. doi:10.1038/s41929-018-0146-x

Rackemann, D. W., and Doherty, W. O. (2011). The Conversion of Lignocellulosics to Levulinic Acid. *Biofuels, Bioprod. Bioref.* 5, 198–214. doi:10.1002/bbb.267

Ruppert, A. M., Weinberg, K., and Palkovits, R. (2012). Hydrogenolysis Goes Bio: from Carbohydrates and Sugar Alcohols to Platform Chemicals. *Angew. Chem. Int. Ed.* 51, 2564–2601. doi:10.1002/anie.201105125

Shao, S., Yang, Y., Sun, K., Yang, S., Li, A., Yang, F., et al. (2021). Electron-Rich Ruthenium Single-Atom Alloy for Aqueous Levulinic Acid Hydrogenation. *ACS Catal.* 11, 12146–12158. doi:10.1021/acscatal.1c03004

Sun, S., Zhang, G., Gauquelin, N., Chen, N., Zhou, J., Yang, S., et al. (2013). Single-atom Catalysis Using Pt/Graphene Achieved through Atomic Layer Deposition. *Sci. Rep.* 3, 175–183. doi:10.1038/srep01775

Sun, T., Zhao, S., Chen, W., Zhai, D., Dong, J., Wang, Y., et al. (2018). Single-atomic Cobalt Sites Embedded in Hierarchically Ordered Porous Nitrogen-Doped Carbon as a superior Bifunctional Electrocatalyst. *Proc. Natl. Acad. Sci. U.S.A.* 115, 12692–12697. doi:10.1073/pnas.1813605115

Sun, X., Chen, C., Liu, S., Hong, S., Zhu, Q., Qian, Q., et al. (2019). Aqueous CO 2 Reduction with High Efficiency Using α-Co(OH) 2 -Supported Atomic Ir Electrocatalysts. *Angew. Chem. Int. Ed.* 58, 4669–4673. doi:10.1002/anie.201900981

Tan, C., Cao, X., Wu, X.-J., He, Q., Yang, J., Zhang, X., et al. (2017). Recent Advances in Ultrathin Two-Dimensional Nanomaterials. *Chem. Rev.* 117, 6225–6331. doi:10.1021/acs.chemrev.6b00558

Wei, H., Huang, K., Wang, D., Zhang, R., Ge, B., Ma, J., et al. (2017). Iced Photochemical Reduction to Synthesize Atomically Dispersed Metals by Suppressing Nanocrystal Growth. *Nat. Commun.* 8, 1490. doi:10.1038/s41467-017-01521-4

Wei, H., Liu, X., Wang, A., Zhang, L., Qiao, B., Yang, X., et al. (2014). FeOx-supported Platinum Single-Atom and Pseudo-single-atom Catalysts for Chemoselective Hydrogenation of Functionalized Nitroarenes. *Nat. Commun.* 5, 5634. doi:10.1038/ncomms6634

Wright, W. R. H., and Palkovits, R. (2012). Development of Heterogeneous Catalysts for the Conversion of Levulinic Acid to γ-Valerolactone. *ChemSusChem* 5, 1657–1667. doi:10.1002/cssc.201200111

Xi, B., and Sun, X. (2019). Single-Atom Catalysts Electrostatically Stabilized by Ionic Liquids. *Chem* 5, 3012–3014. doi:10.1016/j.chempr.2019.11.013

Xue, Z.-H., Luan, D., Zhang, H., and Lou, X. W. (2022). Single-atom Catalysts for Photocatalytic Energy Conversion. *Joule* 6, 92–133. doi:10.1016/j.joule.2021.12.011

Yan, K., Lafleur, T., Wu, G., Liao, J., Ceng, C., and Xie, X. (2013). Highly Selective Production of Value-Added γ-valerolactone from Biomass-Derived Levulinic Acid Using the Robust Pd Nanoparticles. *Appl. Catal. A: Gen.* 468, 52–58. doi:10.1016/j.apcata.2013.08.037

Yang, D., Yu, H., He, T., Zuo, S., Liu, X., Yang, H., et al. (2019). Visible-light-switched Electron Transfer over Single Porphyrin-Metal Atom center for Highly Selective Electroreduction of Carbon Dioxide. *Nat. Commun.* 10, 3844. doi:10.1038/s41467-019-11817-2

Yang, Y., Yang, F., Wang, H., Zhou, B., and Hao, S. (2021). Amine-promoted Ru$_1$/Fe$_3$O$_4$ Encapsulated in Hollow Periodic Mesoporousorganosilica Sphere as a Highly Selective and Stable Catalyst for Aqueous Levulinic Acid Hydrogenation. *J. Colloid Interf. Sci.* 581, 167–176. doi:10.1016/j.jcis.2020.07.114

Ye, L., Duan, X., Wu, S., Wu, T.-S., Zhao, Y., Robertson, A. W., et al. (2019). Self-Regeneration of Au/CeO$_2$ Based Catalysts with Enhanced Activity and Ultra-stability for Acetylene Hydrochlorination. *Nat. Commun.* 10, 914. doi:10.1038/s41467-019-08827-5

Ye, L., Han, Y., Feng, J., and Lu, X. (2020). A Review about GVL Production from Lignocellulose: Focusing on the Full Components Utilization. *Ind. Crops Prod.* 144, 112031. doi:10.1016/j.indcrop.2019.112031

Yi, J.-D., Xu, R., Wu, Q., Zhang, T., Zang, K.-T., Luo, J., et al. (2018). Atomically Dispersed Iron-Nitrogen Active Sites within Porphyrinic Triazine-Based

Frameworks for Oxygen Reduction Reaction in Both Alkaline and Acidic Media. *ACS Energ. Lett.* 3, 883–889. doi:10.1021/acsenergylett.8b00245

Yuan, J., Li, S.-S., Yu, L., Liu, Y.-M., Cao, Y., He, H.-Y., et al. (2013). Copper-based Catalysts for the Efficient Conversion of Carbohydrate Biomass into γ-valerolactone in the Absence of Externally Added Hydrogen. *Energy Environ. Sci.* 6, 3308. doi:10.1039/c3ee40857d

Zhang, H., Li, H., Hu, Y., Venkateswara Rao, K. T., Xu, C., and Yang, S. (2019). Advances in Production of Bio-Based Ester Fuels with Heterogeneous Bifunctional Catalysts. *Renew. Sustain. Energ. Rev.* 114, 109296. doi:10.1016/j.rser.2019.109296

Zhang, H., Wei, J., Dong, J., Liu, G., Shi, L., An, P., et al. (2016). Efficient Visible-Light-Driven Carbon Dioxide Reduction by a Single-Atom Implanted Metal-Organic Framework. *Angew. Chem. Int. Ed.* 55, 14310–14314. doi:10.1002/anie.201608597

Zhang, K., Meng, Q., Wu, H., Yuan, T., Han, S., Zhai, J., et al. (2021). Levulinic Acid Hydrogenation to γ-valerolactone over Single Ru Atoms on a TiO$_2$@nitrogen Doped Carbon Support. *Green. Chem.* 23, 1621–1627. doi:10.1039/d0gc04108d

Zhang, L., Banis, M. N., and Sun, X. (2018). Single-atom Catalysts by the Atomic Layer Deposition Technique. *Natl. Sci. Rev.* 5, 628–630. doi:10.1093/nsr/nwy054

Zhang, L., Han, L., Liu, H., Liu, X., and Luo, J. (2017). Potential-Cycling Synthesis of Single Platinum Atoms for Efficient Hydrogen Evolution in Neutral Media. *Angew. Chem. Int. Ed.* 56, 13694–13698. doi:10.1002/anie.201706921

Zhang, X., Sun, Z., Wang, B., Tang, Y., Nguyen, L., Li, Y., et al. (2018). C-C Coupling on Single-Atom-Based Heterogeneous Catalyst. *J. Am. Chem. Soc.* 140, 954–962. doi:10.1021/jacs.7b09314

Zhang, Z. (2016). Synthesis of γ-Valerolactone from Carbohydrates and its Applications. *ChemSusChem* 9, 156–171. doi:10.1002/cssc.201501089

Zhong, W., Sa, R., Li, L., He, Y., Li, L., Bi, J., et al. (2019). A Covalent Organic Framework Bearing Single Ni Sites as a Synergistic Photocatalyst for Selective Photoreduction of CO$_2$ to CO. *J. Am. Chem. Soc.* 141, 7615–7621. doi:10.1021/jacs.9b02997

Recent Biotechnology Advances in Bio-Conversion of Lignin to Lipids by Bacterial Cultures

Huan Wang[1,2], Xiaodong Peng[3], Hu Li[1]*, Apostolos Giannis[4] and Chao He[5]*

[1]State Key Laboratory Breeding Base of Green Pesticide and Agricultural Bioengineering, Key Laboratory of Green Pesticide and Agricultural Bioengineering, Ministry of Education, State-Local Joint Laboratory for Comprehensive Utilization of Biomass, Center for R&D of Fine Chemicals, Guizhou University, Guiyang, China, [2]Guizhou Industry Polytechnic College, Guiyang, China, [3]Guizhou Institute of Products Quality Inspection and Testing, Guiyang, China, [4]School of Chemical and Environmental Engineering, Technical University of Crete, University Campus, Chania, Greece, [5]Faculty of Engineering and Natural Sciences, Tampere University, Tampere, Finland

The complexity and recalcitrance of the lignin structure is a major barrier to its efficient utilization and commercial production of high-value products. In recent years, the "bio-funneling" transformation ability of microorganisms has provided a significant opportunity for lignin conversion and integrated biorefinery. Based on the chemical structure of lignin, this mini-review introduces the recent advances of lignin depolymerization by bacterial strains and the application of microbial lignin degradation in lipids production. Furthermore, the current challenges, future trends and perspectives for microbe-based lignin conversion to lipids are discussed.

Keywords: lignin, bio-conversion, microbial depolymerization, lipids, bio-funneling

INTRODUCTION

The energy conversion of lignocellulosic biomass can effectively alleviate the pressure of energy crisis and environmental deterioration (Li et al., 2014; Liu et al., 2015; Li et al., 2017; Zhang and Wang, 2020). However, the sustainable and profitable development of the lignocellulose-based biorefinery industry relies on the holistic utilization of all carbon components, including cellulose, hemicellulose, and lignin (Li et al., 2015; Li H. et al., 2019; Zhao et al., 2019; Garlapati et al., 2020; Li et al., 2020a; Li et al., 2020b). Lignin is a three-dimensional biopolymer composed of three different phenylpropanoid monomers randomly polymerized by C-C and C-O bonds (Supanchaiyamat et al., 2019; Ali et al., 2021; Abu-Omar et al., 2021). Because of its high carbon-oxygen ratio and rich aromatics, it is the most promising material for generating products, such as biofuels and other high-value chemicals (Wang H. et al., 2019; Wang et al., 2021). However, the lack of efficient degradation and resource utilization technologies for lignin is the main bottleneck restricting the sustainability and cost-competitiveness of lignocellulose biorefinery (Sethupathy et al., 2022). The pulp and paper industry generates approximately 50 million tons of lignin annually with ca. 98%–99% being combusted for energy generation (Zevallos Torres et al., 2020).

Considering sustainability and industrialization, lignin-based biorefinery faces many challenges (Den et al., 2018; Yaguchi et al., 2020). The heterogeneous structure of lignin leads to its insolubility and diverse aromatics after depolymerization, which increases the difficulty of industrial transformation to target products. The diversity and complexity of linkages among the monomers increase the complexity of degradation. In addition, the degradation of lignin produces toxic inhibitors that require strong tolerance for microbial population.

The effective utilization of lignin has many significant advantages (Huang et al., 2022; Yao et al., 2022; Zhou et al., 2022). Firstly, it can improve the resource utilization efficiency and profitability of
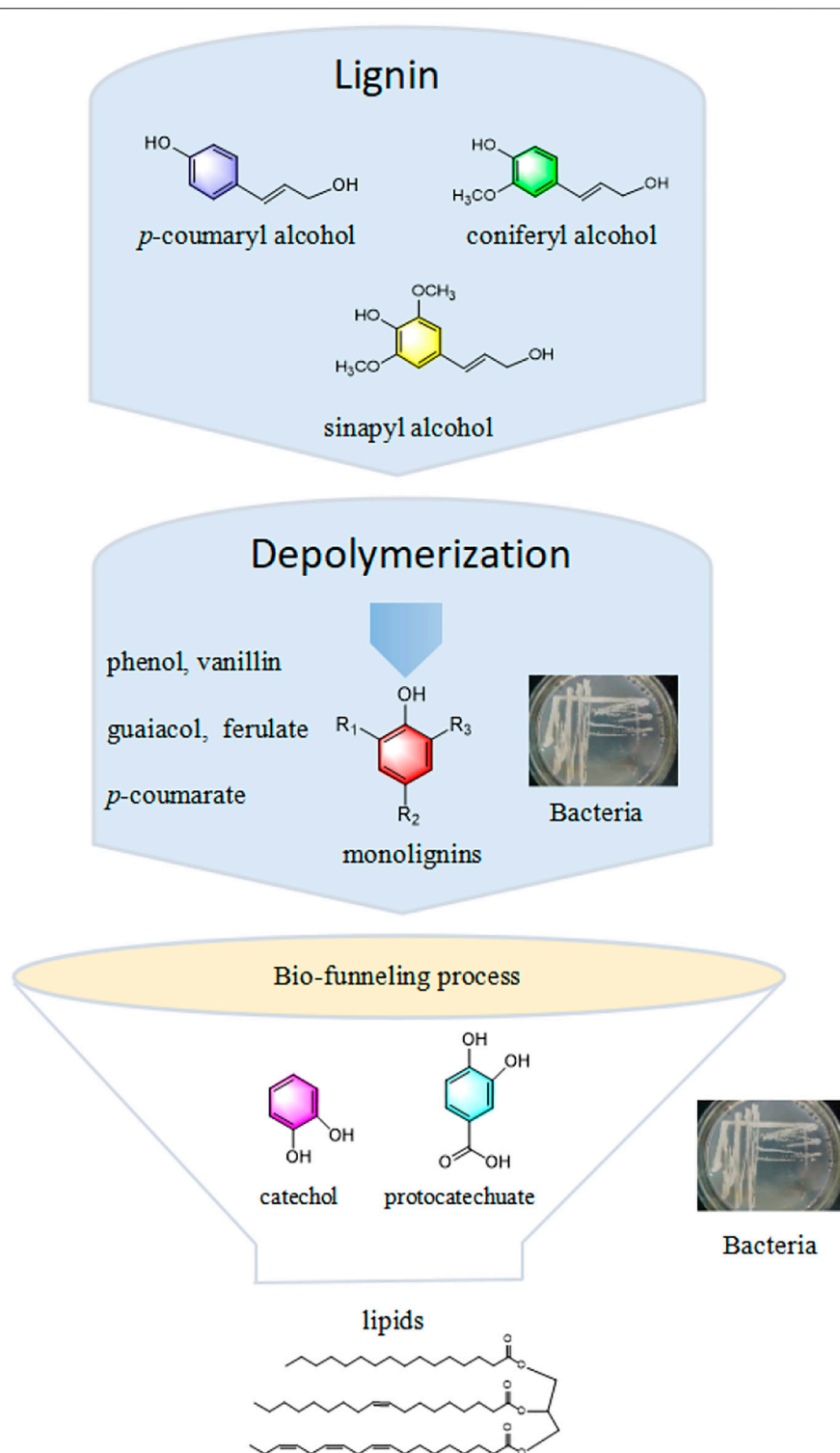
FIGURE 1 | The scheme of lipids production from lignin through a bio-funneling process.

lignocellulosic biomass. Secondly, selective utilization of lignin can avoid inhibition issues resulting from lignin degradation products in the fermentation process and non-productive binding of enzymes. Thirdly, appropriate utilization of lignin could mitigate the potential environmental pollution related to huge wastewater effluents from the pulp and paper industry.

In this regard, bio-valorization is considered potentially advantageous due to its mild condition, eco-friendliness, and

specificity in converting lignin into biofuels and chemicals (Singhania et al., 2022). Generally, lignin-derived bio-conversion mainly involves the microbial depolymerization of lignin into a broad spectrum of low-molecular-weight aromatics through oxidative enzymes secreted by microorganisms. These aromatics are then converted into value-added products, especially lipids, through microbial metabolism (Liu et al., 2019) (**Figure 1**). Conventional biodegradation achieved by fungi (e.g., brown- or white-rot fungi) has some drawbacks in terms of a long pretreatment period and poor environmental adaptability. In contrast, bacteria exhibit rapid reproduction, excellent adaptability to diverse environment, and easier genome editing, making them potential candidates for lignin-degrading strains in the future (Liu D. et al., 2018; Radhika et al., 2022). Therefore, the bio-funneling pathway process has attracted great attention due to its ability to overcome the heterogeneity of lignin-derivatives. The synthesis of lipids from lignin via the bio-funneling pathway using *Rhodococcus* strains has been widely reported in the literature (Li C. et al., 2019). Microorganism pool heterogeneous substrates into intermediates, such as protocatechuate or catechol, through a pathway known as the bio-funneling process. These intermediates further undergo central carbon metabolism to synthesize lipids by the cyclic cleavage, β-ketoadipate pathway (Salvachúa et al., 2015). To date, there are limited published reviews that have specifically addressed the use of bacteria for the production of lipids from lignin. This paper reviews current research advances on the conversion of lignin to lipids via biological pathways and possible strategies to improve lignin biotransformation, demonstrating an effective value chain from lignin to lipids in an eco-friendly and sustainable manner.

BIO-DEPOLYMERIZATION OF LIGNIN TO AROMATIC COMPOUNDS

Because of its natural aromatic skeleton, lignin has great potential for conversion into aromatics as biofuels or value-added chemicals, which plays an important role in improving carbon efficiency (Liao et al., 2020; Weng et al., 2021). Natural lignin mainly consists of three phenylpropanoid units, *p*-coumaryl alcohol (H-type unit), coniferyl alcohol (G-type unit), and sinapyl alcohol (S-type unit) (Becker and Wittmann, 2019), with a different number of methoxylation degrees on the aromatic rings (Mayr et al., 2021). The lignin monomers are conjugated by different bonds to form polymers with high resistance to chemical and biochemical depolymerization. Ether bonds, particularly β-O-4 ether linkages, predominate in lignin (Paananen et al., 2020; Szalaty et al., 2020).

Lignin depolymerization, the process of converting macro-molecular polymers into low-molecular-weight monomers or oligomers, is a key step in lignin valorization (Ragauskas et al., 2014). In nature, lignin degradation is induced by biological factors, such as fungi, bacteria, and abiotic factors (Radhika et al., 2021). Fungi are the most effective lignin-degrading microorganisms, mainly including white rot, brown rot, and soft rot, among which white rot has the strongest degradation

ability (Ponnusamy et al., 2019; Salvachua et al., 2020). Nevertheless, the harsh growth conditions and complex genetic system of fungi greatly limit their application in industry. In addition to fungi, bacteria have also been reported to have the ability to degrade lignin. Although the degradation performance is not as good as that of fungi, bacteria demonstrate strong environmental adaptability (Xu et al., 2021). Screening for bacteria with strong lignin depolymerization capacity and identification of secreted enzymes are crucial for effective lignin utilization (Xu et al., 2019). The direct use of industrial enzymes for depolymerization can avoid severe and complex processes (e.g., high temperature and pressure, hazardous and expensive chemicals, and catalysts). Particularly, oxidases (i.e., laccases and peroxidases) are potential candidates for lignin depolymerization (Hamalainen et al., 2018).

Bacteria Involved in the Depolymerization of Lignin

In the presence of oxygen or under anaerobic conditions, bacteria use lignin as a carbon source and then secrete oxidative enzymes to depolymerize lignin (Weng et al., 2021). *Rhodococcus*, *Proteobacteria*, and *pseudomonas* are the main bacteria that can degrade lignin effectively (Lee et al., 2019). Substrate sources and screening methods are key factors in obtaining bacteria with excellent lignin-degradation performance (Xu et al., 2019). Lignin-degrading bacteria are commonly found in lignin-rich environments, such as pulp and paper wastewater, eroded bamboo slips, soil, rotten wood, compost, and even termite gut (Xu R. et al., 2018). The commonly used screening method is to obtain the bacteria with ligninolytic capacity by using lignin or lignin-derivatives as the sole carbon source, and a suitable secondary screening model is then constructed to differentiate the degradability of lignin. For instance, dyes are often used to indicate the degradation activity of lignin due to its close structure to lignin and decolorization visualization (Xu Z. et al., 2018). *Pseudomonas putida NX-1*, *Klebsiella pneumoniae NX-1*, and *Ochrobactrum tritici* with lignin degradation capability were screened from the leaf molds using Kraft lignin as the sole carbon source, and then their capabilities to degrade lignin were verified by simulating dye decolorization and measuring decomposition enzyme activity efficiently (Xu Z. et al., 2018). The results showed that *Pseudomonas putida* NX-1 was the most capable for degrading lignin and was able to secrete laccase, lignin peroxidase (LiP), and Mn-peroxidase (MnP) efficiently. The researchers obtained two strains of lignin-degrading bacteria from the rainforest by the laccase activity against ABTS and their capabilities to degrade Kraft lignin and lignin model dimer guaiacylglycerol-β-guaiacyl ether with abundant lignin-linkage (Huang et al., 2013). *Bacillus amyloliquefaciens* SL-7 obtained from tobacco straw demonstrated better secretion of ligninolytic enzymes (MnP, LiP, and laccase) and achieved 28.55% of lignin degradation after 15 days with a comparable degradation rate to fungi, which could be an excellent strain for lignin degradation by overcoming the disadvantage of low bacterial activity (Mei et al., 2020).

TABLE 1 | Biosynthesis pathways of lignin to lipids through bacteria.

Strains	Carbon source	Innovative strategies	Yield	References
Rhodococcus opacus DSM 1069	Kraft lignin	O_2-pretreatment under alkaline environment	0.067 mg/ml	Wei et al. (2015)
Rhodococcus opacus	Corn stover	Ammonia fiber expansion-pretreated	32 mg/L	Wang Z. et al. (2019)
Rhodococcus opacus PD630 and *Rhodococcus jostii* RHA1 VanA⁻	Corn stover	Co-fermentation of wild and engineered bacteria	0.39 g lipid/g CDW	He et al. (2017)
Rhodococcus pyridinivorans CCZU-B16	Alkali lignin	Screening of new strains	0.52 g lipid/g CDW	Chong et al. (2017)
Rhodococcus opacus PD630	Corn stover	Multi-stage pretreatment method ALK-AHP	1.3 g/L	Le et al. (2017)
Rhodococcus jostii RHA1	Benzoate (Lignin-degradation products)	Nitrogen-limiting condition	55% of CDW	Amara et al. (2016)
Rhodococcus opacus DSM 1069	Pine organosolv pretreatment effluent	Organic solvent pretreatment	26.99 ± 2.88% of CDW	Wells et al. (2015)

Lignin-Depolymerizing Bacterial Enzymes

Ligninolytic enzymes, which are crucial for lignin valorization, are mainly divided into two groups, i.e., lignin modifying enzymes (LMEs) and lignin-degrading auxiliary enzymes (LDAs) (Iram et al., 2021). LMEs, including laccase and peroxidase (e.g., lignin peroxidase, manganese peroxidase, multifunctional peroxidases, etc.), are predominant oxidases that can directly depolymerize lignin. Although LDAs cannot directly depolymerize lignin, they can assist LMEs in the degradation of lignin (Reshmy et al., 2022). Unlike fungal lignin-depolymerizing oxidases, bacterial lignin depolymerization is dominated by laccase and DyP (Dye decolorizing peroxidase) (de Gonzalo et al., 2016). More importantly, bacterial enzymes possess higher thermal stability and robustness as compared to fungal enzymes.

Most enzymes operate under mild conditions and even acidic conditions, but most technical lignin is undissolvable under acidic conditions. Finnish biotechnology company MetGen Oy designs and supplies a genetically engineered commercial enzyme MetZyme® LIGNO™ which can function at higher pH of 10–11 and elevated temperatures with a certain reduction in lignin molecular weight and increased solubility (Hamalainen et al., 2018). This enzyme-mediated scheme provides high value for lignin valorization commercially. Extreme enzymes and extremophiles are very attractive in the future because of their ability to adapt to harsh processes and perform well in the bio-conversion process, potentially bringing enzymatic lignin decomposition closer to industrial applications (Zhu et al., 2022). Zhu et al. (2017) isolated a salt-tolerant and basophilic strain of *Bacillus ligniniphilus* L1 from abyssal sediments, and then identified 15 aromatics during the bio-conversion of alkaline lignin, exhibiting significant lignin-degrading capability and adaptability to extreme environments.

BIO-CONVERSION OF LIGNIN TO LIPIDS

As attractive feedstocks for biofuel production, lipids can be synthesized from lignin-based aromatic building blocks by oleaginous microorganisms with nearly 20% of lipids accumulation out of their dry cell weight (DCW) (Reshmy

et al., 2022). Prominent oleaginous bacteria can exhibit excellent lipid accumulation capacities, such as *Acinetobacter calcoaceticus* (lipid accumulation up to 27%–38% of their DCW), *Rhodococcus opacus* (25%), and *Bacillus alcalophilus* (18%–24%) (Iram et al., 2021). Biocatalytic processes that integrate upstream depolymerization and bacterial aromatic metabolic pathways (bio-funneling process) can overcome the lignin inherent heterogeneity (Linger et al., 2014). *Rhodococcus* species, the oleaginous microorganisms, have efficient metabolism and tolerability of aromatics derived from lignin and their relative adaptability in genetic manipulation makes them promising for industrial applications (Xiong et al., 2016; Shields-Menard et al., 2017).

In general, the bio-conversion of lignin to lipids after depolymerization generally involves three stages (Chen and Wan, 2017; Lee et al., 2019): 1) conversion of lignin-degraded oligomers or monomers to catechol or protocatechuate via the bio-funneling pathway, 2) ring-opening pathways of the aromatic skeleton and β-ketoadipate pathway to produce acetyl-CoA, and 3) synthesis of lipids by oleaginous microorganisms under deficient conditions (e.g., nitrogen limitation). Microbially involved lignin bioconversion processes often pose a barrier to industrial applications aiming at high yield and high efficiency in lignin use (Ponnusamy et al., 2019).

Bio-conversion of lignin to lipids has been effectively explored in terms of improved technology and development of new processes, such as pretreatment, co-culture, and other promising enhancement technologies, etc. A list of bacteria strains together with innovative strategies to produce lipids is shown in **Table 1**.

Pretreatment

Pretreatment is a crucial step in the integrated biorefinery (Zhang et al., 2021). Monitoring the lipid synthesis from lignin mediated by oleaginous microorganisms, it has been revealed that low-molecule-weight lignin-derived monomers were more favorable for lipid accumulation than macro-molecule of lignin. Therefore, integrating depolymerization processes that can reduce the molecular weight of lignin and break its

inherent recalcitrance, with microbial synthesis processes could be applied to improve the efficiency of lipid accumulation (Li X. et al., 2019).

In the study using *Rhodococcus opacus* DSM 1069 to convert Kraft lignin to lipids, Wei et al. (2015) found that bacteria acted poorly when directly using Kraft lignin as substrate. After O_2-pretreatment of Kraft lignin under an alkaline environment, the bacterium was able to use Kraft lignin and accumulate lipids with a maximum yield of 0.067 mg/ml. As compared to single pretreatment, combined pretreatment produced higher lipid concentration (12.8%–75.6%) because lignin-degrading bacteria released more monomers for use to achieve an optimal lipid yield of 1.83 g/L in fermentation. This indicates that combined pretreatment together with batch fermentation could be a promising strategy for efficient bio-conversion of lignin to lipids (Liu Z.-H. et al., 2018).

Co-Culture

In general, most industrial biosynthesis processes prefer to use a single engineered microorganism to facilitate the production control. But in a single microbe, there is a competition for cellular resources in different metabolic pathways (Borchert et al., 2022). The application of microbial co-culture systems can reduce these catabolic limitations, improve streams towards desired chemicals, or enhance microbial resistance to toxicity (Singh et al., 2019). Although multiple microbial cultures can increase the complexity of the bio-funnelling pathway towards a single product, the selection of compatible partners with synergistic functions could be challenging in the co-culture system (Zuniga et al., 2020). Further investigations are needed to elucidate the interactions between microorganisms and the dynamics of community structure in the system. Given the complementary nature of different bacteria in lignin depolymerization and assimilation, the use of bacterial communities can significantly improve the efficiency of the biological upgrading of lignin for lipids accumulation.

Li X. et al. (2019) set up a wild and engineered *Rhodococcus* co-culture system, which presented excellent capabilities to degrade lignin and accumulate lipids. After selective depletion of glucose by *Rhodococcus* strains, nearly half of the lignin was then depolymerized into monomers for cell growth and lipid synthesis. The highest lignin degradation rate was 23.2% for the single strain fermentation and 33.6% for the three co-cultured strains.

Some bacteria were found to promote the growth of microalgae (Subashchandrabose et al., 2011). The microalgal growth-promoting bacterium *Azospirillum brasilense* increased the total intracellular lipid content after co-immobilization with three strains of microalgae (de-Bashan et al., 2002). Introducing these engineered microbial communities with enhanced capacity provides another new concept for the production of lipids from lignin.

Other Promising Enhancement Technologies

Most of the lignin-derived aromatic compounds are inhibitory to microorganisms, resulting in reduction of the yield and tighter of lignocellulosic-based products (Singh et al., 2019).

Thus, it is imperative to develop robust, tolerant and productive strains for effective biorefinery (Zhang and Bao, 2022). Comprehensive lipidomic research applying adaptive evolution using phenol-only carbon source for *Rhodococcus opacus* PD630 revealed a correlation between the strain's lipid metabolism and phenol tolerance by affecting the constituent of mycolic acid and phospholipid membranes (Henson et al., 2018). Pelleted culture has been extensively studied for its high yield and ease of product collection, the low viscosity of the medium, and thus low energy consumption (Nair et al., 2016). Xu et al. (2022) reported for the first time the spontaneous formation of pellets by bacteria during fermentation with an alkaline treatment solution of maize stover as the carbon source, even in the absence of added chemical coagulants. It was found that the lipid content of the pellets was higher than that of the suspended biomass at low nitrogen concentrations. Moreover, this pellet form of microorganism has the potential for lipid production, suggesting a new strategy for the development of the biofuel industry. Liu et al. (2021) designed the "Plug-In Processes of Lignin" based on advanced pretreatment techniques to achieve a synergy of lignin biochemical conversion and carbohydrate production by reducing molecular weight and enhancing hydrophilic radicals to achieve profitable and sustainable biorefinery.

CONCLUSION

The efficient resource utilization of lignin can significantly improve the economic feasibility of lignocellulosic biorefinery towards sustainability and circularity. Tremendous progress has been made in recent decades in lignin valorization, however, more efforts are still desired to produce high-value compounds from lignin efficiently and economically. Lignin depolymerization plays a crucial role in bioconversion. Microbially mediated lignin depolymerization has become a hot spot of research because of its low energy consumption and eco-friendliness. Lignin-degrading bacteria could be a breakthrough in commercial utilization of lignin due to strong tolerance under extreme conditions, fast reaction rate, and ease of genetic manipulation. Despite some recent breakthroughs in the biotransformation of lignin to lipids, nitrogen optimization for exogenous protein expression and lipid accumulation, and improvement of production efficiency are main challenges in future research work. To address the challenges of lignin biotransformation into lipids, the industrial production of lipids from lignin by bacteria can be achieved by introducing emerging technologies, including predominant pretreatment techniques, adaptive evolutions, and genetic engineering. In the future, synergistic pathways could be elaborated for the production of lipids from the metabolism of sugars and aromatic substances. An effective value chain for depolymerization and bioconversion of lignin to lipids should be established in order to provide promising prospects for the production of biofuels.

AUTHOR CONTRIBUTIONS

HW and XP wrote the original draft. HL conceptualized and edited the review, and acquired the funding. AG edited the manuscript. CH conceptualized and edited the review.

REFERENCES

Abu-Omar, M. M., Barta, K., Beckham, G. T., Luterbacher, J. S., Ralph, J., Rinaldi, R., et al. (2021). Guidelines for Performing Lignin-First Biorefining. *Energy Environ. Sci.* 14 (1), 262–292. doi:10.1039/d0ee02870c

Ali, S. S., Al-Tohamy, R., Koutra, E., El-Naggar, A. H., Kornaros, M., and Sun, J. (2021). Valorizing Lignin-like Dyes and Textile Dyeing Wastewater by a Newly Constructed Lipid-Producing and Lignin Modifying Oleaginous Yeast Consortium Valued for Biodiesel and Bioremediation. *J. Hazard. Mater.* 403, 123575. doi:10.1016/j.jhazmat.2020.123575

Amara, S., Seghezzi, N., Otani, H., Diaz-Salazar, C., Liu, J., and Eltis, L. D. (2016). Characterization of Key Triacylglycerol Biosynthesis Processes in Rhodococci. *Sci. Rep.* 6, 24985. doi:10.1038/srep24985

Becker, J., and Wittmann, C. (2019). A Field of Dreams: Lignin Valorization into Chemicals, Materials, Fuels, and Health-Care Products. *Biotechnol. Adv.* 37 (6), 107360. doi:10.1016/j.biotechadv.2019.02.016

Borchert, A. J., Henson, W. R., and Beckham, G. T. (2022). Challenges and Opportunities in Biological Funneling of Heterogeneous and Toxic Substrates beyond Lignin. *Curr. Opin. Biotechnol.* 73, 1–13. doi:10.1016/j.copbio.2021.06.007

Chen, Z., and Wan, C. (2017). Biological Valorization Strategies for Converting Lignin into Fuels and Chemicals. *Renew. Sust. Energ. Rev.* 73, 610–621. doi:10.1016/j.rser.2017.01.166

Chong, G.-G., Huang, X.-J., Di, J.-H., Xu, D.-Z., He, Y.-C., Pei, Y.-N., et al. (2017). Biodegradation of Alkali Lignin by a Newly Isolated Rhodococcus Pyridinivorans CCZU-B16. *Bioproc. Biosyst. Eng.* 41 (4), 501–510. doi:10.1007/s00449-017-1884-x

de Gonzalo, G., Colpa, D. I., Habib, M. H. M., and Fraaije, M. W. (2016). Bacterial Enzymes Involved in Lignin Degradation. *J. Biotechnol.* 236, 110–119. doi:10.1016/j.jbiotec.2016.08.011

de-Bashan, L. E., Bashan, Y., Moreno, M., Lebsky, V. K., and Bustillos, J. J. (2002). Increased Pigment and Lipid Content, Lipid Variety, and Cell and Population Size of the *Microalgae chlorella* spp. When Co-immobilized in Alginate Beads with the Microalgae-Growth-Promoting Bacterium Azospirillum Brasilense. *Can. J. Microbiol.* 48 (6), 514–521. doi:10.1139/w02-051

Den, W., Sharma, V. K., Lee, M., Nadadur, G., and Varma, R. S. (2018). Lignocellulosic Biomass Transformations via Greener Oxidative Pretreatment Processes: Access to Energy and Value-Added Chemicals. *Front. Chem.* 6, 141–163. doi:10.3389/fchem.2018.00141

Garlapati, V. K., Chandel, A. K., Kumar, S. P. J., Sharma, S., Sevda, S., Ingle, A. P., et al. (2020). Circular Economy Aspects of Lignin: Towards a Lignocellulose Biorefinery. *Renew. Sust. Energ. Rev.* 130, 109977. doi:10.1016/j.rser.2020.109977

Hämäläinen, V., Grönroos, T., Suonpää, A., Heikkilä, M. W., Romein, B., Ihalainen, P., et al. (2018). Enzymatic Processes to Unlock the Lignin Value. *Front. Bioeng. Biotechnol.* 6, 20. doi:10.3389/fbioe.2018.00020

He, Y., Li, X., Ben, H., Xue, X., and Yang, B. (2017). Lipid Production from Dilute Alkali Corn Stover Lignin by Rhodococcus Strains. *ACS Sust. Chem. Eng.* 5 (3), 2302–2311. doi:10.1021/acssuschemeng.6b02627

Henson, W. R., Hsu, F.-F., Dantas, G., Moon, T. S., and Foston, M. (2018). Lipid Metabolism of Phenol-Tolerant Rhodococcus Opacus Strains for Lignin Bioconversion. *Biotechnol. Biofuels* 11, 339. doi:10.1186/s13068-018-1337-z

Huang, C., Jiang, X., Shen, X., Hu, J., Tang, W., Wu, X., et al. (2022). Lignin-enzyme Interaction: A Roadblock for Efficient Enzymatic Hydrolysis of Lignocellulosics. *Renew. Sust. Energ. Rev.* 154. doi:10.1016/j.rser.2021.111822

Huang, X.-F., Santhanam, N., Badri, D. V., Hunter, W. J., Manter, D. K., Decker, S. R., et al. (2013). Isolation and Characterization of Lignin-Degrading Bacteria from Rainforest Soils. *Biotechnol. Bioeng.* 110 (6), 1616–1626. doi:10.1002/bit.24833

Iram, A., Berenjian, A., and Demirci, A. (2021). A Review on the Utilization of Lignin as a Fermentation Substrate to Produce Lignin-Modifying Enzymes and Other Value-Added Products. *Molecules* 26 (10), 2960. doi:10.3390/molecules26102960

Le, R. K., Wells Jr., T., Jr, Das, P., Meng, X., Stoklosa, R. J., Bhalla, A., et al. (2017). Conversion of Corn stover Alkaline Pre-treatment Waste Streams into Biodiesel via Rhodococci. *RSC Adv.* 7 (7), 4108–4115. doi:10.1039/c6ra28033a

Lee, S., Kang, M., Bae, J.-H., Sohn, J.-H., and Sung, B. H. (2019). Bacterial Valorization of Lignin: Strains, Enzymes, Conversion Pathways, Biosensors, and Perspectives. *Front. Bioeng. Biotechnol.* 7, 209. doi:10.3389/fbioe.2019.00209

Li, C., Chen, C., Wu, X., Tsang, C.-W., Mou, J., Yan, J., et al. (2019). Recent Advancement in Lignin Biorefinery: With Special Focus on Enzymatic Degradation and Valorization. *Bioresour. Techn.* 291, 121898. doi:10.1016/j.biortech.2019.121898

Li, H., Guo, H., Fang, Z., Aida, T. M., and Smith, R. L. (2020b). Cycloamination Strategies for Renewable N-Heterocycles. *Green. Chem.* 22, 582–611. doi:10.1039/c9gc03655e

Li, H., Li, Y., Fang, Z., and Smith, R. L., Jr (2019). Efficient Catalytic Transfer Hydrogenation of Biomass-Based Furfural to Furfuryl Alcohol with Recyclable Hf-Phenylphosphonate Nanohybrids. *Catal. Today* 319, 84–92. doi:10.1016/j.cattod.2018.04.056

Li, H., Saravanamurugan, S., Yang, S., and Riisager, A. (2015). Catalytic Alkylation of 2-methylfuran with Formalin Using Supported Acidic Ionic Liquids. *ACS Sust. Chem. Eng.* 3, 3274–3280. doi:10.1021/acssuschemeng.5b00850

Li, H., Wu, H., Yu, Z., Zhang, H., and Yang, S. (2020a). CO$_2$ -Enabled Biomass Fractionation/Depolymerization: A Highly Versatile Pre-Step for Downstream Processing. *ChemSusChem* 13 (14), 3565–3582. doi:10.1002/cssc.202000575

Li, H., Zhang, Q., Bhadury, P., and Yang, S. (2014). Furan-type Compounds from Carbohydrates via Heterogeneous Catalysis. *Curr. Org. Chem.* 18, 547–597. doi:10.2174/13852728113176660138

Li, H., Zhao, W., and Fang, Z. (2017). Hydrophobic Pd Nanocatalysts for One-Pot and High-Yield Production of Liquid Furanic Biofuels at Low Temperatures. *Appl. Catal. B Environ.* 215, 18–27. doi:10.1016/j.apcatb.2017.05.039

Li, X., He, Y., Zhang, L., Xu, Z., Ben, H., Gaffrey, M. J., et al. (2019). Discovery of Potential Pathways for Biological Conversion of poplar wood into Lipids by Co-fermentation of Rhodococci Strains. *Biotechnol. Biofuels* 12, 60–75. doi:10.1186/s13068-019-1395-x

Liao, Y., Koelewijn, S.-F., Van Den Bossche, G., Van Aelst, J., Van Den Bosch, S., Renders, T., et al. (2020). A Sustainable Wood Biorefinery for Low-Carbon Footprint Chemicals Production. *Science* 367 (6484), 1385–1390. doi:10.1126/science.aau1567

Linger, J. G., Vardon, D. R., Guarnieri, M. T., Karp, E. M., Hunsinger, G. B., Franden, M. A., et al. (2014). Lignin Valorization through Integrated Biological Funneling and Chemical Catalysis. *Proc. Natl. Acad. Sci. U.S.A.* 111 (33), 12013–12018. doi:10.1073/pnas.1410657111

Liu, D., Yan, X., Zhuo, S., Si, M., Liu, M., Wang, S., et al. (2018). *Pandoraea* sp. B-6 Assists the Deep Eutectic Solvent Pretreatment of Rice Straw via Promoting Lignin Depolymerization. *Bioresour. Techn.* 257, 62–68. doi:10.1016/j.biortech.2018.02.029

Liu, J., Li, H., Liu, Y.-C., Lu, Y.-M., He, J., Liu, X.-F., et al. (2015). Catalytic Conversion of Glucose to 5-hydroxymethylfurfural over Nano-Sized Mesoporous Al2O3-B2o3 Solid Acids. *Catal. Commun.* 62, 19–23. doi:10.1016/j.catcom.2015.01.008

Liu, Z.-H., Hao, N., Wang, Y.-Y., Dou, C., Lin, F., Shen, R., et al. (2021). Transforming Biorefinery Designs with 'Plug-In Processes of Lignin' to Enable Economic Waste Valorization. *Nat. Commun.* 12 (1), 3912. doi:10.1038/s41467-021-23920-4

Liu, Z.-H., Le, R. K., Kosa, M., Yang, B., Yuan, J., and Ragauskas, A. J. (2019). Identifying and Creating Pathways to Improve Biological Lignin

Valorization. *Renew. Sust. Energ. Rev.* 105, 349–362. doi:10.1016/j.rser.2019.02.009

Liu, Z.-H., Xie, S., Lin, F., Jin, M., and Yuan, J. S. (2018). Combinatorial Pretreatment and Fermentation Optimization Enabled a Record Yield on Lignin Bioconversion. *Biotechnol. Biofuels* 11, 21. doi:10.1186/s13068-018-1021-3

Mayr, S. A., Subagia, R., Weiss, R., Schwaiger, N., Weber, H. K., Leitner, J., et al. (2021). Oxidation of Various Kraft Lignins with a Bacterial Laccase Enzyme. *Int. J. Mol. Sci.* 22 (23), 13161. doi:10.3390/ijms222313161

Mei, J., Shen, X., Gang, L., Xu, H., Wu, F., and Sheng, L. (2020). A Novel Lignin Degradation Bacteria-Bacillus Amyloliquefaciens SL-7 Used to Degrade Straw Lignin Efficiently. *Bioresour. Techn.* 310, 123445. doi:10.1016/j.biortech.2020.123445

Nair, R. B., Lennartsson, P. R., and Taherzadeh, M. J. (2016). Mycelial Pellet Formation by Edible Ascomycete Filamentous Fungi, Neurospora Intermedia. *AMB Expr.* 6 (1), 31. doi:10.1186/s13568-016-0203-2

Paananen, H., Eronen, E., Mäkinen, M., Jänis, J., Suvanto, M., and Pakkanen, T. T. (2020). Base-catalyzed Oxidative Depolymerization of Softwood Kraft Lignin. *Ind. Crops Prod.* 152, 112473. doi:10.1016/j.indcrop.2020.112473

Ponnusamy, V. K., Nguyen, D. D., Dharmaraja, J., Shobana, S., Banu, J. R., Saratale, R. G., et al. (2019). A Review on Lignin Structure, Pretreatments, Fermentation Reactions and Biorefinery Potential. *Bioresour. Techn.* 271, 462–472. doi:10.1016/j.biortech.2018.09.070

Radhika, N. L., Sachdeva, S., and Kumar, M. (2022). Lignin Depolymerization and Biotransformation to Industrially Important Chemicals/Biofuels. *Fuel* 312, 122935. doi:10.1016/j.fuel.2021.122935

Radhika, N. L., Sachdeva, S., and Kumar, M. (2021). Microbe Assisted Depolymerization of Lignin Rich Waste and its Conversion to Gaseous Biofuel. *J. Environ. Manage.* 300, 113684. doi:10.1016/j.jenvman.2021.113684

Ragauskas, A. J., Beckham, G. T., Biddy, M. J., Chandra, R., Chen, F., Davis, M. F., et al. (2014). Lignin Valorization: Improving Lignin Processing in the Biorefinery. *Science* 344 (6185), 1246843. doi:10.1126/science.1246843

Reshmy, R., Athiyaman Balakumaran, P., Divakar, K., Philip, E., Madhavan, A., Pugazhendhi, A., et al. (2022). Microbial Valorization of Lignin: Prospects and Challenges. *Bioresour. Techn.* 344 (Pt A), 126240. doi:10.1016/j.biortech.2021.126240

Salvachúa, D., Karp, E. M., Nimlos, C. T., Vardon, D. R., and Beckham, G. T. (2015). Towards Lignin Consolidated Bioprocessing: Simultaneous Lignin Depolymerization and Product Generation by Bacteria. *Green. Chem.* 17 (11), 4951–4967.

Salvachúa, D., Werner, A. Z., Pardo, I., Michalska, M., Black, B. A., Donohoe, B. S., et al. (2020). Outer Membrane Vesicles Catabolize Lignin-Derived Aromatic Compounds in Pseudomonas Putida KT2440. *Proc. Natl. Acad. Sci. U.S.A.* 117 (17), 9302–9310. doi:10.1073/pnas.1921073117

Sethupathy, S., Murillo Morales, G., Gao, L., Wang, H., Yang, B., Jiang, J., et al. (2022). Lignin Valorization: Status, Challenges and Opportunities. *Bioresour. Techn.* 347, 126696. doi:10.1016/j.biortech.2022.126696

Shields-Menard, S. A., Amirsadeghi, M., Green, M., Womack, E., Sparks, D. L., Blake, J., et al. (2017). The Effects of Model Aromatic Lignin Compounds on Growth and Lipid Accumulation of Rhodococcus Rhodochrous. *Int. Biodeterior. Biodegradation* 121, 79–90. doi:10.1016/j.ibiod.2017.03.023

Singh, A., Bedore, S. R., Sharma, N. K., Lee, S. A., Eiteman, M. A., and Neidle, E. L. (2019). Removal of Aromatic Inhibitors Produced from Lignocellulosic Hydrolysates by Acinetobacter Baylyi ADP1 with Formation of Ethanol by Kluyveromyces Marxianus. *Biotechnol. Biofuels* 12, 91. doi:10.1186/s13068-019-1434-7

Singhania, R. R., Patel, A. K., Raj, T., Chen, C.-W., Ponnusamy, V. K., Tahir, N., et al. (2022). Lignin Valorisation via Enzymes: A Sustainable Approach. *Fuel* 311, 122608. doi:10.1016/j.fuel.2021.122608

Subashchandrabose, S. R., Ramakrishnan, B., Megharaj, M., Venkateswarlu, K., and Naidu, R. (2011). Consortia of Cyanobacteria/Microalgae and Bacteria: Biotechnological Potential. *Biotechnol. Adv.* 29 (6), 896–907. doi:10.1016/j.biotechadv.2011.07.009

Supanchaiyamat, N., Jetsrisuparb, K., Knijnenburg, J. T. N., Tsang, D. C. W., and Hunt, A. J. (2019). Lignin Materials for Adsorption: Current Trend, Perspectives and Opportunities. *Bioresour. Techn.* 272, 570–581. doi:10.1016/j.biortech.2018.09.139

Szalaty, T. J., Klapiszewski, Ł., and Jesionowski, T. (2020). Recent Developments in Modification of Lignin Using Ionic Liquids for the

Fabrication of Advanced Materials-A Review. *J. Mol. Liquids* 301, 112417. doi:10.1016/j.molliq.2019.112417

Wang, H., Peng, X., Zhang, H., Yang, S., and Li, H. (2021). Microorganisms-Promoted Biodiesel Production from Biomass: A Review. *Energy Convers. Manag. X* 12, 100137. doi:10.1016/j.ecmx.2021.100137

Wang, H., Pu, Y., Ragauskas, A., and Yang, B. (2019). From Lignin to Valuable Products-Strategies, Challenges, and Prospects. *Bioresour. Techn.* 271, 449–461. doi:10.1016/j.biortech.2018.09.072

Wang, Z., Li, N., and Pan, X. (2019). Transformation of Ammonia Fiber Expansion (AFEX) Corn stover Lignin into Microbial Lipids by Rhodococcus Opacus. *Fuel* 240, 119–125. doi:10.1016/j.fuel.2018.11.081

Wei, Z., Zeng, G., Huang, F., Kosa, M., Huang, D., and Ragauskas, A. J. (2015). Bioconversion of Oxygen-Pretreated Kraft Lignin to Microbial Lipid with Oleaginous Rhodococcus Opacus DSM 1069. *Green. Chem.* 17 (5), 2784–2789. doi:10.1039/c5gc00422e

Wells, T., Wei, Z., and Ragauskas, A. (2015). Bioconversion of Lignocellulosic Pretreatment Effluent via Oleaginous Rhodococcus Opacus DSM 1069. *Biomass Bioenergy* 72, 200–205. doi:10.1016/j.biombioe.2014.11.004

Weng, C., Peng, X., and Han, Y. (2021). Depolymerization and Conversion of Lignin to Value-Added Bioproducts by Microbial and Enzymatic Catalysis. *Biotechnol. Biofuels* 14 (1), 84–105. doi:10.1186/s13068-021-01934-w

Xiong, X., Lian, J., Yu, X., Garcia-Perez, M., and Chen, S. (2016). Engineering Levoglucosan Metabolic Pathway in Rhodococcus Jostii RHA1 for Lipid Production. *J. Ind. Microbiol. Biotechnol.* 43 (11), 1551–1560. doi:10.1007/s10295-016-1832-9

Xu, B., Li, Q., Pu, Y., Xie, S., Ragauskas, A. J., Arreola-Vargas, J., et al. (2022). A Unique Bacterial Pelletized Cultivation Platform in Rhodococcus Opacus PD630 Enhanced Lipid Productivity and Simplified Harvest for Lignin Bioconversion. *ACS Sust. Chem. Eng.* 10 (3), 1083–1092. doi:10.1021/acssuschemeng.1c05239

Xu, C., Su, X., Wang, J., Zhang, F., Shen, G., Yuan, Y., et al. (2021). Characteristics and Functional Bacteria in a Microbial Consortium for rice straw Lignin-Degrading. *Bioresour. Techn.* 331, 125066. doi:10.1016/j.biortech.2021.125066

Xu, R., Zhang, K., Liu, P., Han, H., Zhao, S., Kakade, A., et al. (2018). Lignin Depolymerization and Utilization by Bacteria. *Bioresour. Techn.* 269, 557–566. doi:10.1016/j.biortech.2018.08.118

Xu, Z., Lei, P., Zhai, R., Wen, Z., and Jin, M. (2019). Recent Advances in Lignin Valorization with Bacterial Cultures: Microorganisms, Metabolic Pathways, and Bio-Products. *Biotechnol. Biofuels* 12, 32–50. doi:10.1186/s13068-019-1376-0

Xu, Z., Qin, L., Cai, M., Hua, W., and Jin, M. (2018). Biodegradation of Kraft Lignin by Newly Isolated *Klebsiella pneumoniae*, *Pseudomonas putida*, and *Ochrobactrum tritici* Strains. *Environ. Sci. Pollut. Res.* 25 (14), 14171–14181. doi:10.1007/s11356-018-1633-y

Yaguchi, A., Franaszek, N., O'neill, K., Lee, S., Sitepu, I., Boundy-Mills, K., et al. (2020). Identification of Oleaginous Yeasts that Metabolize Aromatic Compounds. *J. Ind. Microbiol. Biotechnol.* 47 (9–10), 801–813. doi:10.1007/s10295-020-02269-5

Yao, L., Yang, H., Meng, X., and Ragauskas, A. J. (2022). Towards a Fundamental Understanding of the Role of Lignin in the Biorefinery Process. *Front. Energ. Res.* 9, 895. doi:10.3389/fenrg.2021.804086

Zevallos Torres, L. A., Lorenci Woiciechowski, A., De Andrade Tanobe, V. O., Karp, S. G., Guimarães Lorenci, L. C., Faulds, C., et al. (2020). Lignin as a Potential Source of High-Added Value Compounds: A Review. *J. Clean. Prod.* 263, 121499. doi:10.1016/j.jclepro.2020.121499

Zhang, C., and Wang, F. (2020). Catalytic Lignin Depolymerization to Aromatic Chemicals. *Acc. Chem. Res.* 53 (2), 470–484. doi:10.1021/acs.accounts.9b00573

Zhang, L., Song, Y., Wang, Q., and Zhang, X. (2021). Culturing Rhodotorula Glutinis in Fermentation-Friendly Deep Eutectic Solvent Extraction Liquor of Lignin for Producing Microbial Lipid. *Bioresour. Techn.* 337, 125475. doi:10.1016/j.biortech.2021.125475

Zhang, Y., and Bao, J. (2022). Tolerance of Trichosporon Cutaneum to Lignin Derived Phenolic Aldehydes Facilitate the Cell Growth and Cellulosic Lipid Accumulation. *J. Biotechnol.* 343, 32–37. doi:10.1016/j.jbiotec.2021.09.009

Zhao, W., Chi, X., Li, H., He, J., Long, J., Xu, Y., et al. (2019). Eco-Friendly Acetylcholine-Carboxylate Bio-Ionic Liquids for Controllable N-Methylation and N-Formylation Using Ambient CO₂ at Low Temperatures. *Green. Chem.* 21 (3), 567–577. doi:10.1039/c8gc03549k

Zhou, M., Fakayode, O. A., Ahmed Yagoub, A. E., Ji, Q., and Zhou, C. (2022). Lignin Fractionation from Lignocellulosic Biomass Using Deep Eutectic Solvents and its Valorization. *Renew. Sust. Energ. Rev.* 156, 111986. doi:10.1016/j.rser.2021.111986

Zhu, D., Qaria, M. A., Zhu, B., Sun, J., and Yang, B. (2022). Extremophiles and Extremozymes in Lignin Bioprocessing. *Renew. Sust. Energ. Rev.* 157, 112069. doi:10.1016/j.rser.2021.112069

Zhu, D., Zhang, P., Xie, C., Zhang, W., Sun, J., Qian, W.-J., et al. (2017). Biodegradation of Alkaline Lignin by *Bacillus ligniniphilus* L1. *Biotechnol. Biofuels* 10, 44. doi:10.1186/s13068-017-0735-y

Zuñiga, C., Li, T., Guarnieri, M. T., Jenkins, J. P., Li, C.-T., Bingol, K., et al. (2020). Synthetic Microbial Communities of Heterotrophs and Phototrophs Facilitate Sustainable Growth. *Nat. Commun.* 11 (1), 3803. doi:10.1038/s41467-020-17612-8

Conflict of Interest: The authors declare that the research was conducted in the absence of any commercial or financial relationships that could be construed as a potential conflict of interest.

The reviewer QZ declared a past co-authorship with the author HL to the handling editor.

Publisher's Note: All claims expressed in this article are solely those of the authors and do not necessarily represent those of their affiliated organizations, or those of the publisher, the editors and the reviewers. Any product that may be evaluated in this article, or claim that may be made by its manufacturer, is not guaranteed or endorsed by the publisher.

Selective Hydrogenation of 5-Hydroxymethylfurfural to 2,5-Dimethylfuran Over Popcorn-Like Nitrogen-Doped Carbon-Confined CuCo Bimetallic Catalyst

Peng Hao, Jianliang Zuo*, Wurong Tong, Jing Lin, Qiying Wang and Zili Liu*

School of Chemistry and Chemical Engineering, Guangzhou University, Guangzhou, China

A new type of biomass-based liquid fuel, 2,5-dimethylfuran (DMF), has attracted significant attention owing to its unique physical properties and carbon neutrality. It can be obtained from the hydrogenation of 5-hydroxymethylfurfural (HMF), an important biomass platform compound. In this study, we developed a nitrogen-doped carbon-confined CuCo bimetallic catalyst with a popcorn-like structure for the selective hydrogenation of HMF with high efficiency and adequate stability. Under optimized conditions, 100% HMF conversion and 93.7% DMF selectivity were achieved. The structure of the catalyst was characterized using XRD, XPS, SEM, and TEM. It was observed that carbon spheres, which were covered by nitrogen-doped carbon nanotubes, uniformly formed, while metal particles were confined in the nitrogen-doped carbon nanotubes. The popcorn-like structure exhibited a larger surface area and provided more contact sites, while the confined metal particles were the main active sites. The synergistic effect between Cu and Co was beneficial for DMF selectivity.

Keywords: 5-hydroxylmethylfurfural, CuCo bimetallic catalyst, selective hydrogenation, N-doped carbon nanotubes, 2,5-dimethylfuran

INTRODUCTION

With the increasing consumption of fossil fuels, the problems of resource depletion and the environmental pollution caused by fossil fuels have become increasingly serious. Therefore, there is an urgent need to develop sustainable and clean energy sources. Among them, biomass energy has attracted the attention of researchers as it can realize the carbon cycle and effectively reduce environmental pollution. Notably, 2,5-dimethylfuran (DMF) is considered a high-quality biomass-based liquid fuel owing to its unique physical properties (Tian et al., 2010; Alamillo et al., 2012; Wang H et al., 2019), such as high energy density, high boiling point, and low solvency in water (compared to first-generation bioethanol), and it can be produced by the selective hydrogenation of 5-hydroxymethylfurfural (HMF). HMF is an important biomass-based platform compound obtained from the hydrolysis of cellulose (Hu et al., 2008; Guo et al., 2020). However, because of its abundant reactive functional groups, side reactions and overhydrogenation easily occur during the hydrogenation of HMF to DMF (Zhang et al., 2017; Mishra et al., 2020; Wang et al., 2021). Developing highly efficient catalysts for the selective hydrogenation of HMF to DMF remains a challenge.

The current catalysts for the hydrogenation of HMF can be divided into two types: noble and non-noble metal catalysts. The most important feature of precious metals such as Pd, Pt, Ru, and Rh, is that they can achieve a high yield under mild conditions. Wang et al. (2018) obtained >90% DMF yields using Pt-Co bimetallic catalysts, while Zu et al. (2014) obtained 93.4% DMF yields using Ru/Co_3O_4 catalysts, and Zhang J et al. (2019) obtained 89.7% DMF yields using $PdCl_2$ at room temperature. However, noble metal catalysts are limited by their scarcity and high cost. Therefore, there is an urgent need to develop low-cost, non-noble metal catalysts. Commonly used non-noble metals are Co, Cu, Ni, and Fe. Yang et al. (2019) obtained a 94.1% DMF yield using a synthetic Co/rGO catalyst at 200°C. Akmaz et al. (2019) prepared a Mn/Co bimetallic catalyst and obtained a DMF yield of 91.8%. Zhang Z et al. (2019) prepared a $Co–CoO_x$ catalyst and achieved a DMF yield of 83.3% after 12 h at 170°C. Generally, copper and cobalt are favorable for hydrogenation of C=O, C–O bond, bimetallic catalysts are more active than monometallic catalysts (Guo et al., 2021; Zhao et al., 2022). Although non-noble metal catalysts reduce the cost, they also introduce the disadvantages of requiring harsh reaction conditions and easy deactivation. Thus, the development of an efficient and stable non-noble metal catalyst is crucial. In addition, nitrogen-doped carbon materials have been widely used as catalyst supporter which can anchor and stabilize metal nanoparticles and promote electron transfer to improve the performance of catalysts (Wang et al., 2020; Guo et al., 2021). Based on the aforementioned information, in this study, a nitrogen-doped carbon-confined copper-cobalt bimetallic catalyst was synthesized using a two-step solvothermal-reducing calcination method. It can be observed that the catalyst has a popcorn-like structure, and the surface is evenly covered by carbon nanotubes, which provides more surface area for the contact between the catalyst and the substrate. It has been used in the selective hydrogenation of HMF to DMF and has achieved adequate results. The main paragraph text follows directly on here.

EXPERIMENTAL SECTION

Chemicals

Co $(NO_3)_2 \bullet 6H_2O$, 2-methylimidazole, 5-hydroxymethylfurfural (97.0%), 5-methylfurfural, 2-butanol, urea, and melamine were procured from Shanghai Macklin Biochemical Co. Cu $(NO_3)_2 \bullet 3H_2O$, methanol, tetrahydrofuran (THF), and isopropanol (IPA) were procured from Guangzhou Chemical Reagent Factory. Glucose was procured from Tianjin Zhiyuan Chemical Reagent Co. Ltd.

Preparation of the Catalyst

Copper-cobalt bimetallic catalysts were prepared using a solvothermal-reducing calcination method with 2-methylimidazole as the nitrogen sources and both 2-methylimidazole and glucose as the carbon sources. 3.69 g 2-methylimidazole, 0.5 g glucose, cobalt nitrate hexahydrate and copper nitrate trihydrate with different Cu/Co molar ratios (the

amount of Co remains constant) were dissolved in 60 ml of methanol and stirred for 10 min to facilitate dissolution. This solution was then transferred to a 100 ml Teflon reactor and maintained at 120°C for 12 h. After cooling to room temperature, the solution was filtered five times with methanol and transferred to a vacuum drying oven, where it was allowed to stay overnight at 80°C. Subsequently, the obtained brown precursor powder was calcined in a tube furnace under a reducing H_2 (5%)/N_2 atmosphere at a rate of 2°C/min to 440°C for 8 h and then at a rate of 2°C/min to 900°C for 2 h to obtain the target Cu–Co bimetallic catalyst. The prepared catalyst was named xCuCo–IG (where x represents the molar ratio of copper to cobalt, I represents the nitrogen source 2-methylimidazole, G represents the carbon source glucose). The monometallic catalysts were named Cu-IG and Co-IG, respectively.

For comparison, catalysts with melamine or urea as the nitrogen source were prepared and named 2CuCo–MG and 2CuCo–UG, respectively. A catalyst without a nitrogen source (2CuCo–G) and a catalyst without glucose (2CuCo–I) were also prepared. The catalyst calcined in a N_2 atmosphere was named 2CuCo–IG (N_2).

Characterization

The X-ray diffraction (XRD) patterns of the powder samples were recorded using a BRUKER D8 ADVANCE diffractometer. X-ray photoelectron spectroscopy (XPS) data was measured using a Thermo ESCALAB 250Xi spectrometer. The specific surface area and porosity of the samples were obtained using a Micrometrics ASAP2460. The morphology of each sample was investigated using field emission scanning electron microscopy (SEM, SU8020), and the element mapping was performed using energy dispersive spectrometer (EDS). Transmission electron microscopy (TEM) and high-resolution transmission electron microscopy (HRTEM) images were obtained using a FEI Tecnai G2 F30. The Raman spectral profile was obtained using a Renishaw inVia at an excitation wavelength of 532 nm.

Test of Catalytic Activity

The catalytic performance in the hydrogenation of HMF was investigated in a stainless-steel autoclave. First, 0.2 g of the substrate (HMF), 0.02 g of the catalyst, and 0.05 g of toluene were dissolved in 30 ml of 2-butanol and subsequently poured into the reactor. After installation, hydrogen was purged at least eight times to remove air and charged with H_2 at the corresponding pressure; the agitation speed was modulated to 400 rpm, followed by an increase in the temperature to the target temperature of 180°C. After the reaction was completed and cooled to room temperature, the reaction products were analyzed using the internal standard curve method to determine their conversion and selectivity with an Agilent 6820 gas chromatograph. The calculations for the conversion of HMF and DMF selectivity were performed as follows:

$$\text{Conversion (HMF)} = \left(1 - \frac{n_t}{n_0} \right) \times 100\%,$$

$$\text{Selectivity} = \frac{n_i}{\text{Conv.HMF}} \times 100\%,$$
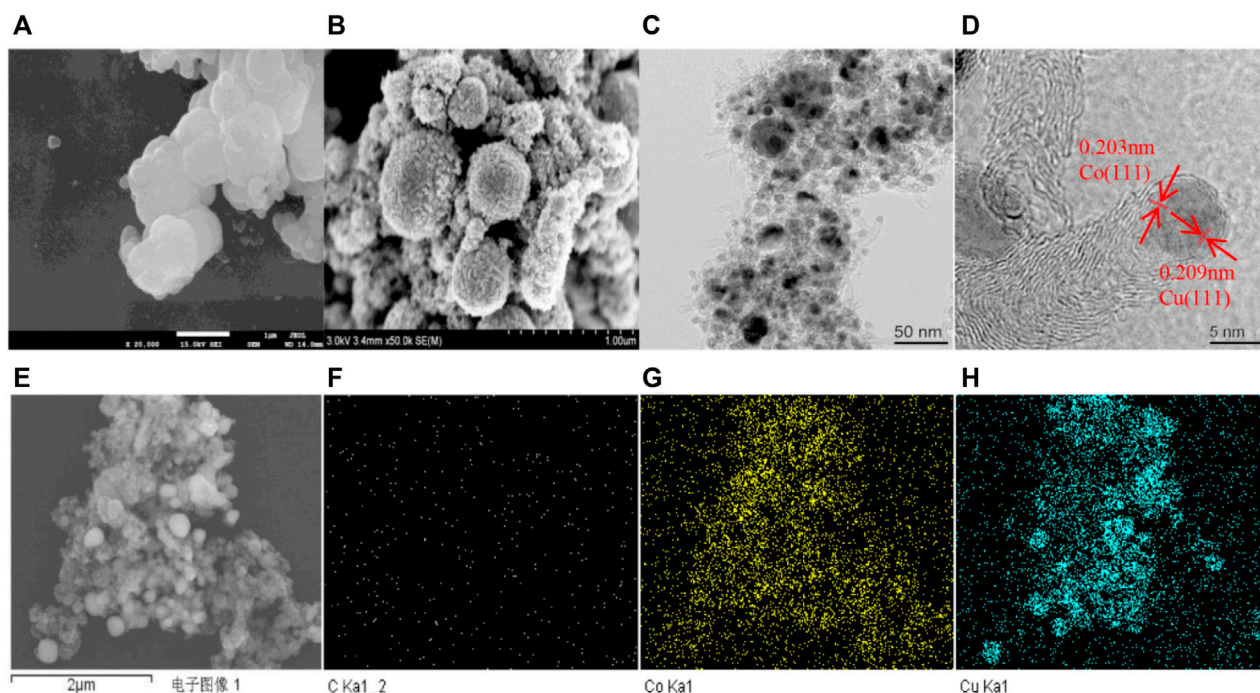
FIGURE 1 | (A) SEM profiles of the precursor, **(B)** 2CuCo–IG obtained after the calcination of H$_2$ (5%)/N$_2$; **(C,D)** TEM and HRTEM profiles of 2CuCo-IG; **(E–H)** the SEM and elemental images of the catalyst 2CuCo–IG.

where n$_t$ represents the molar amount of HMF after the reaction, n$_0$ represents the molar amount of initial HMF, and n$_i$ represents the molar amount of the product after the reaction.

RESULTS AND DISCUSSION

Structural Analysis

First, the 2CuCo–IG catalyst precursor with a Cu/Co molar ratio of 2:1 was synthesized using a one-pot solvothermal reaction of metal salts, glucose (as the carbon source), and 2-methylimidazolem (as the nitrogen source and carbon source). Precursors mainly showed spherical structures with non-smooth surfaces (**Figure 1A**). Soon after the calcination under a H$_2$ (5%)/N$_2$ mixture atmosphere, the catalyst exhibited a popcorn-like structure with carbon balls uniformly covered by carbon nanotubes (**Figure 1B**). TEM and HRTEM images (**Figures 1C,D**) indicated that carbon balls were covered by carbon nanotubes, and Cu–Co metal particles were confined to the tips of the nanotubes with an average size of 6–8 nm. **Figure 1D** shows a lattice fringe of 0.209 nm attributable to the plane of Cu (111) (Liu J et al., 2020; Viar et al., 2020), and a lattice distance of 0.203 nm attributable to the plane of metallic Co (111) (Ma et al., 2020). In addition, the SEM and elemental images of Cu, Co, C in the 2CuCo–IG catalyst showed that copper and cobalt were uniformly dispersed throughout the catalyst (**Figures 1E–H**).

To investigate the reason for the formation of carbon nanotubes, we prepared catalysts such as 2CuCo–G (no
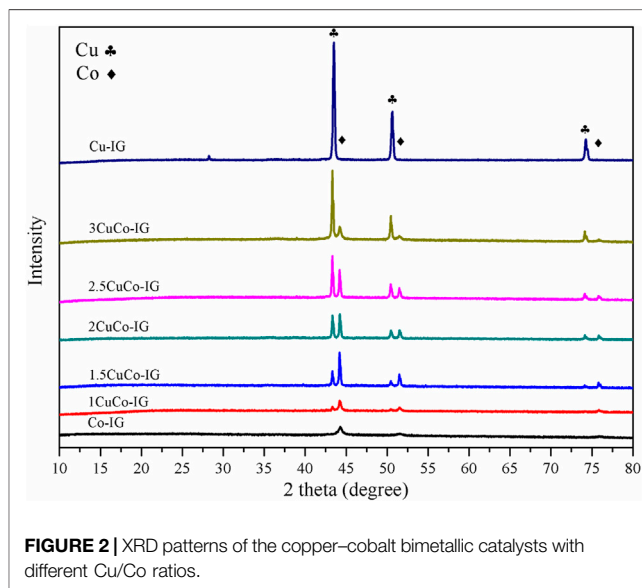
FIGURE 2 | XRD patterns of the copper–cobalt bimetallic catalysts with different Cu/Co ratios.

nitrogen source added), 2CuCo–UG (nitrogen source replaced by urea), 2CuCo–MG (nitrogen source replaced by melamine), and 2CuCo–I (no glucose carbon source added). As shown in **Supplementary Figures S2A–D**, it can be observed that when the nitrogen source was changed, the catalyst structure also changes and no longer develops a popcorn-like structure. When no glucose carbon source was added, no spherical support structure was formed, but the carbon nanotubes still appeared
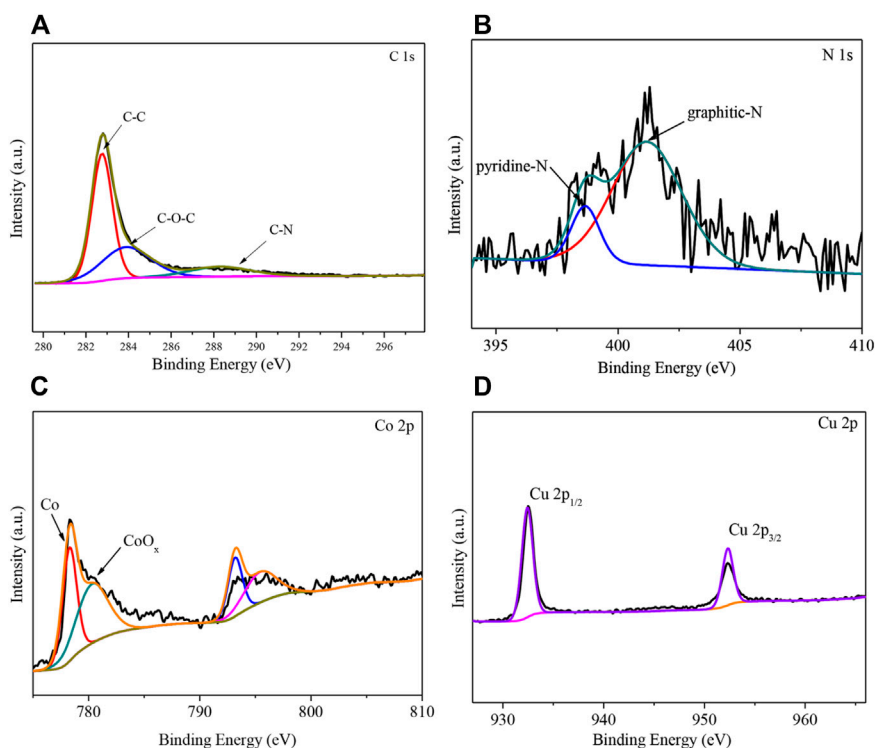
FIGURE 3 | XPS spectra of the catalyst 2CuCo–IG. **(A)** High-resolution spectra of C 1s, **(B)** N 1s, **(C)** Co 2p, and **(D)** Cu 2p.

(**Supplementary Figure S2D**), which indicates that carbon nanotubes are most likely formed during the calcination of 2-methylimidazole. The effect of the calcination atmosphere on the morphology of the catalyst was also investigated (**Supplementary Figure S1**). The carbon nanotubes on the catalyst calcined under a N_2 atmosphere are fewer and significantly finer than those formed under a mixed atmosphere. This means that both the formation and morphologies of carbon nanotubes are highly dependent on the nitrogen source and the calcination atmosphere.

A series of copper-cobalt bimetallic catalysts was prepared with different Cu/Co ratios, and their XRD patterns are shown in **Figure 2**. The diffraction peaks at 43.3°, 50.4°, and 74.1° are attributed to metallic copper (PDF #89-4307) (Chen et al., 2020; Rao et al., 2020; Xu et al., 2021), and those at 44.2°, 51.5°, and 75.9° are attributed to metallic cobalt (PDF #89-2838) (Chen et al., 2017; Solanki and Rode, 2019). It can be observed that mono metal catalyst Cu–IG contains only metallic copper diffraction peak, while Co–IG catalyst contains only metallic cobalt diffraction peak. The CuCo bimetallic catalyst contains both metallic copper and metallic cobalt diffraction peaks, with an increase in the ratio of copper to cobalt, the diffraction peaks of both elements exhibited different variation trends. The diffraction peaks of metallic copper continuously increased as the proportion of metallic copper increased. The diffraction peaks of metallic cobalt also increased initially. However, when this ratio was exceeded 2.5, the diffraction peaks of metallic cobalt decreased. This shows that a suitable ratio of copper to cobalt can improve the crystal structure of metallic cobalt.

The N_2 adsorption/desorption curves of the catalysts are shown in **Supplementary Figure S3**. The existence of hysteresis loops indicated that the prepared catalysts were typical mesoporous materials. The specific surface area and pore size data are listed in **Supplementary Table S1**. Among the catalysts with different Cu/Co ratios, the 2CuCo–IG catalyst had the largest specific surface area, and the large pore volume and the adequate pore diameter improved contact, significantly improving the utilization of the catalyst.

The XPS profiles of the 2CuCo–IG catalyst are shown in **Figure 3**. Two peaks are visible at 284.8 and 286.0 eV in the high-resolution XPS spectrum of C 1s mainly corresponding to C–C and C–O–C (Xia et al., 2016; Rao et al., 2021). The peak near 289.0 eV is attributed to C–N in the catalyst (**Figure 3A**) (Liu L et al., 2020; Zhu K et al., 2020). Two peaks were visible at 398.6 and 401.2 eV in the high-resolution XPS spectrum of N 1s corresponding to pyridine N and graphite N (**Figure 3B**) (Hu et al., 2019). The elemental nitrogen content was determined to be 2.5% using XPS, including 15.0% pyridine nitrogen and 85.0% graphite nitrogen. The high-resolution XPS spectrum of Co 2p shows the characteristic peak of Co^0 at 778.3 eV (Liu M et al., 2020), while the peak at 780.3 eV corresponds to CoO_x (**Figure 3C**) (Zhu J et al., 2020). The diffraction peaks of Cu 2p1/2 and Cu 2p3/2 in the high-resolution XPS spectrum of Cu 2p were present at 952.3 and 932.3 eV; this indicates that the valence state of Cu is in the metallic phase (**Figure 3D**) (Kang et al., 2016), which is consistent with XRD results. The two peaks at 1350 and 1600 cm^{-1} in the Raman spectrum (**Supplementary**

FIGURE 4 | Effect of the different carbon/nitrogen sources and calcination atmospheres on catalyst performance. Reaction conditions: 0.2 g of HMF, 0.04 g of the catalyst, 30 ml of 2-Butanol, 2 MPa H$_2$, 4 h, and an agitation speed of 400 rpm.

FIGURE 5 | Effects of different copper-cobalt ratios on HMF conversion and the DMF yield. Reaction conditions: 0.2 g of HMF, 0.04 g of the catalyst, 30 ml of 2-Butanol, 2 MPa H$_2$, 4 h, and an agitation speed of 400 rpm.
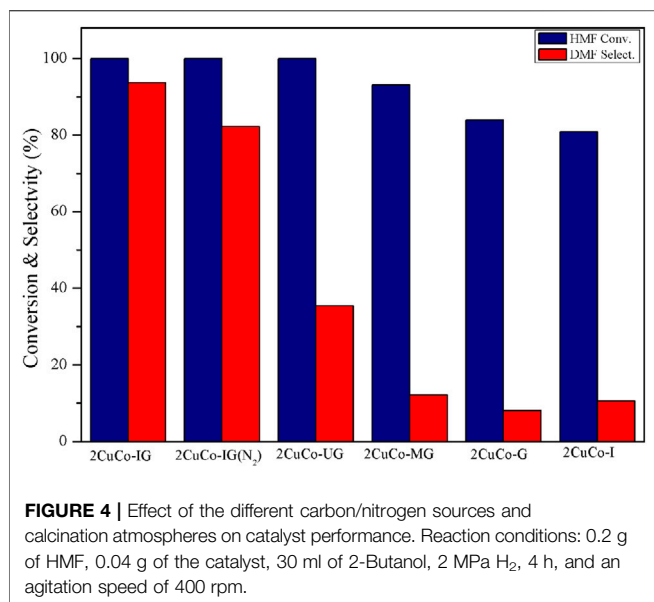
Figure S4) are the D and G bands, respectively (ID/IG = 0.9), indicating a relatively high degree of graphitization of carbon. It should be noted that high contents of graphitic carbon are conducive to the catalytic hydrogenation reaction (Gong et al., 2019).

Hydrogenolysis of 5-Hydroxymethylfurfural to 2,5-Dimethylfuran

The effects of the different carbon/nitrogen sources and calcination atmospheres on the catalyst activity were also investigated (**Figure 4**). Both the catalyst without the addition of a glucose carbon source (2CuCo–I) and that without the addition of 2-methylimidazole as a nitrogen source (2CuCo–G) exhibited very low DMF selectivity. When the nitrogen source was changed to urea or melamine, the selectivity of DMF was only 35.4 and 12.2%, respectively. This implies that both carbon and nitrogen sources are indispensable, and that the type of nitrogen source also has a significant impact on DMF selectivity. The 2CuCo–IG (N$_2$) calcined in a N$_2$ atmosphere showed 82.3% DMF selectivity which is lower than that of the 2CuCo–IG calcined in a H$_2$ (5%)/N$_2$ atmosphere. This may be because the reducing atmosphere is beneficial for formation and dispersion of metallic CuCo particles. As showed in **Supplementary Figure S1**, more nitrogen doped carbon nanotubes in which CuCo bimetal particles were confined were formed in the 2CuCo–IG catalyst because of lower depletion of carbon under reducing atmosphere than inert atmosphere. The calcination atmosphere is also benefit for the thorough reduction of Cu although the carbon also can partially reduction of Cu. On other hand, The ratio of Co^0/CoO$_x$ in the 2CuCo–IG is higher than that in 2CuCo–IG (N$_2$) although both of 2CuCo–IG and 2CuCo–IG (N$_2$) catalyst
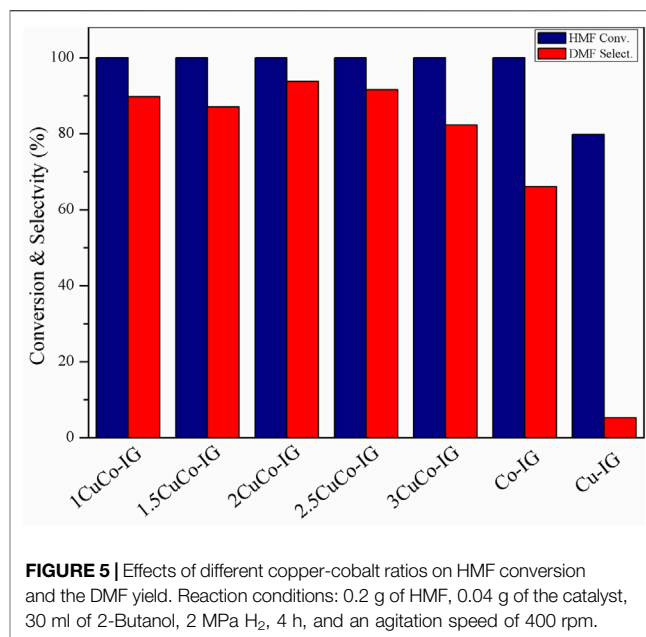
contain metallic Co and oxidation state Co (**Figure 3** and **Supplementary Figure S5**).

The effects of the different Cu/Co ratios on the catalyst activity are shown in **Figure 5**. HMF conversion was 79.8% and DMF selectivity was only 5.3% when a mono-copper metal was used as the catalyst, whereas 100% HMF conversion and 66.0% DMF selectivity were achieved when a mono-cobalt metal was used as the catalyst. All the CuCo bimetallic catalyst showed higher conversion and DMF selectivity than monometallic catalysts. The best proportion was obtained when the copper-to-cobalt ratio was 2, and a 93.7% DMF yield was achieved. By comparison, we speculated that there will be a synergistic effect between Cu and Co which played an important role in improving the catalytic performance.

The effects of the different reaction conditions on the catalytic activity of the selective hydrogenation of HMF to DMF were investigated (**Figure 6**). The selectivity of DMF increased when the temperature gradually increased, and the highest selectivity (93.7%) was obtained at 180°C. Further increasing the temperature will result in the deep hydrogenation of DMF in the C=C bond of the furan ring to form 2,5-Dimethyloxolane (DMTHF), resulting in a decrease in DMF selectivity (**Figure 6A**). The effect of the reaction time is comparable to that of the temperature (**Figure 6B**), and it shows the highest selectivity at 4 h. For the effect of the pressure factor, DMF selectivity rapidly increased when the pressure increased from 1 to 2 MPa; however, excessive pressure can also lead to overhydrogenation (**Figure 6C**). The effect of the reaction solvent on the activity is shown in **Figure 6D**. The use of different solvents caused dramatic changes in the activity level, which indicated that the solvent was present in the reaction. The effect of the solvent will be discussed in the following section. Overall, the catalyst showed the best performance when 2-butanol was used as the solvent.
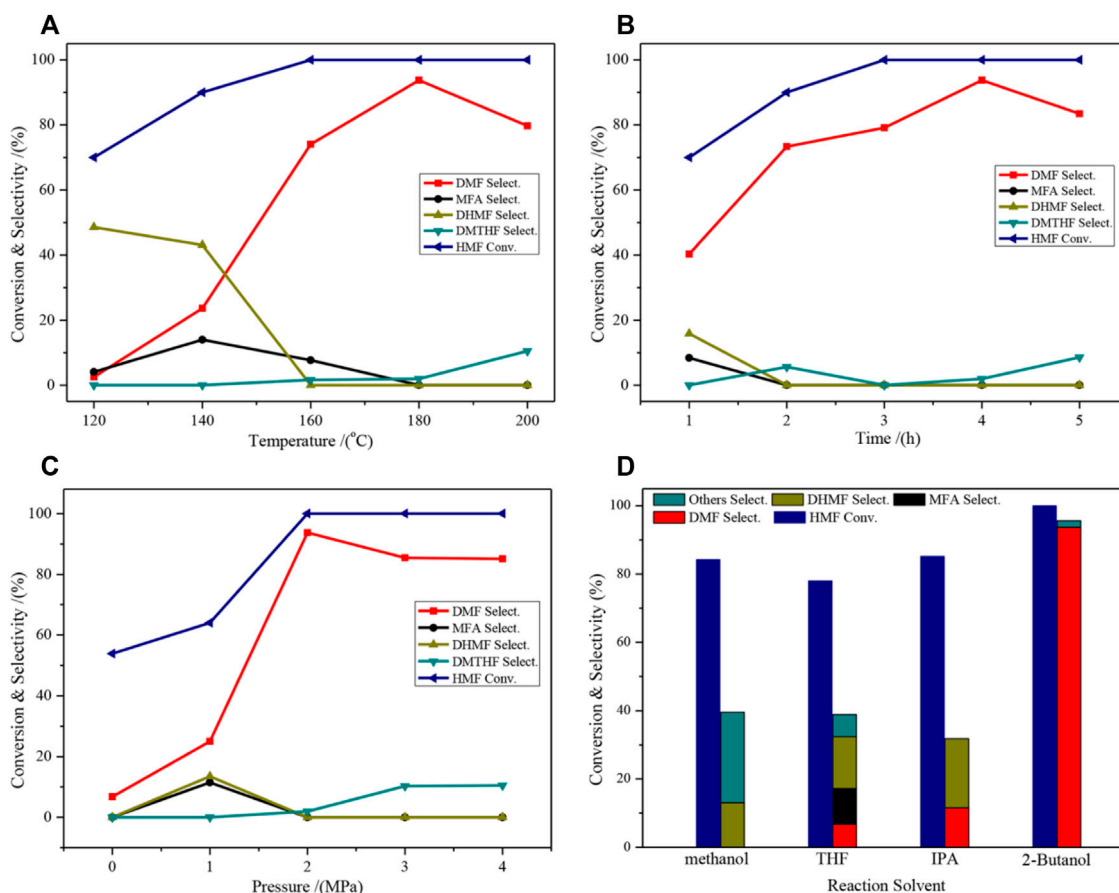
FIGURE 6 | Catalytic performance of HMF hydrogenolysis and distribution of products on the 2CuCo–IG catalyst over different reaction conditions. **(A)** 4 h, 2.0 MPa H_2, 30 ml of 2-Butanol; **(B)** 180°C, 2.0 MPa H_2, 30 ml of 2-Butanol; **(C)** 4 h, 180°C, 30 ml of 2-Butanol; **(D)** 4 h, 180°C, 2.0 MPa H_2, 30 ml of 2-Butanol.
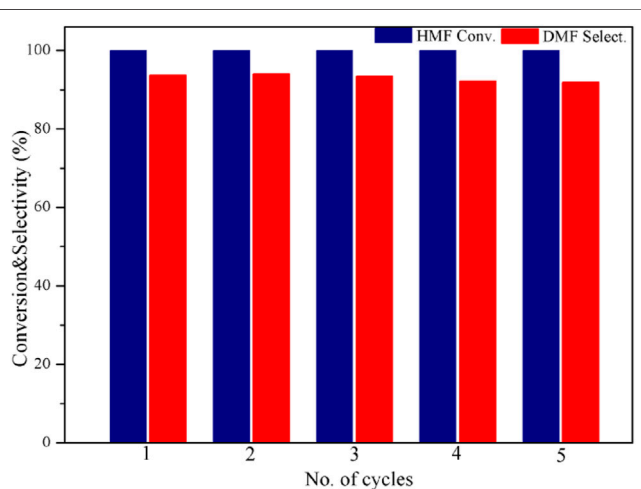
FIGURE 7 | Catalyst cycling performance test. Reaction conditions: 0.2 g of HMF, 0.04 g of the catalyst, 30 ml of 2-Butanol, 2 MPa H_2, 4 h, and an agitation speed of 400 rpm.

The cycling performance of the catalyst is shown in **Figure 7**. Since the catalyst itself is magnetic, it can be recovered easily after the reaction. After five cycles, no distinct decrease was observed in either HMF conversion or DMF selectivity. This indicates that the catalyst is highly stable and adequately reusable.

Reaction Pathway

The hydrogenation of HMF to DMF is divided into two main pathways: routes I and II (**Figure 8**) (Nakagawa et al., 2013; Qian et al., 2015; Wang Q et al., 2019). Route I is the hydrogenation and dehydration of HMF to produce MF, by further hydrogenation to produce MFA and finally DMF. Route II is the hydrogenation of HMF to produce DHMF, followed by hydrogenation and dehydration to produce MFA and finally DMF. DMF could also be transformed into DMTHF by the C=C hydrogenation in the furan ring. The results of the time optimization experiment (**Figure 6B**) showed that the intermediate product that appeared at 1 h was DHMF, indicating that the reaction process was route II.
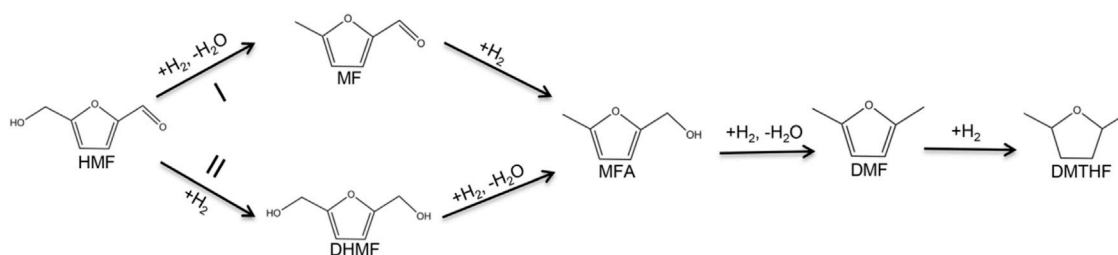
FIGURE 8 | Reaction pathways of the selective hydrogenation of HMF to DMF.

TABLE 1 | Effects of the different reaction conditions on MF conversion and products.

Catalyst	Gas	Solvent	MF Conv.(%)	MFA Select.(%)	DMF Select.(%)	Others Select.(%)
2CuCo–IG	H_2	2-Butanol	78.0	54.8	20.2	0
2CuCo–IG	H_2	Methanol	97.0	17.0	10.0	36.6
2CuCo–IG	N_2	2-Butanol	47.3	33.4	8.5	0
1CuCo–IG	H_2	2-Butanol	70.0	31.0	33.6	0

Reaction conditions: 0.2 g of MF, 0.02 g of the catalyst, 140°C, 2 h, 2 MPa corresponding gas, 30 ml of the corresponding solvent, and an agitation speed of 400 rpm.

TABLE 2 | Effects of the different reaction conditions on MFA conversion and products.

Catalyst	Gas	Solvent	MFA Conv. (%)	DMF Select (%)	DMTHF Select (%)	Others Select (%)
2CuCo–IG	H_2	2-Butanol	72.5	56.7	10.9	0
2CuCo–IG	H_2	Methanol	60.4	6	0	53.9
2CuCo–IG	N_2	2-Butanol	45.8	35.3	5.0	0
1CuCo–IG	H_2	2-Butanol	82.3	64.7	17.3	0

Reaction conditions: 0.2 g of MFA, 0.02 g of the catalyst, 140°C, 2 h, 2 MPa corresponding gas, 30 ml of the corresponding solvent, and an agitation speed of 400 rpm.

To further study the effect of the solvent on product selectivity and the role of Cu/Co at each step of the hydrogenation reaction, a series of hydrogenation reactions was designed using MF with an aldehyde group and a furan ring and MFA with a hydroxyl group and a furan ring as substrates (**Tables 1**, **2**). When methanol was used as the solvent, the selectivity of DMF was lower than that when 2-butanol was used, in both the hydrogenation of MF and MFA. Furthermore, when methanol was used, more etherification occurred, and more condensation products were formed. This may be due to the steric effects of 2-butanol that suppressed etherification and condensation reactions and resulted in the target product DMF.

The effects of the different Cu/Co ratios on the reaction process were investigated (**Tables 1**, **2**). A series of hydrogenation reactions was designed using MF with an aldehyde group and a furan ring and MFA with a hydroxyl group and a furan ring as substrates. In the one and four lines of **Table 1**, it was observed that the higher the copper content, the higher the MF conversion and MFA selectivity in the hydrogenation reaction of MF, which indicates that metallic

copper is active for the hydrogenation of C=O bonds. Meanwhile, the higher the cobalt content, the higher the MFA conversion and DMF selectivity in the hydrogenation reaction of MFA, which indicates that Co/CoO$_x$ is more active for the hydrogenation of C–O bonds. The synergistic effect of copper and cobalt promotes the whole hydrogenation process.

CONCLUSION

In summary, a popcorn-like nitrogen-doped carbon-confined CuCo bimetallic catalyst was prepared using a two-step solvothermal-reducing calcination method. The 2CuCo–IG catalyst performed well in the HMF selective hydrogenation to DMF with an HMF conversion of 100% and a DMF yield of 93.7%. The popcorn-like structure provided more active sites and electrons, and the confinement effect of nitrogen-doped carbon nanotubes and the synergistic effect of copper and cobalt were the main reasons for the high catalytic efficiency. The 2-butanol solvent not only provided hydrogen but also reduced the unwanted reactions of etherification and

condensation using steric effects during the reaction. Meanwhile, the catalyst exhibited adequate recycling performance; thus, it can be reused.

DATA AVAILABILITY STATEMENT

The original contributions presented in the study are included in the article/**Supplementary Material**, further inquiries can be directed to the corresponding authors.

AUTHOR CONTRIBUTIONS

Conceptualization and methodology: JZ and ZL. Validation and investigation: PH and WT. Supervision: JZ and ZL. Writing-original draft: PH. Writing-review and editing, JZ, QW, JL, and ZL. All authors approved the submitted version.

SUPPLEMENTARY MATERIAL

The Supplementary Material for this article can be found online at: https://www.frontiersin.org/articles/10.3389/fchem.2022.882670/full#supplementary-material

REFERENCES

Akmaz, S., Esen, M., Sezgin, E., and Koc, S. N. (2019). Efficient Manganese Decorated Cobalt Based Catalysts for Hydrogenation of 5-hydroxymethylfurfural (HMF) to 2,5-dimethylfuran (DMF) Biofuel. *Can. J. Chem. Eng.* 98, 138–146. doi:10.1002/cjce.23613

Alamillo, R., Tucker, M., Chia, M., Pagán-Torres, Y., and Dumesic, J. (2012). The Selective Hydrogenation of Biomass-Derived 5-hydroxymethylfurfural Using Heterogeneous Catalysts. *Green. Chem.* 14, 1413–1419. doi:10.1039/c2gc35039d

Chen, B., Li, F., Huang, Z., and Yuan, G. (2017). Carbon-coated Cu-Co Bimetallic Nanoparticles as Selective and Recyclable Catalysts for Production of Biofuel 2,5-dimethylfuran. *Appl. Catal. B: Environ.* 200, 192–199. doi:10.1016/j.apcatb.2016.07.004

Chen, N., Zhu, Z., Su, T., Liao, W., Deng, C., Ren, W., et al. (2020). Catalytic Hydrogenolysis of Hydroxymethylfurfural to Highly Selective 2,5-dimethylfuran over FeCoNi/h-BN Catalyst. *Chem. Eng. J.* 381, 122755. doi:10.1016/j.cej.2019.122755

Gong, W., Lin, Y., Chen, C., Al-Mamun, M., Lu, H. S., Wang, G., et al. (2019). Nitrogen-Doped Carbon Nanotube Confined Co-N X Sites for Selective Hydrogenation of Biomass-Derived Compounds. *Adv. Mater.* 31, 1808341. doi:10.1002/adma.201808341

Guo, D., Lai, J., Cheng, F., Zhao, W., Chen, H., Li, H., et al. (2021). Titanium Silicalite-1 Supported Bimetallic Catalysts for Selective Hydrogenolysis of 5-hydroxymethylfurfural to Biofuel 2, 5-dimethylfuran. *Chem. Eng. J. Adv.* 5, 100081. doi:10.1016/j.ceja.2020.100081

Guo, D., Liu, X., Cheng, F., Zhao, W., Wen, S., Xiang, Y., et al. (2020). Selective Hydrogenolysis of 5-hydroxymethylfurfural to Produce Biofuel 2, 5-dimethylfuran over Ni/ZSM-5 Catalysts. *Fuel* 274, 117853. doi:10.1016/j.fuel.2020.117853

Hu, A., Lu, X., Cai, D., Pan, H., Jing, R., Xia, Q., et al. (2019). Selective Hydrogenation of Nitroarenes over MOF-Derived Co@CN Catalysts at Mild Conditions. *Mol. Catal.* 472, 27–36. doi:10.1016/j.mcat.2019.04.008

Hu, S., Zhang, Z., Zhou, Y., Han, B., Fan, H., Li, W., et al. (2008). Conversion of Fructose to 5-hydroxymethylfurfural Using Ionic Liquids Prepared from Renewable Materials. *Green. Chem.* 10, 1280–1283. doi:10.1039/b810392e

Kang, Y., Park, J., and Kang, Y.-C. (2016). Surface Characterization of CuSn Thin Films Deposited by RF Co-sputtering Method. *Surf. Interf. Anal.* 48, 963–968. doi:10.1002/sia.5995

Liu, J., Li, J., He, S., Sun, L., Yuan, X., and Xia, D. (2020). Heterogeneous Catalytic Ozonation of Oxalic Acid with an Effective Catalyst Based on Copper Oxide Modified G-C3n4. *Separat. Purif. Technol.* 234, 116120. doi:10.1016/j.seppur.2019.116120

Liu, L., Li, Y., Pang, Y., Lan, Y., and Zhou, L. (2020). Activation of Peroxymonosulfate with CuCo2O4@kaolin for the Efficient Degradation of Phenacetin. *Chem. Eng. J.* 401, 126014. doi:10.1016/j.cej.2020.126014

Liu M, M., Yuan, L., Fan, G., Zheng, L., Yang, L., and Li, F. (2020). NiCu Nanoparticles for Catalytic Hydrogenation of Biomass-Derived Carbonyl Compounds. *ACS Appl. Nano Mater.* 3, 9226–9237. doi:10.1021/acsanm.0c01857

Ma, N., Song, Y., Han, F., Waterhouse, G. I. N., Li, Y., and Ai, S. (2020). Highly Selective Hydrogenation of 5-hydroxymethylfurfural to 2,5-dimethylfuran at Low Temperature over a Co-N-C/NiAl-MMO Catalyst. *Catal. Sci. Technol.* 10, 4010–4018. doi:10.1039/d0cy00363h

Mishra, D. K., Lee, H. J., Truong, C. C., Kim, J., Suh, Y.-W., Baek, J., et al. (2020). Ru/MnCo2O4 as a Catalyst for Tunable Synthesis of 2,5-bis(hydroxymethyl)furan or 2,5-bis(hydroxymethyl)tetrahydrofuran from Hydrogenation of 5-hydroxymethylfurfural. *Mol. Catal.* 484, 110722. doi:10.1016/j.mcat.2019.110722

Nakagawa, Y., Tamura, M., and Tomishige, K. (2013). Catalytic Reduction of Biomass-Derived Furanic Compounds with Hydrogen. *ACS Catal.* 3, 2655–2668. doi:10.1021/cs400616p

Qian, Y., Zhu, L., Wang, Y., and Lu, X. (2015). Recent Progress in the Development of Biofuel 2,5-dimethylfuran. *Renew. Sustain. Energ. Rev.* 41, 633–646. doi:10.1016/j.rser.2014.08.085

Rao, K. T. V., Hu, Y., Yuan, Z., Zhang, Y., and Xu, C. C. (2021). Green Synthesis of Heterogeneous Copper-Alumina Catalyst for Selective Hydrogenation of Pure and Biomass-Derived 5-hydroxymethylfurfural to 2,5-bis(hydroxymethyl) furan. *Appl. Catal. A: Gen.* 609, 117892. doi:10.1016/j.apcata.2020.117892

Rao, P., Yang, L., Wang, X., Cui, P., Wang, Y., and Zhao, X. (2020). Lattice-compressed and N-Doped Co Nanoparticles to Boost Oxygen Reduction Reaction for Zinc-Air Batteries. *Appl. Surf. Sci.* 525, 146491. doi:10.1016/j.apsusc.2020.146491

Solanki, B. S., and Rode, C. V. (2019). Selective Hydrogenation of 5-HMF to 2,5-DMF over a Magnetically Recoverable Non-noble Metal Catalyst. *Green. Chem.* 21, 6390–6406. doi:10.1039/c9gc03091c

Tian, G., Daniel, R., Li, H., Xu, H., Shuai, S., and Richards, P. (2010). Laminar Burning Velocities of 2,5-Dimethylfuran Compared with Ethanol and Gasoline. *Energy Fuels* 24, 3898–3905. doi:10.1021/ef100452c

Viar, N., Requies, J. M., Agirre, I., Iriondo, A., Gil-Calvo, M., and Arias, P. L. (2020). Ni-Cu Bimetallic Catalytic System for Producing 5-Hydroxymethylfurfural-Derived Value-Added Biofuels. *ACS Sustain. Chem. Eng.* 8, 11183–11193. doi:10.1021/acssuschemeng.0c02433

Wang, H., Zhu, C., Li, D., Liu, Q., Tan, J., Wang, C., et al. (2019). Recent Advances in Catalytic Conversion of Biomass to 5-hydroxymethylfurfural and 2, 5-dimethylfuran. *Renew. Sustain. Energ. Rev.* 103, 227–247. doi:10.1016/j.rser.2018.12.010

Wang, J., Wei, Q., Ma, Q., Guo, Z., Qin, F., Ismagilov, Z. R., et al. (2020). Constructing Co@N-Doped Graphene Shell Catalyst *via* Mott-Schottky Effect for Selective Hydrogenation of 5-hydroxylmethylfurfural. *Appl. Catal. B: Environ.* 263, 118339. doi:10.1016/j.apcatb.2019.118339

Wang, L., Zuo, J., Zhang, Q., Peng, F., Chen, S., and Liu, Z. (2021). Catalytic Transfer Hydrogenation of Biomass-Derived 5-Hydroxymethylfurfural into 2,5-Dihydroxymethylfuran over Co/UiO-66-NH2. *Catal. Lett.* 152, 361–371. doi:10.1007/s10562-021-03635-3

Wang, Q., Feng, J., Zheng, L., Wang, B., Bi, R., He, Y., et al. (2019). Interfacial Structure-Determined Reaction Pathway and Selectivity for 5-(Hydroxymethyl)furfural Hydrogenation over Cu-Based Catalysts. *ACS Catal.* 10, 1353–1365. doi:10.1021/acscatal.9b03630

Wang, X., Liu, Y., and Liang, X. (2018). Hydrogenolysis of 5-hydroxymethylfurfural to 2,5-dimethylfuran over Supported Pt-Co Bimetallic Catalysts under Mild Conditions. *Green. Chem.* 20, 2894–2902. doi:10.1039/c8gc00716k

Xia, B. Y., Yan, Y., Li, N., Wu, H. B., Lou, X. W., and Wang, X. (2016). A Metal-Organic Framework-Derived Bifunctional Oxygen Electrocatalyst. *Nat. Energ.* 1, 15006. doi:10.1038/NENERGY.2015.6

Xu, L., Nie, R., Chen, X., Li, Y., Jiang, Y., and Lu, X. (2021). Formic Acid Enabled Selectivity Boosting in Transfer Hydrogenation of 5-hydroxymethylfurfural to 2,5-furandimethanol on Highly Dispersed Co-nx Sites. *Catal. Sci. Technol.* 11, 1451–1457. doi:10.1039/d0cy01969k

Yang, F., Mao, J., Li, S., Yin, J., Zhou, J., and Liu, W. (2019). Cobalt-graphene Nanomaterial as an Efficient Catalyst for Selective Hydrogenation of 5-hydroxymethylfurfural into 2,5-dimethylfuran. *Catal. Sci. Technol.* 9, 1329–1333. doi:10.1039/c9cy00330d

Zhang, J., Dong, K., and Luo, W. (2019). PdCl2-catalyzed Hydrodeoxygenation of 5-hydroxymethylfurfural into 2,5-dimethylfuran at Room-Temperature Using Polymethylhydrosiloxane as the Hydrogen Donor. *Chem. Eng. Sci.* 201, 467–474. doi:10.1016/j.ces.2019.03.011

Zhang, L., Xi, G., Chen, Z., Qi, Z., and Wang, X. (2017). Enhanced Formation of 5-HMF from Glucose Using a Highly Selective and Stable SAPO-34 Catalyst. *Chem. Eng. J.* 307, 877–883. doi:10.1016/j.cej.2016.09.003

Zhang Z, Z., Yao, S., Wang, C., Liu, M., Zhang, F., Hu, X., et al. (2019). CuZnCoOx Multifunctional Catalyst for *In Situ* Hydrogenation of 5-hydroxymethylfurfural with Ethanol as Hydrogen Carrier. *J. Catal.* 373, 314–321. doi:10.1016/j.jcat.2019.04.011

Zhao, W., Huang, Z., Yang, L., Liu, X., Xie, H., and Liu, Z. (2022). Highly Efficient Syntheses of 2,5-bis(hydroxymethyl)furan and 2,5-dimethylfuran *via* the Hydrogenation of Biomass-Derived 5-hydroxymethylfurfural over a Nickel-Cobalt Bimetallic Catalyst. *Appl. Surf. Sci.* 577, 151869. doi:10.1016/j.apsusc.2021.151869

Zhu, J., Xu, D., Ding, L. J., and Wang, P. c. (2021). CoPd Nanoalloys with Metal-Organic Framework as Template for Both N-Doped Carbon and Cobalt Precursor: Efficient and Robust Catalysts for Hydrogenation Reactions. *Chem. Eur. J.* 27, 2707–2716. doi:10.1002/chem.202003640

Zhu, K., Zhang, M., Feng, X., Qin, L., Kang, S.-Z., and Li, X. (2020). A Novel Copper-Bridged Graphitic Carbon Nitride/porphyrin Nanocomposite with Dramatically Enhanced Photocatalytic Hydrogen Generation. *Appl. Catal. B: Environ.* 268, 118434. doi:10.1016/j.apcatb.2019.118434

Zu, Y., Yang, P., Wang, J., Liu, X., Ren, J., Lu, G., et al. (2014). Efficient Production of the Liquid Fuel 2,5-dimethylfuran from 5-hydroxymethylfurfural over Ru/Co3O4 Catalyst. *Appl. Catal. B: Environ.* 146, 244–248. doi:10.1016/j.apcatb.2013.04.026

Hydrogenolysis of 5-Hydroxymethylfurfural to 2,5-Dimethylfuran Over a Modified CoAl-Hydrotalcite Catalyst

Jing Xia[1], De Gao[1], Feng Han[1], Ruifu Lv[1], Geoffrey I. N. Waterhouse[2] and Yan Li[1]*

[1]College of Chemistry and Material Science, Shandong Agricultural University, Taian, China, [2]School of Chemical Science, The University of Auckland Private Bag, Auckland, New Zealand

The catalytic hydrogenolysis of 5-hydroxymethylfurfural (HMF) to 2,5-dimethylfuran (DMF) is a promising route towards sustainable liquid fuels with a high energy density. Herein, a novel CuCoNiAl-containing mixed metal oxide catalyst (CuCoNiAl-MMO) was prepared by calcination a layered double hydroxide (LDH) precursor in N_2 at 500 °C, then applied for the catalytic hydrogenolysis of HMF to DMF. The effects of reaction time, reaction temperature and hydrogen pressure on DMF selectivity were investigated. Under relatively mild reaction conditions (180°C, 1.0 MPa H_2, 6.0 h), CuCoNiAl-MMO showed both a high initial activity and selectivity for hydrogenolysis of HMF to DMF, with HMF conversion rate of 99.8% and DMF selectivity of 95.3%. Catalysts characterization studies using scanning electron microscopy (SEM), transmission electron microscopy (TEM), X-ray diffraction (XRD) and X-ray photoelectron spectroscopy (XPS) revealed the presence of various metal oxides and metallic copper on the surface of the CuCoNiAl-MMO catalyst, with the presence of mixed metal-oxide-supported metallic Cu nanoparticles being responsible good hydrogenolysis activity of the catalyst for selective DMF synthesis.

Keywords: 5-hydroxymethylfurfural, 2,5-dimethylfuran, hydrogenolysis, hydrotalcite, metal oxide

1 INTRODUCTION

Climate change caused by anthropogenic greenhouse gas emissions is a major environmental concern (Bond, Doherty et al., 2013). Most of these emissions are in the form of CO_2 from the burning of fossil fuels for energy. Therefore, in order to reduce the harm to the environment and reduce the dependence on fossil fuel energy, the search for low-cost, safe, environmentally friendly, sustainable development of new energy has become a growing concern of people. Amongst fuels which can be produced sustainably, biomass derived products represent an excellent choice (Nakagawa et al., 2013; Zhang and Deng, 2015). Biomass can be converted into chemical energy and stored by photosynthesis, which is then converted into valuable chemicals and fuels by appropriate treatment methods. 5-Hydroxymethylfurfural (HMF), as a biomass platform compound readily obtained from sucrose and fructose, can be catalytically converted into a range of useful products, including 2,5-bis(hydroxymethyl)furan (DHMF), 1,6-hexanediol (HDO), 2,5-dimethyltetrahydrofuran (DMTHF), and 2,5-dimethylfuran (DMF) (Wang Q. et al., 2019). In these compounds, DMF is a liquid biofuel with high octane number, water insolubility, and high energy density. These characteristics are similar to many existing transportation fuels, making DMF an ideal and promising transportation liquid biofuel (Viar et al., 2019). The aldehyde group and
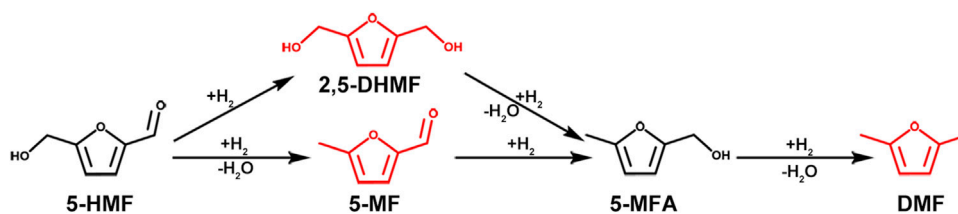
FIGURE 1 | Two reaction pathways for the hydrogenolysis of HMF to DMF.

hydroxymethyl group on the furan ring of 5-HMF are easy to react in the presence of catalyst and hydrogen donor, and hydrodehydration becomes DMF. In general, there are two possible reaction pathways for conversion of HMF into DMF, as shown in **Figure 1**. In Pathway 1, the aldehyde group on HMF is first hydrogenated to form DHMF, followed by hydrohydrolysis of the hydroxyl group on the furan ring to form 5-methylfurfuryl alcohol (5-MFA), an important reaction intermediate in the synthesis of DMF. In Pathway 2, the hydroxyl group in HMF hydrolyzes and dehydrates to generate 5-methylfurfural (5-MF), then the aldehyde group on 5-MF is hydrogenated to generate 5-MFA, after which the hydroxyl group on 5-MFA is further hydrolyzed to DMF.

To date, heterogeneous noble metal-based [such as Pt (Luo et al., 2016; Shi et al., 2016), Ru (Feng et al., 2020; Wang et al., 2020) and Pd (Nakagawa and Tomishige, 2010; Zhang J. et al., 2019)] catalysts offer the best all-round performance in the field of HMF hydrogenation to DMF. Luo et al. prepared a carbon-supported Pt_3Ni alloy nanoparticle catalyst, which efficiently converted HMF to DMF (98% yield) at 3.3 MPa H_2 and 160–200°C (Luo et al., 2016). Zu et al. prepared a Ru/Co_3O_4 catalyst by simple coprecipitation method. Under low reaction temperature and H_2 pressure conditions (130°C, 0.7 MPa), the yield of DMF reached 93.4% (Zu et al., 2014). Mhadmhan et al. prepared a Cu-Pd bimetallic catalyst on reduced graphene oxide (RGO), which offered good performance for the hydrogenation of HMF to DMF with 2-propanol as a hydrogen donor (96% HMF conversion and 95% DMF yield) (Mhadmhan et al., 2019). However, the high cost of these noble metal-based based catalysts are obstacles for the large scale conversion of HMF to DMF, motivating the search for low-cost catalysts based on non-noble metals. Dinesh et al. synthesized a Ni-Cu/HT catalyst by the deposition precipitation method, achieving a DMF yield of 83% at 85°C, 0.6 MPa H_2 pressure and 100 mg catalyst load (Gupta et al., 2020). Chen et al. prepared carbon-coated Cu-Co bimetallic nanoparticles (Cu-Co@Carbon) by heat-treating a bimetallic oxide precursor. The Cu-Co@Carbon catalyst afforded a DMF yield of 99.4% at 180°C and a H_2 pressure of 5 MPa over 8 h in a batch reactor, which was superior to supported precious metal catalysts (Chen et al., 2017). Yang et al. prepared a 2%Ni-20%Co/C catalyst, which was capable of selectively producing DMF in a high yield (95%) from biomass-derived HMF under mild conditions (130°C, 1 MPa H_2) (Yang et al., 2016). In these catalysts, synergies between the supported metals and the acid-base surface sites on the support promote the activation of

hydrogen, thereby resulting in enhanced catalyst activity for the hydrogenolysis of HMF to DMF (Yang et al., 2016; Gupta et al., 2020).

Layered double hydroxides (LDHs), also known as hydrotalcite-like compounds (HTlcs), are a type of 2D layered material with general formula $[(M^{2+})_{1-x} (M^{3+})_x (OH)_2]^{x+}(A_{x/m}^{m-} \cdot nH_2O]$. The LDH structure consists of positively charge sheets containing divalent and trivalent metal cations ions octahedrally coordinated by oxygen, with the interlayer region containing charge-balancing anions and water molecules. Calcination of LDH materials in air or an inert atmosphere above certain temperatures results in collapse of the 2D layered structure and the formation composite oxides (MMO) *via* topological transformation processes. Depending on the temperature and calcination environment, sometimes supported metal nanoparticle catalysts can be obtained. The LDH-derived catalyst obtained via these approaches typically possess the advantages of large specific surface area, high thermal stability and excellent dispersion of the metal and metal oxide phases (Xu et al., 2011; Mishra et al., 2018). Owing to the wide range of cations that can be accommodated in the LDH structure (e.g. divalent cations include Ca^{2+}, Mg^{2+}, Fe^{2+}, Co^{2+}, Mn^{2+}, Ni^{2+}, Cu^{2+}, or Zn^{2+} and trivalent cations include Al^{3+}, Fe^{3+}, Co^{3+}, and Ni^{3+}), it is possible to make a diverse range of catalysts with different surface properties via this strategy. Zhang et al. used a hydrotalcite precursor to synthesize an inexpensive copper-based catalyst for the selective transfer hydrogenation of biomass-based HMF with methanol as both a solvent and hydrogen donor (Zhang and Chen, 2017). Ma et al. prepared a NiCoTi-8 catalyst by heat treatment of a NiCoTi-LDH precursor, with the catalyst offering good performance for the hydrogenolysis of HMF to DMF (Ma et al., 2020). Zhang et al. prepared a $CuZnCoO_x$ ternary catalyst, which converted HMF to DMF (yield 99%) in the presence of ethanol as a hydrogen donor (Zhang Z. et al., 2019). The intercalation of the small anionic metal complexes in the interlayer region of LDH provides a further approach for modifying the chemical composition and physical properties (e.g. specific surface area and surface acidity/basicity) of the LDH-derived MMO catalysts (Ma et al., 2011; Zhang J. et al., 2019; Qin et al., 2020). Tailoring the surface composition and surface properties of the catalysts is therefore a good approach for realizing a high HMF conversion and selective DMF production.

In this study, a four-metal hydrotalcite CuCoNiAl-LDH precursor was prepared by a one-pot hydrothermal method.

After calcination at 500°C in a nitrogen environment, CuCoNiAl-MMO was obtained, which was then applied HMF hydrogenation to generate DMF. CuCoNiAl-MMO afforded a HMF conversion of 99.8% rate and DMF yield of 95.3% under mild conditions (180°C, 1.0 MPa H_2), and could be recycled three times whilst maintaining stability. Characterization studies verified that the formation of MMO-supported zero-valent Cu and Co nanoparticles accounted for the excellent performance of the CuCoNiAl-MMO catalyst in the hydrogenolysis of HMF.

2 MATERIALS AND METHODS

2.1 Materials

Copper nitrate trihydrate ($Cu(NO_3)_2 \cdot 3H_2O$, ≥99%) was purchased from Aladdin Chemical Trading Co. Ltd. Cobalt (II) nitrate hexahydrate ($Co(NO_3)_2 \cdot 6H_2O$, ≥98%), nickel (II) chloride hexahydrate ($NiCl_2 \cdot 6H_2O$, ≥98%), and 5-hydroxymethyl furfural ($C_6H_6O_3$, ≥98%) were purchased from Shanghai D&B Biological Science and Technology Co. Ltd. Aluminum nitrate nonahydrate ($Al(NO_3)_3 \cdot 9H_2O$, >97%) was purchased from BASF Chemical Trading Co. Ltd. (TianJin, China). Urea ($CO(NH_2)_2$, ≥99.0%), ethanol absolute (CH_3CH_2OH, ≥99.7%), and tetrahydrofuran (C_4H_8O, ≥99.0%) were purchased from Tianjin Kaitong Chemical Reagent Co. Ltd. The experimental water was deionized water. The hydrogen used in the experiment was 99.9% pure.

2.2 Preparation of CuCoNiAl-MMO

First, the catalyst precursor CuCoNiAl-LDH was prepared using a hydrothermal method. Briefly, 0.01 mol $Cu(NO_3)_2 \cdot 3H_2O$, 0.01 mol $Co(NO_3)_2 \cdot 6H_2O$, 0.01 mol $NiCl_2 \cdot 6H_2O$, 0.01 mol $Al(NO_3)_3 \cdot 9H_2O$ and 0.15 mol of urea were dissolved in 100 ml of deionized water. The molar ratio of Cu/Co/Ni/Al was 1:1:1:1. The resulting solution was then stirred at room temperature for 1 h. Next, the solution was transferred to a 100 ml autoclave and hydrothermal reacted in an oven at 120°C for 6 h. After the reaction device was cooled to room temperature, the solid product was collected, washed with deionized water to pH = 7, and dried at 90°C for 10 h. The product obtained is denoted herein as CuCoNiAl-LDH. CuCoNiAl-MMO was obtained by calcination CuCoNiAl-LDH in a tube furnace at 500°C under a nitrogen atmosphere for 5 h. For reference purposes, several other LDH precursors (CoAl-LDH and CuCoAl-LDH) were also prepared, which yielded CoAl-MMO and CuCoAl-MMO, respectively, after calcination at 500°C in nitrogen environment.

2.3 Hydrogenation Tests

The catalytic hydrogenation experiments of HMF were carried out in a 50 ml autoclave. In a typical experiment, the reactor was charged with 0.25 g of HMF, 0.1 g of catalyst, and 10 ml of tetrahydrofuran (THF). To remove other gases, the reactor was purged three times with H2 before the reaction. Then, the reactor was charged with H_2 (1.0 MPa). Reactions were carried out at 180°C for 6 h with stirring at

560 rpm. After the reaction, the reaction solution was collected, and the supernatant was collected by centrifugation. Biphenyl (0.1 g) was then added to the supernatant liquid as an internal standard. Finally, the liquid samples were analyzed on a Shimadzu GC-2010 gas chromatograph equipped with a AE-SE-54 column and a flame ionization detector (FID). The HMF conversion and product selectivities were calculated with reference to the internal standard.

2.4 Catalyst Recycling Tests

After the HMF hydrogentation test, the used solid catalyst was collected by centrifugation, washed with ethanol three times, then dried at 80°C in the oven. Finally, the catalyst was heated at 500°C for 5 h in a tube furnace before reuse.

2.5 Catalyst Characterization

SEM analysis was performed on NoVaTM Nano SEM 430 scanning electron microscope (FEI, United States) with electron acceleration voltage of 20 kV. High-resolution transmission electron microscopy (HRTEM) images were acquired on a FEI Tecnai G20 (United States) instrument with an accelerating voltage of 300 kV. The XRD patterns were obtained by Japanese Rigaku Smartlab SE XRD diffractometer, with Cu Kα source (λ = 0.154 nm, 40 kV) as the light source, and the scanning speed of data acquisition was 2°/min. TGA analysis was performed in air using a thermogravimetric analyzer (TA SDT Q600). The N_2 flow rate was 100 ml/min and the heating rate was 10°C/min. FT-IR spectra were in the wavelength range of 4,000–400/cm and were collected on a Thermo Scientific Nicolet 380 spectrometer (United States). XPS maps were obtained on the K-alpha XPS system (Thermo Fisher Scientific, United States) equipped with a monochrome Al Kα source (hν = 1,486.6 eV). Binding energy scale calibration was performed using C 1s (284.8 eV). N_2 adsorption and desorption isotherms at 77 K were measured on a Tristar 3,000 instrument (Micromeritics Instrument Corp). Samples were degassed at 373 K for 12 h before data acquisition. BET and BJH methods were used to calculate the surface area and pore volume of samples, respectively. Temperature-programmed desorption experiments of NH_3 (NH_3-TPD) were performed on an AutoChem II 2920 V5.02 instrument (Micromeritics instrument Corp). In the NH_3-TPD experiment, 100 mg of the catalyst was pretreated under argon atmosphere at 300°C for 2 h to remove the surface adsorbed species. The catalyst was then cooled to 50°C and exposed to a 2000 ppm NH_3/Ar atmosphere for 2 h to achieve NH_3 adsorption saturation. Then the catalyst was reacted in 50 ml/min argon solution for 1 h, and finally the catalyst was heated from 50 to 800°C at a heating rate of 10°C/min. The thermal conductivity detector (TCD) detected the change of NH_3 with temperature. Pyridine infrared (Py-IR) spectra were obtained by testing on a PE Frontier FT-IR spectrometer (PerkinElmer). The sample was vacuum-degassed at 350°C for 2 h, followed by adsorption of pyridine vapor (saturated vapor pressure) at room temperature for 0.5 h. For H_2-TPR analysis, the catalyst was
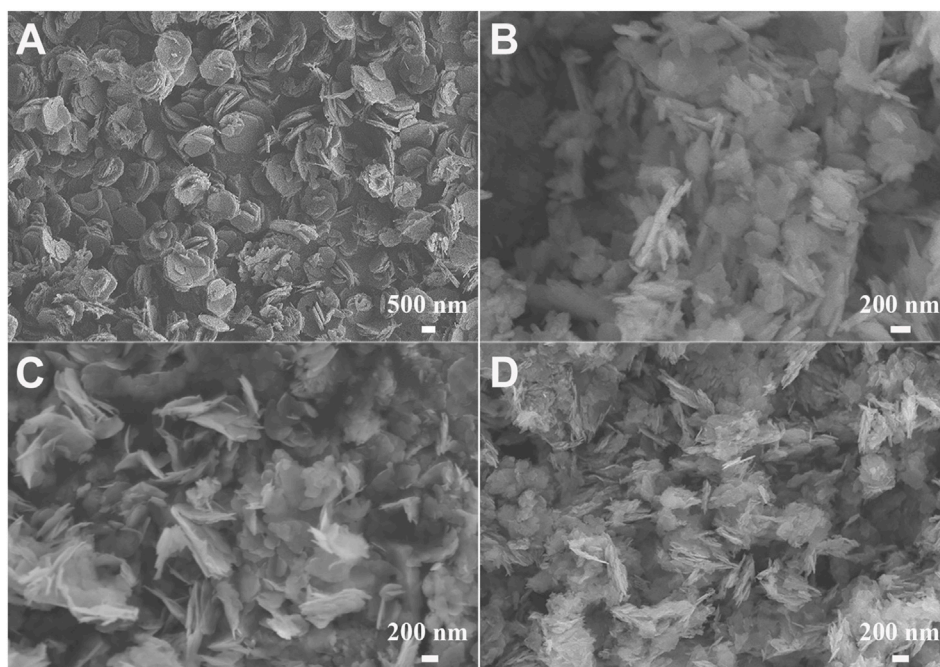
FIGURE 2 | SEM images of **(A)** CoAl-LDH, **(B)** CuCoAl-LDH, **(C)** CuCoNiAl-LDH, and **(D)** CuCoNiAl-MMO.
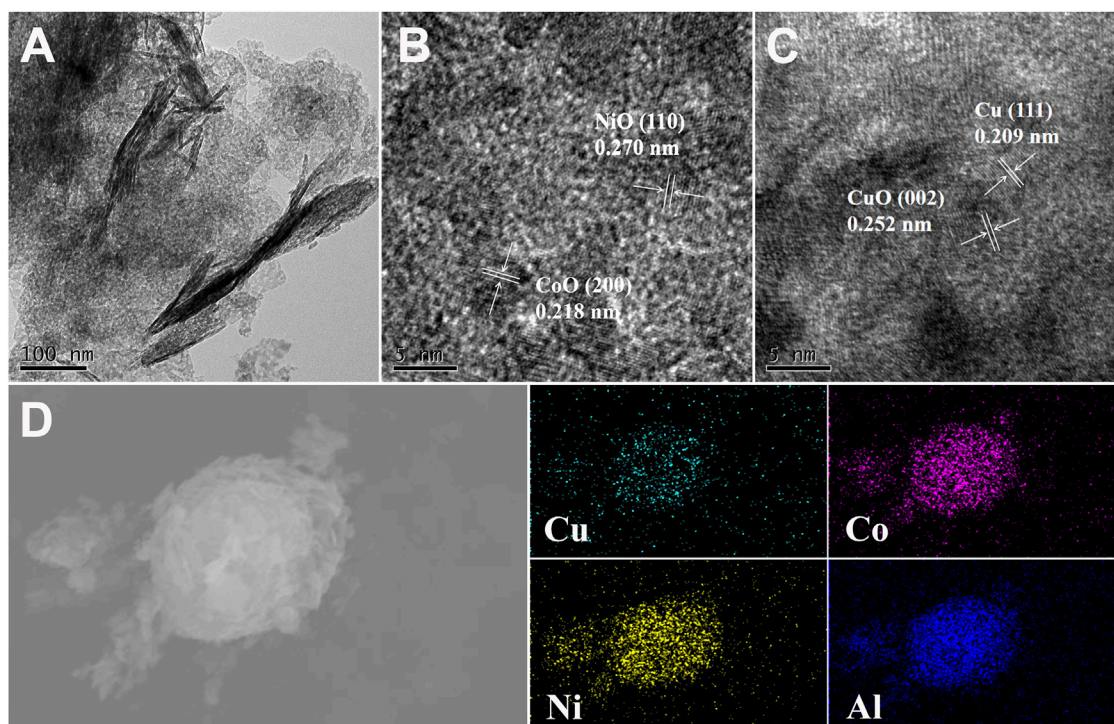
FIGURE 3 | (A) TEM and **(B)**, **(C)** HRTEM images of CuCoNiAl-MMO, **(D)** SEM-EDS image and corresponding element maps for CuCoNiAl-MMO.

heated at 300°C for 2 h under a He atmosphere, then cooled to 50°C and kept at a flow of He (50 ml/min) for 1 h. Next, a mixed gas of 5% H₂/He (50 ml/min) was introduced and the catalyst was heated from 50 to 800°C at a rate of 10°C/min. Elemental analysis data were collected by atomic emission spectrometer (ICP-AES).
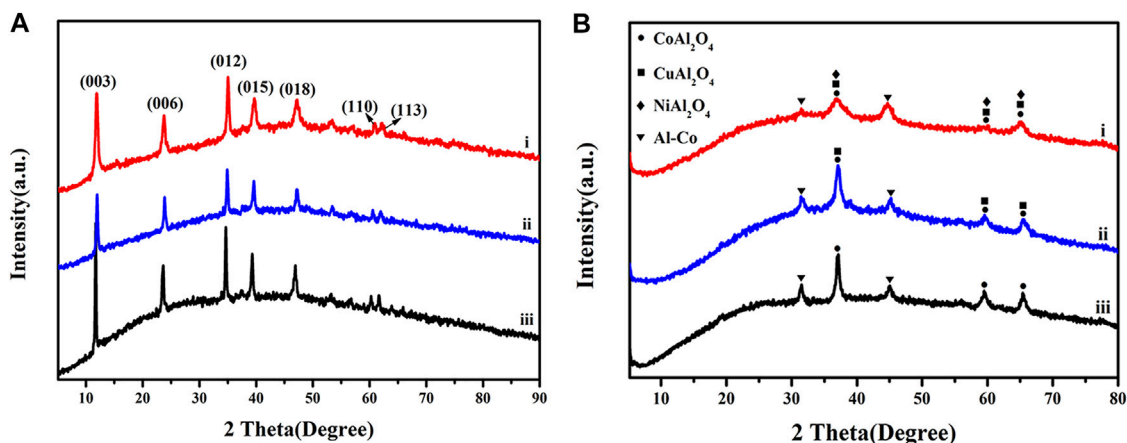
FIGURE 4 | XRD patterns for **(A)** CuCoNiAl-LDH **(i)**, CuCoAl-LDH **(ii)** and CoAl-LDH **(iii)**, and **(B)** CuCoNiAl-MMO **(I)**, CuCoAl-MMO **(ii)** and CoAl-MMO **(iii)**.

3 RESULTS AND DISCUSSION

3.1 Catalyst Characterization
3.1.1 SEM
The morphologies of the CoAl-LDH, CuCoAl-LDH and CuCoNiAl-LDH precursors were first examined by SEM (**Figure 2**). The CoAl-LDH sample consisted of uniformly sized hexagonal platelets that were stacked on top of each other (**Figure 2A**). This structure is typical for LDH materials. The CuCoAl-LDH sample also contained stacked platelets, but the platelet size and shape were less uniform (**Figure 2B**). The morphology of CuCoNiAl-LDH was similar to that of CuCoAl-LDH (**Figure 2C**). CuCoNiAl-LDH was calcined under N_2 at 500°C for 5 h to obtain CuCoNiAl-MMO (**Figure 2D**), which retained some of the stacked platelet structure of the LDH precursor.

3.1.2 TEM
In order to better understand the structure and element composition of the CuCoNiAl-MMO catalyst, TEM and HRTEM analyses were performed. **Figure 3A** shows that CuCoNiAl-MMO retained some of the layered structure of the LDH precursor. HRTEM images of CuCoNiAl-MMO (**Figures 3B,C**) provided more detailed information about the components present in the sample. In **Figure 3B**, nanoparticles with lattice fringes of 0.218 and 0.270 nm are observed, corresponding to CoO (200) and NiO (110) planes, respectively (Zhu et al., 2018; Li et al., 2019). In **Figure 3C**, nanoparticles with lattice fringes of 0.209 and 0.252 nm are observed, which can readily be assigned to Cu (111) and CuO (002) planes, respectively (Gao et al., 2018; Luo et al., 2020). No obvious latticle fringes associated with an Al-containing phase were seen, suggesting that alumina was likely present in an amorphous phase (i.e. an amorphous alumina). Next, the element distribution in CuCoNiAl-MMO was probed by EDS element mapping analysis. As shown in **Figure 3D**, Cu, Co, Ni and Al were are evenly distributed throughout the catalyst, consistent with expectations for LDH-derived catalysts. Results suggests that the four metals (in their respective metallic an oxide

forms) were in intimate contact and thus could potentially act synergistically to boost the catalytic activity of CuCoNiAl-MMO for HMF hydrogenation.

3.1.3 XRD
Figure 4A shows XRD patterns for the LDH precursors. All show characteristic sets of (003), (006) and (012) reflections at 11.8, 23.7 and 34.8° typical for stacked LDH materials. After calcination at 500°C in N_2, the characteristic reflections disappeared due to collapse of the LDH interlayers, and were instead replaced by peaks associated mainly with oxide phases, as shown in **Figure 4B**. The XRD patterns for CuCoNiAl-MMO, CuCoAl-MMO, and CoAl-MMO were similar, showing peaks at similar positions and peaks with the same relative intensities, consistent with the formation of spinel-like MAl_2O_4 oxides (Gao et al., 2018). The XRD pattern of CoAl-MMO contained peaks at 37.1, 59.5 and 65.5°, corresponding to the (311), (511) and (440) phases of $CoAl_2O_4$ (PDF#-38–0,814), respectively. In addition, further peaks were observed around 31.4° and 45.0°, typical for the (100) and (110) reflections, respectively, an Al-Co alloy (PDF#-29–0,021). The XRD patterns of CuCoAl-MMO, showed peaks at 37.1, 59.5 and 65.5°, corresponding to the (220), (311) and (440) crystal planes, respectively, of $CuAl_2O_4$ (PDF#-33–0,448). The presence of the Al-Co alloy was also evident by peaks at 31.4° and 45.0°. For CuCoNiAl-MMO, in addition to the CoAl2O4 and CuAl2O4 phases, peaks at 37.1, 59.5 and 65.5° might be due to the (311), (511) and (440) reflections of $NiAl_2O_4$ (PDF#-10–0,339). These overlap with peaks for $CuAl_2O_4$. By HRTEM, lattice fringes associated with Cu metal, NiO, CuO and CoO were seen. These phases were not detected by XRD, suggesting that were surface phases and present in relatively low abundance relative to the MAl_2O_4 and Al-Co phases. Cu_2AlO_4, $CoAl_2O_4$, and $NiAl_2O_4$ belong to the spinel phase, which are typical metal-based oxides with high catalytic activity, and their tetrahedral and octahedral centers provide multiple sites to accommodate different metal cations (Dasgupta et al., 2016; O'Quinn et al., 2017; Qi et al., 2022). In addition, the spinel phase is thermally stable, which can make the structure of the catalyst more stable (Ma et al., 2011).

FIGURE 5 | XPS spectra for CuCoNiAl-MMO samples: **(A)** survey spectrum; **(B)** Cu 2p spectrum; **(C)** Co 2p spectrum; **(D)** Ni 2p spectrum; **(E)** Al 2p spectrum and **(F)** O 1s spectrum.
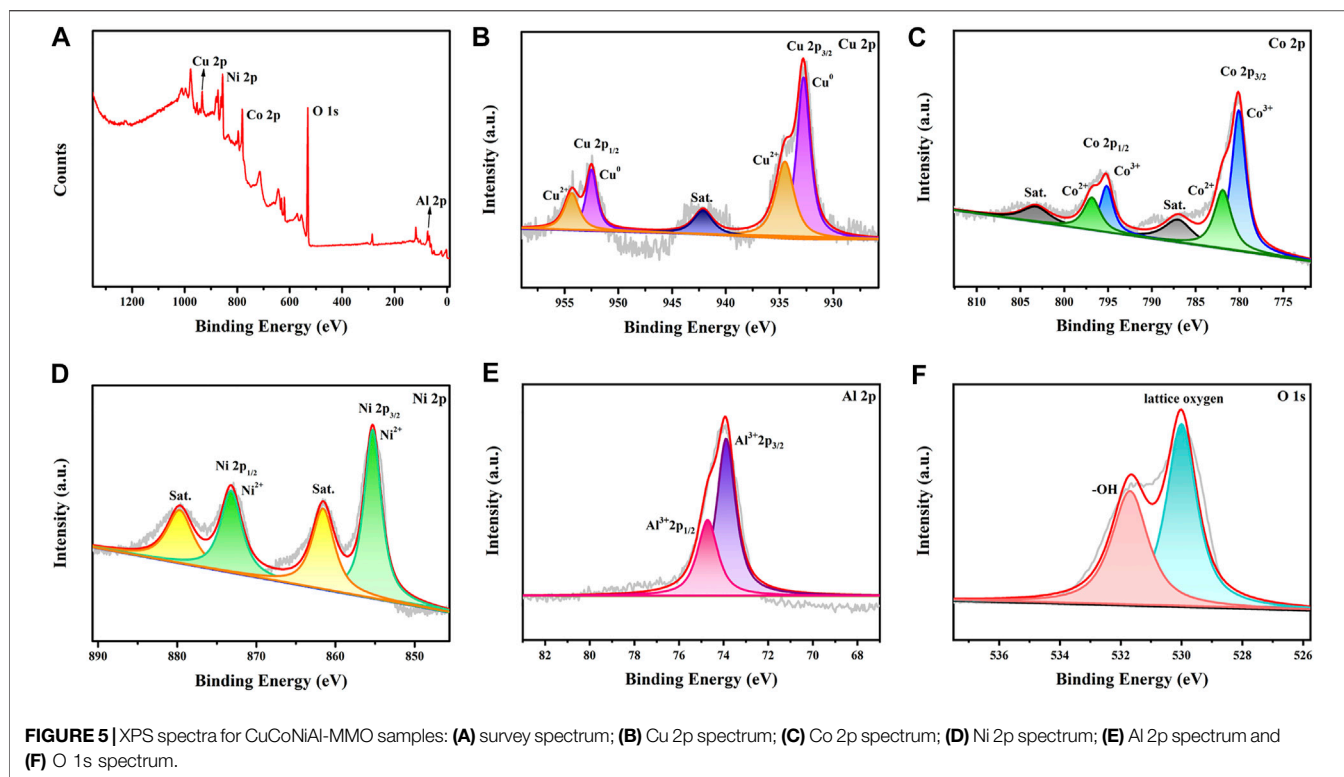
The Al-containing component acts both as a carrier and as a physical spacer to suppress the aggregation of metal particles, thereby ensuring high dispersion (Gao et al., 2018).

3.1.4 XPS

The valence states of the metals in the CuCoNiAl-MMO catalyst were probed by XPS. The survey spectrum of CuCoNiAl-MMO is shown in **Figure 5A**, revealing the presence of Cu, Co, Ni, Al and O elements. The Cu 2p XPS spectrum showed three characteristic sets of peaks, each having a 2:1 area ration for the $2p_{3/2}$ and $2p_{1/2}$ peaks. The Cu $2p_{3/2}$; Cu $2p_{1/2}$ and satellite peaks at 932.6, 952.5 and 942.1 eV, respectively, indicate the presence of Cu species exists in the form of Cu^0 ($2p_{3/2}$ = 932.8 eV, $2p_{1/2}$ = 952.5 eV) and Cu^{2+} ($2p_{3/2}$ = 934.5 eV, $2p_{1/2}$ = 954.3 eV) in CuO or Cu_2AlO_4 (**Figure 5B**) (Shang et al., 2020; Umasankar et al., 2020). The Co 2p XPS spectrum (**Figure 5C**) showed two distinct sets of peaks: Co^{2+} ($2p_{3/2}$ = 781.9 eV, $2p_{1/2}$ = 796.8 eV) and Co^{3+} ($2p_{3/2}$ = 780.3 eV, $2p_{1/2}$ = 795.2 eV). In addition, two Co 2p shake-up satellites were observed at 787.8 and 803.5 eV (Liao et al., 2020). Therefore, it can be concluded that cobalt exists mainly existed in the form of oxides in the near surface region of the sample (CoAl alloys seen by XRD may have been surface oxidized). The Ni 2p XPS spectrum (**Figure 5D**) showed peaks at 855.2 and 873.1 eV (2:1 area ratio), which can be easily assigned to the Ni $2p_{3/2}$ and Ni $2p_{1/2}$ peak, respectively of Ni(II) (Ma et al., 2020) in NiO or $NiAl_2O_4$. The presence of shake-up satellite peaks in the Ni 2p spectrum further confirmed the presence of Ni^{2+}. The Al 2p spectrum (**Figure 5E**) can be deconvoluted into two Gauss-Lorentz sub-peaks at 73.8 and 74.7 eV (2:1 area ratio), which were assigned to an Al^{3+}-containing oxide species ($2p_{3/2}$ and $2p_{1/}$

FIGURE 6 | TG-DTA curves for CuCoNiAl-LDH in N_2. The heating rate was 10°C/min.
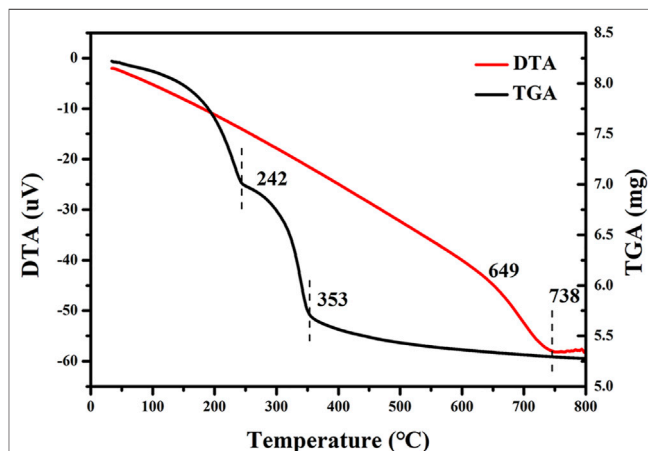
$_2$, respectively) (Motamedi and Cadien, 2014). The O 1s (**Figure 5F**) XPS spectrum for CuCoNiAl-MMO contained peaks due to lattice oxygen in metal oxides (529.9 eV) and -OH (531.5 eV). The XPS data are basically consistent with the XRD characterization results.

3.1.5 TG–DTA

Figure 6 shows the TG-DTA curve obtained by calcination CuCoNiAl-LDH in N_2. A large mass loss was observed around 242°C, resulting from the removal of water from the LDH
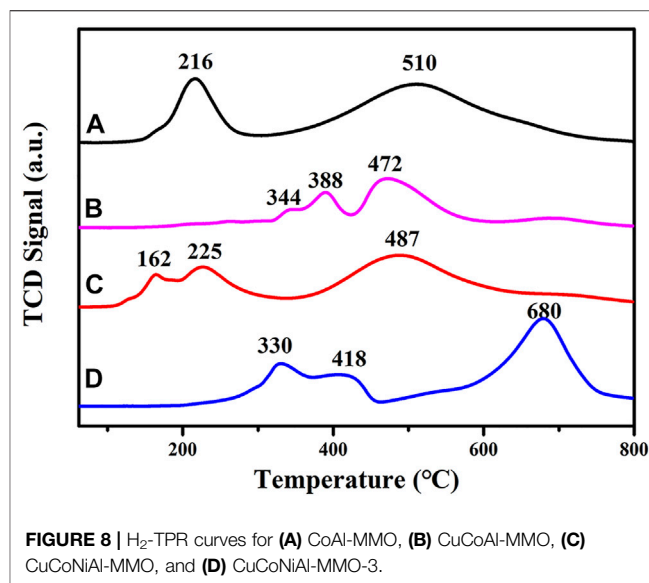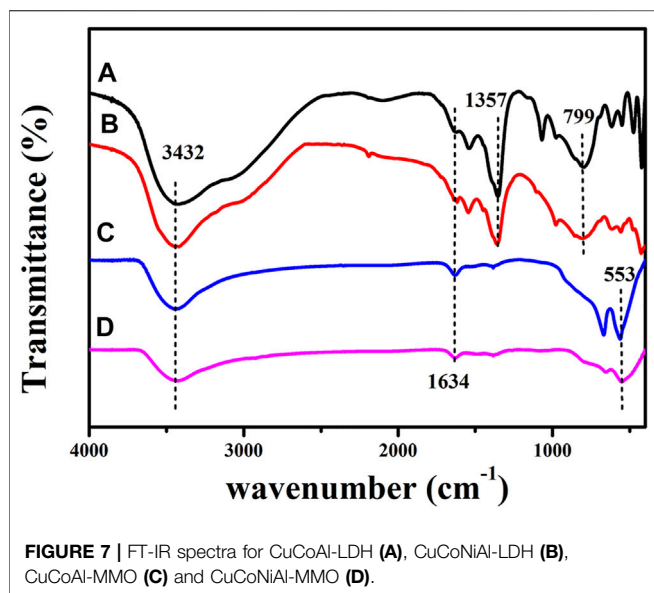
FIGURE 7 | FT-IR spectra for CuCoAl-LDH **(A)**, CuCoNiAl-LDH **(B)**, CuCoAl-MMO **(C)** and CuCoNiAl-MMO **(D)**.

FIGURE 8 | H$_2$-TPR curves for **(A)** CoAl-MMO, **(B)** CuCoAl-MMO, **(C)** CuCoNiAl-MMO, and **(D)** CuCoNiAl-MMO-3.

TABLE 1 | Summary of N$_2$ physisorption-data for CuCoNiAl-LDH and CuCoNiAl-MMO.

Catalyst	BET surface area (m^2/g)	BJH surface area (m^2/g)	Pore volume (cm^3/g)	Pore diameter (Å
CuCoNiAl-LDH	59.2	66.4	0.48	286.7
CuCoNiAl-MMO	148.6	168.2	0.83	197.1

interlayer (Ardanuy and Velasco, 2011). Greater mass loss occurred between 242–353°C, which is associated with dehydroxylation of LDH flakes and decomposition of nitrate/carbonate anions in the interlayer (Zheng and Chen, 2017). Above 353°C, the product was stable against large mass losses. Based on the TG-DTA curves, a temperature of 500°C was selected for the preparation of the CuCoNiAl-MMO catalyst.

3.1.6 FT-IR

Figure 7 shows the FT-IR spectra for CuCoAl-LDH, CuCoNiAl-LDH, CuCoAl-MMO, and CuCoNiAl-MMO. The FT-IR spectra of CuCoAl-LDH and CuCoNiAl-LDH showed a broad absorption peak at 3,432 cm^{-1}, due to O-H stretching vibrations of the hydroxyl groups and water in the LDH interlayer region. The bending vibration of the interlayer water molecules occurs at 1,634 cm^{-1}. The peaks at 799 cm^{-1} and 1,357 cm^{-1} belong to the stretching of CO$_3^{2-}$ (Zheng and Chen, 2017) ions in the LDH interlayer. In an aqueous solution containing dissolved CO$_2$, the interlayer nitrate of LDHs are easily exchanged for carbonate (Auxilio et al., 2008). After calcination at 500°C, the sharp absorption peak representing CO$_3^{2-}$ disappeared completely. New features appeared below 800 cm^{-1}, which are related to M-O stretching vibrations (Li et al., 2017). This further proves that oxide phases were the main product of LDH calcination in N$_2$.

3.1.7 Specific Surface Area

The specific surface area and porosity of CuCoNiAl-LDH and CuCoNiAl-MMO were determined by N$_2$ physisorption at 77 K.

Table 1 shows the specific surface area and pore size distribution data of CuCoNiAl-LDH and CuCoNiAl-MMO calculated by Brunauer Emmett Teller (BET) and Barrett Joyner Halenda (BJH) methods, respectively. The BET specific surface area of CuCoNiAl-MMO was 2.5 times higher than that of the LDH precursor. The BJH cumulative pore volume of CuCoNiAl-MMO was 1.74 times that of CuCoNiAl-LDH, consistent with the former containing smaller mesopores. Results show that the collapse of the laminate structure in CuCoNiAl-LDH with calcination to 500°C resulted in a solid product with a high surface area and abundant pores (Ma et al., 2011), as is evident in the SEM image of CuCoNiAl-MMO in **Figure 2D**.

3.1.8 H$_2$-TPR

H$_2$-TPR spectra for the four catalysts, CoAl-MMO, CuCoAl-MMO, CuCoNiAl-MMO and CuCoNiAl-MMO-3 (the aged catalyst after three cycles of HMF hydrogenation) are shown in **Figure 8**. For the CoAl-MMO sample (curve a), two H$_2$ consumption peaks are observed at 216 and 510°C. The first peak at 216°C is due to the reduction of Co$_3$O$_4$ to CoO, and the second peak at 510°C is due to the reduction of CoO to metallic cobalt (Zu et al., 2014). For CuCoAl-MMO, three reduction peaks are found. The peaks are associated with the two step reduction of Cu^{2+} to Cu$^+$ to Cu (Gao et al., 2018) and the higher temperature peak with the reduction of Co^{2+} (i.e., partial reduction of CuAl$_2$O$_4$/Co$_2$AlO$_4$ (Koso et al., 2009; Shi et al., 2016)). The lowering of the reduction temperature for the Co^{2+} to Co metal transition in the presence of Cu^{2+} may be due to the

TABLE 2 | Performance comparison of different catalysts for the selective hydrogenolysis of HMF.

Catalyst	Conversion (%)	Selectivity (%)		
		DMF	5-MF	5-MFA
CoAl-MMO	15.9	44.7	41.5	13.8
CoNiAl-MMO	31.4	84.5	11.6	3.9
CuCoAl-MMO	39.5	81.6	13.9	4.5
CuCoNiAl-MMO	99.8	95.3	2.2	0.4

Reaction conditions: HMF (0.25 g), tetrahydrofuran (THF, 10 ml), catalyst (0.1 g), T = 180°C, p(H_2) = 1.0 MPa, 6 h.

strong interaction between Cu^{2+} and the Co/Al oxide matrix (Wang X. et al., 2019). Thee reduction peaks were seen in H_2-TPR spectrum of CuCoNiAl-MMO (curve c) at 162, 225 and 487°C. The peak at 162°C is due to the reduction of CuO to Cu^+, the peak at 225°C to the reduction of Co^{3+} to Co^{2+} (as CoO), and the peak at 487°C to the reduction of CoO to cobalt metal. Based on the results, in can be concluded that cobalt in the samples is closely associated with copper and nickel. These interactions promote the reduction of Co and were expected to modify the performance

of the catalyst (Gupta et al., 2020; Umasankar et al., 2020). The used CuCoNiAl-MMO-3 catalyst showed TPR peaks at 330, 418, and 680°C. These peaks are discussed below.

3.2 Catalytic Performance Analysis
3.2.1 Catalyst Performance Tests
Following the catalyst characterization studies, the catalytic performance of the three catalysts CoAl-MMO, CoNiAl-MMO, CuCoAl-MMO and CuCoNiAl-MMO for the conversion of HMF to DMF was studied. Experiments used tetrahydrofuran as the solvent, 1.0 MPa H_2, reaction temperature 180°C for 6 h. **Table 2** compares the performance of the different catalysts. The conversion rate of HMF and the selectivity to DMF on the CoAl-MMO catalyst were both very low, with the reaction producing mainly intermediate products. CoNiAl-MMO and CuCoAl-MMO were prepared by introducing Ni and Cu elements into the catalyst, respectively. The conversion rate of HMF was improved, and the selectivity of DMF was also significantly improved. Combining the four metals, the CuCoNiAl-MMO catalyst offered outstanding performance, with a HMF conversion of 99.8% and the

FIGURE 9 | Effect of **(A)** reaction time, **(B)** temperature, **(C)** H_2 pressure, and **(D)** catalytic test runs on the HMF hydrogenation performance of CuCoNiAl-MMO. Reaction conditions: **(A)** 0.1 g catalyst, 1.0 MPa H_2, 0.25 g HMF, 180°C **(B)** 0.1 g catalyst, 1.0 MPa H_2, 0.25 g HMF, 6 h **(C)** 0.1 g catalyst, 0.25 g HMF, 6 h, 180°C, and **(D)** 0.1 g catalyst, 1.0 MPa H_2, 0.25 g HMF, 6 h, 180°C.
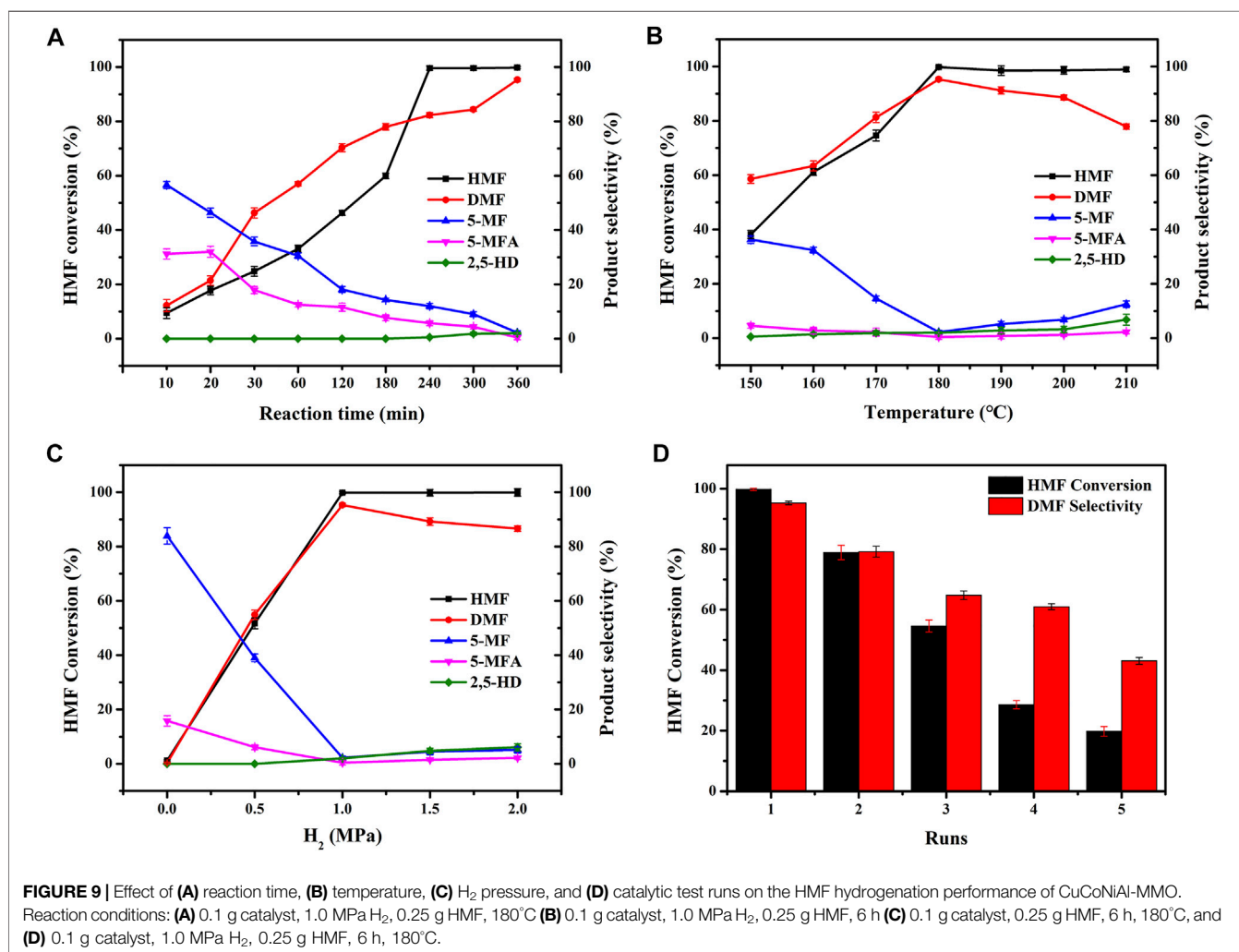
selectivity of DMF is 95.3%. Therefore, CuCoNiAl-MMO is an excellent catalyst for this hydrogenation reaction.

3.2.2 Exploration of Experimental Conditions

In order to further investigate the excellent catalytic performance of CuCoNiAl-MMO for the selective hydrogenation of HMF to DMF, we explored the effects of reaction time, temperature and H_2 pressure on the reaction (**Figures 9A–C**). **Figure 9A** shows the effect of reaction time. We analyzed the reaction mixture at reaction times of from 10 min to 6 h. The conversion of HMF and the selectivity to DMF increased gradually over the first 4 h, with the HMF conversion plateauing from 4–6 h. At 6 h, the HMF conversion and selectivity to DMF were 99.8 and 95.3%, respectively. Intermediates such as 5-MF, 5-MFA decreased with reaction times, whereas the by-product 2,5-hexanedione (2,5-HD) formed at the longer reaction times. **Figure 9B** shows the effect of reaction temperature on HMF hydrogenation over the CuCoNiAl-MMO catalyst. In the temperature range of 150–180°C, the conversion rate of HMF and the selectivity to DMF gradually increased with the increase of temperature, whilst the content of 5-MF and 5-MFA progressively decreased. The reaction was optimal around 180°C. Above 180°C, the content of the intermediate products (5-MF) and by-products (2,5-HD) increased, since DMF can be hydrogenated to generate 2,5-HD. **Figure 9C** shows the influence of hydrogen pressure on HMF hydrogenation over the CuCoNiAl-MMO catalyst. When no hydrogen was in the reaction system, the conversion rate of HMF is almost negligible. The conversion rate of HMF and the selectivity of DMF both increased with an increase in the hydrogen pressure, with the best catalyst activity and selectivity to DMF being obtained at a hydrogen pressure is 1.0 MPa. When the hydrogen pressure increased further, DMF was hydrogenated to 2,5-HD, the lowering the selectivity to DMF. Therefore, considering the safety of the experiment, we chose hydrogen pressure of 1.0 MPa for subsequent catalytic tests. Based on the results, we could deduce the reaction path of HMF conversion into DMF. HMF hydrogenolysis dehydration produces 5-MF, with the 5-MF then hydrogenated to produce 5-MFA. Finally, 5-MFA is further hydrogenolyzed into DMF. In addition, we also tested the recycling performance of the catalyst (**Figure 9D**). After three cycles use of the catalyst, the catalytic performance dropped significantly. The reasons for the deactivation of the catalyst are discussed below.

3.2.3 ICP-AES

In order to explore the reason why the catalytic performance of CuCoNiAl-MMO catalyst decreased sharply after three cycles of HMF hydrogenation tests, ICP-AES was used to probe the bulk chemical composition of CuCoNiAl-MMO and CuCoNiAl-MMO-3, with the aim of identifying any element losses during the catalyst tests. As shown in **Table 3**, the concentrations of Co and Al decreased significantly after three cycles of catalyst tests. Among them, Co is an important active metal, and its reduction affects the catalytic performance of the catalyst. The Al-containing component as a carrier has the effect of inhibiting the aggregation of metal particles and ensuring high dispersibility, and its reduction

TABLE 3 | The concentration of Cu, Co, Ni, Al in CuCoNiAl-MMO and CuCoNiAl-MMO-3 catalysts.

Catalyst	Cu (%)	Co (%)	Ni (%)	Al (%)
CuCoNiAl-MMO	14.00	23.59	41.84	20.56
CuCoNiAl-MMO-3	16.16	18.93	49.40	15.50

reduces the stability of the catalyst structure, thereby affecting the performance of the catalyst.

Figure 10 shows SEM images for the fresh and used CuCoNiAl-MMO catalyst. After the three test cycles, the resulting CuCoNiAl-MMO-3 catalyst had a denser structure with smaller sheet sizes. This might have reduced the availability of active sites on the catalyst surface, thereby reducing the hydrogenation performance. In addition, the CuCoNiAl-MMO-3 catalyst was also characterized by H_2-TPR to study the changes caused by the catalytic tests. **Figure 8** (curve d) shows that the reduction peaks moved to high temperature using the catalyst three times for HMF hydrogenation (i.e., the surface species were less reducible compared to the fresh catalyst). This was likely due to particle aggregation and a change in the type of metal/oxide species on catalyst surface.

3.2.4 NH$_3$-TPD

NH$_3$-TPD was used to examine the acid sites on the surface of CuCoNiAl-MMO and CuCoNiAl-MMO-3. Results are shown in **Figure 11A**. Based on the NH$_3$ desorption temperature, the strengths of the acidic sites can be classified as weak (<250°C), medium (250–400 C), and strong (>400 C) (Srivastava et al., 2017). Both CuCoNiAl-MMO and CuCoNiAl-MMO-3 showed NH$_3$ desorption peaks in the 100–200 C, 300–500 C, and 500–800 C regions, indicating that each catalyst contained weak acid, medium acid and strong acid sites. After three cycles of use, the amount of strong acid sites in the catalyst increased significantly. Strong acid sites are involved in C-C bond cleavage reactions such as catalytic cracking, skeletal isomerization, transalkylation, and disproportionation. Weak acid centers are involved in reactions of C-H bond cleavage, such as hydrogen transfer, hydration, cyclization, alkylation, etc. However, if the catalyst is too acidic, it will be deactivated by carbon deposition. Therefore, the abundance of strong acid sites is not conducive for HMF hydrogenolysis to DMF. Next, pyridine adsorption infrared tests (Py-IR) were conducted. As shown in **Figure 11B**, it can be seen that CuCoNiAl-MMO has more acidic sites for adsorption than CuCoNiAl-MMO-3. Both catalysts showed bands at 1,445 cm^{-1} and 1,488 cm^{-1}, consistent with the adsorption of pyridine on Lewis acid sites. In addition, a weak absorption peak at 1,540 cm^{-1} was seen due to pyridine adsorption on Brønsted acid (B) sites. The adsorption band at 1,596 cm^{-1} arises from hydrogen bonding between pyridine and OH (Brønsted acid center) (Zhao and Lercher, 2012). Notably, the amount of Lewis acid and Brønsted acid sites determined by Py-IR on the catalysts were much lower compared with those identified by NH$_3$-TPD analysis, consistent with the presence of a large quantity of acidic OH groups on the surface of the catalysts (Zhang and Chen, 2017). In the presence of acid groups on the
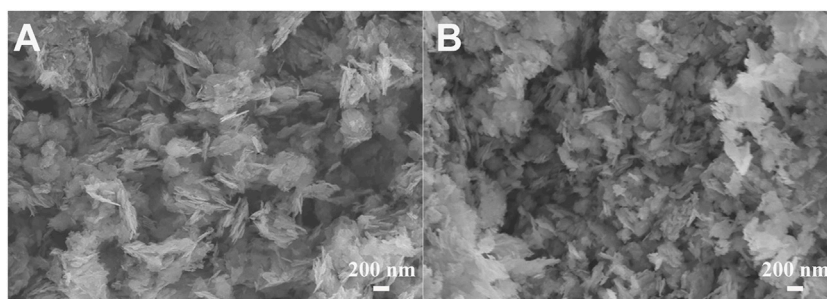
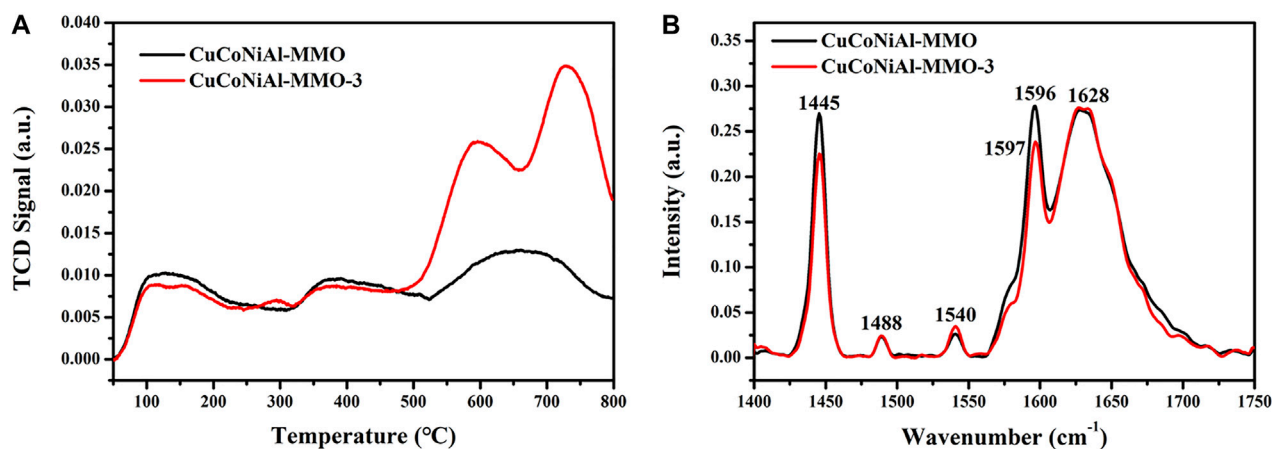**FIGURE 10 |** SEM images of **(A)** CuCoNiAl-MMO, **(B)** CuCoNiAl-MMO-3.

FIGURE 11 | Characterization of surface acidity of the different catalysts. **(A)** NH_3-TPD **(B)** Py-IR spectra for CuCoNiAl-MMO and CuCoNiAl-MMO-3.
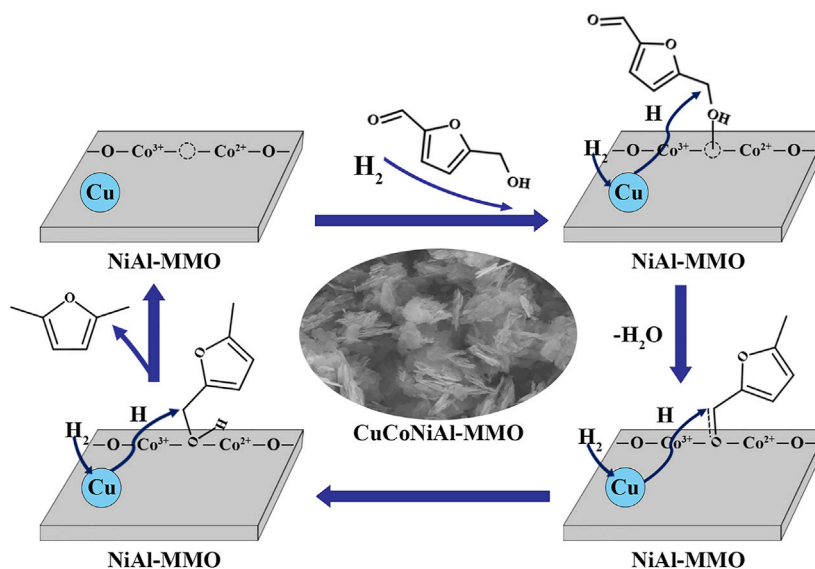

FIGURE 12 | Reaction mechanism for DMF formation by HMF hydrogenolysis on CuCoNiAl-MMO.

catalyst surface, the hydroxyl group ($-CH_2-OH$) in HMF preferentially undergoes a dehydroxylation reaction to form 5-MF (Guo et al., 2020).

3.3 Experimental Principle Exploration

Figure 12 illustrates a possible reaction mechanism for the hydrogenation of HMF on CuCoNiAl-MMO. There are two general ways to hydrogenate HMF to produce DMF (**Figure 1**). Route 1: The aldehyde group on HMF is hydrogenated to generate DHMF, after which the -OH on DHMF is hydrogenated and dehydrated to form 5-MFA, and finally, the -OH on 5-MFA is then hydrogenated and dehydrated to form the final product DMF. Route 2: Hydrogenation and dehydration of -OH on HMF to produce MF, hydrogenation of the aldehyde group on 5-MF to produce 5-MFA, and -OH on 5-MFA hydrogenated and dehydrated to produce the final product DMF. Both approaches have a common intermediate product 5-MFA. Our experiments identified 5-MF is the intermediate product with no DHMF being detected, thus the CuCoNiAl-MMO catalyst uses route 2: HMF→5-MF→5-MFA→DMF. As shown in **Figure 12**: First, the metal nanoparticles (Cu) and Lewis acid sites (CoO_x) on the catalyst surface can activate H_2 and $-CH_2OH$, respectively. The oxygen in hydroxymethylfurfural $-CH_2-OH$ is activated by Lewis acid sites (CoO_x) and then attacked by H atoms created by the metal nanoparticles (Cu), leading to hydrodeoxygenation to 5-MF. Secondly, the aldehyde groups in 5-MF were activated by the oxygen vacancies formed by Co^{2+}, and hydrogenated to form 5-MFA. Finally, the -OH hydrodehydration on 5-MFA produces DMF, which is the final product. As a carrier, NiAl-MMO can isolate metal crystallites, inhibit sintering and increase the specific surface area of the catalyst. In addition to the main reaction pathways, 2-hexanol and 2,5-HD are formed as by-products from DMF hydrogenation.

4 CONCLUSION

A CuCoNiAl-MMO catalyst was successively prepared by calcination a CuCoNiAl-LDH precursor at 500°C for 5 h in N_2. The developed CuCoNiAl-MMO catalyst offered excellent initial atctivity and selectivity for the hydrogenolysis of HMF to DMF under very mild conditions (tetrahydrofuran solvent, 180°C for 6 h, 1.0 MPa H_2). Under these conditions, CuCoNiAl-MMO afforded a HMF conversion rate of 99.8% and the DMF selectivity of 95.3%. Loss of Co and Al during the catalytic tests, together with densification of the catalyst structure and an increase in the amount of strong acid sites, meant that the initial catalytic activity was lost after three cycles of catalytic tests. LDH precursors offer a facile route to prepare highly active catalysts for HMF hydrogenation to DMF under mild conditions, though further work is needed to stabilize the structure/activity of the initially formed MMO-based catalysts.

DATA AVAILABILITY STATEMENT

The original contributions presented in the study are included in the article/Supplementary Material, further inquiries can be directed to the corresponding author.

AUTHOR CONTRIBUTIONS

JX: Visualization, Formal analysis, Writing—original draft, Writing—review and editing. DG: Methodology, Data curation. FH: Validation, Data curation, Funding acquisition. RL: Data curation. GW: Conceptualization, Writing—review and editing. YL: Conceptualization, Supervision, Writing—review and editing, Funding acquisition.

REFERENCES

Ardanuy, M., and Velasco, J. I. (2011). Mg-Al Layered Double Hydroxide Nanoparticles. *Appl. Clay Sci.* 51 (3), 341–347. doi:10.1016/j.clay.2010.12.024

Auxilio, A. R., Andrews, P. C., Junk, P. C., Spiccia, L., Neumann, D., Raverty, W., et al. (2008). Functionalised Pseudo-boehmite Nanoparticles as an Excellent Adsorbent Material for Anionic Dyes. *J. Mat. Chem.* 18 (21), 2466. doi:10.1039/b715545j

Bond, T. C., Doherty, S. J., Fahey, D. W., Forster, P. M., Berntsen, T., DeAngelo, B. J., et al. (2013). Bounding the Role of Black Carbon in the Climate System: A Scientific Assessment. *J. Geophys. Res. Atmos.* 118 (11), 5380–5552. doi:10.1002/jgrd.50171

Chen, B., Li, F., Huang, Z., and Yuan, G. (2017). Carbon-Coated Cu-Co Bimetallic Nanoparticles as Selective and Recyclable Catalysts for Production of Biofuel 2,5-Dimethylfuran. *Appl. Catal. B Environ.* 200, 192–199. doi:10.1016/j.apcatb.2016.07.004

Dasgupta, S., Das, B., Li, Q., Wang, D., Baby, T. T., Indris, S., et al. (2016). Toward On-And-Off Magnetism: Reversible Electrochemistry to Control Magnetic Phase Transitions in Spinel Ferrites. *Adv. Funct. Mat.* 26 (41), 7507–7515. doi:10.1002/adfm.201603411

Feng, L., Li, X., Lin, Y., Liang, Y., Chen, Y., and Zhou, W. (2020). Catalytic Hydrogenation of 5-Hydroxymethylfurfural to 2,5-Dimethylfuran over Ru Based Catalyst: Effects of Process Parameters on Conversion and Products Selectivity. *Renew. Energy* 160, 261–268. doi:10.1016/j.renene.2020.06.123

Gao, Z., Li, C., Fan, G., Yang, L., and Li, F. (2018). Nitrogen-Doped Carbon-Decorated Copper Catalyst for Highly Efficient Transfer Hydrogenolysis of 5-Hydroxymethylfurfural to Convertibly Produce 2,5-Dimethylfuran or 2,5-Dimethyltetrahydrofuran. *Appl. Catal. B Environ.* 226, 523–533. doi:10.1016/j.apcatb.2018.01.006

Guo, D., Liu, X., Cheng, F., Zhao, W., Wen, S., Xiang, Y., et al. (2020). Selective Hydrogenolysis of 5-hydroxymethylfurfural to Produce Biofuel 2, 5-dimethylfuran over Ni/ZSM-5 Catalysts. *Fuel* 274, 117853. doi:10.1016/j.fuel.2020.117853

Gupta, D., Kumar, R., and Pant, K. K. (2020). Hydrotalcite Supported Bimetallic (Ni-Cu) Catalyst: A Smart Choice for One-Pot Conversion of Biomass-Derived Platform Chemicals to Hydrogenated Biofuels. *Fuel* 277, 118111. doi:10.1016/j.fuel.2020.118111

Koso, S., Furikado, I., Shimao, A., Miyazawa, T., Kunimori, K., and Tomishige, K. (2009). Chemoselective Hydrogenolysis of Tetrahydrofurfuryl Alcohol to 1,5-Pentanediol. *Chem. Commun.* (15), 2035–2037. doi:10.1039/b822942b

Li, D., Liu, Q., Zhu, C., Wang, H., Cui, C., Wang, C., et al. (2019). Selective Hydrogenolysis of 5-hydroxymethylfurfural to 2,5-dimethylfuran over Co3O4 Catalyst by Controlled Reduction. *J. Energy Chem.* 30, 34–41. doi:10.1016/j.jechem.2018.03.008

Li, Q., Man, P., Yuan, L., Zhang, P., Li, Y., and Ai, S. (2017). Ruthenium Supported on CoFe Layered Double Oxide for Selective Hydrogenation of 5-Hydroxymethylfurfural. *Mol. Catal.* 431, 32–38. doi:10.1016/j.mcat.2017.01.011

Liao, W., Zhu, Z., Chen, N., Su, T., Deng, C., Zhao, Y., et al. (2020). Highly Active Bifunctional Pd-Co9S8/S-CNT Catalysts for Selective Hydrogenolysis of 5-hydroxymethylfurfural to 2,5-dimethylfuran. *Mol. Catal.* 482, 110756. doi:10.1016/j.mcat.2019.110756

Luo, J., Lee, J. D., Yun, H., Wang, C., Monai, M., Murray, C. B., et al. (2016). Base Metal-Pt Alloys: A General Route to High Selectivity and Stability in the Production of Biofuels from HMF. *Appl. Catal. B Environ.* 199, 439–446. doi:10.1016/j.apcatb.2016.06.051

Luo, S., Song, H., Philo, D., Oshikiri, M., Kako, T., and Ye, J. (2020). Solar-Driven Production of Hydrogen and Acetaldehyde from Ethanol on Ni-Cu Bimetallic Catalysts with Solar-To-Fuels Conversion Efficiency up to 3.8. *Appl. Catal. B-Environ.* 272, 118965. doi:10.1016/j.apcatb.2020.118965

Ma, N., Song, Y., Han, F., Waterhouse, G. I. N., Li, Y., and Ai, S. (2020). Multifunctional NiCoTi Catalyst Derived from Layered Double Hydroxides for Selective Hydrogenation of 5-Hydroxymethylfurfural to 2,5-Dimethylfuran. *Catal. Lett.* 151, 517–525. doi:10.1007/s10562-020-03323-8

Ma, W., Zhao, N., Yang, G., Tian, L., and Wang, R. (2011). Removal of Fluoride Ions from Aqueous Solution by the Calcination Product of Mg-Al-Fe Hydrotalcite-like Compound. *Desalination* 268 (1-3), 20–26. doi:10.1016/j.desal.2010.09.045

Mhadmhan, S., Franco, A., Pineda, A., Reubroycharoen, P., and Luque, R. (2019). Continuous Flow Selective Hydrogenation of 5-Hydroxymethylfurfural to 2,5-Dimethylfuran Using Highly Active and Stable Cu-Pd/Reduced Graphene Oxide. *ACS Sustain. Chem. Eng.* 7 (16), 14210–14216. doi:10.1021/acssuschemeng.9b03017

Mishra, G., Dash, B., and Pandey, S. (2018). Layered Double Hydroxides: A Brief Review from Fundamentals to Application as Evolving Biomaterials. *Appl. Clay Sci.* 153, 172–186. doi:10.1016/j.clay.2017.12.021

Motamedi, P., and Cadien, K. (2014). XPS Analysis of AlN Thin Films Deposited by Plasma Enhanced Atomic Layer Deposition. *Appl. Surf. Sci.* 315, 104–109. doi:10.1016/j.apsusc.2014.07.105

Nakagawa, Y., Tamura, M., and Tomishige, K. (2013). Catalytic Reduction of Biomass-Derived Furanic Compounds with Hydrogen. *ACS Catal.* 3 (12), 2655–2668. doi:10.1021/cs400616p

Nakagawa, Y., and Tomishige, K. (2010). Total Hydrogenation of Furan Derivatives over Silica-Supported Ni-Pd Alloy Catalyst. *Catal. Commun.* 12 (3), 154–156. doi:10.1016/j.catcom.2010.09.003

O'Quinn, E. C., Shamblin, J., Perlov, B., Ewing, R. C., Neuefeind, J., Feygenson, M., et al. (2017). Inversion in Mg1-xNixAl2O4 Spinel: New Insight into Local Structure. *J. Am. Chem. Soc.* 139 (30), 10395–10402. doi:10.1021/jacs.7b04370

Qi, Y., Xiao, X., Mei, Y., Xiong, L., Chen, L., Lin, X., et al. (2022). Modulation of Brønsted and Lewis Acid Centers for Ni X Co 3− X O 4 Spinel Catalysts: Towards Efficient Catalytic Conversion of Lignin. *Adv. Funct. Mater.* 32 (15), 2111615. doi:10.1002/adfm.202111615

Qin, Y., Wang, F., Shang, J., Iqbal, M., Han, A., Sun, X., et al. (2020). Ternary NiCoFe-Layered Double Hydroxide Hollow Polyhedrons as Highly Efficient Electrocatalysts for Oxygen Evolution Reaction. *J. Energy Chem.* 43, 104–107. doi:10.1016/j.jechem.2019.08.014

Shang, Y., Liu, C., Zhang, Z., Wang, S., Zhao, C., Yin, X., et al. (2020). Insights into the Synergistic Effect in Pd Immobilized to MOF-Derived Co-CoOx@N-doped Carbon for Efficient Selective Hydrogenolysis of 5-Hydroxylmethylfurfural. *Ind. Eng. Chem. Res.* 59 (14), 6532–6542. doi:10.1021/acs.iecr.9b07099

Shi, J., Wang, Y., Yu, X., Du, W., and Hou, Z. (2016). Production of 2,5-Dimethylfuran from 5-Hydroxymethylfurfural over Reduced Graphene Oxides Supported Pt Catalyst under Mild Conditions. *Fuel* 163, 74–79. doi:10.1016/j.fuel.2015.09.047

Srivastava, S., Jadeja, G. C., and Parikh, J. (2017). Influence of Supports for Selective Production of 2,5-Dimethylfuran via Bimetallic Copper-Cobalt Catalyzed 5-Hydroxymethylfurfural Hydrogenolysis. *Chin. J. Catal.* 38 (4), 699–709. doi:10.1016/S1872-2067(17)62789-X

Umasankar, S., Tamizhdurai, P., Santhana krishnan, P., Narayanan, S., Mangesh, V. L., and Shanthi, K. (2020). Effect of Copper on NiCu Bimetallic Catalyst Supported on SBA-16 for the Catalytic Hydrogenation of 5-Hydroxymethylfurfural to 2,5-Dimethylfuran. *Biomass Bioenergy* 143, 105868. doi:10.1016/j.biombioe.2020.105868

Viar, N., Requies, J. M., Agirre, I., Iriondo, A., and Arias, P. L. (2019). Furanic Biofuels Production from Biomass Using Cu-Based Heterogeneous Catalysts. *Energy* 172, 531–544. doi:10.1016/j.energy.2019.01.109

Wang, Q., Feng, J., Zheng, L., Wang, B., Bi, R., He, Y., et al. (2019). Interfacial Structure-Determined Reaction Pathway and Selectivity for 5-(Hydroxymethyl)furfural Hydrogenation over Cu-Based Catalysts. *ACS Catal.* 10 (2), 1353–1365. doi:10.1021/acscatal.9b03630

Wang, Q., Guan, X., Kang, L., Wang, B., Sheng, L., and Wang, F. R. (2020). Polyphenylene as an Active Support for Ru-Catalyzed Hydrogenolysis of 5-Hydroxymethylfurfural. *ACS Appl. Mat. Interfaces* 12 53712–53718. doi:10.1021/acsami.0c11888

Wang, X., Liang, X., Li, J., and Li, Q. (2019). Catalytic Hydrogenolysis of Biomass-Derived 5-Hydroxymethylfurfural to Biofuel 2, 5-Dimethylfuran. *Appl. Catal. A General* 576, 85–95. doi:10.1016/j.apcata.2019.03.005

Xu, Z. P., Zhang, J., Adebajo, M. O., Zhang, H., and Zhou, C. (2011). Catalytic Applications of Layered Double Hydroxides and Derivatives. *Appl. Clay Sci.* 53 (2), 139–150. doi:10.1016/j.clay.2011.02.007

Yang, P., Xia, Q., Liu, X., and Wang, Y. (2016). High-yield Production of 2,5-dimethylfuran from 5-hydroxymethylfurfural over Carbon Supported Ni-Co Bimetallic Catalyst. *J. Energy Chem.* 25 (6), 1015–1020. doi:10.1016/j.jechem.2016.08.008

Zhang, J., and Chen, J. (2017). Selective Transfer Hydrogenation of Biomass-Based Furfural and 5-Hydroxymethylfurfural over Hydrotalcite-Derived Copper Catalysts Using Methanol as a Hydrogen Donor. *ACS Sustain. Chem. Eng.* 5 (7), 5982–5993. doi:10.1021/acssuschemeng.7b00778

Zhang, J., Dong, K., and Luo, W. (2019). PdCl2-catalyzed Hydrodeoxygenation of 5-hydroxymethylfurfural into 2,5-dimethylfuran at Room-Temperature Using Polymethylhydrosiloxane as the Hydrogen Donor. *Chem. Eng. Sci.* 201, 467–474. doi:10.1016/j.ces.2019.03.011

Zhang, Z., and Deng, K. (2015). Recent Advances in the Catalytic Synthesis of 2,5-Furandicarboxylic Acid and its Derivatives. *ACS Catal.* 5 (11), 6529–6544. doi:10.1021/acscatal.5b01491

Zhang, Z., Yao, S., Wang, C., Liu, M., Zhang, F., Hu, X., et al. (2019). CuZnCoOx Multifunctional Catalyst for *In Situ* Hydrogenation of 5-hydroxymethylfurfural with Ethanol as Hydrogen Carrier. *J. Catal.* 373, 314–321. doi:10.1016/j.jcat.2019.04.011

Zhao, C., and Lercher, J. A. (2012). Upgrading Pyrolysis Oil over Ni/HZSM-5 by Cascade Reactions. *Angew. Chem. Int. Ed.* 51 (24), 5935–5940. doi:10.1002/ange.20110830610.1002/anie.201108306

Zheng, Y., and Chen, Y. (2017). Preparation of polypropylene/Mg-Al Layered Double Hydroxides Nanocomposites through Wet Pan-Milling: Formation of a Second-Staging Structure in LDHs Intercalates. *RSC Adv.* 7 (3), 1520–1530. doi:10.1039/c6ra26050k

Zhu, C., Liu, Q., Li, D., Wang, H., Zhang, C., Cui, C., et al. (2018). Selective Hydrodeoxygenation of 5-Hydroxymethylfurfural to 2,5-Dimethylfuran over Ni Supported on Zirconium Phosphate Catalysts. *ACS Omega* 3 (7), 7407–7417. doi:10.1021/acsomega.8b00609

Zu, Y., Yang, P., Wang, J., Liu, X., Ren, J., Lu, G., et al. (2014). Efficient Production of the Liquid Fuel 2,5-dimethylfuran from 5-hydroxymethylfurfural over Ru/Co3O4 Catalyst. *Appl. Catal. B Environ.* 146, 244–248. doi:10.1016/j.apcatb.2013.04.026

Titania Nanotubes-Bonded Sulfamic Acid as an Efficient Heterogeneous Catalyst for the Synthesis of *n*-Butyl Levulinate

Shuolin Zhou[1]*, Min Lei[1], Junzhuo Bai[1], Xianxiang Liu[2]*, Lu Wu[1], Min Long[1], Keying Huang[1] and Dulin Yin[2]

[1]School of Elementary Education, Changsha Normal University, Changsha, China, [2]National and Local Joint Engineering Laboratory for New Petro-chemical Materials and Fine Utilization of Resources, Key Laboratory of the Assembly and Application of Organic Functional Molecules of Hunan Province, College of Chemistry and Chemical Engineering, Hunan Normal University, Changsha, China

The titania nanotubes-bonded sulfamic acid (TNTs-NHSO$_3$H) catalyst was designed and successfully fabricated by the post-synthesis modification method. The as-prepared catalyst was characterized by a variety of characterization techniques, including Fourier transform infrared (FT-IR) spectroscopy, X-ray photoelectron spectroscopy (XPS), transmission electron microscopy (TEM), scanning electron microscopy (SEM), X-ray diffraction (XRD) analysis, and thermogravimetry-differential thermal gravimetry (TG-DTG). The crystal structure of the TNTs still maintained during the modification process. Although the BET surface area was decreased, the amount of Brønsted acid sites can be efficiently fabricated on the TNTs. The catalytic activity of TNTs-NHSO$_3$H was examined for the synthesis of *n*-butyl levulinate (BL) from levulinic acid (LA) and furfuryl alcohol (FA). A relatively high selectivity (99.6%) at 99.3% LA conversion was achieved for esterification of levulinic acid owing to the strong Brønsted acidity sites. And also, the TNTs-NHSO$_3$H catalyst exhibited a higher reactivity for alcoholysis of FA and the yield of BL reached 90.4% with 100% FA conversion was obtained under the mild conditions.

Keywords: TiO$_2$ nanotubes, heterogenous catalyst, levulinate esters, esterification, alcoholysis

INTRODUCTION

The increasing worldwide fossil fuel consumption and the increasing greenhouse gases emission and other environmental hazards have prompted people to seek other energy sources. The efficient conversion of available and diverse biomass resources into biofuel is an attractive and promising strategy (Gaurav et al., 2017; Alonso et al., 2010). Levulinate esters (LAEs), as a typical representative derived from the bio-based feedstock, have received significant attention. Because they have strong stability, high lubricity, good fluidity, and low combustion oxygen demand, which are similar to fatty acid methyl esters in biodiesel (Christensen et al., 2011). In addition, levulinate esters are one of the most potential platform compounds since their molecular structure contains a carbonyl and ester groups which have high reactivity and can be further applied to produce many important chemicals, such as γ-valerolactone (Zhang et al., 2020) and pyrrolidone (Shen et al., 2019). Furthermore, alkyl levulinates are also the crucial chemicals for other industrially important applications, such as green solvents, plasticizers, and flavoring agents (Wu et al., 2021). Hence, the synthesis of levulinate esters
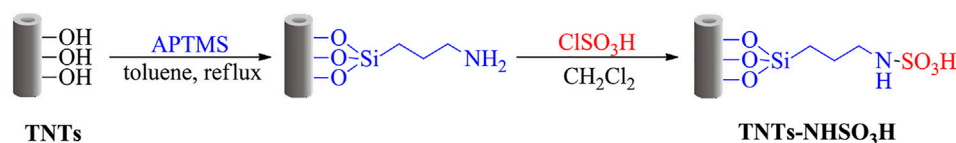
SCHEME 1 | Preparation steps for fabricating titania nanotubes-bonded sulfamic acid.

has received abundant attention in recent years from academia and industry, and increasing effort has been devoted to the development of synthetic pathways, the design of novel and efficient catalysts, and optimizing the catalytic process (Démolis et al., 2014).

Up to now, there are several developed potential pathways for the synthesis of LAEs in the presence of various acid catalysts (Tian et al., 2021; Liu et al., 2020). Commercially the acid-catalyzed reactions are largely carried out by different mineral acidic catalysts such as H_2SO_4, HCl, and H_3PO_4, which often suffer from severe corrosion, product separation and purification, waste, and safety problems. From the practical point of view, readily separated and recovered heterogeneous catalysts, therefore, are more environmentally friendly would be desirable. Among heterogeneous catalysts, TiO_2 nanotubes (TNTs) materials have attracted extensive attention owing to their chemical stability, large surface area, non-toxicity, and low production cost (Roy et al., 2011). In the past few years, TNTs synthesized by a simple alkaline hydrothermal treatment have been used as a solid acid catalyst for various acid-catalyzed organic transformations (Kitano et al., 2010; Li et al., 2015; de Carvalho et al., 2017). The amount and strength of origin acid sites on the TNTs, however, would be limited in the catalytic applications (Adeleye et al., 2021). It is worth noting that TNTs have a high concentration of hydroxyl groups (–OH) on the surface, which makes them flexible in functionalization with a wide range of organic groups, particular with organosiloxane agents. 3-Aminopropyltrimethoxysilane (APTMS) (Duong et al., 2018), 3-aminopropyltriethoxysilane (APTES) (Pontón et al., 2014), [1-(2-amino-ethyl)-3-aminopropyl]trimethoxy silane (AAPTS) (Wang et al., 2013), octadecyltrimethoxysilane (OTS) (Chao et al., 2013), and octadecyltrichlorosilane (ODS) (Niu and Cai, 2009) have been reported in the literature as chemical modifiers of the TNT surface. Furthermore, hydrothermally synthesized TNTs can be further functionalized by the integration of acidic functional groups to increase the acidity of TNTs in our previous work (Zhou L. et al., 2018; Zhou et al., 2019; Zhou et al., 2022). These studies mean that TNTs as a support material that can be rationally designed and modified as a much higher performance solid acid catalyst, which would bring a wide range of catalytic applications. Moreover, hybrid organic-inorganic materials in the catalytic reaction can provide a synergic and cooperative behavior toward chemo selective and favorable products with high yields (Wight and Davis, 2002).

In pursuit of our recent studies to develop hybrid organic-inorganic solid acid catalysts, the TiO_2 nanotubes surface was first functionalized with NH_2 groups through the APTMS grafting and the SO_3H groups were covalently linked to surface NH_2 groups by using chlorosulfonic acid as a sulfonating reagent. In
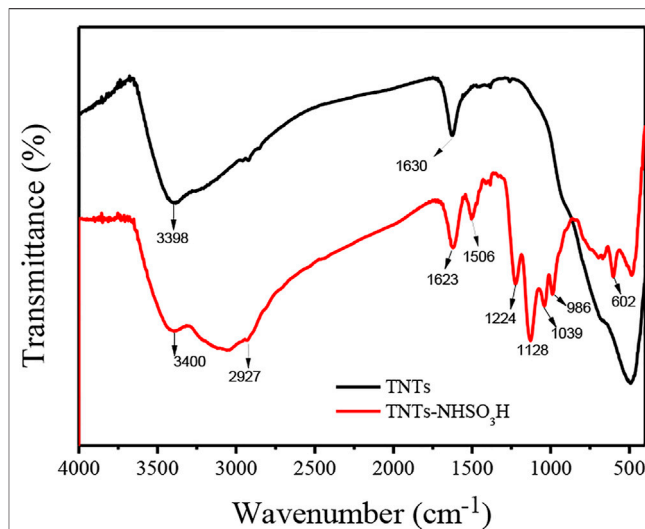
FIGURE 1 | FT-IR spectra of TNTs and TNTs-NHSO$_3$H.

the present work, schematic procedures for surface modification on TiO_2 nanotubes through chemical treatment are presented in **Scheme 1**. The physicochemical properties of the synthesized TNTs-NHSO$_3$H catalyst were characterized by FT-IR, XPS, SEM, TEM, XRD, TGA, and N_2 physisorption techniques. The potential catalytic activity of TNTs-NHSO$_3$H was investigated in the synthesis of high value-added *n*-butyl levulinate from esterification of levulinic acid (LA) and alcoholysis of furfuryl alcohol (FA), respectively.

EXPERIMENTAL

Materials

TiO_2 nanoparticles (anatase, >99.9%), 3-amino-propyltrimethoxysilane (APTMS), LA, and FA were purchased from Aladdin (Shanghai, China) and used as received. Toluene was purchased from Sinopharm Chemical Reagent Co., Ltd. (Shanghai, China) and was freshly distilled before use. Other reagents were of analytical grade and used without further purification. Experimental water was prepared by a Millipore Milli-Q pure water system.

Catalyst Preparation
Preparation of TNTs

TNTs were synthesized by a hydrothermal synthesis method, according to the reported literature with some slight
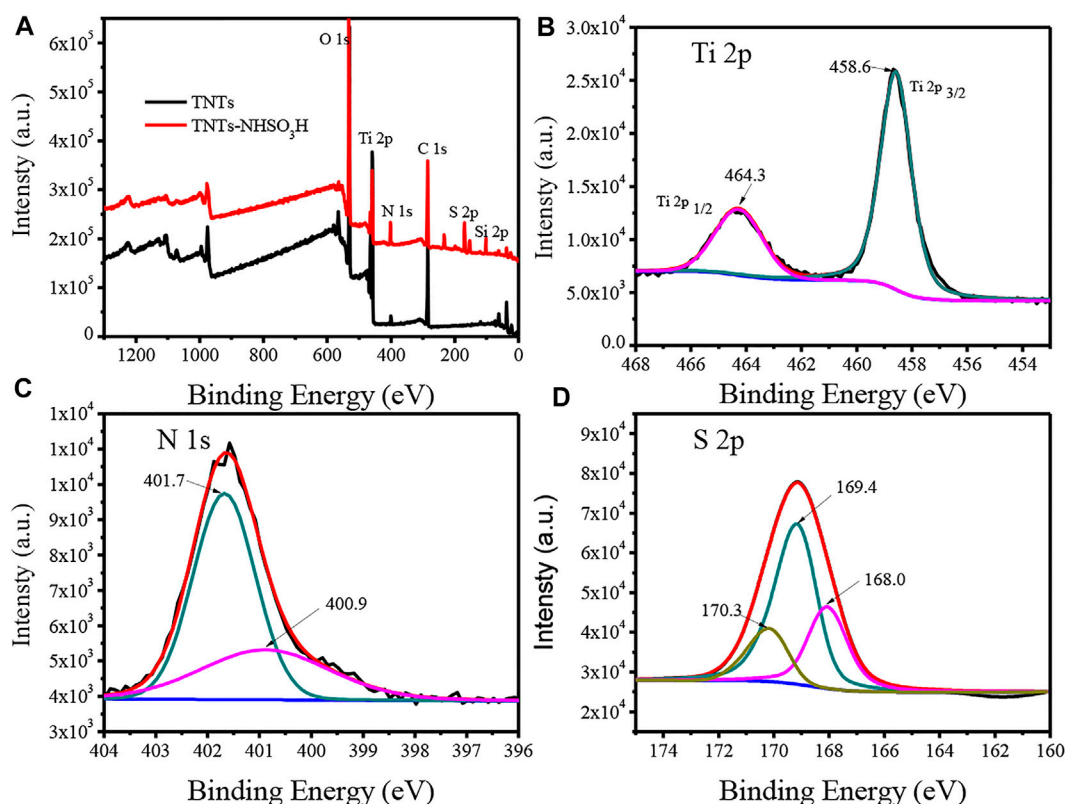
FIGURE 2 | XPS spectra of TNTs and the synthesized TNTs-NHSO$_3$H: **(A)** full spectra of samples; **(B)** Ti 2p peaks; **(C)** N 1s peaks; **(D)** S 2p peaks.

modifications (Kasuga et al., 1999). 2.0 g of TiO$_2$ nanoparticles with a particle size of 60 nm were mixed with 60 ml of 10 mol/L NaOH aqueous solution, followed by hydrothermal treatment at 150 C in a Teflon-lined autoclave for 24 h. After cooling, the treated powders were thoroughly washed with 0.1 mol/L HCl and water until the pH value of the washing solution reached 7.0, and subsequently filtered by 0.22 μm filters and dried one night at 80 C under vacuum. The obtained material is labeled as TNTs.

Preparation of TNTs-NHSO$_3$H

1 g of TNTs was suspended in 20 ml of dry toluene in a 50 ml round-flask and then 3-amino-propyltrimethoxysilane was added. The mixture was refluxed by stirring for 24 h. After the reaction was finished, the solid product was collected by centrifugation, washed three times with chloroform and acetone, respectively, and then dried in a vacuum oven at 80°C. The obtained solid powder was preloaded with 30 ml of dry dichloromethane in a suction flask equipped with a constant-pressure dropping funnel. A certain amount of chlorosulfonic acid was added dropwise over a period of 30 min at room temperature while the mixture was stirred slowly in an ice bath. After the addition was completed, the mixture was further stirred for 4 h. Then, the dichloromethane was removed, and the solid sample was washed with ethanol and

dried in a vacuum at 70 C. The resultant solid was designed as TNTs-NHSO$_3$H.

Characterization

Fourier transform infrared spectra (FT-IR) of the samples were collected by the KBr pellet technique on a Nicolet 370 infrared spectrophotometer (Thermo Nicolet, American) in the range 500–4,000 cm^{-1}. X-ray photoelectron spectroscopy (XPS) was tested by a Thermo fisher scientific using Mono Al Kα radiation, and binding energies were calibrated at 12.0 kV and 6.0 mA, respectively. The morphologies of the catalyst were investigated by using transmission scanning microscopy (TEM) with an acceleration voltage of 200 kV (JEOL 2100, Japan). The surface morphology of the TNTs-NHSO$_3$H catalyst was observed using a scanning electron microscope (SEM, Carl Zeiss Sigma-HD). X-ray diffraction (XRD) studies were carried out using a Bruker diffractometer with Cu Kα radiation to survey the crystal structure over a 2θ range of 10–80°. N$_2$ adsorption-desorption isotherms were recorded with an ASAP 2400 physisorption instrument made by Micromeritics Corporation (American). Prior to measurement, all samples were dried under vacuum at 333 K for 24 h. Pore size distribution was calculated using the Barrett–Joyner–Halenda (BJH) method. Thermogravimetric analysis (TGA) curves were
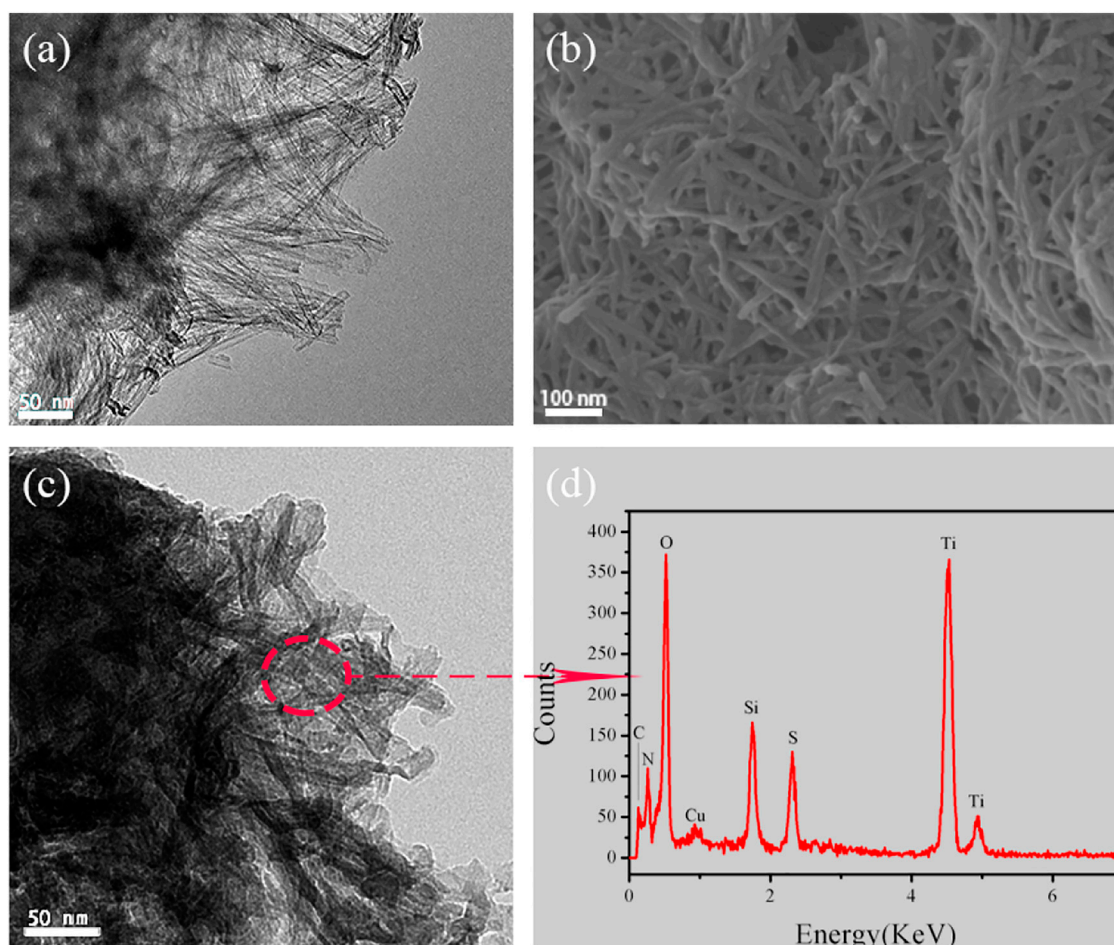
FIGURE 3 | (A) Representative TEM image of TNTs. **(B–C)** SEM and TEM images of TNTs-NHSO$_3$H. **(D)** EDX spectrum of TNTs-NHSO$_3$H.

recorded in airflow on a Netzsch Model STA 409 PC instrument with a heating rate of 20K/min from room temperature to 973 K using α-Al$_2$O$_3$ as the standard material. The number of acid sites in each sample was determined by the acid-base titration method.

Catalytic Test

Esterification of LA With *n*-Butanol

In a typical procedure, the mixture of LA (3 mmol) and *n*-butanol (30 mmol) together with the catalyst (5 wt% of LA) were added to a round-bottom flask and was heated at the required reaction temperature in an oil bath under solvent-free condition. At periodic intervals, 0.2 ml of the reaction solution was withdrawn and centrifuged to separate the catalyst and was analyzed by Gas chromatography (GC).

Alcoholysis of FA With *n*-Butanol

In a typical run, 1 mmol of FA and 5 ml of *n*-butanol together with a prescribed amount of the catalyst were added to a 25 ml round bottom flask equipped with a reflux condenser under atmospheric pressure. The round bottom flask was heated in an oil bath at reaction temperatures ranging from 90–120°C. At periodic intervals,

the reaction mixture was withdrawn and centrifuged to separate the catalyst and was analyzed by Gas chromatography (GC).

Reaction Intermediates Analysis

The reaction intermediates were identified by GC–MS, a Shimadzu GC system equipped with a capillary (30 m length, 0.32 mm internal diameter, 0.25 μm film thickness). Mass spectrometer conditions were: ionization mode: EI, electron energy 70 Ev; interface temperature: 250°C; ion source temperature: 200°C; mass scan range: 40–640 m/z, solvent delay 3.0 min. The flow rate of the carrier gas (helium) was 1.0 ml min^{-1}. A split ratio of 1:50 was used for the injection of 0.2 μl of the solutions. The NIST05 S.LIB library was used for the mass spectrum analysis.

RESULTS AND DISCUSSION

Characterization of Catalyst

FT-IR spectra for TNTs and TNTs-NHSO$_3$H samples are presented in **Figure 1**. Generally, the broad peak present

FIGURE 4 | X-ray diffraction patterns of TNTs and TNTs-NHSO$_3$H.

FIGURE 5 | **(A)** TG and **(B)** DTG of analysis of the TNTs-NHSO$_3$H catalyst.

FIGURE 6 | N$_2$ adsorption–desorption isotherms and pore size distributions (inset) for **(A)** TNTs and **(B)** TNTs-NHSO$_3$H.
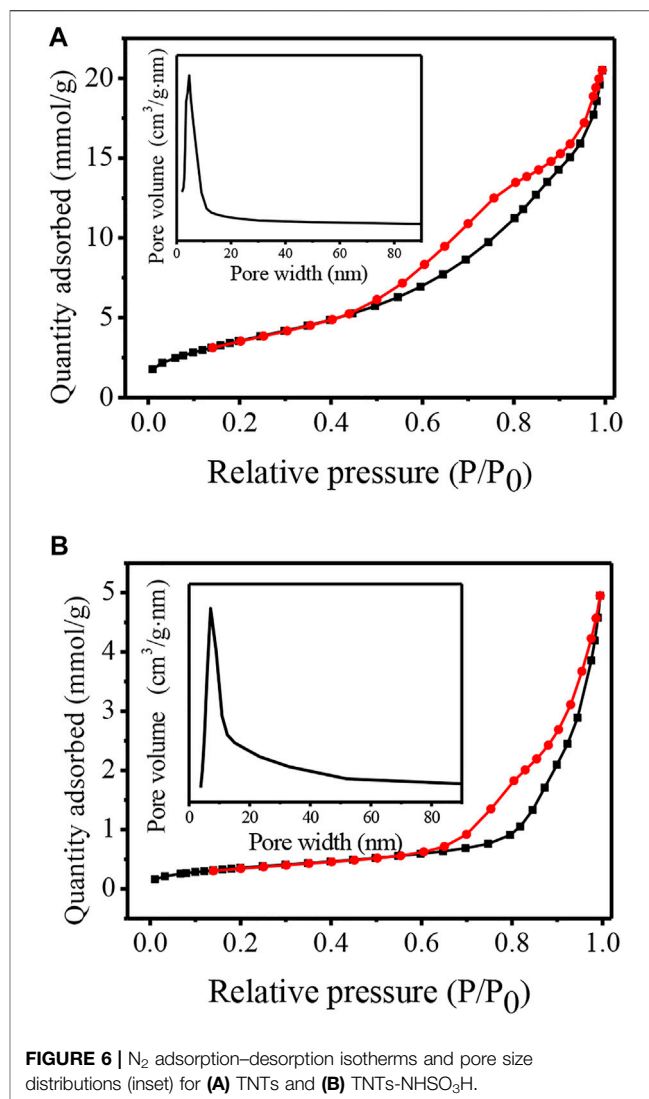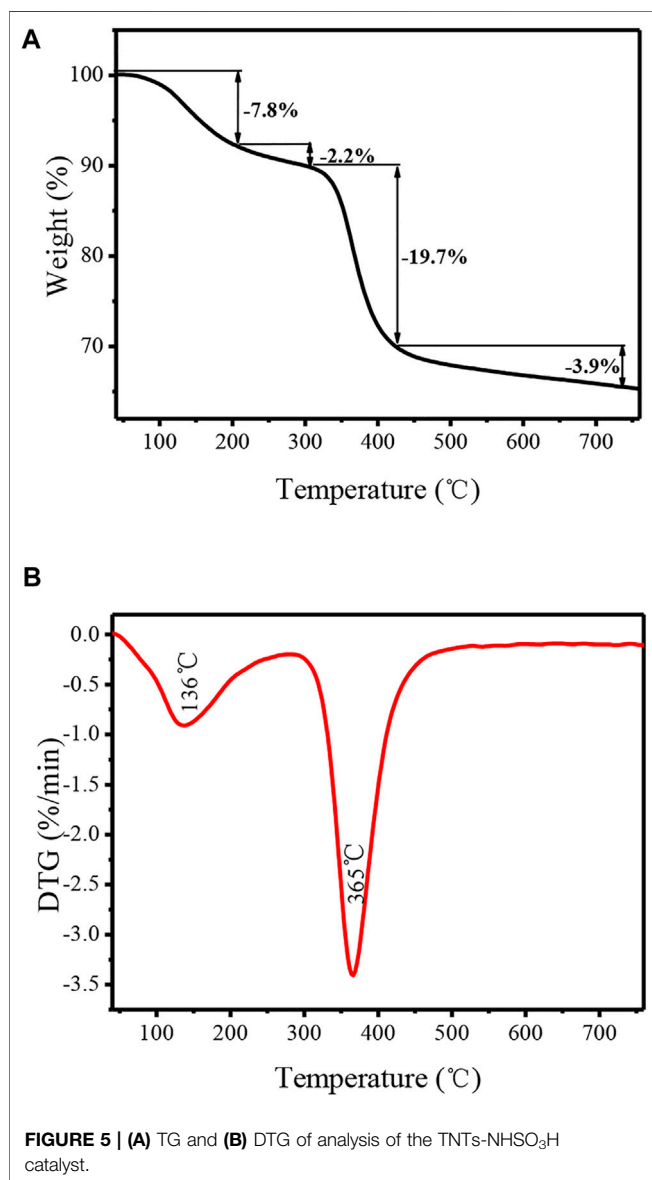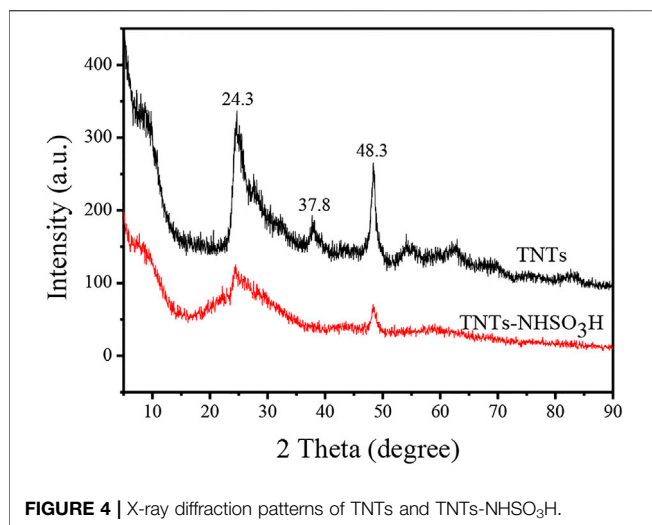
around 3,214–3,600 cm^{-1} and the low-intensity peak at 1,630 cm^{-1} are attributed to the stretching vibration of interlayer water molecules and surface OH groups, respectively. In the case of TNTs, the band below 1,200 cm^{-1} is attributed to Ti-O-Ti vibration and the peak around 490 cm^{-1} can be interpreted as the crystal lattice vibration of TiO$_6$ octahedra (Silva et al., 2017). The new absorption peaks in the frequency range of 2,800–2,960 cm^{-1} in the TNTs-NHSO$_3$H catalyst are ascribed to the C-H vibration of the aminopropyl segment (Pontón et al., 2014). The peak around 986 cm^{-1} could be interpreted as the Ti-O-Si band. Meanwhile, the band at 1,039 cm^{-1} is ascribed to Si-O stretching vibration. The peaks at 1,128 cm^{-1} and 1,224 cm^{-1} can be assigned to the sulfonyl moiety groups formed by the reaction of chlorosulfonic acid with amino groups (Kassaee et al., 2011).

The surface chemical compositions and bonding environments for TNTs and TNTs-NHSO$_3$H were further analyzed by X-ray photoelectron spectroscopy (XPS), and the results are shown in **Figure 2**. From the full scan XPS
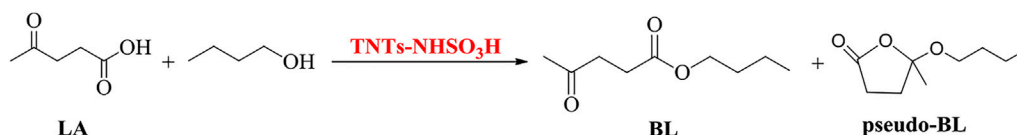
SCHEME 2 | Esterification of LA with *n*-butanol over the TNTs-NHSO₃H catalyst.

FIGURE 7 | **(A)** Catalytic activities over TNTs and TNTs-NHSO₃H. Reaction conditions: 5 wt% catalyst dosage, reaction time 4h, 120°C. **(B)** Effect of reaction temperature. Reaction conditions: 5 wt% catalyst dosage, reaction time 4 h. **(C)** Effect of reaction time. Reaction conditions: 5 wt% catalyst dosage, 120°C. **(D)** Effect of catalyst dosage. Reaction conditions: 120°C, reaction time 6 h.

of samples, it can be seen that the TNTs-NHSO₃H sample is composed of C, N, O, S, Si, and Ti elements (**Figure 2A**), which are consistent with the elements expected to be obtained by the preparation route. **Figure 2B** shows the Ti 2p spectra of the TNTs-NHSO₃H sample. The binding energy of Ti 2p at 458.6 and 464.3 eV is correspond to the Ti 2p3/2 and Ti 2p1/2, respectively. The binding energy of Ti 2p in the catalyst is consistent with that of pure TNTs, supporting that the oxidation state of Ti in the as-prepared TNTs-NHSO₃H is Ⅳ (Wang et al., 2018). As can be found in **Figure 2C**, the N 1s signal can be resolved into two peaks. The peak located at 400.9 eV can be assigned to the typical nitrogen present in APTMS. Another peak located at 401.7 eV for the N 1s peak can reasonably be attributed to N-S bonds (Kaid et al., 2020). **Figure 2D** depicts the XPS spectra of S 2p of TNTs-NHSO₃H. It is observed that S 2p has a strong peak at 169.4 eV, which is the characteristic peak of typical S=O bonds (Veisi et al., 2016).

Two peaks located at 168.0 and 170.3 eV can be assigned to the S-O and S-N, respectively (Song et al., 2015). These results indicate the formation of the desired catalytic system.

The acid amount of the catalyst was determined by the ion-exchanged method using an aqueous solution saturated with NaCl as an exchange agent. The acid density of TNTs-NHSO₃H is up to 2.27 mmol/g, which implies that a certain amount of Brönsted acidity sites can be constructed on the surface of TNTs.

The morphology of TNTs and TNTs-NHSO₃H was revealed by SEM and TEM, and the results are displayed in **Figure 3**. As illustrated by the TEM images, the TNTs sample shows the uniform open-ended tubes can be long up to several hundred nanometers (**Figure 3A**). It is worthy to note that the morphology of tubes in TNTs-NHSO₃H was still maintained (**Figures 3B,C**). The surface of titanate nanotubes was coated with a layer of silicon dioxide in the presence of dry toluene, which is the result

SCHEME 3 | Alcoholysis of FA with n-butanol over the TNTs-NHSO₃H catalyst.
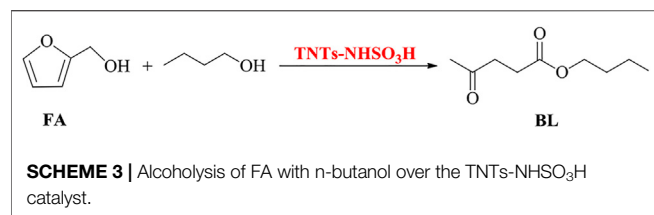
of the silanization of surface OH groups with APTMS. This means that more acidity sites can be constructed and immobilized on the TNTs surface by the following functionalization of amino groups in organ siloxane agents. According to the EDX spectrum of an area in **Figure 3C**, there are five elements, C, N, O, S, Si, and Ti, which can be ascertained in the TNTs-NHSO₃H (**Figure 3D**). The percent of N and S is 7.5 and 7 wt%, respectively. This result is consistent with the result previously obtained by XPS, indicating the material was successfully fabricated using a post-synthesis modification strategy.

The XRD pattern of the TNTs and TNTs-NHSO₃H are displayed in **Figure 4**. The TNTs had an XRD pattern that corresponds to the anatase crystal phase of titania. The peak exhibited at a 2θ value of 9.8 indicates the presence of a layered crystal structure formed in the hydrothermal process. It can be seen that all other diffraction peaks at the 2θ value of around 24.3°, 37.8°, and 48.3° are typical characteristic peaks of TNTs (Lu

et al., 2017). The XRD pattern of the as-prepared TNTs-NHSO₃H catalyst can well match the characteristic diffraction peaks of TNTs. It should be noted that there is a slight decrease in the intensity ratios of different peaks, which may be caused by the surface modification during the preparation process.

In order to further study the surface modification of TiO₂ nanotubes by organic functional groups, the catalyst was characterized by a thermogravimetric analyzer, and the obtained thermogravimetric curves are presented in **Figure 5**. It can be seen that a significant weight loss in the range of 100–200 C can be attributed to the elimination of water molecule which was physically adsorbed on the surface and into the pores of TNTs. An endothermic peak with a maximum of 136°C can be observed on the corresponding DTG curve. Also, there is a slight weight loss in the range of 200–300 C, which possibly corresponds to the dehydroxylation of TNTs. This phenomenon is consistent with the reported values for the TNT material (Preda et al., 2015). There is an obvious weight loss that started at 300°C, which is mainly attributed to the decomposition of the covalently bound organic functional groups from TNTs-NHSO₃H. The weight loss of approximately 19.7% in the range of 300–430°C is due to the removal of the organic motif. Furthermore, a strong and sharp endothermic DTG signal was observed at 365°C. In addition, the observed weight loss of approximately 3.9% occurs between 430 and 600°C which may be related to the thermal decomposition of

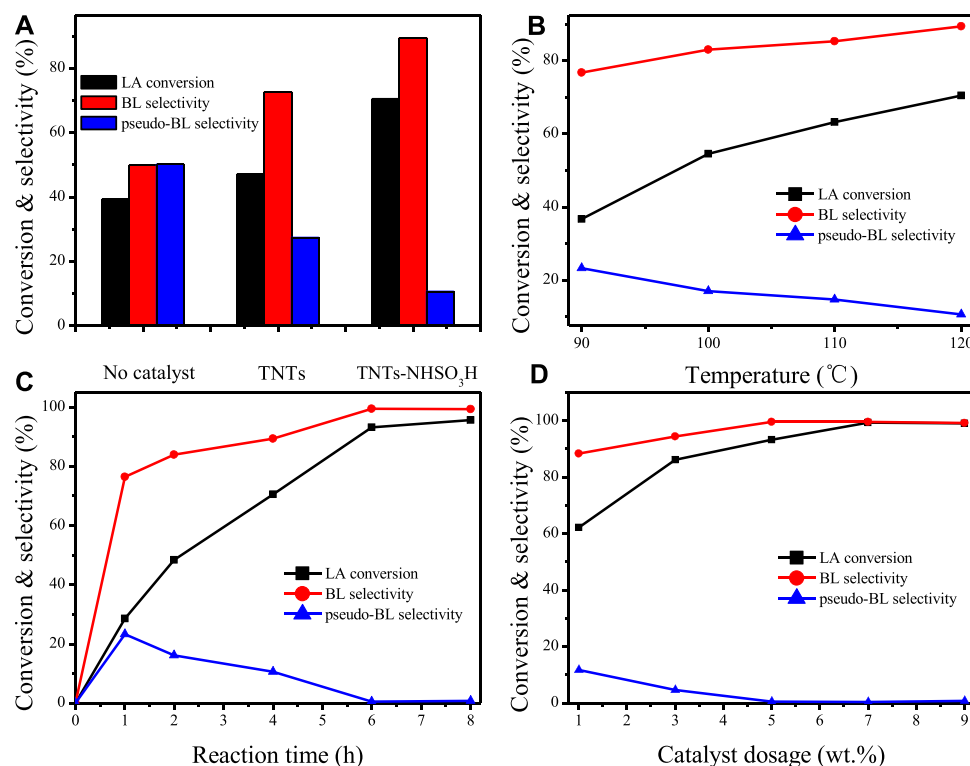**FIGURE 8 | (A)** Catalytic activities over TNTs and TNTs-NHSO₃H. Reaction conditions: 0.1 g catalyst, reaction time 8h, 120°C. **(B)** Effect of reaction temperature. Reaction conditions: 0.1 g catalyst, reaction time 8 h. **(C)** Effect of reaction time. Reaction conditions: 0.1 catalysts, 120°C. **(D)** Effect of catalyst dosage. Reaction conditions: 120°C, reaction time 8 h.
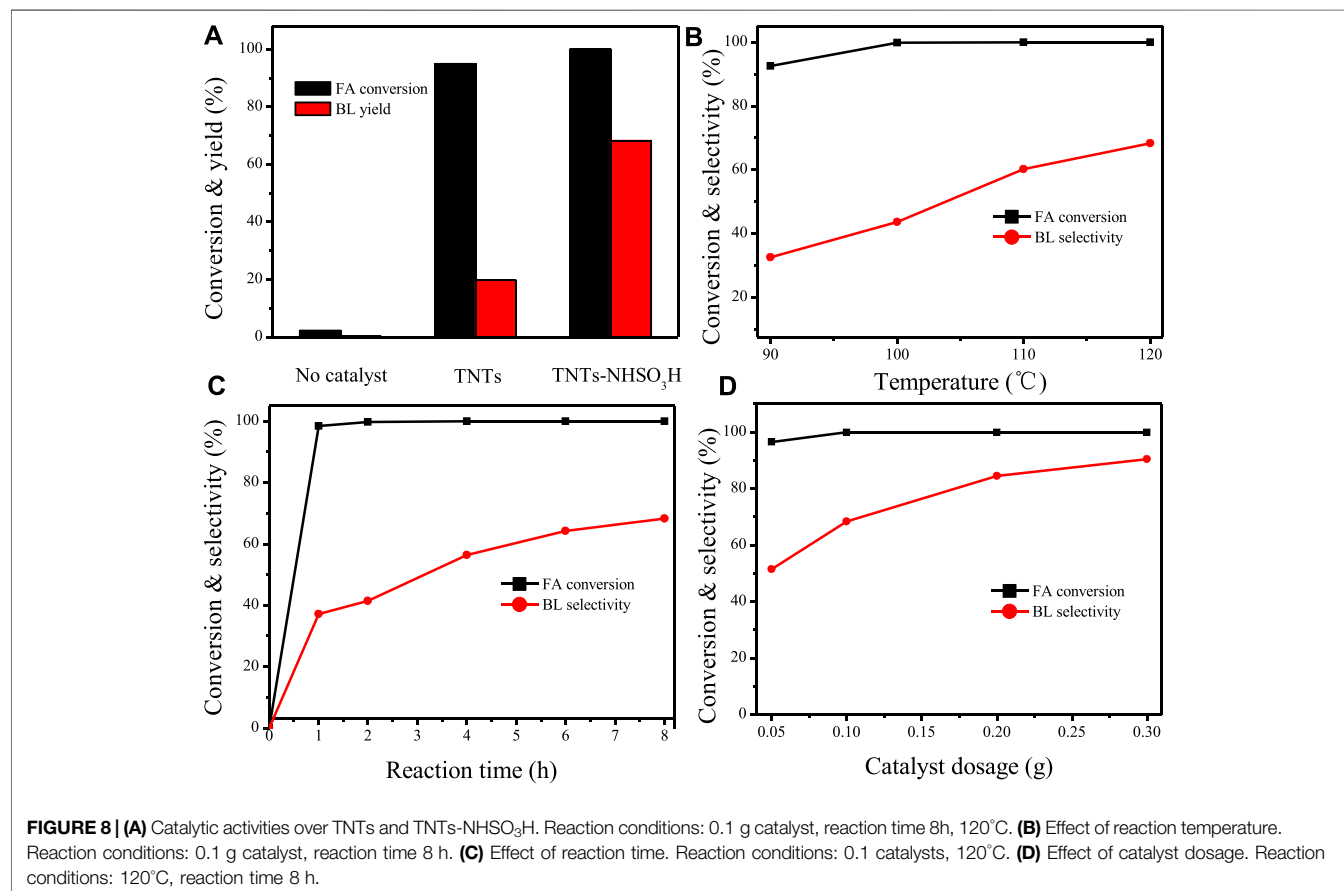
Catalyst	Substrate	Temp. (°C)	Time (h)	BL yield (%)	Ref
TNTs-NHSO$_3$H	LA	120	6	98.9	This work
Meso-ZSM-5	LA	120	5	82.2	Morawala et al. (2019)
H$_3$PW$_{12}$O$_{40}$/Al-MCM-41	LA	120	4	90.0	Najafi Chermahini and Nazeri, (2017)
Sulfonated glucose-derived amorphous carbon	LA	100	4	90.5	Yang et al. (2018)
SnTUD$_{-1}$	LA	120	4	90.5	Pachamuthu et al. (2019)
NER@3DOM/m-OS	LA	40	12	74.6	Zhou S et al. (2018b)
TNTs-NHSO$_3$H	FA	120	8	90.4	This work
SMWP	FA	120	5	90.6	Yang et al. (2020)
[MIMBS]$_5$ [AlW$_{12}$O$_{40}$]	FA	120	6	94	Hao et al. (2017)
UiO-66(Hf)-SO$_3$H	FA	120	4	72	Gupta and Kantam, (2019)
KCC-1/Pr-SO$_3$H	FA	120	3	81.9	Mohammadbagheri and Najafi Chermahini, (2018)
GC-PTSA-AC	FA	120	4	91.0	Yang et al. (2019)

FIGURE 9 | Reusability of TNTs-NHSO₃H toward **(A)** esterification of LA and **(B)** alcoholysis of FA. Reaction conditions for **(A)**: LA 3 mmol; n-butanol 30 mmol; 120°C; 6h; 7wt% catalyst. Reaction conditions for **(B)**: FA 1 mmol; n-butanol 5 ml; 120°C; 8h; 0.3 g catalyst.
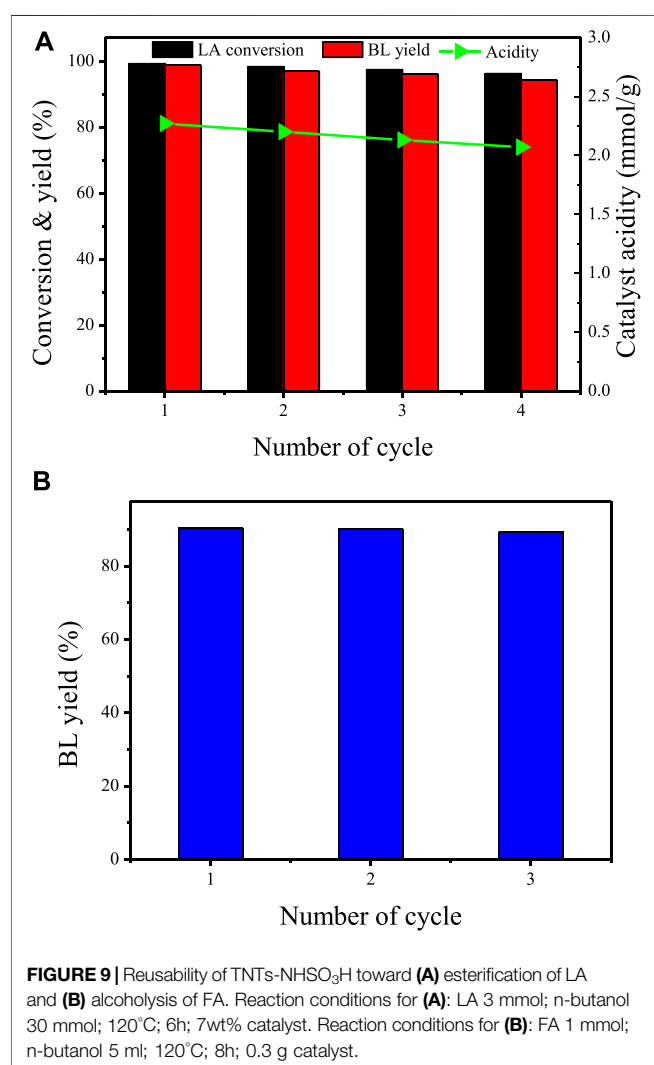
the organic residues. From the TG/DTG analysis, it is understood that the TNTs-NHSO₃H catalyst has greater thermal stability,

which confirms that it can be used for organic reaction temperatures below 300°C.

Figure 6 shows the N₂ adsorption-desorption isotherms and the corresponding pore size distribution curves of TNTs and TNTs-NHSO₃H. According to IUPAC classification, the TNT material exhibits the typical type IV isotherm with a hysteresis loop, confirming the mesoporous nature of TNTs. The surface area of TNTs is 300 m²/g. As shown in **Figure 6A**(inset), the pore size distribution presents the maximum positioned at 4.6 nm, corresponding to the inner nanotubular cavity of TNTs. This result suggests that TNTs had a uniform nanotubular structure. After functionalization of the parent material, the remarkable change in the N₂ adsorption-desorption isotherm curve was observed in **Figure 6B**. It is worth noting that the surface area of TNTs-NHSO₃H decreased to 29 m²/g. It is inferred that a part of the organosiloxane agents was confined inside the nanotubes, especially near the ends of the nanotubes, as TNTs possess a large fraction of voids in the interior, which resulted in the partial blocking of the tubular channel of TNTs-NHSO₃H. Although the BET surface area of TNTs-NHSO₃H is decreased in comparison to that of pure TNTs, it is still favorable for the acid-catalyzed reactions due to the more accessible acidic sites on the inside or outside of TNTs.

Catalytic Performances
Esterification of LA With *n*-Butanol
The catalytic performance of TNTs-NHSO₃H was first tested for the esterification of LA with *n*-butanol (**Scheme 2**) and the results are illustrated in **Figure 7**. The reaction products, *n*-butyl levulinate (BL) and *p*seudo-n-butyl levulinate (*pseudo*-BL) were detected by GC-MS techniques. Similar results were also observed by several authors (Ciptonugroho et al., 2016; Chaffey et al., 2021). As shown in **Figure 7A** remarkable catalytic performance of TNTs-NHSO₃H was observed since LA conversion (70.5%) with high selectivity (89.4%) to BL was achieved. The appearance of Brønsted acid centers in the TNTs-NHSO₃H catalyst is the primary reason for higher catalytic performance. To appraise the effects of reaction temperature, systematic studies were carried out at different temperature ranges from 90 to 120°C for 4 h (**Figure 7B**). The relative increase in both the LA conversion and BL selectivity was obtained when the

temperature was raised from 90 to 120°C. This result suggests that the relatively high reaction temperature is favorable for the conversion of *pseudo*-BL to BL and thereby improving the selectivity of BL. It should be noted that TNTs-NHSO$_3$H showed good catalytic activity at 120°C giving high conversion and high selectivity. **Figure 7C** shows the reaction time on LA conversion and BL selectivity in the range of 1–8 h at 120°C. It is found that the LA conversion and BL selectivity was increased with reaction time. A relatively high selectivity (99.5%) at 93.2% LA conversion was achieved after 6 h. However, there was no significant increase in conversion or yield with further prolonged time to 8 h. The effect of catalyst dosage on the conversion and yield was estimated while keeping the other variables constant and the results are plotted in **Figure 7D**. It was found that the LA conversion and the BL yield increased with the increasing amount of the catalyst. The optimum catalyst weight was found to be 7 wt% with 99.3% LA conversion because the further increase of the amount of catalyst exhibited a slight increment in conversion as well as yield.

Alcoholysis of FA With *n*-Butanol

The catalytic performance of the TNTs-NHSO$_3$H catalyst was further tested by synthesis of *n*-butyl levulinate from FA (**Scheme 3**) and the results are illustrated in **Figure 8**. A 19.7% yield of BL was achieved in the presence of the TNT sample. The catalytic activity of the TNTs was attributed to the number of Lewis acidic sites on its surface (Kitano et al., 2010). It is important to mention that the catalyst TNTs-NHSO$_3$H exhibited high activity for alcoholysis of FA with *n*-butanol giving a high yield of BL (**Figure 8A**). Based on this result, the effects of the variable parameters, including reaction temperature, reaction time, and catalyst dosage on the alcoholysis of FA to BL were investigated. As illustrated in **Figure 8B**, the BL yield was strongly affected by the reaction temperature. At a low reaction temperature (90°C), the BL yield was relatively low (32.5%). However, when the reaction temperature was increased from 90 to 120 C, the yield of BL increased significantly. This is because the higher reaction temperature facilitates the conversion of FA into BL. However, when the reaction temperature was further increased, there was no significant increase in the BL yield. This may be attributed to the undesired side reactions that occurred at higher temperatures (Huang et al., 2016). **Figure 8C** displayed the effect of reaction time on the production of BL. Complete conversion was reached around 1 h, whereas the initial yield of BL was low. It is noteworthy that the yield of BL gradually increases with an increase in reaction time from 1–8 h. There is no remarkable change after 6 h, and the maximum yield (68.3%) was obtained at 8 h. As shown in **Figure 8D**, BL yield was highly affected by catalyst dosage. It can be easily found that by increasing the catalyst amount up to 0.3 g, the yield of BL reached 90.4% with 100% FA conversion. This clearly indicates the fact that the increase of the loading of catalyst provides the more available acidic sites, thereby promoting the conversion of intermediate product to the target product.

Additionally, the catalytic performance of TNTs-NHSO$_3$H was better than that of other systems listed in **Table 1**. It is clear from the table that TNTs-NHSO$_3$H worked as an acid catalyst exhibiting excellent catalytic performance in the synthesis of n-butyl levulinate

from both LA and FA. More works to tune the catalytic properties of the catalyst and to characterize the surface acid properties are underway.

Reusability

To understand the recyclability of TNTs-NHSO$_3$H, the consecutive runs under the optimum conditions were performed in the esterification of levulinic acid with n-butanol. After each cycle, the spent catalyst was recovered by centrifugation, washed with ethanol, and dried for the next run. As presented in **Figure 9A**, the activity loss of TNTs-NHSO$_3$H is neglectable after four cycles, and a yield of the desired product BL was still maintained at 95.6%. It is worthy to note that the acidity of the catalyst declined from 1.28 to 1.06 mmol g^{-1} after four consecutive recycles. The FT-IR analysis of the spent catalyst (**Supplementary Figure S1**) also confirmed that the active functional groups of the catalyst were relatively stable, providing the evidence for heterogeneous nature of TNTs-NHSO$_3$H. In addition, repeated runs of the alcoholysis reaction of FA with n-butanol were carried out under the above optimum conditions, and the results are displayed in **Figure 9B**. It was found that the catalyst was reused with a slight decrease in BL yield. This may be due to the black carbonaceous species, formed by the polymerization of the FA (Zhu et al., 2017), decreasing the accessibility of the substrates to the active sites.

CONCLUSION

In this study, titanate nanotubes were obtained through hydrothermal synthesis and then covalently linked sulfamic groups through the APTMS grafting and chlorosulfonic acid as a sulfonating reagent. The catalyst was fully characterized by various physicochemical characterization techniques, and the corresponding results suggest that the strong sulfonic acid groups were successfully grafted on the titanate nanotube surface. The as-prepared TNTs-NHSO$_3$H catalyst was used as a Brønsted solid acid for the synthesis of *n*-butyl levulinate from LA and FA. The excellent acid catalytic performance was observed in the synthesis of *n*-butyl levulinate from both the esterification of LA and the alcoholysis of FA under mild conditions. These results demonstrated that the obtained catalyst can be utilized as a potential candidate for the synthesis of LAEs and other value-added chemicals from biomass.

DATA AVAILABILITY STATEMENT

The original contributions presented in the study are included in the article/**Supplementary Material**, further inquiries can be directed to the corresponding author.

AUTHOR CONTRIBUTIONS

SZ: conceived and designed the research and produced the original manuscript, project administration. ML: investigation, writing-original draft preparation, data curation. JB: formal

analysis, writing-original draft preparation. XL: conceived and designed the research, writing-review editing, supervision. LW: methodology, formal analysis. ML: validation, data analysis. KH: catalyst characterization, DY: designed the research.

and Collaborative Innovation Center of New Chemical Technologies for Environmental Benignity and Efficient Resource Utilization.

SUPPLEMENTARY MATERIAL

The Supplementary Material for this article can be found online at: https://www.frontiersin.org/articles/10.3389/fchem.2022.894965/full#supplementary-material

REFERENCES

Adeleye, A. T., John, K. I., Adeleye, P. G., Akande, A. A., and Banjoko, O. O. (2021). One-Dimensional Titanate Nanotube Materials: Heterogeneous Solid Catalysts For Sustainable Synthesis Of Biofuel Precursors/Value-Added Chemicals—A Review. *J. Mater. Sci.* 56, 18391–18416. doi:10.1007/s10853-021-06473-1

Alonso, D. M., Bond, J. Q., and Dumesic, J. A. (2010). Catalytic Conversion of Biomass to Biofuels. *Green. Chem.* 12, 1493–1513. doi:10.1039/c004654j

Chaffey, D. R., Bere, T., Davies, T. E., Apperley, D. C., Taylor, S. H., and Graham, A. E. (2021). Conversion of Levulinic Acid to Levulinate Ester Biofuels by Heterogeneous Catalysts in the Presence of Acetals and Ketals. *Appl. Catal. B: Environ.* 293, 120219. doi:10.1016/j.apcatb.2021.120219

Chao, H.-P., Lee, C.-K., Juang, L.-C., and Hsieh, T.-Y. (2013). Sorption of Organic Compounds with Different Water Solubility on Octadecyltrichlorosilane-Modified Titanate Nanotubes. *J. Taiwan Inst. Chem. Eng.* 44, 111–116. doi:10.1016/j.jtice.2012.08.005

Christensen, E., Williams, A., Paul, S., Burton, S., and McCormick, R. L. (2011). Properties and Performance of Levulinate Esters as Diesel Blend Components. *Energy Fuels.* 25, 5422–5428. doi:10.1021/ef201229j

Ciptonugroho, W., Al-Shaal, M. G., Mensah, J. B., and Palkovits, R. (2016). One Pot Synthesis of WO/mesoporous-ZrO₂ Catalysts for the Production of Levulinic-Acid Esters. *J. Catal.* 340, 17–29. doi:10.1016/j.jcat.2016.05.001

Démolis, A., Essayem, N., and Rataboul, F. (2014). Synthesis and Applications of Alkyl Levulinates. *ACS Sustainable Chem. Eng.* 2, 1338–1352. doi:10.1021/sc500082n

de Carvalho, D. C., Oliveira, A. C., Ferreira, O. P., Filho, J. M., Tehuacanero-Cuapa, S., and Oliveira, A. C. (2017). Titanate Nanotubes as Acid Catalysts for Acetalization of Glycerol with Acetone: Influence of the Synthesis Time and the Role of Structure on the Catalytic Performance. *Chem. Eng. J.* 313, 1454–1467. doi:10.1016/j.cej.2016.11.047

Duong, H. P., Hung, C.-H., Dao, H. C., Le, M. D., and Chen, C.-Y. (2018). Modification of TiO₂ Nanotubes with 3-aminopropyl Triethoxysilane and its Performances in Nanocomposite Coatings. *New J. Chem.* 42, 8745–8751. doi:10.1039/c8nj00642c

Gaurav, N., Sivasankari, S., Kiran, G., Ninawe, A., and Selvin, J. (2017). Utilization of Bioresources for Sustainable Biofuels: A Review. *Renew. Sustainable Energ. Rev.* 73, 205–214. doi:10.1016/j.rser.2017.01.070

Gupta, S. S. R., and Kantam, M. L. (2019). Catalytic Conversion of Furfuryl Alcohol or Levulinic Acid into Alkyl Levulinates Using a Sulfonic Acid-Functionalized Hafnium-Based Mof. *Catal. Commun.* 124, 62–66. doi:10.1016/j.catcom.2019.03.003

Hao, R., He, J., Zhao, L., and Zhang, Y. (2017). HPAs and POM-Based ILs Catalyzed Effective Conversion of Furfuryl Alcohol to Alkyl Levulinate. *ChemistrySelect.* 2, 7918–7924. doi:10.1002/slct.201701675

Huang, Y.-B., Yang, T., Zhou, M.-C., Pan, H., and Fu, Y. (2016). Microwave-Assisted Alcoholysis of Furfural Alcohol into Alkyl Levulinates Catalyzed by Metal Salts. *Green. Chem.* 18, 1516–1523. doi:10.1039/c5gc01581b

Kaid, M. M., Gebreil, A., El-Hakam, S. A., Ahmed, A. I., and Ibrahim, A. A. (2020). Sulfamic Acid Incorporated HKUST-1: A Highly Active Catalyst and Efficient Adsorbent. *RSC Adv.* 10, 15586–15597. doi:10.1039/d0ra01063d

Kassaee, M. Z., Masrouri, H., and Movahedi, F. (2011). Sulfamic Acid-Functionalized Magnetic Fe₃O₄ Nanoparticles as an Efficient and Reusable

Catalyst for One-Pot Synthesis of α-amino Nitriles in Water. *Appl. Catal. A: Gen.* 395, 28–33. doi:10.1016/j.apcata.2011.01.018

Kasuga, T., Hiramatsu, M., Hoson, A., Sekino, T., and Niihara, K. (1999). Titania Nanotubes Prepared by Chemical Processing. *Adv. Mater.* 11, 1307–1311. doi:10.1002/(sici)1521-4095

Kitano, M., Nakajima, K., Kondo, J. N., Hayashi, S., and Hara, M. (2010). Protonated Titanate Nanotubes as Solid Acid Catalyst. *J. Am. Chem. Soc.* 132, 6622–6623. doi:10.1021/ja100435w

Li, S., Li, N., Li, G., Li, L., Wang, A., Cong, Y., et al. (2015). Protonated Titanate Nanotubes as a Highly Active Catalyst for the Synthesis of Renewable Diesel and Jet Fuel Range Alkanes. *Appl. Catal. B: Environ.* 170-171, 124–134. doi:10.1016/j.apcatb.2015.01.022

Liu, X., Yang, W., Zhang, Q., Li, C., and Wu, H. (2020). Current Approaches to Alkyl Levulinates via Efficient Valorization of Biomass Derivatives. *Front. Chem.* 8, 794. doi:10.3389/fchem.2020.00794

Lu, S.-x., Zhong, H., Mo, D.-m., Hu, Z., Zhou, H.-l., and Yao, Y. (2017). A H-Titanate Nanotube with superior Oxidative Desulfurization Selectivity. *Green. Chem.* 19, 1371–1377. doi:10.1039/c6gc03573f

Mohammadbagheri, Z., and Najafi Chermahini, A. (2018). KCC-1/Pr-SO₃H as an Efficient Heterogeneous Catalyst for Production of N-Butyl Levulinate from Furfuryl Alcohol. *J. Ind. Eng. Chem.* 62, 401–408. doi:10.1016/j.jiec.2018.01.020

Morawala, D., Dalai, A., and Maheria, K. (2019). Rice Husk Mediated Synthesis of Meso-Zsm-5 and its Application in the Synthesis of N-Butyl Levulinate. *J. Porous Mater.* 26, 677–686. doi:10.1007/s10934-018-0664-6

Najafi Chermahini, A., and Nazeri, M. (2017). Esterification of the Levulinic Acid with N-Butyl and Isobutyl Alcohols over Aluminum-Containing MCM-41. *Fuel Processing TechnologyTechnol.* 167, 442–450. doi:10.1016/j.fuproc.2017.07.034

Niu, H., and Cai, Y. (2009). Preparation of Octadecyl and Amino Mixed Group Modified Titanate Nanotubes and its Efficient Adsorption to Several Ionic or Ionizable Organic Analytes. *Anal. Chem.* 81, 9913–9920. doi:10.1021/ac901531k

Pachamuthu, M. P., Srinivasan, V. V., Karvembu, R., and Luque, R. (2019). Preparation of Mesoporous Stannosilicates SnTUD-1 and Catalytic Activity in Levulinic Acid Esterification. *Microporous Mesoporous Mater.* 287, 159–166. doi:10.1016/j.micromeso.2019.05.061

Pontón, P. I., d'Almeida, J. R. M., Marinkovic, B. A., Savić, S. M., Mancic, L., Rey, N. A., et al. (2014). The Effects of the Chemical Composition of Titanate Nanotubes and Solvent Type on 3-aminopropyltriethoxysilane Grafting Efficiency. *Appl. Surf. Sci.* 301, 315–322. doi:10.1016/j.apsusc.2014.02.071

Preda, S., Rutar, M., Umek, P., and Zaharescu, M. (2015). A Study of thermal Properties of Sodium Titanate Nanotubes Synthesized by Microwave-Assisted Hydrothermal Method. *Mater. Res. Bull.* 71, 98–105. doi:10.1016/j.materresbull.2015.07.015

Roy, P., Berger, S., and Schmuki, P. (2011). TiO2 Nanotubes: Synthesis and Applications. *Angew. Chem. Int. Ed.* 50, 2904–2939. doi:10.1002/anie.201001374

Shen, Q., Zhang, Y., Zhang, Y., Tan, S., and Chen, J. (2019). Transformations of Biomass-Based Levulinate Ester into γ-valerolactone and Pyrrolidones Using Carbon Nanotubes-Grafted N-Heterocyclic Carbene Ruthenium Complexes. *J. Energ. Chem.* 39, 29–38. doi:10.1016/j.jechem.2019.01.007

Silva, T. A., Diniz, J., Paixão, L., Vieira, B., Barrocas, B., Nunes, C. D., et al. (2017). Novel Titanate Nanotubes-Cyanocobalamin Materials: Synthesis and

Enhanced Photocatalytic Properties for Pollutants Removal. *Solid State. Sci.* 63, 30–41. doi:10.1016/j.solidstatesciences.2016.11.008

Song, D., An, S., Lu, B., Guo, Y., and Leng, J. (2015). Arylsulfonic Acid Functionalized Hollow Mesoporous Carbon Spheres for Efficient Conversion of Levulinic Acid or Furfuryl Alcohol to Ethyl Levulinate. *Appl. Catal. B: Environ.* 179, 445–457. doi:10.1016/j.apcatb.2015.05.047

Tian, Y., Zhang, F., Wang, J., Cao, L., and Han, Q. (2021). A Review on Solid Acid Catalysis for Sustainable Production of Levulinic Acid and Levulinate Esters from Biomass Derivatives. *Bioresour. Technology.* 342, 125977. doi:10.1016/j.biortech.2021.125977

Veisi, H., Taheri, S., and Hemmati, S. (2016). Preparation of Polydopamine Sulfamic Acid-Functionalized Magnetic Fe₃O₄ Nanoparticles with a Core/ Shell Nanostructure as Heterogeneous and Recyclable Nanocatalysts for the Acetylation of Alcohols, Phenols, Amines and Thiols under Solvent-free Conditions. *Green. Chem.* 18, 6337–6348. doi:10.1039/c6gc01975g

Wang, H., Zheng, L., Liu, G., and Zhou, Y. (2018). Enhanced Adsorption of Ag+ on Triethanolamine Modified Titanate Nanotubes. *Colloids Surf. A: Physicochemical Eng. Aspects.* 537, 28–35. doi:10.1016/j.colsurfa.2017.09.049

Wang, L., Liu, W., Wang, T., and Ni, J. (2013). Highly Efficient Adsorption of Cr(VI) from Aqueous Solutions by Amino-Functionalized Titanate Nanotubes. *Chem. Eng. J.* 225, 153–163. doi:10.1016/j.cej.2013.03.081

Wight, A. P., and Davis, M. E. (2002). Design and Preparation of Organic–Inorganic Hybrid Catalysts. *Chem. Rev.* 102, 3589–3614. doi:10.1021/cr010334m

Wu, G., Shen, C., Liu, S., Huang, Y., Zhang, S., and Zhang, H. (2021). Research Progress on the Preparation and Application of Biomass Derived Methyl Levulinate. *Green. Chem.* 23, 9254–9282. doi:10.1039/d1gc03474j

Yang, J., Ao, Z., Wu, H., Zhang, S., Chi, C., Hou, C., et al. (2020). Waste Paper-Derived Magnetic Carbon Composite: A Novel Eco-Friendly Solid Acid for the Synthesis of N-Butyl Levulinate from Furfuryl Alcohol. *Renew. Energ.* 146, 477–483. doi:10.1016/j.renene.2019.06.167

Yang, J., Li, G., Zhang, L., and Zhang, S. (2018). Efficient Production of N-Butyl Levulinate Fuel Additive from Levulinic Acid Using Amorphous Carbon Enriched with Oxygenated Groups. *Catalysts.* 8, 14. doi:10.3390/catal8010014

Yang, J., Zhang, H., Ao, Z., and Zhang, S. (2019). Hydrothermal Carbon Enriched with Sulfonic and Carboxyl Groups as an Efficient Solid Acid Catalyst for Butanolysis of Furfuryl Alcohol. *Catal. Commun.* 123, 109–113. doi:10.1016/j.catcom.2019.02.016

Zhang, S., Li, J., Shang, N.-Z., Gao, S.-T., Wang, C., and Wang, Z. (2020). Conversion of Biomass-Derived Levulinate Esters to γ-Valerolactone with a Robust CuNi Bimetallic Catalyst. *New J. Chem.* 44, 15671–15676. doi:10.1039/d0nj02874f

Zhou, L., He, Y., Ma, L., Jiang, Y., Huang, Z., Yin, L., et al. (2018). Conversion of Levulinic Acid into Alkyl Levulinates: Using Lipase Immobilized on Meso-Molding Three-Dimensional Macroporous Organosilica as Catalyst. *Bioresour. Technology* 247, 568–575. doi:10.1016/j.biortech.2017.08.134

Zhou, S., Jiang, D., Liu, X., Chen, Y., and Yin, D. (2018). Titanate Nanotubes-Bonded Organosulfonic Acid as Solid Acid Catalyst for Synthesis of Butyl Levulinate. *RSC Adv.* 8, 3657–3662. doi:10.1039/c7ra12994g

Zhou, S., Lai, J., Liu, X., Huang, G., You, G., Xu, Q., et al. (2022). Selective Conversion of Biomass-Derived Furfuryl Alcohol into N-Butyl Levulinate over Sulfonic Acid Functionalized TiO₂ Nanotubes. *Green. Energ. Environ.* 7, 257–265. doi:10.1016/j.gee.2020.09.009

Zhou, S., Liu, X., Lai, J., Zheng, M., Liu, W., Xu, Q., et al. (2019). Covalently Linked Organo-Sulfonic Acid Modified Titanate Nanotube Hybrid Nanostructures for the Catalytic Esterification of Levulinic Acid with N-Butyl Alcohol. *Chem. Eng. J.* 361, 571–577. doi:10.1016/j.cej.2018.12.111

Zhu, S., Guo, J., Wang, X., Wang, J., and Fan, W. (2017). Alcoholysis: A Promising Technology for Conversion of Lignocellulose and Platform Chemicals. *ChemSusChem.* 10, 2547–2559. doi:10.1002/cssc.201700597

Recent Advances in the Catalytic Conversion of Biomass to Furfural in Deep Eutectic Solvents

Xu Zhang[1,2], Peng Zhu[1,2], Qinfang Li[1,2] and Haian Xia[1,2]*

[1]*Jiangsu Co-Innovation Center of Efficient Processing and Utilization of Forest Resources, College of Chemical Engineering, Nanjing Forestry University, Nanjing, China, [2]Jiangsu Provincial Key Lab for the Chemistry and Utilization of Agro-forest Biomass, College of Chemical Engineering, Nanjing Forestry University, Nanjing, China*

Lignocellulose is recognized as an ideal raw material for biorefinery as it may be converted into biofuels and value-added products through a series of chemical routes. Furfural, a bio-based platform chemical generated from lignocellulosic biomass, has been identified as a very versatile alternative to fossil fuels. Deep eutectic solvents (DES) are new "green" solvents, which have been employed as green and cheap alternatives to traditional organic solvents and ionic liquids (ILs), with the advantages of low cost, low toxicity, and biodegradability, and also have been proven to be effective media for the synthesis of biomass-derived chemicals. This review summarizes the recent advances in the conversion of carbohydrates to furfural in DES solvent systems, which mainly focus on the effect of adding different catalysts to the DES system, including metal halides, water, solid acid catalyst, and certain oxides, on the production of furfural. Moreover, the challenges and perspectives of DES-assisted furfural synthesis in biorefinery systems are also discussed in this review.

Keywords: biomass, deep eutectic solvents, furfural, catalysis, solid acid

1 INTRODUCTION

Lignocellulose is a prominent biorefining raw material due to its wide availability and renewability, which helps to alleviate energy depletion (Somerville et al., 2010). In most lignocellulosic feedstocks, the proportions of cellulose, hemicellulose, and lignin are 30%–40%, 30%–35%, and 11%–25%, respectively. (Wang et al., 2016). Cellulose and hemicellulose separated from lignocellulose can be converted to high-value platform chemicals (e.g., 5-HMF and furfural) (**Supplementary figure S1**) (Bozell and Petersen, 2010).

Furfural is mainly obtained by hydrolysis and dehydration of xylan, which is abundant in hemicellulose and serves as a bridge between biomass and fuels, and chemicals. Furfural is widely used in oil refining, plastics manufacturing, pharmaceutical, and agrochemical industries, as well as a direct gasoline additive (Song et al., 2017; Luo et al., 2019; Song et al., 2020). Inorganic acids are utilized as the preferred catalysts for furfural production in the industry because furfural is produced in an acidic reaction system. High operating expenses, equipment corrosion, low furfural yields, and high energy consumption are all issues for this process (Mittal et al., 2017). Extraction of furfural from the reaction medium employing efficient catalysts or extraction solvents is a viable way for improving furfural yields. Some non-protonic solvents (e.g., tetrahydrofuran (THF), methyl isobutyl ketone (MIBK), and γ-pentyl lactone) are interesting solvents for furfural extraction because of their good ability to extract furfural. To extract furfural into the organic phase while minimizing side
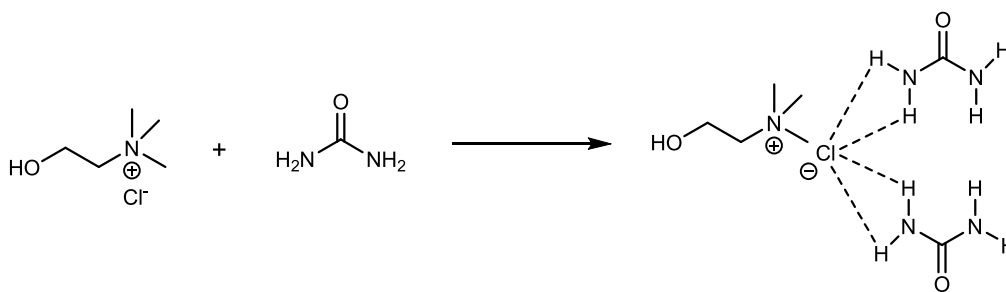
FIGURE 1 | Hydrogen-bond interactions proposed for choline chloride/urea (1:2) eutectic mixture.

reactions in the aqueous phase, a biphasic reaction system is used. However, high reaction temperatures (150–230°C) are required for aqueous/organic biphasic systems (Romo et al., 2018). Ionic liquids with good solubility, chemical, and thermal stability, and enhanced catalytic activity were found to be alternative solvents, and polysaccharide dehydration in ionic liquids could be achieved at temperatures below 140°C (Wang et al., 2017; Wu et al., 2017). However, ionic liquids, are expensive and have poor biocompatibility.

Alternative deep eutectic solvents (DES) have been considered as a result of ongoing research on ionic liquids, which have similar properties to ionic liquids but are less expensive and entirely biodegradable (Hansen et al., 2021). DES are eutectic mixtures of hydrogen bond acceptor (HBA) and hydrogen bond donor (HBD) mixed in a certain ratio with a melting point lower than that of either component. For example, melting temperatures of chloroform and urea are 302°C and 135°C, respectively, and the resulting molar ratio of 1:2 chloroform/ urea DES is liquid at 12°C (Abbott et al., 2003). DES has been used in biomass processing, for instance, fractionation and pretreatment of lignocellulose, as well as the catalytic conversion of carbohydrates (Satlewal et al., 2018).

The first half of this paper briefly covers DES and the mechanism of DES interacting with lignocellulose, with a focus on furfural synthesis. The second section summarizes the latest advances in the addition of various catalysts to DES systems for furfural production. This review also puts forward the challenges and perspectives for producing furfural from biomass using DES solvents.

2 DEEP EUTECTIC SOLVENTS

Deep Eutectic Solvents is a low melting point mixture of two or more component pairs consisting of HBD interacting with HBA (e.g., quaternary ammonium salts) via hydrogen bonding. Charge separation domains are promoted by hydrogen bonds (H-bonds) between HBA and HBD, showing a large decrease in the melting point of the DES mixture compared to the initial compounds, and the stronger H-bonds result in a bigger fall in melting point (Abbott et al., 2004). DES has been successfully applied in metallurgy and electrodeposition (Abbott et al., 2001; Abbott et al., 2006), biomass processing (Abbott et al., 2007; Francisco et al., 2012), fuel desulfurization (Jablonský et al., 2015), CO_2 adsorption (Li et al.,

2013), biodiesel purification (Li et al., 2008), biotransformation (Abbott et al., 2005), etc. since its first appearance in 2001 (Morrison et al., 2009). It can also be used as an effective extractant and has a wide range of applications in analytical sciences (Cunha and Fernandes, 2018), including chromatographic separation (Cai and Qiu, 2019), electrochemical analysis, liquid and solid sample decomposition (Chen Y.-L. et al., 2018), synthesis and modification of novel adsorbent materials (Hashemi et al., 2018).

2.1 Deep Eutectic Solvents Preparation and Principle

Autocorrelation intermolecular interactions, which are most likely induced by mixed entropy, van der Waals contacts, hydrogen bonding, and/or ionic bonding (**Figure 1**, exemplified for choline ChCl/urea 1:2), are responsible for the formation of DES (Abbott et al., 2003; Francisco et al., 2013; Hammond et al., 2016; Zahn et al., 2016; Mohd Zaid et al., 2017; Wagle et al., 2017; Delgado-Mellado et al., 2018; van Osch et al., 2019). Hydrogen bonds are the most important intramolecular bonds among these bonds between HBD and halide anions in DES (Perkins et al., 2014; Mbous et al., 2017). Hydrogen bonds are responsible for the generation of the room temperature liquid phase of DES (Smith et al., 2014), the enormous network of hydrogen bonds that generates the inherent qualities of DES, such as low melting point, low volatility, non-flammability, low vapor pressure, dipole nature, thermal stability, high solubility, and adjustability (Zhang et al., 2012; Florindo et al., 2014).

Heating and stirring, vacuum evaporation, grinding, and freeze-drying are the most common methods for preparing DES. The most common preparation method is heating and stirring, in which the components are mixed and stirred for a certain time at a set temperature (50°C–100°C) until a clear liquid is generated (Florindo et al., 2014; Yang et al., 2019). In addition, the excessive temperature may influence the formation of DES by this approach, resulting in the production of some contaminants (esters, HCl) (Florindo et al., 2014). Grinding is a better method when ChCl and carboxylic acid are used to obtain DES because the mixed components are ground in a mortar at room temperature until a homogeneous liquid is formed (Florindo et al., 2014). The evaporation method involves dissolving the components in water, evaporating most of the water under a vacuum at 50°C, and then drying it to a consistent weight in a

FIGURE 2 | Typical structures of hydrogen bond donors (HBDs) and bond acceptors (HBAs) for DES synthesis.
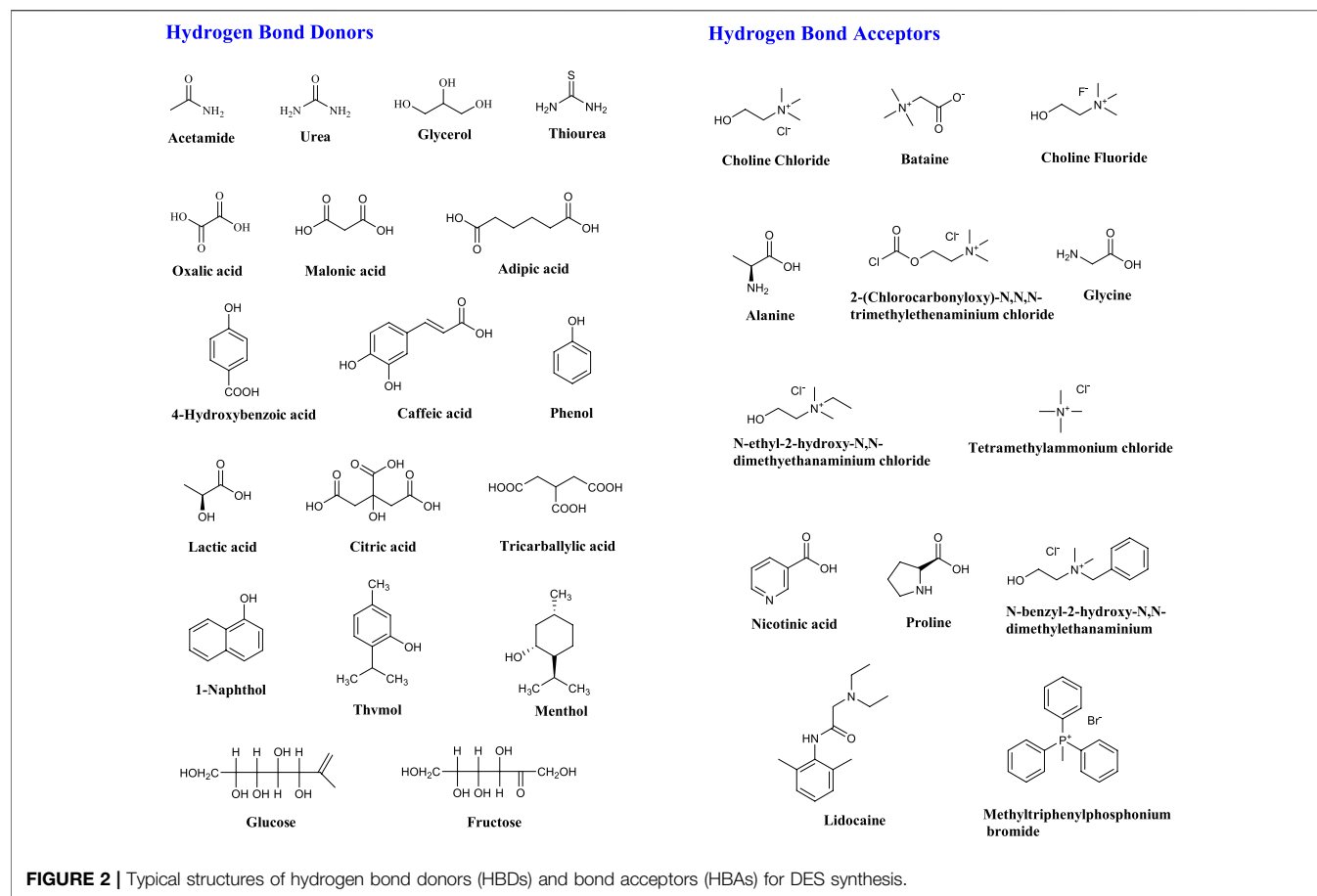
TABLE 1 | The general formula for the classification of DES. Reprinted from ref. (Smith et al., 2014). Copyright 2014 American Chemical Society.

Entry	Type	Through-form	Composition	Terms
1	Type I	$Cat^+X^-zMCl_x$	Organic and metal salts	M = Zn, Sn, Fe, Al, Ga, In
2	Type II	$Cat^+X^-zMClx \cdot yH_2O$	Organic salts and metal hydrates	M = Cr, Co, Cu, Ni, Fe
3	Type III	Cat^+X^-zRZ	Organic salts and HBD	Z = $CONH_2$, COOH, OH
4	Type IV	$MCl_x^+RZ = MCl_{x-1}^+RZ + MCl_{x+1}^-$	Metal chloride hydrate and HBD	M = Al, Zn and Z = $CONH_2$, OH

Cat^+: Any ammonium (NR_4^+), phosphonium (PR_4^+), or sulfonium cation (SR_3^+) (Yiin et al., 2021).
X^-: A Lewis base, generally a halide anion (F^-, Cl^-, Br^-, I^-, etc.).
z: The number of molecules Y that interact with the anion.

desiccator (Dai et al., 2013). The components are dissolved in 5% water and then freeze-dried to generate a clear and transparent liquid (Gutierrez et al., 2009).

2.2 Deep Eutectic Solvents Categories

Most DES are obtained from non-ionic substances, such as salts and molecular components (**Figure 2**) (Zhang et al., 2012). The general formula for DES is Cat^+X^-zY (Smith et al., 2014). DES was first proposed and classified into four categories by Abbott et al., in 2003 (**Table 1**) (Abbott et al., 2003) (Smith et al., 2014).

Type II DES employs hydrated metal halides, which are less expensive and less susceptible to atmospheric moisture than type I metal salts, making them popular in the industry (Smith et al.,

2014). The most widely used DES is type III DES, which has the advantages of simple and low-cost preparation (Smith et al., 2014), being environmentally friendly and mostly biodegradable, not reacting with water, and having a high potential for lignocellulosic biomass processing, so this review will mainly focus on type III DES. In fact, in addition to the four types of DES mentioned above, type V has been developed, which is made up entirely of nonionic, molecular HBA, and HBD. These nonionic DES overcome the drawbacks of quaternary ammonium salt-based DES, such as expense, hydrophobicity, and viscosity, and exhibit the ability to recover and recycle DES by evaporation. However, the research aspect of V-type DES is not mature enough to be described here due to its late discovery (Abranches et al., 2019).

FIGURE 3 | Disruption of lignin carbohydrate complexes with DES. Reprinted from ref. (Satlewal et al., 2018). Copyright 2018 Elsevier Inc.

2.3 Catalytic and Solubilizing Effects of DES on Lignocellulose

2.3.1 Dissolution

Lignocellulosic biomass has a complicated structural and chemical mechanism for resistance to microbial and enzymatic deconstruction, as well as a natural resistance known as "b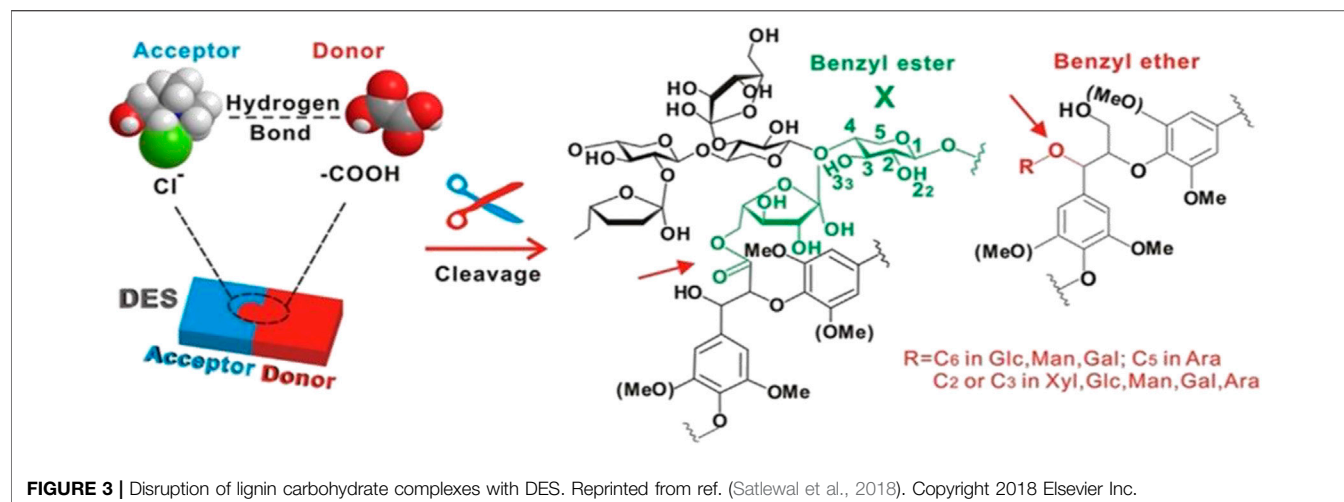iomass resistance," which significantly inhibits biomass conversion into value-added products (Himmel Michael et al., 2007; Mettler et al., 2012). This "biomass resistance" is considered to arise mainly from lignin and lignin-carbohydrate complexes, which are cross-linked to carbohydrates (especially hemicellulose) through a network of strong covalent and hydrogen bonds with benzyl esters, benzyl ethers, and phenyl glycosides functional groups (Liu et al., 2017). The crosslinking degree of the lignin-carbohydrate complex is associated with increased cell wall stiffness and resistance to enzymatic digestion. To achieve an efficient deconstruction process, these crosslinks must be destroyed by the chemical hydrolysis of ester bonds (Grabber et al., 1998; McCann and Carpita, 2015). Strong hydrogen bonding ligands in ionic liquids (ILs) preferentially solubilize lignin and hemicellulose in biomass while maintaining biopolymer integrity (Carrozza et al., 2019). Inspired by the high solubilization capacity of ILs for lignocellulose, DES has attracted increasing interest as an inexpensive alternative to ILs. DES can deliver and accept protons, which enables the formation of hydrogen bonds with other compounds, thus enhancing their solubilization properties (Pandey et al., 2017). Acidic DES (HBD: lactic, malic, and oxalic acids) are very effective in lignin solubilization (Xu et al., 2016; Liu et al., 2017; Yiin et al., 2017; Liu et al., 2019; Ramesh et al., 2020; Yiin et al., 2021). One of the reasons why DES selectively dissolves lignin over cellulose is that both cellulose and DES have strong hydrogen bonding networks, solubilizing cellulose in DES requires dissociation and reorganization of both hydrogen-bonding networks to generate a thermodynamically more stable network. However, the cohesive energy of cellulose is so strong that it may prevent its solubilization in any DES (Vigier et al., 2015). As shown in **Figure 3**, chloride ions

present in DES can establish hydrogen bonds with hydroxyl groups that are present in carbohydrates and lignin, disrupting the carbohydrate-lignin bonding connections and hydrolyzing the LCC to remove hemicellulose while also enhancing enzyme accessibility and hydrolysis yields (Satlewal et al., 2018; Lee and Wu, 2021). DES can effectively dissolve the lignin and remove amorphous cellulose from lignocellulose. As a result, DES can fractionate lignocellulose to promote hemicellulose and lignin utilization while also improving cellulose crystallinity.

2.3.2 Catalysis

DES formed by combining ChCl and carboxylic acids is commonly used in the production of furan compounds. ChCl-based DES has been found to be effective for xylan solubilization in biomass pretreatment processes in recent studies (Chen et al., 2018b; Chen et al., 2018c; Shen et al., 2019). These DES based on ChCl-carboxylic acid can act as both solvents and catalysts. After lignin removal with the help of DES, hemicellulose, and cellulose were converted to furfural and hydroxymethylfurfural, respectively (Parsell et al., 2015). Hemicellulose is more readily depolymerized than cellulose (especially under acidic conditions) due to its non-crystalline nature (Brandt et al., 2013). After disruption of the hemicellulose polymer by chloride ions in DES, the carboxylic acids can provide the required protons to break down the sugar-1,4 glycosidic bonds in xylan to produce xylose, which can then be dehydrated to furfural (Enslow and Bell, 2012; Li et al., 2019). Unlike hemicellulose, the quantity and strength of hydrogen bonds established with cellulose determine cellulose's dissolution (Lynam et al., 2017). To increase the output of furans, novel DES that can concurrently catalyze hemicellulose and cellulose must be discovered.

3 CATALYTIC CONVERSION OF BIOMASS TO FURFURAL IN DEEP EUTECTIC SOLVENTS

The conversion of carbohydrates to furans is a hot research topic in the biorefining of lignocellulose (Li et al., 2016; Peleteiro et al.,

TABLE 2 | Furfural production in a neat DES system (no catalyst).

Entry	Substrate	DES (mass ratio)	T (°C)	T(min)	Yield (%)	References
1	hemicellulose[a]	ChCl/p-TSA (1:1)	120	90	85.4	Arora et al. (2021)
2	hemicellulose[a]	ChCl/LA (1:1)	120	90	51.4	Arora et al. (2021)
3	corn husk	ChCl/OA (1:1)	100	120	52	Bodachivskyi et al. (2019)
4	Softwood	ChCl/OA (1:1)	100	300	55	Bodachivskyi et al. (2019)
5	U. lactuca	ChCl/OA (1:1)	100	120	60	Bodachivskyi et al. (2019)
6	P. cruentum	ChCl/OA (1:1)	100	240	72	Bodachivskyi et al. (2019)

LA, lactic acid; OA, oxalic acid.
[a]two-step method.

2016; Fan et al., 2018). The acid-catalyzed hydrolysis and dehydration of pentosans in lignocellulose produces furfural. Two methods are generally used to produce furfural in the DES system. In the "two-step method" in which the lignin carbohydrate complex is destroyed by pretreatment, the hemicellulose-derived sugar is selectively dissolved from the biomass, and then the acidified aqueous DES solution is used to produce furfural from the xylose-rich pretreatment solution (Arora et al., 2021), and the "one-step method" in which the acidified DES is used to produce furfural by directly treating pentosan or biomass (Lee et al., 2019; Rusanen et al., 2021). The reaction can be further enhanced to promote furfural synthesis if Brønsted acid or Lewis acid catalyst is added to the DES system to some extent (Wang et al., 2018; Chen and Wan, 2019). Recent progress in the addition of various catalysts to DES systems for furfural production is shown in the chart.

3.1 Catalysis in Neat DES System

Furfural is produced by dehydration of xylose in an acidic medium (Enslow and Bell, 2012). HBD for various acidic complexing agents such as oxalic acid, citric acid, p-toluene sulfonic acid, trichloroacetic acid, and other acidic complexing agents with ionizable protons is named Brønsted acidic deep eutectic solvents (BADES) in acidic DES (ADES) (Qin et al., 2020). The acidic HBD can catalyze the hydrolysis of hemicellulose to form xylose or arabinose, which is further dehydrated to produce furfural by releasing three water molecules (Marcotullio and De Jong, 2010; Cai et al., 2014). The acidic strength of the acid catalyst/solvent is well known to play a critical role in the hydrolysis of hemicellulose (Choudhary et al., 2012; Wang et al., 2015; Delbecq et al., 2018), and it is thus critical to optimize and mediate ADES acidity (Kore and Srivastava, 2011). The higher the pH grew closer to 1, the larger the productivity of furfural, according to Arora et al. (2021). The yield of furfural was 85.4% after treatment of hemicellulose with ChCl: p-toluene sulfonic acid (p-TSA) = 1: 1 and pH = 1 at 120°C for 1.5 h (**Table 2**, entry 1). When the pH was increased from 1 to 3, the yield of furfural reduced to 51.4% (**Table 2**, entry 2) (Arora et al., 2021). The effect of acidity on the yield of furfural was also confirmed by Cornelius et al. when comparing choline chloride-dicarboxylate-based low eutectic solvents. The increasing carbon chain length of dicarboxylic acid HBD boosts the electron feeding effect of alkyl groups, reducing the strength of the hydrogen bond formed between

HBA and HBD as well as the hydrogen feeding capacity of DES, according to the reaction mechanism. Finally, because the concentration of H^+ in the dehydration and hydrolysis reaction system is lowered, which is detrimental to furfural production, DES (oxalic acid) with short carbon chain dicarboxylic acid gives greater furfural yields (Lee et al., 2019). Lurii and others used ChCl/OA at 100°C to convert certain underappreciated terrestrial and marine biomass into furfural, yielding up to 72% (**Table 2**, entries 3–6), further demonstrating the superiority of oxalic acid as an HBD (Bodachivskyi et al., 2019). Although larger yields of furfural can be achieved without the use of a catalyst in a neat DES system, DES has drawbacks such as higher viscosity that cannot be overlooked. Although neat DES has absolute advantages for compounds with low water solubility, and better yields of furfural can be achieved in this system, practical issues such as time-consuming solvent transfer and inefficient mass transfer due to DES drawbacks such as higher viscosity cannot be neglected. Exploring some novel DES with low viscosity, high acidity, and good thermal stability is the main research topic in the future.

3.2 Catalyst in Deep Eutectic Solvents System
3.2.1 Water

In biomass, water contributes to hemicellulose saccharification and xylose recovery. The addition of water in the DES system also reduces the viscosity of the DES (Dai et al., 2015), allowing for better DES penetration into the lignocellulosic matrix (New et al., 2019), improved mass transfer, and increased delignification, all of which aid hemicellulose extraction and subsequent furfural production (Loow et al., 2017). As a result, one of the most important influencing factors for hemicellulose conversion is the amount of water in the system. Annu et al. investigated the effect of different water contents on the yield of furfural in a deep eutectic solvent system. In the MIBK/DES biphasic system, higher furfural yields of 62% and 37.5% (**Table 3**, entry 1–2) were obtained for the sugar mixture and birch sawdust, respectively, when 32.9 wt% water was added to the microwave reactor (Rusanen et al., 2021). Water can promote furfural production, but too much water in the system can be harmful to getting enough furfural. When the amount of water injected exceeded 40 wt%, the yield of furfural decreased significantly (Rusanen et al., 2021). Excess water breaks the hydrogen bond

TABLE 3 | Adding water in the DES system for furfural production.

Entry	Substrate	DES (mass ratio)	T (°C)	T(min)	Yield (%)	References
1	Xylose	ChCl/Gly (1:3)	160	10	62	Rusanen et al. (2021)
2	birch sawdust	ChCl/Gly (1:3)	170	10	37.5	Rusanen et al. (2021)
3	oil palm fronds	ChCl/OA (1:1)	100	135	26.3	Lee et al. (2019)
4	xylose[a]	ChCl/EG (1:2)	180	30	75.6	Chen and Wan, (2019)
5	oil palm fronds[a]	ChCl/OA (1:1)	120	60	56.5	Lee et al. (2021)
6	Xylan	ChCl/MA (1:3)	150	2.5	75	Morais et al. (2020)

Gly, glycerol; OA, oxalic acid; EG, ethylene glycol; MA, malic acid.
[a]*two-step method.*

TABLE 4 | Adding metal chlorides in the DES system for furfural production.

Entry	Substrate	DES (mass ratio)	Catalyst	T (°C)	T(min)	Yield (%)	References
1	Xylose	ChCl/CA (2:1)	$AlCl_3 \cdot 6H_2O$	140	25	73.1	Zhang and Yu, (2013)
2	xylan	ChCl/CA (2:1)	$AlCl_3 \cdot 6H_2O$	140	35	68.6	Zhang and Yu, (2013)
3	eucalyptus	ChCl/OA (1:1)	$AlCl_3$	140	90	70.3	Wang et al. (2018)
4	xylose	ChCl/OA (1:1)	$AlCl_3 \cdot 6H_2O$	100	60	60.4	Zhang et al. (2014)
5	xylan	ChCl/OA (1:1)	$FeCl_3 \cdot 6H_2O$	100	70	38.4	Zhang et al. (2014)
6	xylan	ChCl/OA (1:1)	$AlCl_3 \cdot 6H_2O$	100	70	55.5	Zhang et al. (2014)
7	xylose	ChCl/FA (1:6)	$SnCl_4 \cdot 5H_2O$	120	120	60.6	Yu et al. (2019a)
8	xylose	ChCl/FA (1:6)	$AlCl_3$	120	30	39.8	Yu et al. (2019a)
9	xylose	ChCl/FA (1:6)	$CeCl_3 \cdot 7H_2O$	120	30	39.1	Yu et al. (2019a)
10	xylose	ChCl/FA (1:6)	$ZrCl_4$	120	30	32.8	Yu et al. (2019a)

FA, formic acid; OA, oxalic acid; CA, citric acid.

between HBD and HBA and also promotes the formation of humins, thus obtaining a low furfural yield (Hammond et al., 2017; Gabriele et al., 2019). When comparing the yield of furfural before and after the addition of water, direct treatment of oil palm leaves with ChCl/OA aqueous solution (16.4 wt% H_2O) at 100°C after the addition of 2 ml of water enhanced the production of furfural from 9.74% to 26.3%. (**Table 3**, entry 3) (Lee et al., 2019). A biphasic system was created using a ChCl: EG aqueous solution (30 percent water) combined with acetone (2:7), and xylose was reacted at 180°C for 30 min to get a high furfural yield of 75.6% (**Table 3**, entry 4) (Chen and Wan, 2019). The hydrogen bond between HBD and HBA can be weakened by the right amount of water employed in DES, making them more accessible and reactive. A deep eutectic solvent treatment with choline chloride-oxalic acid aqueous solution (16.4 wt% H_2O) was added following ultrasonication of oil palm leaves to disrupt the LCC structure, yielding a furfural yield of 56.5% (**Table 3**, entry 5) (Lee et al., 2021). Unlike other similar studies, they used ultrasonic lignocellulose pretreatment. This technique produces acetic acid, which can efficiently increase furfural conversion while reducing reaction time (Lee et al., 2021). In the biphasic system, xylan was used as a starting material and 5 wt% water was added to ChCl/malic acid, then the system was heated by microwave at 150°C for 2.5 min to obtain a high yield of furfural (75%) (**Table 3**, entry 6) (Morais et al., 2020). This set of experiments was the shortest reaction time among these groups of similar experiments, and high yields of furfural were obtained. When compared to the traditional hydrothermal approach, either ultrasonic pretreatment or microwave heating can employ a

shorter reaction time to get higher yields but raises the cost of industrial applications. The appropriate amount of water facilitates the production of furfural, but when the amount of water exceeds a certain threshold, the internal structure of DES is destroyed, and the interaction between DES and biomass is hampered, resulting in a reduction in furfural yield. Water mitigated several intrinsic flaws of DES and enhanced furfural yield, but this was limited. Compared to the reaction systems with the addition of Lewis acid, the furfural yield is lower when only DES acted as Brønsted acid without the presence of Lewis acid in the reaction because Lewis acid may catalyze the isomerization of xylose to xylulose, which is then further dehydrated to generate furfural. Finding an appropriate Lewis acid catalyst as well as deep eutectic solvents that are water-resistant is a pressing issue that must be addressed.

3.2.2 Metal Chlorides
Metal chlorides have been widely used as catalysts in the synthesis of furfural from lignocellulose (Chen et al., 2018b; Chen and Wan, 2019; Yu et al., 2019b). Metal chloride increases furfural yield due to the action of metal cations and Cl^- (Gravitis et al., 2001; Marcotullio and De Jong, 2010). For example, using ChCl/ citric acid aqueous solution as the solvent and adding $AlCl_3 \cdot 6H_2O$ catalyst, 73.1% furfural yield (**Table 4**, entry 1) can be obtained from xylose and 68.6% (**Table 4**, entry 2) from xylan (Zhang and Yu, 2013). On aldose or aldose polymers, metal chlorides have an excellent isomerization impact. The addition of metal chloride to DES produced Lewis and Brønsted acid reaction medium. The metal chloride promoted the enolization of xylose and improved

TABLE 5 | Effect of the catalysts on the furfural yield in the DES system.

Entry	Substrate	DES (mass ratio)	Catalyst	T (°C)	T(min)	Yield (%)	References
1	xylan	ChCl/MA (1:3)	LiBr	157.3	1.74	89.5	Morais et al. (2021)
2	corncob	Betaine/LA	DES-SG (SiO₂)[a]	170	30	45.3	Bodachivskyi et al. (2019)
3	corncob	Betaine/LA	SG(SiO₂)[a]	170	30	38.7	Bodachivskyi et al. (2019)
4	sugarcane bagasse[b]	ChCl/EG (1:2)	Sn-SS[c]	170	20	62.3	Li et al. (2021a)
5	corn stover	ChCl/EG (1:2)	SO₄²⁻/SnO₂-CS[a]	170	30	61.8	Ji et al. (2021)
6	corn stover	ChCl/EG (1:2)	SO₄²⁻/SnO₂-CS, MgCl₂	170	30	68.2	Ji et al. (2021)
7	xylose	ChCl/Gly (1:2)	HCOOH	180	30	58.3	Li et al. (2021b)
8	native cellulose	ChCl/OA (1.5:1)	TiO₂	140	30	53.2[d]	da Silva Lacerda et al. (2015)

MA, malic acid; EG, ethylene glycol; LA, lactic acid; Gly, glycerol; OA, oxalic acid.
[a]SG: sol–gel method.
[b]Two-step method.
[c]SS: Shrimp shell.
[d]Yield of HMF + Furfural.

the selectivity and yield of furfural (Marcotullio and de Jong, 2011), and it catalyzes the dehydration of xylose to form furfural, through xylose isomerization to xylulose (Binder et al., 2010; vom Stein et al., 2011; Yang et al., 2012). When the biphasic system is applied in combination with the catalyst, excellent yields of furfural can be obtained. A high furfural yield of 70.3% (**Table 4**, entry 3) could be obtained by adding a specified amount of metal chloride as a catalyst to the DES (ChCl/OA)/MIBK biphasic system to react with eucalyptus (Wang et al., 2018). Zhang et al. studied the conversion of xylose to furfural by trivalent metal chlorides in ChCl-oxalic acid at 100°C, with the greatest furfural yields of 60.4% and 55.5% (**Table 4**, entries 4, 6) from xylose and xylan, respectively. $AlCl_3 \cdot 6H_2O$ was demonstrated to be the most efficient in generating furfural from xylose (Zhang et al., 2014). However, the thermal stability of ChCl/oxalic acid is poor at temperatures above 379 K (Zhang et al., 2014). A comparative investigation by Qiang et al. found that adding $SnCl_4 \cdot 5H_2O$ (**Table 4**, entries 7–10) to the ChCl/formic (Fa) system was the most successful (Yu et al., 2019a). Because the metal cation catalyzed the conversion of carbohydrates to furfural is related to its ionization potential, the furfural yields produced with different metal chlorides can vary. Although metal chlorides have good results for furfural yield, certain drawbacks should not be ignored, such as difficulty in separation and recovery, instability, and toxicity. Alkali metal salt catalysts have a limited function in furfural production, and combining alkali metal salts with acid catalysts in deep eutectic solvents improves furfural production. Metal chlorides dissolved in DES are difficult to be recovered for reuse, which is contrary to the principle of green chemistry. In industrial applications, new extractants are needed to separate metal chlorides from DES, or catalysts that are insoluble in DES are required.
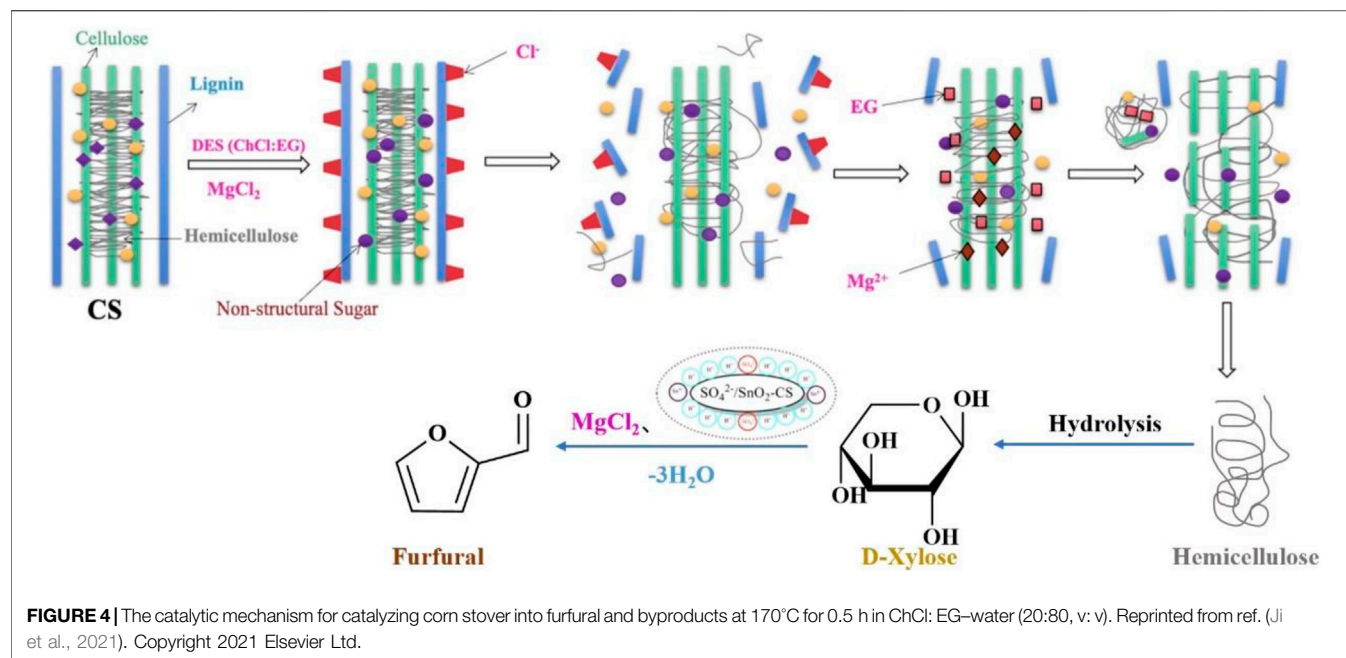
3.2.3 Alkali Metal Halides
Alkali metal halides have been shown to increase the yield of furfural when added to solvent systems (water or non-polar solvents) (Enslow and Bell, 2015; Mellmer et al., 2019), mainly in biphasic systems to afford the "salting out" effect and thus increase the strong extraction of furfural from the aqueous phase into the organic phase. Similarly, they play a crucial role in the kinetics of xylose dehydration

in acidic media. Eduarda and coworkers compared the differences of eight alkali metal salts added to DES to increase furfural yield: sodium chloride (NaCl), sodium bromide (NaBr), sodium iodide (NaI), potassium chloride (KCl), potassium bromide (KBr), potassium iodide (KI), lithium chloride (LiCl) and lithium bromide (LiBr). In comparison to the unadded halide salts, NaBr, NaI, KI, and LiBr exhibited improvement in furfural yield to a certain extent (Morais et al., 2021). The carbon cation is generated after the loss of water from xylose in the dehydration process of xylose to furfural, which is stabilized by the presence of halides. When a metal cation with significant hydrophilic characteristics interacts with the negatively charged xylose, it prevents the carbon cation from rehydration, stabilizing the generated carbon cation (Enslow and Bell, 2015). The carbon cation is a reactive intermediate that can undergo rearrangement to form 2,5-no-hydroxy sugars, which are then further dehydrated to produce furfural (Enslow and Bell, 2015). The halide anion serves as a stabilizing agent interacting with critical intermediate in the DES system, whereas the cation largely interacts with the chloride anion, and these interactions then influence xylose solvation and dehydration. The yield of furfural was then further optimized, and it was found that adding LiBr to ChCl/MA (5 wt% H_2O) at 175.3°C for 1.74 min resulted in a high furfural yield of 89.5% (**Table 4**, entry 1) (Morais et al., 2021). Alkali metal halides can boost the yield of furfural by increasing the salting effect of the biphasic system, but in the complex lignocellulose structure, alkali metal salts cannot cooperate with DES to accelerate the isomerization of xylose and thus decrease the yield of furfural more efficiently. Alkali metal salt catalysts have a limited function in furfural production, and combining alkali metal salts with acid catalysts in DES improves furfural production.

3.2.4 Solid Acid Catalysts
To avoid the potential corrosiveness and high energy cost of homogeneous catalysis (Li Y.-Y. et al., 2021), many solid acids have been used in furfural production which provides high furfural yields. A new heterogeneous catalyst B: LA-SG (SiO₂) was prepared by immobilizing the deep eutectic solvent betaine/lactate on silica using the original tetraethyl silicate as the silica source by the sol-gel method. High furfural yields (45.3%) were obtained from corn cobs using the B: LA-SG (SiO₂) catalyst (2.5 wt%) in water at 170°C for 0.5 h (**Table 5**, entry 2) (Li et al.,

FIGURE 4 | The catalytic mechanism for catalyzing corn stover into furfural and byproducts at 170°C for 0.5 h in ChCl: EG–water (20:80, v: v). Reprinted from ref. (Ji et al., 2021). Copyright 2021 Elsevier Ltd.

2022). However, the catalyst did not have an excellent catalytic performance in the production of furfural, owing to a lack of acidic sites in the catalyst. Lewis and Brønsted acid sites can isomerize aldose-ketose and accelerate furfural formation via ring dehydration (Li et al., 2022). Li et al. creatively used spent shrimp shells as a starting material to prepare sulfonated tin-based solid acids (Sn-SS) for the conversion of sugarcane bagasse (SB) to furfural in DES (ChCl/EG)-water at 170°C for 20 min, yielding 62.3% furfural (**Table 5**, entry 4) (Li et al., 2021a). The hydrogen bonds in SB were broken by ChCl/EG, and the Sn-SS solid acid could pretreat and depolymerize SB. Sn-SS contains Lewis and Brønsted acid sites, which can catalyze biomass into furfural. Unlike the previous study, Ji et al. directly used maize stover (CS) as a support to prepare the SO_4^{2-}/SnO_2-CS catalysts for the production of furfural in ChCl: EG-water (20:80, v: v) at 170°C for 0.5 h, and a high furfural yield of up to 61.8% (**Table 5**, entry 5) was obtained (Ji et al., 2021). Compared with some traditional metal-based solid acids, biomass-based solid acids have the advantages of being less expensive, unique in structure, environmentally friendly, and easy preparation. The spongy and squishy shape of CS allows it to immobilize additional functional groups on its surface or inside it (Jiang et al., 2020). During the synthesis of furfural, chlorides can stabilize the transition state and intermediate structures, and reduce the occurrence of undesired side reactions (**Figure 4**) (Campos Molina et al., 2012; Ji et al., 2021). For instance, $MgCl_2$ was added to the reaction system to improve the furfural yield up to 68.2% (**Table 5**, entry 6) (Ji et al., 2021). Both research groups use waste biomass as a source of catalysts, which is in keeping with the concept of sustainable and green chemistry. Solid catalysts, on the other hand, have difficulty recovering due to the higher viscosity of DES or insoluble by-products such as humins compounds clinging to them. Solid acid catalysts can flexibly tune the number of acidic sites to efficiently boost furfural yield,

but the fabrication procedure is complicated and the catalyst stability is not very good, posing an economic barrier for practical application on a large scale. Reactions incorporating solid catalysts often require high energy, and most DES are thermally unstable and do not function optimally at high temperatures. Future research will focus on the development of novel highly efficient solid acid catalysts that are both inexpensive, robust, and facile to prepare, as well as deep eutectic solvents with improved thermal stability.

3.2.5 Other Catalysts

Other additions, such as oxides, organic acids, and heterogeneous catalysts, can boost furfural yields in addition to the foregoing catalysts. The addition of HCOOH has been shown to give a high furfural yield (58.3%) from biomass-derived xylose in the ChCl: Gly-water system within 30 min at 180°C (**Table 5**, entry 7), compared to the reaction system without the addition of catalyst (Li et al., 2021b). The simplest organic acid, HCOOH, can be employed as a dehydration catalyst in the production of furfural, overcoming the main disadvantage of corrosive inorganic acid catalysts to some extent. The addition of oxides can also improve the furfural yield, Viviane et al. mixed ChCl/OA, sulfolane, substrate, TiO_2, and water to catalyze lignocellulosic materials and obtained the greatest yield of 53.2% for HMF + furfural (**Table 5**, entry 8) (da Silva Lacerda et al., 2015).

4 CONCLUSION AND PERSPECTIVE

This review summarizes the most recent progress on the conversion of biomass to furfural using various catalysts in DES systems. Unlike previous aqueous and organic systems, which required high temperatures and had low furfural yields, the DES/biphasic systems (DES/organic solvent) can achieve high

furfural yield at lower temperatures and avoid the formation of humins by subsequent side reactions due to high furfural concentration. The ability to create furans at higher substrate concentrations and superior lignocellulose separation are two advantages of deep eutectic solvents. The addition of an appropriate catalyst promotes the dehydration of xylose/xylan into furfural with higher yields. At present, the manufacture of high-yield furfural utilizing a deep eutectic solvent is still in its initial stages of development, with numerous challenges and innovation constraints.

(1) When employing an organic phase and a deep eutectic solvent for a biphasic system, large yields can only be achieved in the laboratory, but it is very difficult for industrial applications. The extraction efficiency of organic solvents is high, but recovery requires energy-intensive devices and most organic solvents are toxic.

(2) It is necessary and cumbersome to firstly transform hemicellulose of lignocellulose into xylan with high yields because lignocellulose has recalcitrant in order to obtain high furfural yield, which results in the loss of some hemicellulose.

(3) Recycling deep eutectic solvents is a more energy-efficient and environmentally benign solution from the standpoint of sustainable development. On the other hand, deep eutectic solvents are polluted and cannot be reused due to their high viscosity and the fact that a portion of the catalyst will stay in DES.

(4) Some deep eutectic solvents have poor thermal stability, while some solid catalysts (e.g., Nb_2O_5) can only function at higher temperatures, resulting in a suboptimal reaction.

Recently, it has been discovered that there exists hydrophobic DES, which can extract furfural from water efficiently and can replace the role of organic solvent in the DES/biphasic system, thus alleviating the high energy consumption due to organic solvent. It is urgent to develop novel deep eutectic solvents and to explore a sustainable and more cost-effective biorefinery method for producing furfural from lignocellulosic biomass.

AUTHOR CONTRIBUTIONS

XZ: Conceptualization, formal analysis, investigation, resources, writing original draft, visualization. PZ: Writing review and editing. QL: Investigation, formal analysis. HX: Writing review and editing, funding acquisition.

SUPPLEMENTARY MATERIAL

REFERENCES

Abbott, A. P., Boothby, D., Capper, G., Davies, D. L., and Rasheed, R. K. (2004). Deep Eutectic Solvents Formed between Choline Chloride and Carboxylic Acids: Versatile Alternatives to Ionic Liquids. *J. Am. Chem. Soc.* 126 (29), 9142–9147. doi:10.1021/ja048266j

Abbott, A. P., Capper, G., Davies, D. L., McKenzie, K. J., and Obi, S. U. (2006). Solubility of Metal Oxides in Deep Eutectic Solvents Based on Choline Chloride. *J. Chem. Eng. Data* 51 (4), 1280–1282. doi:10.1021/je060038c

Abbott, A. P., Capper, G., Davies, D. L., Munro, H. L., Rasheed, R. K., and Tambyrajah, V. (2001). Preparation of Novel, Moisture-Stable, Lewis-acidic Ionic Liquids Containing Quaternary Ammonium Salts with Functional Side Chains. *Chem. Commun.* 19, 2010–2011. doi:10.1039/b106357j

Abbott, A. P., Capper, G., Davies, D. L., Rasheed, R. K., and Shikotra, P. (2005). Selective Extraction of Metals from Mixed Oxide Matrixes Using Choline-Based Ionic Liquids. *Inorg. Chem.* 44 (19), 6497–6499. doi:10.1021/ic0505450

Abbott, A. P., Capper, G., Davies, D. L., Rasheed, R. K., and Tambyrajah, V. (2003). Novel Solvent Properties of Choline Chloride/urea mixturesElectronic Supplementary Information (ESI) Available: Spectroscopic Data. See http://www.rsc.Org/suppdata/cc/b2/b210714g/. *Chem. Commun.* 1, 70–71. doi:10.1039/b210714g

Abbott, A. P., Capper, G., McKenzie, K. J., and Ryder, K. S. (2007). Electrodeposition of Zinc-Tin Alloys from Deep Eutectic Solvents Based on Choline Chloride. *J. Electroanal. Chem.* 599 (2), 288–294. doi:10.1016/j.jelechem.2006.04.024

Abranches, D. O., Martins, M. A. R., Silva, L. P., Schaeffer, N., Pinho, S. P., and Coutinho, J. A. P. (2019). Phenolic Hydrogen Bond Donors in the Formation of Non-ionic Deep Eutectic Solvents: the Quest for Type V DES. *Chem. Commun.* 55 (69), 10253–10256. doi:10.1039/c9cc04846d

Arora, S., Gupta, N., and Singh, V. (2021). pH-Controlled Efficient Conversion of Hemicellulose to Furfural Using Choline-Based Deep Eutectic Solvents as Catalysts. *ChemSusChem* 14 (18), 3953–3958. doi:10.1002/cssc.202101130

Binder, J. B., Blank, J. J., Cefali, A. V., and Raines, R. T. (2010). Synthesis of Furfural from Xylose and Xylan. *ChemSusChem* 3 (11), 1268–1272. doi:10.1002/cssc.201000181

Bodachivskyi, I., Kuzhiumparambil, U., and Williams, D. B. G. (2019). Catalytic Valorization of Native Biomass in a Deep Eutectic Solvent: A Systematic Approach toward High-Yielding Reactions of Polysaccharides. *ACS Sustain. Chem. Eng.* 8 (1), 678–685. doi:10.1021/acssuschemeng.9b06528

Bozell, J. J., and Petersen, G. R. (2010). Technology Development for the Production of Biobased Products from Biorefinery Carbohydrates-The US Department of Energy's "Top 10" Revisited. *Green Chem.* 12 (4), 539. doi:10.1039/b922014c

Brandt, A., Gräsvik, J., Hallett, J. P., and Welton, T. (2013). Deconstruction of Lignocellulosic Biomass with Ionic Liquids. *Green Chem.* 15 (3), 550. doi:10.1039/c2gc36364j

Cai, C. M., Zhang, T., Kumar, R., and Wyman, C. E. (2014). Integrated Furfural Production as a Renewable Fuel and Chemical Platform from Lignocellulosic Biomass. *J. Chem. Technol. Biotechnol.* 89 (1), 2–10. doi:10.1002/jctb.4168

Cai, T., and Qiu, H. (2019). Application of Deep Eutectic Solvents in Chromatography: A Review. *TrAC Trends Anal. Chem.* 120, 115623. doi:10.1016/j.trac.2019.115623

Campos Molina, M. J., Mariscal, R., Ojeda, M., and López Granados, M. (2012). Cyclopentyl Methyl Ether: a Green Co-solvent for the Selective Dehydration of Lignocellulosic Pentoses to Furfural. *Bioresour. Technol.* 126, 321–327. doi:10.1016/j.biortech.2012.09.049

Carrozza, C. F., Papa, G., Citterio, A., Sebastiano, R., Simmons, B. A., and Singh, S. (2019). One-pot Bio-Derived Ionic Liquid Conversion Followed by Hydrogenolysis Reaction for Biomass Valorization: A Promising Approach Affecting the Morphology and Quality of Lignin of Switchgrass and Poplar. *Bioresour. Technol.* 294, 122214. doi:10.1016/j.biortech.2019.122214

Chen, Y.-L., Zhang, X., You, T.-T., and Xu, F. (2018a). Deep Eutectic Solvents (DESs) for Cellulose Dissolution: a Mini-Review. *Cellulose* 26 (1), 205–213. doi:10.1007/s10570-018-2130-7

Chen, Z., Bai, X., and A, C. (2018b). High-Solid Lignocellulose Processing Enabled by Natural Deep Eutectic Solvent for Lignin Extraction and Industrially Relevant Production of Renewable Chemicals. *ACS Sustain. Chem. Eng.* 6 (9), 12205–12216. doi:10.1021/acssuschemeng.8b02541

Chen, Z., Reznicek, W. D., and Wan, C. (2018c). Aqueous Choline Chloride: A Novel Solvent for Switchgrass Fractionation and Subsequent Hemicellulose

Conversion into Furfural. *ACS Sustain. Chem. Eng.* 6 (5), 6910–6919. doi:10.1021/acssuschemeng.8b00728

Chen, Z., and Wan, C. (2019). A Novel Deep Eutectic Solvent/acetone Biphasic System for High-Yield Furfural Production. *Bioresour. Technol. Rep.* 8, 100318. doi:10.1016/j.biteb.2019.100318

Choudhary, V., Sandler, S. I., and Vlachos, D. G. (2012). Conversion of Xylose to Furfural Using Lewis and Brønsted Acid Catalysts in Aqueous Media. *ACS Catal.* 2 (9), 2022–2028. doi:10.1021/cs300265d

Cunha, S. C., and Fernandes, J. O. (2018). Extraction Techniques with Deep Eutectic Solvents. *TrAC Trends Anal. Chem.* 105, 225–239. doi:10.1016/j.trac.2018.05.001

da Silva Lacerda, V., López-Sotelo, J. B., Correa-Guimarães, A., Hernández-Navarro, S., Sánchez-Bascones, M., Navas-Gracia, L. M., et al. (2015). A Kinetic Study on Microwave-Assisted Conversion of Cellulose and Lignocellulosic Waste into Hydroxymethylfurfural/furfural. *Bioresour. Technol.* 180, 88–96. doi:10.1016/j.biortech.2014.12.089

Dai, Y., van Spronsen, J., Witkamp, G.-J., Verpoorte, R., and Choi, Y. H. (2013). Natural Deep Eutectic Solvents as New Potential Media for Green Technology. *Anal. Chim. Acta* 766, 61–68. doi:10.1016/j.aca.2012.12.019

Dai, Y., Witkamp, G.-J., Verpoorte, R., and Choi, Y. H. (2015). Tailoring Properties of Natural Deep Eutectic Solvents with Water to Facilitate Their Applications. *Food Chem.* 187, 14–19. doi:10.1016/j.foodchem.2015.03.123

Delbecq, F., Wang, Y., Muralidhara, A., El Ouardi, K., Marlair, G., and Len, C. (2018). Hydrolysis of Hemicellulose and Derivatives-A Review of Recent Advances in the Production of Furfural. *Front. Chem.* 6, 146. doi:10.3389/fchem.2018.00146

Delgado-Mellado, N., Larriba, M., Navarro, P., Rigual, V., Ayuso, M., García, J., et al. (2018). Thermal Stability of Choline Chloride Deep Eutectic Solvents by TGA/FTIR-ATR Analysis. *J. Mol. Liq.* 260, 37–43. doi:10.1016/j.molliq.2018.03.076

Enslow, K. R., and Bell, A. T. (2012). The Kinetics of Brønsted Acid-Catalyzed Hydrolysis of Hemicellulose Dissolved in 1-Ethyl-3-Methylimidazolium Chloride. *RSC Adv.* 2 (26), 10028. doi:10.1039/c2ra21650g

Enslow, K. R., and Bell, A. T. (2015). The Role of Metal Halides in Enhancing the Dehydration of Xylose to Furfural. *ChemCatChem* 7 (3), 479–489. doi:10.1002/cctc.201402842

Fan, G., Wang, Y., Hu, Z., Yan, J., Li, J., and Song, G. (2018). Synthesis of 5-hydroxymethyl Furfural from Cellulose via a Two-step Process in Polar Aprotic Solvent. *Carbohydr. Polym.* 200, 529–535. doi:10.1016/j.carbpol.2018.08.043

Florindo, C., Oliveira, F. S., Rebelo, L. P. N., Fernandes, A. M., and Marrucho, I. M. (2014). Insights into the Synthesis and Properties of Deep Eutectic Solvents Based on Cholinium Chloride and Carboxylic Acids. *ACS Sustain. Chem. Eng.* 2 (10), 2416–2425. doi:10.1021/sc500439w

Francisco, M., van den Bruinhorst, A., and Kroon, M. C. (2012). New Natural and Renewable Low Transition Temperature Mixtures (LTTMs): Screening as Solvents for Lignocellulosic Biomass Processing. *Green Chem.* 14 (8), 2153. doi:10.1039/c2gc35660k

Francisco, M., van den Bruinhorst, A., and Kroon, M. C. (2013). Low-transition-temperature Mixtures (LTTMs): a New Generation of Designer Solvents. *Angew. Chem. Int. Ed.* 52 (11), 3074–3085. doi:10.1002/anie.201207548

Gabriele, F., Chiarini, M., Germani, R., Tiecco, M., and Spreti, N. (2019). Effect of Water Addition on Choline Chloride/glycol Deep Eutectic Solvents: Characterization of Their Structural and Physicochemical Properties. *J. Mol. Liq.* 291, 111301. doi:10.1016/j.molliq.2019.111301

Grabber, J. H., Hatfield, R. D., and Ralph, J. (1998). Diferulate Cross-Links Impede the Enzymatic Degradation of Non-lignified Maize Walls. *J. Sci. Food Agric.* 77 (2), 193–200. doi:10.1002/(sici)1097-0010(199806)77:2<193::aid-jsfa25>3.0.co;2-a

Gravitis, J., Vedernikov, N., Zandersons, J., and Kokorevics, A. (2001). Furfural and Levoglucosan Production from Deciduous Wood and Agricultural Wastes. *Chem. Mater. Renew. Resour.*, 110–122. doi:10.1021/bk-2001-0784.ch009

Gutiérrez, M. C., Ferrer, M. L., Mateo, C. R., and del Monte, F. (2009). Freeze-drying of Aqueous Solutions of Deep Eutectic Solvents: a Suitable Approach to Deep Eutectic Suspensions of Self-Assembled Structures. *Langmuir* 25 (10), 5509–5515. doi:10.1021/la900552b

Hammond, O. S., Bowron, D. T., and Edler, K. J. (2016). Liquid Structure of the Choline Chloride-Urea Deep Eutectic Solvent (Reline) from Neutron Diffraction and Atomistic Modelling. *Green Chem.* 18 (9), 2736–2744. doi:10.1039/c5gc02914g

Hammond, O. S., Bowron, D. T., and Edler, K. J. (2017). The Effect of Water upon Deep Eutectic Solvent Nanostructure: An Unusual Transition from Ionic Mixture to Aqueous Solution. *Angew. Chem. Int. Ed.* 56 (33), 9782–9785. doi:10.1002/anie.201702486

Hansen, B. B., Spittle, S., Chen, B., Poe, D., Zhang, Y., Klein, J. M., et al. (2021). Deep Eutectic Solvents: A Review of Fundamentals and Applications. *Chem. Rev.* 121 (3), 1232–1285. doi:10.1021/acs.chemrev.0c00385

Hashemi, B., Zohrabi, P., and Dehdashtian, S. (2018). Application of Green Solvents as Sorbent Modifiers in Sorptive-Based Extraction Techniques for Extraction of Environmental Pollutants. *TrAC Trends Anal. Chem.* 109, 50–61. doi:10.1016/j.trac.2018.09.026

Himmel, M. E., Ding, S.-Y., Johnson, D. K., Adney, W. S., Nimlos, M. R., Brady, J. W., et al. (2007). Biomass Recalcitrance: Engineering Plants and Enzymes for Biofuels Production. *Science* 315 (5813), 804–807. doi:10.1126/science.1137016

Jablonský, M., Škulcová, A., Kamenská, L., Vrška, M., and Šíma, J. (2015). Deep Eutectic Solvents: Fractionation of Wheat Straw. *BioResources* 10 (4), 8047. doi:10.15376/biores.10.4.8039-8047

Ji, L., Tang, Z., Yang, D., Ma, C., and He, Y.-C. (2021). Improved One-Pot Synthesis of Furfural from Corn Stalk with Heterogeneous Catalysis Using Corn Stalk as Biobased Carrier in Deep Eutectic Solvent-Water System. *Bioresour. Technol.* 340, 125691. doi:10.1016/j.biortech.2021.125691

Jiang, Q., Yang, G., Kong, F., Fatehi, P., and Wang, X. (2020). High Acid Biochar-Based Solid Acid Catalyst from Corn Stalk for Lignin Hydrothermal Degradation. *Polymers* 12 (7), 1623. doi:10.3390/polym12071623

Kore, R., and Srivastava, R. (2011). Synthesis and Applications of Novel Imidazole and Benzimidazole Based Sulfonic Acid Group Functionalized Brönsted Acidic Ionic Liquid Catalysts. *J. Mol. Catal. A Chem.* 345 (1-2), 117–126. doi:10.1016/j.molcata.2011.06.003

Lee, C. B. T. L., and Wu, T. Y. (2021). A Review on Solvent Systems for Furfural Production from Lignocellulosic Biomass. *Renew. Sustain. Energy Rev.* 137, 110172. doi:10.1016/j.rser.2020.110172

Lee, C. B. T. L., Wu, T. Y., Cheng, C. K., Siow, L. F., and Chew, I. M. L. (2021). Nonsevere Furfural Production Using Ultrasonicated Oil Palm Fronds and Aqueous Choline Chloride-Oxalic Acid. *Industrial Crops Prod.* 166, 113397. doi:10.1016/j.indcrop.2021.113397

Lee, C. B. T. L., Wu, T. Y., Ting, C. H., Tan, J. K., Siow, L. F., Cheng, C. K., et al. (2019). One-pot Furfural Production Using Choline Chloride-Dicarboxylic Acid Based Deep Eutectic Solvents under Mild Conditions. *Bioresour. Technol.* 278, 486–489. doi:10.1016/j.biortech.2018.12.034

Li, C., Li, D., Zou, S., Li, Z., Yin, J., Wang, A., et al. (2013). Extraction Desulfurization Process of Fuels with Ammonium-Based Deep Eutectic Solvents. *Green Chem.* 15 (10), 2793. doi:10.1039/c3gc41067f

Li, H., Dai, Q., Ren, J., Jian, L., Peng, F., Sun, R., et al. (2016). Effect of Structural Characteristics of Corncob Hemicelluloses Fractionated by Graded Ethanol Precipitation on Furfural Production. *Carbohydr. Polym.* 136, 203–209. doi:10.1016/j.carbpol.2015.09.045

Li, Q., Di, J., Liao, X., Ni, J., Li, Q., He, Y.-C., et al. (2021a). Exploration of Benign Deep Eutectic Solvent-Water Systems for the Highly Efficient Production of Furfurylamine from Sugarcane Bagasse via Chemoenzymatic Cascade Catalysis. *Green Chem.* 23 (20), 8154–8168. doi:10.1039/d1gc03010h

Li, Q., Ma, C., Di, J., Ni, J., and He, Y.-C. (2022). Catalytic Valorization of Biomass for Furfuryl Alcohol by Novel Deep Eutectic Solvent-Silica Chemocatalyst and Newly Constructed Reductase Biocatalyst. *Bioresour. Technol.* 347, 126376. doi:10.1016/j.biortech.2021.126376

Li, Q., Ren, J.-Q., Li, Q., Di, J.-H., Ma, C., and He, Y. (2021b). Sustainable Conversion of Biomass-Derived D-Xylose to Furfuryl Alcohol in a Deep Eutectic Solvent-Water System. *ACS Sustain. Chem. Eng.* 9 (30), 10299–10308. doi:10.1021/acssuschemeng.1c02965

Li, X., Hou, M., Han, B., Wang, X., and Zou, L. (2008). Solubility of CO2 in a Choline Chloride + Urea Eutectic Mixture. *J. Chem. Eng. Data* 53 (2), 548–550. doi:10.1021/je700638u

Li, X., Yang, J., Xu, R., Lu, L., Kong, F., Liang, M., et al. (2019). Kinetic Study of Furfural Production from Eucalyptus Sawdust Using H-SAPO-34 as Solid Brønsted Acid and Lewis Acid Catalysts in Biomass-Derived Solvents. *Industrial Crops Prod.* 135, 196–205. doi:10.1016/j.indcrop.2019.04.047

Li, Y.-Y., Li, Q., Zhang, P.-Q., Ma, C.-L., Xu, J.-H., and He, Y.-C. (2021c). Catalytic Conversion of Corncob to Furfuryl Alcohol in Tandem Reaction with Tin-Loaded Sulfonated Zeolite and NADPH-dependent Reductase Biocatalyst. *Bioresour. Technol.* 320 (Pt A), 124267. doi:10.1016/j.biortech.2020.124267

Liu, Q., Yuan, T., Fu, Q.-j., Bai, Y.-y., Peng, F., and Yao, C.-l. (2019). Choline Chloride-Lactic Acid Deep Eutectic Solvent for Delignification and Nanocellulose Production of Moso Bamboo. *Cellulose* 26 (18), 9447–9462. doi:10.1007/s10570-019-02726-0

Liu, Y., Chen, W., Xia, Q., Guo, B., Wang, Q., Liu, S., et al. (2017). Efficient Cleavage of Lignin-Carbohydrate Complexes and Ultrafast Extraction of Lignin Oligomers from Wood Biomass by Microwave-Assisted Treatment with Deep Eutectic Solvent. *ChemSusChem* 10 (8), 1692–1700. doi:10.1002/cssc.201601795

Loow, Y.-L., Wu, T. Y., Lim, Y. S., Tan, K. A., Siow, L. F., Md. Jahim, J. J., et al. (2017). Improvement of Xylose Recovery from the Stalks of Oil Palm Fronds Using Inorganic Salt and Oxidative Agent. *Energy Convers. Manag.* 138, 248–260. doi:10.1016/j.enconman.2016.12.015

Luo, Y., Li, Z., Li, X., Liu, X., Fan, J., Clark, J. H., et al. (2019). The Production of Furfural Directly from Hemicellulose in Lignocellulosic Biomass: A Review. *Catal. Today* 319, 14–24. doi:10.1016/j.cattod.2018.06.042

Lynam, J. G., Kumar, N., and Wong, M. J. (2017). Deep Eutectic Solvents' Ability to Solubilize Lignin, Cellulose, and Hemicellulose; Thermal Stability; and Density. *Bioresour. Technol.* 238, 684–689. doi:10.1016/j.biortech.2017.04.079

Marcotullio, G., and De Jong, W. (2010). Chloride Ions Enhance Furfural Formation from D-Xylose in Dilute Aqueous Acidic Solutions. *Green Chem.* 12 (10), 1739. doi:10.1039/b927424c

Marcotullio, G., and de Jong, W. (2011). Furfural Formation from D-Xylose: the Use of Different Halides in Dilute Aqueous Acidic Solutions Allows for Exceptionally High Yields. *Carbohydr. Res.* 346 (11), 1291–1293. doi:10.1016/j.carres.2011.04.036

Mbous, Y. P., Hayyan, M., Hayyan, A., Wong, W. F., Hashim, M. A., and Looi, C. Y. (2017). Applications of Deep Eutectic Solvents in Biotechnology and Bioengineering-Promises and Challenges. *Biotechnol. Adv.* 35 (2), 105–134. doi:10.1016/j.biotechadv.2016.11.006

McCann, M. C., and Carpita, N. C. (2015). Biomass Recalcitrance: a Multi-Scale, Multi-Factor, and Conversion-specific Property: Fig. 1. *Exbotj* 66 (14), 4109–4118. doi:10.1093/jxb/erv267

Mellmer, M. A., Sanpitakseree, C., Demir, B., Ma, K., Elliott, W. A., Bai, P., et al. (2019). Effects of Chloride Ions in Acid-Catalyzed Biomass Dehydration Reactions in Polar Aprotic Solvents. *Nat. Commun.* 10 (1), 1132. doi:10.1038/s41467-019-09090-4

Mettler, M. S., Vlachos, D. G., and Dauenhauer, P. J. (2012). Top Ten Fundamental Challenges of Biomass Pyrolysis for Biofuels. *Energy Environ. Sci.* 5 (7), 7797. doi:10.1039/c2ee21679e

Mittal, A., Black, S. K., Vinzant, T. B., O'Brien, M., Tucker, M. P., and Johnson, D. K. (2017). Production of Furfural from Process-Relevant Biomass-Derived Pentoses in a Biphasic Reaction System. *ACS Sustain. Chem. Eng.* 5 (7), 5694–5701. doi:10.1021/acssuschemeng.7b00215

Mohd Zaid, H. F., Chong, F. K., and Abdul Mutalib, M. I. (2017). Extractive Deep Desulfurization of Diesel Using Choline Chloride-Glycerol Eutectic-Based Ionic Liquid as a Green Solvent. *Fuel* 192, 10–17. doi:10.1016/j.fuel.2016.11.112

Morais, E. S., Freire, M. G., Freire, C. S. R., Coutinho, J. A. P., and Silvestre, A. J. D. (2020). Enhanced Conversion of Xylan into Furfural Using Acidic Deep Eutectic Solvents with Dual Solvent and Catalyst Behavior. *ChemSusChem* 13 (4), 784–790. doi:10.1002/cssc.201902848

Morais, E. S., Freire, M. G., Freire, C. S. R., and Silvestre, A. J. D. (2021). Enhanced Furfural Production in Deep Eutectic Solvents Comprising Alkali Metal Halides as Additives. *Molecules* 26 (23), 7374. doi:10.3390/molecules26237374

Morrison, H. G., Sun, C. C., and Neervannan, S. (2009). Characterization of Thermal Behavior of Deep Eutectic Solvents and Their Potential as Drug Solubilization Vehicles. *Int. J. Pharm.* 378 (1-2), 136–139. doi:10.1016/j.ijpharm.2009.05.039

New, E. K., Wu, T. Y., Tien Loong Lee, C. B., Poon, Z. Y., Loow, Y.-L., Wei Foo, L. Y., et al. (2019). Potential Use of Pure and Diluted Choline Chloride-Based Deep Eutectic Solvent in Delignification of Oil Palm Fronds. *Process Saf. Environ. Prot.* 123, 190–198. doi:10.1016/j.psep.2018.11.015

Pandey, A., BhawnaDhingra, D., Dhingra, D., and Pandey, S. (2017). Hydrogen Bond Donor/Acceptor Cosolvent-Modified Choline Chloride-Based Deep

Eutectic Solvents. *J. Phys. Chem. B* 121 (16), 4202–4212. doi:10.1021/acs.jpcb.7b01724

Parsell, T., Yohe, S., Degenstein, J., Jarrell, T., Klein, I., Gencer, E., et al. (2015). A Synergistic Biorefinery Based on Catalytic Conversion of Lignin Prior to Cellulose Starting from Lignocellulosic Biomass. *Green Chem.* 17 (3), 1492–1499. doi:10.1039/c4gc01911c

Peleteiro, S., Santos, V., Garrote, G., and Parajó, J. C. (2016). Furfural Production from Eucalyptus Wood Using an Acidic Ionic Liquid. *Carbohydr. Polym.* 146, 20–25. doi:10.1016/j.carbpol.2016.03.049

Perkins, S. L., Painter, P., and Colina, C. M. (2014). Experimental and Computational Studies of Choline Chloride-Based Deep Eutectic Solvents. *J. Chem. Eng. Data* 59 (11), 3652–3662. doi:10.1021/je500520h

Qin, H., Hu, X., Wang, J., Cheng, H., Chen, L., and Qi, Z. (2020). Overview of Acidic Deep Eutectic Solvents on Synthesis, Properties and Applications. *Green Energy & Environ.* 5 (1), 8–21. doi:10.1016/j.gee.2019.03.002

Ramesh, R., Nair, A., Jayavel, A., Sathiasivan, K., Rajesh, M., Ramaswamy, S., et al. (2020). Choline Chloride-Based Deep Eutectic Solvents for Efficient Delignification of Bambusa Bambos in Bio-Refinery Applications. *Chem. Pap.* 74 (12), 4533–4545. doi:10.1007/s11696-020-01259-2

Romo, J. E., Bollar, N. V., Zimmermann, C. J., and Wettstein, S. G. (2018). Conversion of Sugars and Biomass to Furans Using Heterogeneous Catalysts in Biphasic Solvent Systems. *ChemCatChem* 10 (21), 4805–4816. doi:10.1002/cctc.201800926

Rusanen, A., Lappalainen, K., Kärkkäinen, J., and Lassi, U. (2021). Furfural and 5-Hydroxymethylfurfural Production from Sugar Mixture Using Deep Eutectic Solvent/MIBK System. *ChemistryOpen* 10 (10), 1004–1012. doi:10.1002/open.202100163

Satlewal, A., Agrawal, R., Bhagia, S., Sangoro, J., and Ragauskas, A. J. (2018). Natural Deep Eutectic Solvents for Lignocellulosic Biomass Pretreatment: Recent Developments, Challenges and Novel Opportunities. *Biotechnol. Adv.* 36 (8), 2032–2050. doi:10.1016/j.biotechadv.2018.08.009

Shen, X.-J., Wen, J.-L., Mei, Q.-Q., Chen, X., Sun, D., Yuan, T.-Q., et al. (2019). Facile Fractionation of Lignocelluloses by Biomass-Derived Deep Eutectic Solvent (DES) Pretreatment for Cellulose Enzymatic Hydrolysis and Lignin Valorization. *Green Chem.* 21 (2), 275–283. doi:10.1039/c8gc03064b

Smith, E. L., Abbott, A. P., and Ryder, K. S. (2014). Deep Eutectic Solvents (DESs) and Their Applications. *Chem. Rev.* 114 (21), 11060–11082. doi:10.1021/cr300162p

Somerville, C., Youngs, H., Taylor, C., Davis, S. C., and Long, S. P. (2010). Feedstocks for Lignocellulosic Biofuels. *Science* 329 (5993), 790–792. doi:10.1126/science.1189268

Song, S., Di, L., Wu, G., Dai, W., Guan, N., and Li, L. (2017). Meso-Zr-Al-beta Zeolite as a Robust Catalyst for Cascade Reactions in Biomass Valorization. *Appl. Catal. B Environ.* 205, 393–403. doi:10.1016/j.apcatb.2016.12.056

Song, S., Fung Kin Yuen, V., Di, L., Sun, Q., Zhou, K., and Yan, N. (2020). Integrating Biomass into the Organonitrogen Chemical Supply Chain: Production of Pyrrole and D -Proline from Furfural. *Angew. Chem. Int. Ed.* 59 (45), 19846–19850. doi:10.1002/anie.202006315

van Osch, D. J. G. P., Dietz, C. H. J. T., van Spronsen, J., Kroon, M. C., Gallucci, F., van Sint Annaland, M., et al. (2019). A Search for Natural Hydrophobic Deep Eutectic Solvents Based on Natural Components. *ACS Sustain. Chem. Eng.* 7 (3), 2933–2942. doi:10.1021/acssuschemeng.8b03520

Vigier, K. D. O., Chatel, G., and Jérôme, F. (2015). Contribution of Deep Eutectic Solvents for Biomass Processing: Opportunities, Challenges, and Limitations. *ChemCatChem* 7 (8), 1250–1260. doi:10.1002/cctc.201500134

vom Stein, T., Grande, P. M., Leitner, W., and Domínguez de María, P. (2011). Iron-catalyzed Furfural Production in Biobased Biphasic Systems: from Pure Sugars to Direct Use of Crude Xylose Effluents as Feedstock. *ChemSusChem* 4 (11), 1592–1594. doi:10.1002/cssc.201100259

Wagle, D. V., Adhikari, L., and Baker, G. A. (2017). Computational Perspectives on Structure, Dynamics, Gas Sorption, and Bio-Interactions in Deep Eutectic Solvents. *Fluid Phase Equilibria* 448, 50–58. doi:10.1016/j.fluid.2017.04.018

Wang, S., Zhao, Y., Lin, H., Chen, J., Zhu, L., and Luo, Z. (2017). Conversion of C5 Carbohydrates into Furfural Catalyzed by a Lewis Acidic Ionic Liquid in Renewable γ-valerolactone. *Green Chem.* 19 (16), 3869–3879. doi:10.1039/c7gc01298e

Wang, W., Ren, J., Li, H., Deng, A., and Sun, R. (2015). Direct Transformation of Xylan-type Hemicelluloses to Furfural via SnCl4 Catalysts in Aqueous and

Biphasic Systems. *Bioresour. Technol.* 183, 188–194. doi:10.1016/j.biortech.2015.02.068

Wang, Y., Fan, C., Hu, H., Li, Y., Sun, D., Wang, Y., et al. (2016). Genetic Modification of Plant Cell Walls to Enhance Biomass Yield and Biofuel Production in Bioenergy Crops. *Biotechnol. Adv.* 34 (5), 997–1017. doi:10.1016/j.biotechadv.2016.06.001

Wang, Z.-K., Shen, X.-J., Chen, J.-J., Jiang, Y.-Q., Hu, Z.-Y., Wang, X., et al. (2018). Lignocellulose Fractionation into Furfural and Glucose by AlCl3-Catalyzed DES/MIBK Biphasic Pretreatment. *Int. J. Biol. Macromol.* 117, 721–726. doi:10.1016/j.ijbiomac.2018.05.232

Wu, C., Yuan, W., Huang, Y., Xia, Y., Yang, H., Wang, H., et al. (2017). Conversion of Xylose into Furfural Catalyzed by Bifunctional Acidic Ionic Liquid Immobilized on the Surface of Magnetic γ-Al2O3. *Catal. Lett.* 147 (4), 953–963. doi:10.1007/s10562-017-1982-z

Xu, G.-C., Ding, J.-C., Han, R.-Z., Dong, J.-J., and Ni, Y. (2016). Enhancing Cellulose Accessibility of Corn Stover by Deep Eutectic Solvent Pretreatment for Butanol Fermentation. *Bioresour. Technol.* 203, 364–369. doi:10.1016/j.biortech.2015.11.002

Yang, D., Zhang, S., Sun, X.-g., Jiang, D.-e., and Dai, S. (2019). Deep Eutectic Solvents Formed by Quaternary Ammonium Salts and Aprotic Organic Compound Succinonitrile. *J. Mol. Liq.* 274, 414–417. doi:10.1016/j.molliq.2018.10.150

Yang, Y., Hu, C.-W., and Abu-Omar, M. M. (2012). Synthesis of Furfural from Xylose, Xylan, and Biomass Using AlCl3·6 H2O in Biphasic Media via Xylose Isomerization to Xylulose. *ChemSusChem* 5 (2), 405–410. doi:10.1002/cssc.201100688

Yiin, C. L., Quitain, A. T., Yusup, S., Uemura, Y., Sasaki, M., and Kida, T. (2017). Choline Chloride (ChCl) and Monosodium Glutamate (MSG)-based Green Solvents from Optimized Cactus Malic Acid for Biomass Delignification. *Bioresour. Technol.* 244 (Pt 1), 941–948. doi:10.1016/j.biortech.2017.08.043

Yiin, C. L., Yap, K. L., Ku, A. Z. E., Chin, B. L. F., Lock, S. S. M., Cheah, K. W., et al. (2021). Recent Advances in Green Solvents for Lignocellulosic Biomass Pretreatment: Potential of Choline Chloride (ChCl) Based Solvents. *Bioresour. Technol.* 333, 125195. doi:10.1016/j.biortech.2021.125195

Yu, Q., Bai, R., Wang, F., Zhang, Q., Sun, Y., Zhang, Y., et al. (2019a). A Sustainable System for Maleic Acid Synthesis from Biomass-derived Sugar. *J. Chem. Technol. Biotechnol.* 95 (3), 751–757. doi:10.1002/jctb.6260

Yu, Q., Song, Z., Zhuang, X., Liu, L., Qiu, W., Shi, J., et al. (2019b). Catalytic Conversion of Herbal Residue Carbohydrates to Furanic Derivatives in a Deep Eutectic Solvent Accompanied by Dissolution and Recrystallisation of Choline Chloride. *Cellulose* 26 (15), 8263–8277. doi:10.1007/s10570-019-02372-6

Zahn, S., Kirchner, B., and Mollenhauer, D. (2016). Charge Spreading in Deep Eutectic Solvents. *Chemphyschem* 17 (21), 3354–3358. doi:10.1002/cphc.201600348

Zhang, L.-X., Yu, H., Yu, H.-B., Chen, Z., and Yang, L. (2014). Conversion of Xylose and Xylan into Biorenewable Choline Chloride-Oxalic Acid Deep Eutectic Solvent with the Addition of Metal Chloride. *Chin. Chem. Lett.* 25 (8), 1132–1136. doi:10.1016/j.cclet.2014.03.029

Zhang, L., and Yu, H. (2013). Conversion of Xylan and Xylose into Furfural in Biorenewable Deep Eutectic Solvent with Trivalent Metal Chloride Added. *BioResources* 8, 6014. doi:10.15376/biores.8.4.6014-6025

Zhang, Q., De Oliveira Vigier, K., Royer, S., and Jérôme, F. (2012). Deep Eutectic Solvents: Syntheses, Properties and Applications. *Chem. Soc. Rev.* 41 (21), 7108–7146. doi:10.1039/c2cs35178a

Conflict of Interest: The authors declare that the research was conducted in the absence of any commercial or financial relationships that could be construed as a potential conflict of interest.

Publisher's Note: All claims expressed in this article are solely those of the authors and do not necessarily represent those of their affiliated organizations, or those of the publisher, the editors and the reviewers. Any product that may be evaluated in this article, or claim that may be made by its manufacturer, is not guaranteed or endorsed by the publisher.

Recent Advances in the Catalytic Hydroconversion of 5-Hydroxymethylfurfural to Valuable Diols

Zexing Huang[1], Jianhua Wang[1], Jing Lei[2], Wenguang Zhao[1], Hao Chen[2], Yongjun Yang[2]*, Qiong Xu[1] and Xianxiang Liu[1]*

[1]National and Local Joint Engineering Laboratory for New Petro-Chemical Materials and Fine Utilization of Resources, Key Laboratory of the Assembly and Application of Organic Functional Molecules of Hunan Province, Hunan Normal University, Changsha, China, [2]Chenzhou Gao Xin Material Co., Ltd., Chenzhou, China

Biomass, a globally available resource, is a promising alternative feedstock for fossil fuels, especially considering the current energy crisis and pollution. Biomass-derived diols, such as 2,5-bis(hydroxymethyl)furan, 2,5-bis(hydroxymethyl)-tetrahydrofuran, and 1,6-hexanediol, are a significant class of monomers in the polyester industry. Therefore, the catalytic conversion of biomass to valuable diols has received extensive research attention in the field of biomass conversion and is a crucial factor in determining the development of the polyester industry. 5-Hydroxymethylfurfural (HMF) is an important biomass-derived compound with a C6-furanic framework. The hydroconversion of HMF into diols has the advantages of being simple to operate, inexpensive, environmentally friendly, safe, and reliable. Therefore, in the field of diol synthesis, this method is regarded as a promising approach with significant industrialization potential. This review summarizes recent advances in diol formation, discusses the roles of catalysts in the hydroconversion process, highlights the reaction mechanisms associated with the specificities of each active center, and provides an outlook on the challenges and opportunities associated with the research on biomass-derived diol synthesis.

Keywords: biomass, 5-hydroxymethylfurfural, hydroconversion, diols, catalysis

INTRODUCTION

Non-renewable fossil resources are pivotal for economic growth, and their consumption has surged steadily in recent decades (Zhou et al., 2011; Kucherov et al., 2018). Currently, more than 85% of the global energy demand is met using fossil fuel resources (Chen et al., 2018). Considering the probable impending energy crisis, the use of renewable resources and development of sustainable energy technology have been a focus area of research in recent years (Zhu et al., 2016; Wan et al., 2021). Traditional industries emit massive amounts of CO_2 into the atmosphere, contributing to climate change and global warming (Ravishankara et al., 2015). Biomass conversion, which is a promising alternative to energy production using fossil hydrocarbons, has the potential to alleviate the energy crisis while effectively utilizing greenhouse gas emissions through completing the CO_2 cycle (Nakagawa et al., 2013; Hu et al., 2018a; Deng et al., 2021).

5-Hydroxymethylfurfural (HMF), a widely used biomass platform chemical, has C=O, C-OH, and C=C bonds, all of which promote a variety of reactions. Reducing different types of unsaturated

TABLE 1 | Catalytic performance of catalysts for the conversion of HMF.

Entry	Catalyst	Hydrogen Donor	Solvent	T (°C)	p (MPa)	t (h)	Yield (%)	Ref
1[a]	Ru/MnCo$_2$O$_4$	H$_2$	methanol	100	8.2	4.0	98.5	Mishra et al. (2020)
2[a]	Co@C	H$_2$	methanol	110	3.0	6.0	96.0	Arias et al. (2020)
3[a]	meso-Cu/Al$_2$O$_3$	H$_2$	Ethanol	70	5.0	3.5	98.6	Kim et al. (2021)
4[a]	imp-Cu/Al$_2$O$_3$	H$_2$	Ethanol	70	5.0	3.5	72.3	Kim et al. (2021)
5[a]	cp-Cu/Al$_2$O$_3$	H$_2$	Ethanol	70	5.0	3.5	93.0	Kim et al. (2021)
6[a]	Cu/Al$_2$O$_3$	H$_2$	methanol	130	3.0	1.0	92.1	Rao et al. (2021)
7[a]	Ni$_x$Co$_y$	H$_2$	THF	100	0.5	4.0	93.1	Zhao et al. (2021)
8[a]	Zr-DTPA	isopropanol	isopropanol	140	/	4.0	95.2	He et al. (2021)
9[a]	Zr-HTC	isopropanol	isopropanol	120	/	4.0	99.2	Hu et al. (2018a)
10[a]	MZCCP	isopropanol	isopropanol	140	/	2.0	93.4	Hu et al. (2019)
11[a]	ZrBa-SBA	isopropanol	isopropanol	150	/	2.5	90.6	Wei et al. (2018)
12[a]	Hf-LigS	isopropanol	isopropanol	100	/	2.0	90.0	Zhou et al. (2019)
13[a]	Zr-LigS	isopropanol	isopropanol	100	/	1.0	60.6	Zhou et al. (2019)
14[a]	CuO-Fe$_3$O$_4$/AC	Ethanol	Ethanol	150	/	5.0	92.4	Fan et al.(2019)
15[a]	ZrBa-SBA	isopropanol	isopropanol	150	/	2.5	90.6	Zhang et al. (2020)
16[b]	Ru/CeO$_x$	H$_2$	1-butanol/ water	130	2.8	12.0	89.0	Alamillo et al. (2012)
17[b]	Ru (methylallyl)2COD	H$_2$	toluene	120	1.0	16.0	87.0	Cadu et al. (2018)
18[b]	Ni-Al	H$_2$	Dioxane	60	6	6	96.2	Kong et al. (2015)
19[b]	Ni-Co-Al	H$_2$	methanol	120	4	4	89.0	Yao et al. (2016)

[a]yield to BHMF.
[b]yield to BHMTHF.

groups in HMF, various derivatives of HMF can be produced, such as 5-methylfurfural (MF) (Sun et al., 2019), 2,5-dimethylfuran (DMF) (Guo et al., 2020), 2,5-bis(hydroxymethyl)furan (BHMF) (Zhao et al., 2022), 2,5-bis(hydroxymethyl)-tetrahydrofuran (BHMTHF) (Kong et al., 2015), and 1,6-hexanediol (1,6-HD) (Yao et al., 2016). Selectivity is a crucial parameter in chemical reactions involving the major HMF derivatives utilized in a variety of industrial applications, including fuel production, polyurethane manufacturing, and polymer production (Chernyshev et al., 2017; Stadler et al., 2019; Li et al., 2021). Diol products derived from HMF have significant industrial value and development potential as key monomers for polyurethane and polyester manufacturers. Hence, the number of studies on HMF has been rapidly increasing.

Even though several reviews have summarized topics such as HMF oxidation/reduction and synthesis suitable for industrial production (Troiano et al., 2020; Yan et al., 2020), none of them have focused on introducing breakthroughs in research on biomass-derived diols. Hence, in this review, we summarize recent advances in the hydroconversion of HMF, emphasizing the formation of high-value diols *via* the selective hydrogenation of various functional groups on HMF, and analyze the synergistic effects of various catalyst components, to aid the advancement of biomass transformation research.

PRODUCTION OF DIOLS WITH RING STRUCTURES

This section summarizes recent advances in the catalytic hydrogenation of HMF to produce diols with ring structures, such as BHMF and BHMTHF. Diols formed through the hydrogenation of carbonyl inside HMF while retaining the ring structure are extremely useful in the synthesis of a variety of foams, polyethers, and crown ethers (Zhang et al., 2017; Kucherov et al., 2018). As a furan molecule, BHMF is more thermally and chemically stable than HMF (Zhu et al., 2021). Consequently, it is preferred as an industrial raw material for furan derivatives over HMF. Owing to the strong ring structure and symmetrical diol functional group, BHMF has unique advantages over conventional polyesters, especially for the production of linear or cross-linked polyurethane (Zhang et al., 2017). Additionally, BHMTHF should be more widely used than BHMF, as it has a low probability of forming by-products during polymerization (Stadler et al., 2019). For comparison, the experimental data are summarized in **Table 1**.

Hydrogenation of Carbonyl Inside HMF to BHMF With H$_2$

The majority of hydrogenation reactions use H$_2$ as a hydrogen donor because of the high BHMF yield obtained at relatively mild reaction temperatures in hydrogen environments (Gilkey et al., 2016). Ru/MnCo$_2$O$_4$ displayed high catalytic activity in methanol at a temperature of 100°C and a pressure of 8.2 MPa H$_2$ for 4 h (Mishra et al., 2020). The high yield of BHMF (98.5%) was due to the high dissociation capacity of Ru, Brønsted acidity of the MnCo$_2$O$_4$ spinel support surface, and increase in the Lewis acidity induced by ruthenium nanoparticles. In comparison to noble metals, transition metals have lower costs and adequate reserves, and consequently, they have attracted considerable attention from researchers. As a result, Co, which is a transition metal, has been widely used for the catalytic
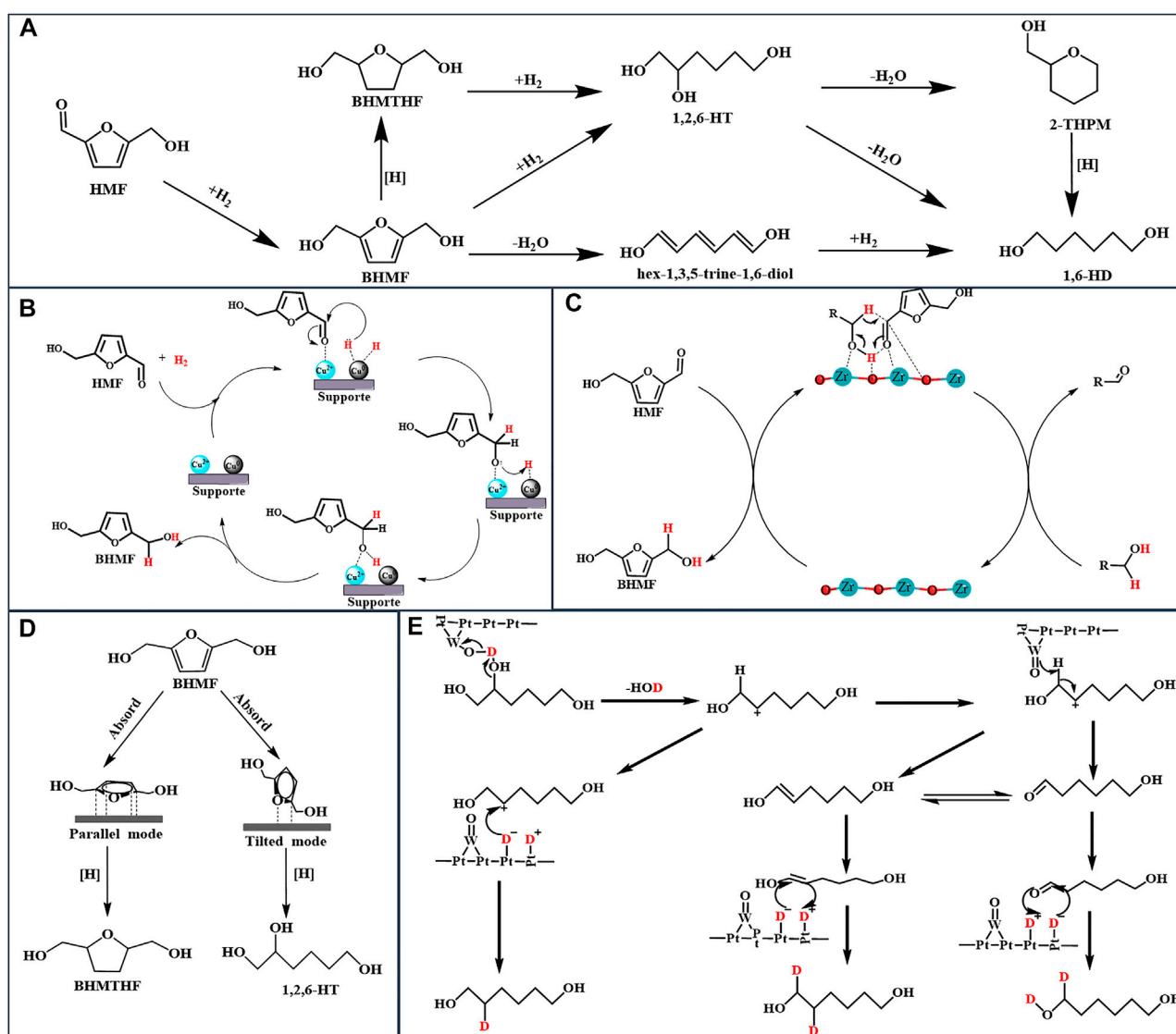
FIGURE 1 | (A): The route of formation of 1,6-HT from HMF; **(B)**: Mechanism for the selective conversion of HMF to BHMF over the Cu/Al$_2$O$_3$ catalyst **(C)**: Mechanism for the CTH of HMF to BHMF over the Zr-based catalyst **(D)**: Adsorption configurations of BHMF **(E)**: Mechanism for the selective cleavage of C–OH over the Pt-WO$_x$/TiO$_2$ catalyst.

conversion of HMF to BHMF. A hydrothermally synthesized monodispersed metallic Co catalyst, Co@C, was used in the selective hydrogenation of HMF, resulting in a 96.0% yield of BHMF at 110°C and 1 MPa H$_2$ for 6 h with methanol as the solvent (Arias et al., 2020). According to this study, the excellent performance of the Co@C catalyst is attributable to the minuscule Co^0 nanoparticles coated on the surface of the carbon shell, which provide sufficient catalytic activity.

As previously mentioned, smaller metal nanoparticles have higher dispersion and a more number of catalytically active sites (Arias et al., 2020). Hence, the regulation of the size of the active metal center is critical when designing metal catalysts. Kim's work provides in-depth guidelines regarding the same for researchers. Kim developed structurally different copper-alumina catalysts, including

meso-Cu/Al$_2$O$_3$, cp-Cu/Al$_2$O$_3$, and imp-Cu/Al$_2$O$_3$, via solvent-deficient precipitation (SDP), coprecipitation (CP), and impregnation (IMP) methods, respectively, and used them to catalyze the hydrogenation of HMF (Kim et al., 2021). Under the same reaction conditions, as shown in **Table 1**, entries 4, 5, and 6, the meso-Cu/Al$_2$O$_3$ catalyst outperformed both impregnated and co-precipitated Cu/Al$_2$O$_3$ catalysts in terms of catalytic activity. This phenomenon is attributable to the fact that SDP approaches provide catalysts with a higher BET surface area, which is 1.5 and 2 times larger than that obtained via cp-Cu/Al$_2$O$_3$ and imp-Cu/Al$_2$O$_3$, respectively; Additionally, it provides a Cu surface area more than double of that achieved using other methods, especially for meso-Cu/Al$_2$O$_3$. The SDP method, which utilizes NH$_4$HCO$_3$ as the precipitator rather than NaHCO$_3$, transforms Cu^{2+} in the solvent

into a fine and uniformly distributed solid crystal, resulting in better dispersion than other catalysts. Along with the size of the metal nanoparticles, the proportion of different active centers significantly influences the catalytic effect. Rao and co-workers described the mechanism of hydrogenation of HMF by Cu/Al_2O_3 in detail. As illustrated in **Figure 1B**, the coexistence of Cu^0 and Cu^{2+} species on the catalyst surface affects the catalytic performance (Rao et al., 2021). First, the presence of electrophilic Cu^{2+} aids the adsorption and activation of the C=O group of HMF via the oxygen lone pair. Hydrogen is dissociated on the Cu^0, and the activated carbonyl group on Cu^0 is then hydrogenated, resulting in the production of BHMF. Notably, different synthetic methods always result in diverse catalytic performance and physical properties of the catalysts.

Under certain reaction conditions, monometallic catalysts cannot simultaneously provide high conversion and selectivity. However, bimetallic systems can outperform monometallic catalysts in terms of catalytic activity owing to the synergistic effects induced by the geometric and electronic interactions of both metals involved (Elsayed et al., 2020; Zhang et al., 2020). Zhao and co-workers used a nickel–cobalt bimetallic catalyst to catalyze the hydrogenation reaction of HMF, obtaining a yield of 93.1% BHMF in a tetrahydrofuran (THF) solvent at 0.5 MPa hydrogen pressure and a reaction temperature of 100°C for 4 h (Zhao et al., 2021). An analysis of the effect on the Ni:Co ratio revealed that Ni exhibited strong catalytic reduction activity, resulting in C-O bond cleavage for the production of DMF, whereas Co inhibited the hydrogenolysis reaction, allowing BHMF to be retained and increasing BHMF selectivity. According to kinetic study results, the active energy required for HMF to BHMF conversion, 39.98 kJ mol^{-1}, is significantly lower than that required for MF, 62.64 kJ mol^{-1}, whereas the active energy required by BHMF for further transformation, 76.25 kJ mol^{-1}, is higher than that of MF, 44.21 kJ mol^{-1}, which is the crucial reason for the high yield of BHMF. Notably, the general reason for catalyst performance degradation after the repeated usage is that the substances absorbed on the catalyst surface during reaction warp the active sides, and this issue can be resolved through calcination in a suitable atmosphere (Huo et al., 2021; Zhao et al., 2022).

Meerwein-Ponndorf-Verley Reaction of HMF to BHMF

While H_2 as a hydrogen donor has the advantage of a low reaction temperature, it also has a number of disadvantages, including storage risk, transportation constraints, and minimal safety (Hu et al., 2018b). In comparison to H_2, alcohol has the advantages of being easy to transport, having a large supply, and being completely safe. Therefore, researchers have focused on the use of various alcohols as hydrogen donors to convert HMF into BHMF via the Meerwein-Ponndorf-Verley (MPV) reaction. Recently, Elsayed et al. reported the use of a magnetic catalyst, $CuO-Fe_3O_4/AC$, to selectively hydrogenate HMF via catalytic transfer hydrogenation (CTH). Although $CuO-Fe_3O_4/AC$ catalyzed the conversion of HMF to BHMF efficiently at 150°C with a 92% yield of BHMF, the reduction of Cu^{2+} by ethanol hinders the reusability of the catalyst (Elsayed et al., 2020). Hence,

the development of highly efficient and stable catalysts is crucial for the formation of BHMF from HMF via the CTH strategy.

To accomplish the formation of BHMF *via* CTH, zirconium is commonly used as an active center in the design of a catalyst because Zr^{2+} has a strong adsorption capacity and electronegativity, which cause the substrate to form a six-membered ring with the alcohol, utilizing the Lewis base synergistically to complete the MPV reaction (Hu et al., 2018a). **Figure 1C** illustrates the related steps in detail. Although feasible, the CTH of HMF necessitates a high reaction temperature to achieve high conversion using a common supported catalyst. Enhancing the Lewis acid-base property of the catalyst to improve catalytic activity can efficiently reduce the required temperature. Hu and co-workers synthesized a series of high-performance zirconium-containing organic-inorganic nanohybrid catalysts with isopropanol as a clean hydrogen donor (**Table 1**, entries 8–10) (Hu et al., 2018a; Hu et al., 2019; He et al., 2021). In comparison to the supported catalyst (Alamillo et al., 2012; Wei et al., 2018), **Table 1**, entries 12 and 13, these metal ligand catalysts efficiently catalyzed the conversion of HMF into BHMF at a mild reaction temperature of 120–140°C with a superior BHMF yield of 93.4–99.2%. Their excellent CTH capacity and stability are due to the Lewis acid-base coordination of organo-functional groups with zirconium (He et al., 2021). Zhou and co-workers evaluated a series of inorganic-biopolymer hybrids (Hf, Zr, Fe, Al, and Zn-Ligs) for catalytic performance to CTH of HMF at 100°C with isopropanol as the hydrogen donor, and the obtained results indicated that only Hf-Ligs and Zr-Ligs showed BHMF selectivity (Zhou et al., 2019). The use of Hf-Ligs as the catalyst resulted in a 90.0% yield of BHMF, which was significantly higher than the yield of Zr-Ligs (60.6%). As Hf-Ligs have the highest base/acid molar ratio among the reported Zr-based catalysts, the CTH reaction temperature is reduced to 100°C.

Many studies have revealed that secondary alcohols are more active than primary alcohols owing to their lower reduction potential, which implies that they can more easily supply hydrogen and promote the CTH of HMF (Fan et al., 2021). There are two shortcomings while considering alcohol as a hydrogen donor in the literature reported: 1) Temperatures required for the reaction are usually high because the active energy required for converting HMF to BHMF *via* CTH is nearly twice as much as that required while using H_2, and 2) when compared to the alcohol oxidized into the corresponding aldehyde or ketone, H_2 as a hydrogen donor has the benefit of producing no by-products.

Reduction of the Furan Ring Inside HMF to BHMTHF

For the synthesis of BHMTHF, Ru-based catalysts are typically utilized. Cadu pointed that carbene ligands offered moderate activity and selectivity, with a preference for unsaturated backbones and for bulky aromatic substitution pattern. Di-phosphorus containing ligands offered the highest conversion, leading to a good isolated yield of a mixture of BHMTHF, 87.0% (Cadu et al., 2018). Under optimal reaction conditions, the

catalytic conversion of HMF to BHMTHF by Ru/CeO$_x$ yields 89.0% with slight ring-opening by-products, 1,2,6-hexanetriol (1,2,6-HT) and 1,2,5-hexanetriol (1,2,5-HT) (Alamillo et al., 2012). In addition, the non-noble metal based catalysts has been applied in synthesis BHMTHF. Kong synthesized Ni-Al hydrotalcite-like catalyst and used it in formation of BHMTHF. The Ni-Al reduced at 450°C exhibited excellent performance to catalytic hydrogenation of HMF into BHMTHF, 96.2% yield under 6Mpa at 60°C for 6 h (Kong et al., 2015).

The above literatures indicated that preventing C-O cleavage is the key for high selectivity of BHMTHF. Yao and co-workers demonstrated that HMF can be converted directly to 1,2,6-HT by opening the furan ring without converting it first to BHMTHF (Yao et al., 2016). The ring-opening reaction did not occur in the upper layer below 100°C but accelerated rapidly as the reaction temperature increased to 120°C. Increasing the temperature resulted in a significant decrease in the 1,2,6-HT yield (41.9–20.1%), but no significant change in the BHMTHF yield (14.6–14.5%) was observed, indicating the attainment of an equilibrium between the amount of BHMTHF generation and consumption. Yang and co-workers prepared a Pd supported on layered double hydroxides (LDHs) catalyst for the selective hydrogenation of aromatic furfurals into aliphatic tetrahydrofurfural derivatives with over 92.0% selectivity and achieving a close-to-complete conversion of HMF (Yang et al., 2020). The effects on the solvent suggest that the polar solvent can prevent LDHs from adsorbing carbonyls, resulting in excellent selectivity for tetrahydrofurfural derivatives. As shown in **Figure 1D**, different HMF adsorption configurations on metal surfaces result in different product distributions. The C-O-C of BHMF activated by the catalyst was strongly adsorbed on the catalyst surface and then cleaved by reactive hydrogen. Correspondingly, the catalyst triggered the parallel adsorption of the furan ring of BHMTHF and then reduced it to BHMTHF. The geometric selectivity of the two absorption modes is due to the structure of LDHs, which prevents BHMF from moving. Notably, LDH catalysts exhibit the ability for parallel adsorption to the furan ring (Yao et al., 2016; Yang et al., 2020; Kong et al., 2015).

STRAIGHT CHAIN DIOL PRODUCTION

Apart from the catalytic hydrogenation of the carbonyl group on the furan ring, the furan ring undergoes a variety of diverse and complex reactions, as illustrated in **Figure 1A** (Buntara et al., 2011; Yao et al., 2016; Enjamuri et al., 2020). Among those products, 1,6-HD is the key monomer of polyesters, polyester polyols, and polyurethanes (Krishna et al., 2017; Li et al., 2016; Zhang et al., 2017). Owing to its low environmental impact and high performance, 1,6-HD is widely used, primarily in polyurethanes. Because of the high requirements for downstream products, such as thermoplastic polyurethanes, elastomers, and coatings, the demand for 1,6-HD is increasing rapidly. Excellent properties, such as a high mechanical strength, low glass transition temperature, and high heat resistance, lead to unique advantages compared to other polyurethanes. Despite the

fact that the overall output of 1,6-HD reached over 15.65 t/a in 2018, the global 1,6-HD market continues to grow at a rapid pace owing to the rising polyurethane demand (Enjamuri et al., 2020).

Buntara and co-workers demonstrated for the first time that 1,6-HD can be synthesized using HMF via a multi-step process that comprises the hydrogenation of the furan ring to BHMTHF, followed by the cleavage of the C-O-C bond to 1,2,6-HT and 1,6-HD (Buntara et al., 2011). According to a 2018 study, the Pt-WO$_x$/TiO$_2$ catalyst catalyzes the cleavage of the C-O-C bond inside BHMTHF to form 1,2,6-HT, which is then converted into 1,6-HD (He et al., 2018). The H atoms (H$^+$ and e$^-$) produced through hydrogen dissociation diffuse across TiO$_2$, during which electrons reduce Ti^{4+} to Ti^{3+} and then react with a W=O species, reducing W^{6+} to W^{5+} to form a Brønsted acid site, W-OH, as illustrated in **Figure 1E**. Finally, the Brønsted acid site catalyzed C-O cleavage of BHMTHF and 1,2,6-HT to complete hydrodeoxidation. Stephens and co-workers reported a mechanistic study of the conversion of 1,2,6-HT to 1,6-HD over Pt-WO$_x$/TiO. Using D$_2$ and H$_2$, the hydroxyl group on C2 was dehydrated, resulting in carbocation via W-OH species, and thereafter, W-O- acquired the hydrogen atom on C1 to form an aldehyde, which interacted with D$_2$ to form 1,6-HD (Stephens et al., 2020). Noble metals have a high hydrogen dissociation capacity and reduce metal oxides to metal hydroxides or create oxygen vacancies to catalyze the dehydration of hydroxyl groups. As a result, the design of catalysts, with metal oxidation and noble metals, has emerged as a prominent strategy for the selective cleavage of C-OH (Guan et al., 2020; Stephens et al., 2020).

Furthermore, there is an efficient strategy for the direct conversion of HMF into 1,6-HD utilizing double-layered catalysts of Pd/SiO$_2$ + Ir–ReO$_x$/SiO$_2$ in a fixed-bed reactor (Xiao et al., 2016). The bottom layer Pd/SiO$_2$ catalyst was used for the hydrogenation of the furan ring and carbonyl to BHMTHF, and Ir–ReO$_x$/SiO$_2$ was used for the hydrodeoxygenation of BHMTHF to 1,6-HD. When THF was replaced with water, the yield of 1,6-HD increased, but the yield of BHMTHF decreased. The yield of 1,6-HD decreased as the amount of water increased owing to the formation of hexanol during hydrogenolysis. Water acts as a polar solvent, causing the oxonium to escape. The hydrogenolysis of 1,2,6-HT is a challenging step in 1,6-HD synthesis. Therefore, it is necessary to investigate novel reaction pathways. For the first time, the Pd/ZrP catalyst was employed to directly synthesize 1,6-HD from HMF at atmospheric pressure using formic acid (FA) (Tuteja et al., 2014). The dissociation of FA distributed on the catalyst, formation of *in situ* hydrogen, and adsorption to C-O-C and C=O bonds via electrostatic interactions with the acidic ZrP support contributed to this outcome. Mechanistic studies indicated that HMF was adsorbed onto the active center and that the support of the catalyst enabled the direct conversion of the furan ring into hex-1,3,5-trine-1,6-diol under the action of acidic sites. With three conjugated C=C bonds, the intermediate reacted with H$_2$ derived from FA *via* Pd to form 1,6-HD. Despite new literature and research into 1,6-HD, converting HMF into 1,6-HD with a high yield *via* a one-step process remains challenging with the existing technology.

CONCLUSIONS AND PERSPECTIVES

Biomass has received significant interest in recent decades as a renewable feedstock. Highly efficient catalysts play an important role in selective biomass conversion. In this respect, metal catalysts have been extensively used in the hydrogenation of HMF with promising results. To synthesize BHMF, it is necessary to selectively reduce the C=O bond rather than cleave the C-H bond. The generation of nonaromatic diols from HMF should be the focus of future research. Notably, the polyester industry has a high demand for 1,6-HD, which is synthesized *via* the ring-opening reaction of BHMF or BHMTHF and reduction of the hydroxyl of 1,2,6-HT (1,6-HEXANEDIOL MARKET, 2019; GLOBAL 1,5-PENTANEDIOL MARKET, 2019). For a number of reasons, the formation of diols is difficult: 1) Despite prior research demonstrating the feasibility of using nickel- and cobalt-based catalysts for the synthesis of BHMTHF from HMF, the reduction or ring-opening of the furan ring requires a high H_2 pressure; 2) the hydroxyl group has a low reactivity without the conjugation of the furan ring. These are the challenges that hinder the development of diol production.

Considering the current state of development, some prospects for the advancement of diol production are identified as follows: 1) Using a liquid hydrogen donor to convert HMF to biomass-derived diols employing a non-noble metal catalyst seems promising owing to the abundance of biomass, ease of transportation, and safety. FA as a hydrogen donor does not produce any additional by-products, and being a Brønsted acid, FA can assist in the ring-opening reaction of substances, allowing the formation of 1,6-HD efficiently. Although alcohol oxidation occurs while using the CTH strategy to form BHMF, the low-boiling-point ketone and aldehyde can be removed via purification. 2) The conversion of BHMF into a valuable derivative appears to be more promising than the conversion of HMF, which is neither thermally nor chemically stable. Hence, employing glucose or even cellulose as a raw material to directly synthesize BHMF with high selectivity seems advantageous. Zhang and co-workers achieved a 48.2% BHMF yield in a fixed bed reactor by directly converting fructose at 140°C over a Cu/ZnO/Al$_2$O$_3$ catalyst. The conversion of cellulose to BHMF might lead to significant advancements in biomass research. 3) The catalysis of the Brønsted acid, which forms up on metal oxidation after reaction with H atoms for the C-O bond, is essential for the cleavage of the C-OH and C-O-C bonds. Although noble metal catalysts can successfully catalyze the synthesis of 1,6-HD, their high costs render the diol production challenging. Therefore, developing a non-noble metal catalyst to catalyze the synthesis of 1,6-HD is a challenge that must be addressed. Employing a metal-ligand catalyst with a Brønsted acidic functional group could represent a breakthrough in the production of the 1,6-HD from HMF using a non-noble catalyst. Acidic functional groups act directly on the C-O bond, instead of metal oxidation. The direct formation of 1,6-HD from HMF, as the main monomer of the polymer, is expected to inspire researchers working in the field of biomass conversion.

AUTHOR CONTRIBUTIONS

ZH: Investigation, Methodology, Writing-Original draft preparation. JW: Data curation, Formal analysis. JL: Validation. WZ: Methodology, Visualization. HC: Data curation. YY: Conceptualization, Project administration, Funding acquisition. QX: Writing-review and editing. XL: Conceptualization, Project administration, Funding acquisition, Supervision.

ACKNOWLEDGMENTS

REFERENCES

1,6-HEXANEDIOL MARKET (2019). *1, 6-Hexanediol Market by Application (Polyurethanes, Coatings, Acrylates, Adhesives, Polyester Resins, and Plasticizers) and Region (Europe, APAC, North America, South America, and Middle East & Africa). Global Forecast to 2025*; Market Publisher, Report Database

Alamillo, R., Tucker, M., Chia, M., Pagán-Torres, Y., and Dumesic, J. (2012). The Selective Hydrogenation of Biomass-Derived 5-Hydroxymethylfurfural Using Heterogeneous Catalysts. *Green Chem.* 14, 1413–1419. doi:10.1039/c2gc35039d

Arias, K. S., Carceller, J. M., Climent, M. J., Corma, A., and Iborra, S. (2020). Chemoenzymatic Synthesis of 5-Hydroxymethylfurfural (HMF)-Derived Plasticizers by Coupling HMF Reduction with Enzymatic Esterification. *ChemSusChem* 13, 1864–1875. doi:10.1002/cssc.201903123

Buntara, T., Noel, S., Phua, P. H., Melián-Cabrera, I., de Vries, J. G., and Heeres, H. J. (2011). Caprolactam from Renewable Resources: Catalytic Conversion of 5-Hydroxymethylfurfural into Caprolactone. *Angew. Chem.* 123, 7221–7225. doi:10.1002/ange.201102156

Cadu, A., Sekine, K., Mormul, J., Ohlmann, D. M., Schaub, T., and Hashmi, A. S. K. (2018). Homogeneous Catalysed Hydrogenation of HMF. *Green Chem.* 20, 3386–3393. doi:10.1039/c8gc01025k

Chen, S., Wojcieszak, R., Dumeignil, F., Marceau, E., and Royer, S. (2018). How Catalysts and Experimental Conditions Determine the Selective Hydroconversion of Furfural and 5-Hydroxymethylfurfural. *Chem. Rev.* 118, 11023–11117. doi:10.1021/acs.chemrev.8b00134

Chernyshev, V. M., Kravchenko, O. A., and Ananikov, V. P. (2017). Conversion of Plant Biomass to Furan Derivatives and Sustainable Access to the New Generation of Polymers, Functional Materials and Fuels. *Russ. Chem. Rev.* 86, 357–387. doi:10.1070/rcr4700

Deng, X., Zhao, P., Zhou, X., and Bai, L. (2021). Excellent Sustained-Release Efficacy of Herbicide Quinclorac with Cationic Covalent Organic Frameworks. *Chem. Eng. J.* 405, 126979. doi:10.1016/j.cej.2020.126979

Enjamuri, N., and Darbha, S. (2020). Solid Catalysts for Conversion of Furfural and its Derivatives to Alkanediols. *Catal. Rev.* 62, 566–606. doi:10.1080/01614940.2020.1744327

Fan, Y., Zhuang, C., Li, S., Wang, Y., Zou, X., Liu, X., et al. (2021). Efficient Single-Atom Ni for Catalytic Transfer Hydrogenation of Furfural to Furfuryl Alcohol. *J. Mat. Chem. A* 9, 1110–1118. doi:10.1039/d0ta10838c

Gilkey, M. J., and Xu, B. (2016). Heterogeneous Catalytic Transfer Hydrogenation as an Effective Pathway in Biomass Upgrading. *ACS Catal.* 6, 1420–1436. doi:10.1021/acscatal.5b02171

GLOBAL 1,5-PENTANEDIOL MARKET (2019). *Global 1,5-Pentanediol Market 2018 by Manufacturers. Regions, Type and Application.* Forecast to 2023. Market Publisher, Report Database.

Guan, W., Chen, X., Hu, H., Tsang, C.-W., Zhang, J., Lin, C. S. K., et al. (2020). Catalytic Hydrogenolysis of Lignin β-O-4 Aryl Ether Compound and Lignin to Aromatics over Rh/Nb$_2$O$_5$ under Low H$_2$ Pressure. *Fuel Process. Technol.* 203, 106392. doi:10.1016/j.fuproc.2020.106392

Guo, D., Liu, X., Cheng, F., Zhao, W., Wen, S., Xiang, Y., et al. (2020). Selective Hydrogenolysis of 5-Hydroxymethylfurfural to Produce Biofuel 2, 5-Dimethylfuran over Ni/ZSM5 Catalysts. *Fuel* 274, 117853. doi:10.1016/j.fuel.2020.117853

He, A., Hu, L., Zhang, Y., Jiang, Y., Wang, X., Xu, J., et al. (2021). High-Efficiency Catalytic Transfer Hydrogenation of Biomass-Based 5-Hydroxymethylfurfural to 2,5-Bis(Hydroxymethyl)furan over a Zirconium-Carbon Coordination Catalyst. *ACS Sustain. Chem. Eng.* 9, 15557–15570. doi:10.1021/acssuschemeng.1c05618

He, J., Burt, S. P., Ball, M., Zhao, D., Hermans, I., Dumesic, J. A., et al. (2018). Synthesis of 1,6-Hexanediol from Cellulose Derived Tetrahydrofuran-Dimethanol with Pt-WOx/TiO$_2$ Catalysts. *ACS Catal.* 8, 1427–1439. doi:10.1021/acscatal.7b03593

Hu, L., Li, T., Xu, J., He, A., Tang, X., Chu, X., et al. (2018a). Catalytic Transfer Hydrogenation of Biomass-Derived 5-Hydroxymethylfurfural into 2,5-Dihydroxymethylfuran over Magnetic Zirconium-Based Coordination Polymer. *Chem. Eng. J.* 352, 110–119. doi:10.1016/j.cej.2018.07.007

Hu, L., Song, J., Jiang, J., He, A., and Xu, J. (2019). Zirconium-Containing Organic-Inorganic Nanohybrid as a Highly Efficient Catalyst for the Selective Synthesis of Biomass-Derived 2,5-Dihydroxymethylfuran in Isopropanol. *Waste Biomass Valor* 11, 3485–3499. doi:10.1007/s12649-019-00703-z

Hu, L., Xu, J., Zhou, S., He, A., Tang, X., Lin, L., et al. (2018b). Catalytic Advances in the Production and Application of Biomass-Derived 2,5-Dihydroxymethylfuran. *ACS Catal.* 8, 2959–2980. doi:10.1021/acscatal.7b03530

Huo, J., Tessonnier, J-P., and Shanks, B. H. (2021). Improving Hydrothermal Stability of Supported Metal Catalysts for Biomass Conversions: a Review. *ACS Catal.* 11, 5248

Kim, J., Bathula, H. B., Yun, S., Jo, Y., Lee, S., Baik, J. H., et al. (2021). Hydrogenation of 5-hydroxymethylfurfural into 2,5-bis(hydroxymethyl) furan over Mesoporous Cu-Al$_2$O$_3$ Catalyst: From Batch to Continuous Processing. *J. Industrial Eng. Chem.* 102, 186–194. doi:10.1016/j.jiec.2021.06.039

Kong, X., Zheng, R., Zhu, Y., Ding, G., Zhu, Y., and Li, Y.-W. (2015). Rational Design of Ni-Based Catalysts Derived from Hydrotalcite for Selective Hydrogenation of 5-Hydroxymethylfurfural. *Green Chem.* 17, 2504–2514. doi:10.1039/c5gc00062a

Krishna, S. H., Mcclelland, D. J., Rashke, Q. A., Dumesic, J. A., and Huber, G. W. (2017). Hydrogenation of Levoglucosenone to Renewable Chemicals. *Green Chem.* 19, 1278–1285. doi:10.1039/c6gc03028a

Kucherov, F. A., Romashov, L. V., Galkin, K. I., and Ananikov, V. P. (2018). Chemical Transformations of Biomass-Derived C6-Furanic Platform Chemicals for Sustainable Energy Research, Materials Science, and Synthetic Building Blocks. *ACS Sustain. Chem. Eng.* 6, 8064–8092. doi:10.1021/acssuschemeng.8b00971

Li, C., Li, J., Qin, L., Yang, P., and Vlachos, D. G. (2021). Recent Advances in the Photocatalytic Conversion of Biomass-Derived Furanic Compounds. *ACS Catal.* 11, 11336–11359. doi:10.1021/acscatal.1c02551

Li, Y., Cheng, H., Zhang, C., Zhang, B., Liu, T., Wu, Q., et al. (2016). Reductive Amination of 1,6-Hexanediol with Ru/Al$_2$O$_3$ Catalyst in Supercritical Ammonia. *Sci. China Chem.* 60, 920

Mishra, D. K., Lee, H. J., Truong, C. C., Kim, J., Suh, Y.-W., Baek, J., et al. (2020). Ru/MnCo$_2$O$_4$ as a Catalyst for Tunable Synthesis of 2,5-bis(hydroxymethyl)furan or 2,5-bis(hydroxymethyl)tetrahydrofuran from Hydrogenation of 5-Hydroxymethylfurfural. *Mol. Catal.* 484, 110722. doi:10.1016/j.mcat.2019.110722

Nakagawa, Y., Tamura, M., and Tomishige, K. (2013). Catalytic Reduction of Biomass-Derived Furanic Compounds with Hydrogen. *ACS Catal.* 3, 2655–2668. doi:10.1021/cs400616p

Rao, K. T. V., Hu, Y., Yuan, Z., Zhang, Y., and Xu, C. C. (2021). Green Synthesis of Heterogeneous Copper-Alumina Catalyst for Selective Hydrogenation of Pure and Biomass-Derived 5-Hydroxymethylfurfural to 2,5-Bis(hydroxymethyl)furan. *Appl. Catal. A General* 609, 117892. doi:10.1016/j.apcata.2020.117892

Ravishankara, A. R., Rudich, Y., and Pyle, J. A. (2015). Role of Chemistry in Earth's Climate. *Chem. Rev.* 115, 3679–3681. doi:10.1021/acs.chemrev.5b00226

Stadler, B. M., Wulf, C., Werner, T., Tin, S., and De Vries, J. G. (2019). Catalytic Approaches to Monomers for Polymers Based on Renewables. *ACS Catal.* 9, 8012–8067. doi:10.1021/acscatal.9b01665

Stephens, K. J., Allgeier, A. M., Bell, A. L., Carlson, T. R., Cheng, Y., Douglas, J. T., et al. (2020). A Mechanistic Study of Polyol Hydrodeoxygenation over a Bifunctional Pt-WOx/TiO$_2$ Catalyst. *ACS Catal.* 10, 12996–13007. doi:10.1021/acscatal.0c03475

Sun, G., An, J., Hu, H., Li, C., Zuo, S., and Xia, H. (2019). Green Catalytic Synthesis of 5-Methylfurfural by Selective Hydrogenolysis of 5-Hydroxymethylfurfural over Size-Controlled Pd Nanoparticle Catalysts. *Catal. Sci. Technol.* 9, 1238–1244. doi:10.1039/c9cy00039a

Troiano, D., Orsat, V., and Dumont, M.-J. (2020). Status of Biocatalysis in the Production of 2,5-Furandicarboxylic Acid. *ACS Catal.* 10, 9145

Tuteja, J., Choudhary, H., Nishimura, S., and Ebitani, K. (2014). Direct Synthesis of 1,6-Hexanediol from HMF over a Heterogeneous Pd/ZrP Catalyst Using Formic Acid as Hydrogen Source. *ChemSusChem* 7, 96–100. doi:10.1002/cssc.201300832

Wan, Y., and Lee, J.-M. (2021). Toward Value-Added Dicarboxylic Acids from Biomass Derivatives via Thermocatalytic Conversion. *ACS Catal.* 11, 2524–2560. doi:10.1021/acscatal.0c05419

Wei, J., Cao, X., Wang, T., Liu, H., Tang, X., Zeng, X., et al. (2018). Catalytic Transfer Hydrogenation of Biomass-Derived 5-Hydroxymethylfurfural into 2,5-Bis(hydroxymethyl)furan over Tunable Zr-Based Bimetallic Catalysts. *Catal. Sci. Technol.* 8, 4474–4484. doi:10.1039/c8cy00500a

Xiao, B., Zheng, M., Li, X., Pang, J., Sun, R., Wang, H., et al. (2016). Synthesis of 1,6-hexanediol from HMF over Double-Layered Catalysts of Pd/SiO$_2$ + Ir-ReOx/SiO$_2$ in a Fixed-Bed Reactor. *Green Chem.* 18, 2175–2184. doi:10.1039/c5gc02228b

Yan, L., Zhang, Q., Deng, W., Zhang, Q., and Wang, Y. (2020). Catalytic Valorization of Biomass and Bioplatforms to Chemicals through Deoxygenation. *Adv. Catal.* 66, 1

Yang, Y., Wang, Y., Li, S., Shen, X., Chen, B., Liu, H., et al. (2020). Selective Hydrogenation of Aromatic Furfurals into Aliphatic Tetrahydrofurfural Derivatives. *Green Chem.* 22, 4937

Yao, S., Wang, X., Jiang, Y., Wu, F., Chen, X., and Mu, X. (2016). One-step Conversion of Biomass-Derived 5-Hydroxymethylfurfural to 1,2,6-Hexanetriol over Ni–Co–Al Mixed Oxide Catalysts under Mild Conditions. *ACS Sustain Chem. Eng.* 2, 173

Zhang, D., and Dumont, M.-J. (2017). Advances in Polymer Precursors and Bio-Based Polymers Synthesized from 5-Hydroxymethylfurfural. *J. Polym. Sci. Part A Polym. Chem.* 55, 1478–1492. doi:10.1002/pola.28527

Zhang, J., Qi, Z., Liu, Y., Wei, J., Tang, X., He, L., et al. (2020). Selective Hydrogenation of 5-Hydroxymethylfurfural into 2,5-Bis(hydroxymethyl) furan over a Cheap Carbon-Nanosheets-Supported Zr/Ca Bimetallic CatalystElsayed I, Jackson M A, Hassan E B (2020). Hydrogen-free Catalytic Reduction of Biomass-Derived 5-hydroxymethylfurfural into 2,5-bis(hydroxymethyl)furan Using Copper–Iron Oxides Bimetallic Nanocatalyst. *Energy fuels.* 34, 84321774–84391785. doi:10.1021/acs.energyfuels.0c01128

Zhao, W., Huang, Z., Yang, L., Liu, X., Xie, H., and Liu, Z. (2022). Highly Efficient Syntheses of 2,5-bis(hydroxymethyl)furan and 2,5-dimethylfuran via the Hydrogenation of Biomass-Derived 5-hydroxymethylfurfural over a Nickel-Cobalt Bimetallic Catalyst. *Appl. Surf. Sci.* 577, 151869. doi:10.1016/j.apsusc.2021.151869

Zhao, W., Zhu, X., Zeng, Z., Lei, J., Huang, Z., Xu, Q., et al. (2022). Cu-Co Nanoparticles Supported on Nitrogen-Doped Carbon: an Efficient Catalyst for Hydrogenation of 5-Hydroxymethylfurfural into 2,5-Bis(hydroxymethyl)furan. *Mol. Catal.* 524, 112304. doi:10.1016/j.mcat.2022.112304

Zhou, C.-H., Xia, X., Lin, C.-X., Tong, D.-S., and Beltramini, J. (2011). Catalytic Conversion of Lignocellulosic Biomass to Fine Chemicals and Fuels. *Chem. Soc. Rev.* 40, 5588–5617. doi:10.1039/c1cs15124j

Zhou, S., Dai, F., Chen, Y., Dang, C., Zhang, C., Liu, D., et al. (2019). Sustainable Hydrothermal Self-Assembly of Hafnium-Lignosulfonate Nanohybrids for Highly Efficient Reductive Upgrading of 5-hydroxymethylfurfural. *Green Chem.* 21, 1421–1431. doi:10.1039/c8gc03710h

Zhu, B., Chen, C., Huai, L., Zhou, Z., Wang, L., and Zhang, J. (2021). 2,5-Bis(hydroxymethyl)furan: A New Alternative to HMF for Simultaneously Electrocatalytic Production of FDCA and H_2 over CoOOH/Ni Electrodes. *Appl. Catal. B Environ.* 297, 120396. doi:10.1016/j.apcatb.2021.120396

Zhu, H., Luo, W., Ciesielski, P. N., Fang, Z., Zhu, J. Y., Henriksson, G., et al. (2016). Wood-derived Materials for Green Electronics, Biological Devices, and Energy Applications. *Chem. Rev.* 116, 9305–9374. doi:10.1021/acs.chemrev.6b00225

Conflict of Interest: Authors JL, HC, and YY were employed by the company Chenzhou Gao Xin Material Co., Ltd.

The remaining authors declare that the research was conducted in the absence of any commercial or financial relationships that could be construed as a potential conflict of interest.

Publisher's Note: All claims expressed in this article are solely those of the authors and do not necessarily represent those of their affiliated organizations, or those of the publisher, the editors and the reviewers. Any product that may be evaluated in this article, or claim that may be made by its manufacturer, is not guaranteed or endorsed by the publisher.

Unsupported MoS₂-Based Catalysts for Bio-Oil Hydrodeoxygenation: Recent Advances and Future Perspectives

Jing Cao, Youming Zhang, Li Wang, Cen Zhang* and Congshan Zhou

Department of Chemistry and Chemical Engineering, Hunan Institute of Science and Technology, Yueyang, China

In recent years, unsupported MoS$_2$-based catalysts have been reported as promising candidates in the hydrodeoxygenation (HDO) of bio-oil. However, preparing MoS$_2$-based catalysts with both high activity and good stability for HDO reaction is still challenging and of great importance. Hence, this mini-review is focused on the recent development of unsupported MoS$_2$-based HDO catalysts from the understanding of catalyst design. The three aspects including morphology and defect engineering, metal doping, and deactivation mechanism are highlighted in adjusting the HDO performance of MoS$_2$-based catalysts. Finally, the key challenges and future perspectives about how to design efficient catalysts are also summarized in the conclusions.

Keywords: bio-oil, hydrodeoxygenation, unsupported MoS$_2$, morphology, defect, metal doping, deactivation

INTRODUCTION

With the continuous consumption of fossil fuels, the energy problem has become more serious in modern society. Therefore, a lot of research studies in the energy field have focused on finding a new fuel that can replace traditional fossil fuels, which could be compatible with existing infrastructure, sustainable, and reduce CO$_2$ emissions (Jiang et al., 2021). In recent years, bio-oil obtained from flash pyrolysis of biomass is considered a potential fuel in the future because of its wide range of raw materials and renewable (Qu et al., 2021).

Compared with fossil fuels, the oxygen content in bio-oil is very high (up to 40 wt.%). This component characteristic results in the disadvantages of low heating value, high viscosity and acidity, and poor thermal stability. Therefore, bio-oil must be upgraded through hydrodeoxygenation (HDO) to reduce the oxygen content before being used as an excellent fuel (**Figure 1A**). Thus, developing catalysts with excellent catalytic performance is crucial for the bio-oil HDO process. As the most commonly used catalysts for hydrodesulfurization (HDS) in industry, supported transition metal sulfides (CoMoS/Al$_2$O$_3$ or NiMoS/Al$_2$O$_3$) also have been frequently investigated in the HDO reaction due to their low cost and mature technology. However, the HDO activity of supported catalysts is not very ideal, which usually requires harsh reaction conditions of 300°C or above. Under high reaction temperature, the sulfide catalysts will undergo a fast deactivation due to sulfur loss without sulfur compensation from external sources during the reaction process (Wandas et al., 1996; Wang et al., 2015a; Liu et al., 2017). Recently, unsupported MoS$_2$-based catalysts have been reported to show much better HDS and HDO activity than supported counterparts because of the high density of active sites, which is especially suitable for dealing with large molecules (Wang et al., 2009; Wang et al., 2014b). More importantly, the unsupported catalysts provide an ideal platform for studying the structure-performance relationship due to the absence of support. Over the past decade, a lot of
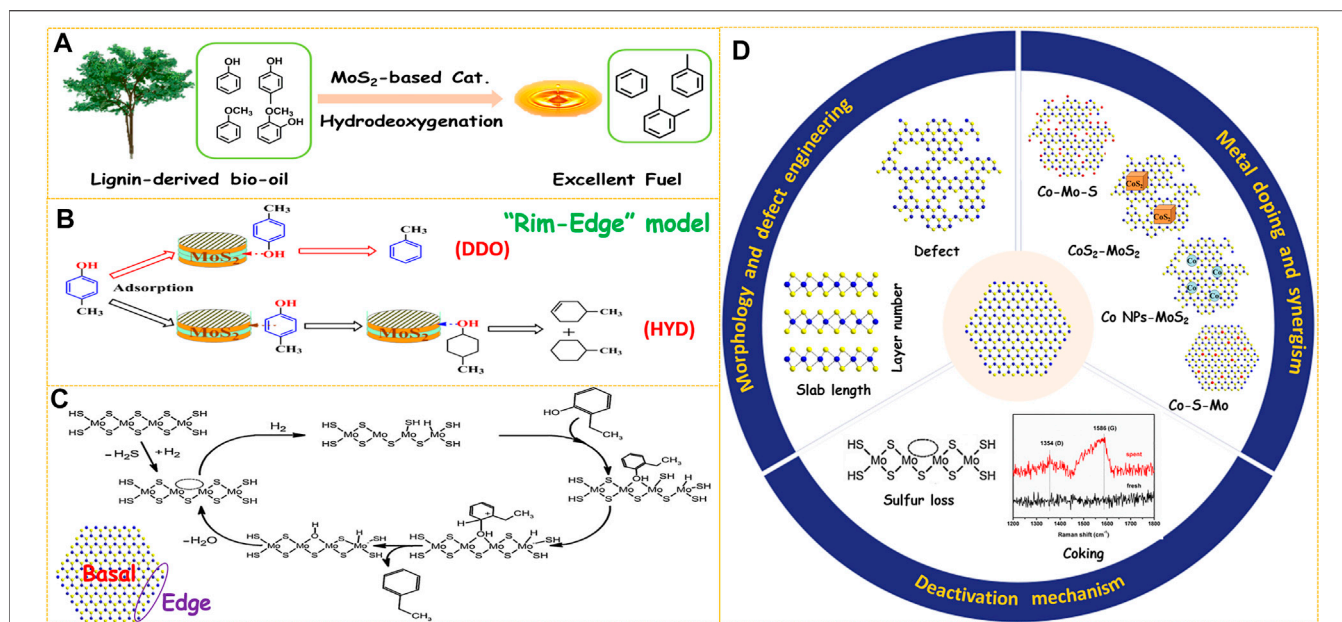
FIGURE 1 | **(A)** Upgrading of lignin-derived bio-oil through HDO process. **(B)** Reaction pathways over MoS₂-based catalysts. Reproduced with permission from (Wang et al., 2014d). Copyright (2014) American Chemical Society. **(C)** Proposed HDO mechanism of 2-ethylphenol on MoS₂-based catalyst. Reproduced with permission from (Mortensen et al., 2011). Copyright (2011) Elsevier. **(D)** Three aspects to improve the HDO performance of MoS₂-based catalysts.

studies have been carried out on how to improve the HDO activity, selectivity, and stability of unsupported MoS₂-based catalysts.

Hence, in this mini-review, we firstly reviewed in detail how to study the structure-performance relationship through morphology and defect engineering of MoS₂ catalysts. Then, the effect of metal doping on the active phase structure and HDO performance of the MoS₂ catalyst are summarized. Moreover, the deactivation mechanism and how to inhibit the deactivation of MoS₂-based catalysts in the HDO process is also introduced. Finally, we analyzed the challenges and future opportunities to design highly efficient unsupported MoS₂-based HDO catalysts.

MORPHOLOGY AND DEFECT ENGINEERING

MoS₂ is a typical two-dimensional layered compound, which has two morphology parameters of slab length and layer number (**Figure 1D**). These two parameters could be visualized by high-resolution transmission electron microscopy (HRTEM) observation from the length and number of black fringes in the HRTEM images, respectively (Lai et al., 2016; Cao et al., 2021b). For unsupported MoS₂-based catalysts, it is important to boost the number of active sites by increasing the Mo dispersion. Hence, shortening the slab length or decreasing the layer number of MoS₂ can both improve its HDO activity. Due to the weak Van der Waals force between the adjacent layers, MoS₂ can be easily exfoliated into few-layer or even single-layer nanosheets by some physical or chemical methods (Zhu et al., 2018; Cao et al., 2021c).

A simple and effective hydrazine-assisted liquid exfoliation method was developed to exfoliate the commercial MoS₂ to few-layer nanosheets (Liu et al., 2016). The HDO activity was remarkably enhanced for few-layer MoS₂ nanosheets due to the exposure of more active surface sites. In addition, the layer number of bulk MoS₂ was further decreased to monolayer by *n*-butyllithium exfoliation, and the conversion was extraordinarily improved from 25.8% of bulk MoS₂ to 98.7% of single-layer MoS₂ in the HDO of 4-methylphenol (Liu et al., 2017). This result demonstrates that preparing few-layer, especially monolayer MoS₂ is an effective way to design highly efficient HDO catalysts. Various methods have been developed to synthesize unsupported MoS₂ catalysts such as hydrothermal (Cao et al., 2021a; Zhang C. et al., 2021), ball milling (Wang C. et al., 2014), thermal decomposition (Yi et al., 2011), and solution method (Genuit et al., 2005). Among the abovementioned methods, the hydrothermal method is most widely used due to the advantages of simple operation and controllable morphology of the product. In the hydrothermal procedure, temperature, pH value, and surfactants showed a great effect on the morphology of the MoS₂ product. For example, an acidic environment in the hydrothermal process was helpful to facilitate the nucleation and prepare smaller MoS₂ particles, thus resulting in enhanced activity in the HDO of *p*-cresol (Wang et al., 2015b; Zhang C. et al., 2018). A higher initial synthesis temperature could promote fast nucleation and shorten the MoS₂ slab length (Zhang et al., 2015). The layer number of MoS₂ was adjusted successfully by adding different types of surfactants in the hydrothermal procedure and then the morphology-performance relation in the HDO of 4-methylphenol was studied (Wang et al., 2014d). There are two parallel reaction

routes for the HDO of phenols over MoS$_2$-based catalysts, which are defined as direct deoxygenation (DDO) and hydrogenation-dehydration (HYD). It was found that MoS$_2$ catalyst with lower stacking showed a higher HYD selectivity, and the DDO route was favored by using MoS$_2$ with higher stacking degree (**Figure 1B**). This phenomenon was well explained by the Rim-Edge model proposed in the HDS field (Daage and Chianelli, 1994). Therefore, the HDO selectivity could be precisely regulated by adjusting the layer number of MoS$_2$ particles.

Generally, the coordinatively unsaturated sites (CUS) on the edge planes are considered active centers of MoS$_2$ catalysts while the atoms on the basal planes are catalytically inert (**Figure 1C**) (Lauritsen et al., 2004). Therefore, creating defects on the basal planes is another important approach to increase the number of active sites (**Figure 1D**). Some strategies such as etching (Zhang W. et al., 2018; Wang et al., 2020), gas treatment (Li et al., 2019), or plasma bombardment (Tao et al., 2015) have been utilized to create defect sites on the basal planes. The location and type of defects can be directly observed by HRTEM, and the quantity information can be obtained by electron paramagnetic resonance (EPR) characterization (Wu et al., 2020). Recently, we have synthesized MoS$_2$ nanosheets with rich defects through *in situ* etching by adding excess sulfur sources *via* a simple one-pot hydrothermal method (Zhang C. et al., 2021). The HDO activity was improved 1.7 folds through defect engineering within the basal planes. Zhang et al. reported a facile H$_2$O$_2$ etching strategy to tailor the concentration of sulfur vacancies by altering the H$_2$O$_2$/MoS$_2$ molar ratio (Zhang Y. et al., 2021). The catalytic performance evaluation results revealed a linear relationship between the HDO activity and the degree of sulfur vacancies, further suggesting that sulfur vacancies acted as catalytic centers for the HDO reaction. The synthesis of amorphous MoS$_2$ with low crystallinity is also one of the means to increase the number of defects. It was found that incorporating organic solvents or hydrazine in the hydrothermal method was conducive to obtaining amorphous MoS$_2$ with a defect-rich structure. A bent and multilayered amorphous MoS$_2$ was synthesized by utilizing (NH$_4$)$_2$MoS$_4$ as a raw material and decalin as an organic solvent, and the HDO activity was enhanced by 31% compared with the crystalline MoS$_2$(Yoosuk et al., 2012). Co-doped MoS$_2$ nanoflowers with abundant defects by adding hydrazine to the hydrothermal system was prepared, which displayed an excellent p-cresol HDO performance (Song et al., 2018a). More importantly, the defects on the basal planes could provide additional anchor sites to accommodate promoter atoms. Recently, we have found that the content of the Co-Mo-S active phase was improved significantly by creating numerous defects on the basal planes of MoS$_2$ support even impregnated with the same amount of Co promoters (Zhang C. et al., 2021). As a result, the Co-doped few-layer and defect-rich MoS$_2$ achieved a 100% HDO conversion of p-cresol and 99.7% selectivity of toluene at 230°C. The increased surface sulfur defects produced by H$_2$O$_2$ etching were ideal platforms for stabilizing Co atoms to form the Co-Mo-S phase. The HDO activity of Co-MoS$_2$ catalysts was increased 3.4 times by optimizing the etching conditions (Zhang Y. et al., 2021).

METAL DOPING AND SYNERGISM STUDY

In general, the activity of unpromoted MoS$_2$ is far from sufficient for catalyzing the HDO reaction effectively. Hence, it is essential to weaken the Mo-S bond through metal doping to reduce the formation temperature of sulfur vacancy. Co is the most commonly used metal to promote MoS$_2$ because the DDO route is more favored for Co-doped catalysts which could minimize the H$_2$ consumption. Based on the reported literature, there are mainly four different structures of catalytic centers for Co-promoted MoS$_2$ catalysts (**Figure 1D**): (I) Co-Mo-S, (II) CoS$_2$-MoS$_2$, (III) Co-S-Mo (or called Co atom-MoS$_2$), and (IV) Co NPs-MoS$_2$ (NPs: nanoparticles). The four different catalytic active phases were obtained by tailored preparation methods, which resulted in a variety of synergistic mechanisms.

The Co-Mo-S model is the most accepted active phase structure in the field of HDS, in which Co atoms are preferentially located on the edge planes of MoS$_2$. In our recent work, Co-doped nano-MoS$_2$ catalysts with Co-Mo-S as an active phase were obtained by impregnating the as-prepared MoS$_2$ with Co(CH$_3$COO)$_2$ followed by sulfidation in H$_2$S/H$_2$ atmosphere (Cao et al., 2021a). The temperature-programmed reduction (TPR) results displayed that the reduction peak was shifted from 285°C for MoS$_2$ to 224°C for Co-doped nano-MoS$_2$, which suggests a greatly decreased temperature for producing coordinative unsaturated sites (CUS). Also, it was found the Co content had a huge effect on the structure of the active phase and catalytic performance. If a small amount of Co are introduced, all Co atoms are preferentially located at the edge planes to form the Co-Mo-S phase. When the content of Co is further increased, the Co$_9$S$_8$ phase is gradually formed after the edge sites are fully occupied. However, too much Co content is not suggested because the larger Co$_9$S$_8$ would block some of the active sites. Also, the optimized catalyst with a Co/(Co + Mo) molar ratio of 0.3 had both Co-Mo-S and small Co$_9$S$_8$ particles, which embodies a synergistic effect between Co-Mo-S and Co$_9$S$_8$ phases. The HDO activity and toluene selectivity were improved dramatically from 16.9 to 65.0% of MoS$_2$ to 98.7 and 98.9% of Co/MoS$_2$-0.3 at 220°C. Another well-known model in the field of hydrorefining is the Remote-Control model, in which the independent Co$_x$S$_y$ phase acts the role to provide spillover hydrogen. Wang et al. adopted a two-step hydrothermal method which obtained separated CoS$_2$ and MoS$_2$ phases in the resulted catalysts rather than the Co-Mo-S phase prepared by one-step hydrothermal method (Wang et al., 2016b). The CoS$_2$/MoS$_2$ showed an excellent HDO activity of 97.8% and a high toluene selectivity of 99.2% at 250°C. The unprecedented HDO performance was attributed to the large surface area and the synergism between CoS$_2$ and MoS$_2$. More interestingly, the CoS$_2$ and MoS$_2$ interface was *in situ* reconstructed into Co-Mo-S by H$_2$ pre-reduction treatment, resulting in a large amount of surface Co-Mo-S active phase toward efficient HDO of p-cresol (Liu et al., 2020). In early electrochemical research, researchers found that sulfur vacancy has a strong adsorption capacity for Co complexes. On the basis of this discovery, Liu et al. prepared a single-layer MoS$_2$ catalyst doped with isolated Co atoms (Co-^{S}MoS$_2$) by hydrothermal treatment of monolayer MoS$_2$ with

TABLE 1 | Comparison of the catalytic performance in the HDO of *p*-cresol for MoS$_2$-based catalysts from the literatures.

Entry	Catalyst	Conditions					Catalytic performance			Ref.
		T (°C)	P (MPa)	t (h)	Catalyst (g)	Reactor type	*p*-cresol (mmol)	Conv. (%)	Toluene Select. (%)	
1	Co/MoS$_2$-FL-DR	230	3.0	\	0.5	Continuous	2.3	100	99.7	Zhang et al. (2021a)
2	Co/nano-MoS$_2$	220	3.0	\	0.5	Continuous	2.3	98.7	98.9	Cao et al. (2021a)
3	Co-Mo-S	275	4.0	4	0.3	Batch	138.9	100	92.2	Wang et al. (2014b)
4	CoS$_2$/MoS$_2$	250	4.0	1	0.03	Batch	44.4	98	99	Wang et al. (2016b)
5	Flower-like Co-doped MoS$_2$	300	4.0	4	0.02	Batch	5.2	99.8	97.9	Song et al. (2018a)
6	CoMoS	300	4.0	3	0.02	Batch	5.0	100	100	Song et al. (2018b)
7	Flower-like Co-Mo-S	275	4.0	5	0.1	Batch	133.3	85.6	97.5	Wang et al. (2016c)
8	CoMo/Al$_2$O$_3$	360	7.0	1	1.0	Batch	4.0	95	18	Wandas et al. (1996)
9	CoMoS	300	3.0	6	0.01	Batch	1.3	99.1	94.4	Liu et al. (2020)
10	Co-^{S}MoS$_2$	180	3.0	8	0.02	Batch	2.6	97.6	98.4	Liu et al. (2017)
11	Co-MoS$_{2-x}$	120	3.0	6	0.04	Batch	5.2	97.4	99.5	Wu et al. (2020)
12	Pt-MoS$_{2-x}$	120	5.0	10	0.2	Batch	2.4	100	3.7	Wu et al. (2022)
13	Ni-Mo-S	300	4.0	6	0.6	Batch	125	99.9	28.8	Wang et al. (2015a)
14	NiS$_2$//MoS$_2$	275	4.0	4	0.3	Batch	125	95.8	35.6	Wang et al. (2016a)
15	NiMoWS	300	3.0	5	0.2	Batch	25.6	97.8	87.2	Wang et al. (2014a)
16	Ni-Mo-W-S	300	4.0	6	0.2	Batch	41.7	97.9	30.1	Wang et al. (2014c)
17	Fe/MoS$_2$	250	4.0	3	0.03	Batch	29.6	96.3	94.5	Guo et al. (2019)

Co(thiourea)$_4^{2+}$. The EXAFS and HAADF-STEM characterization results confirmed that single Co atoms were covalently bonded to the sulfur vacancies on the basal planes to form a new Co-S-Mo active phase (Liu et al., 2017). The theoretical calculation results showed that the proximal sites around Co-S-Mo were energetically favorable for the formation of sulfur vacancies, thus making Co-^{S}MoS$_2$ an extremely active and selective catalyst in the HDO reactions. Meanwhile, superior stability was also observed due to the low operating temperature at 180°C. An *in situ* interfacial reactions was adopted to prepare MoS$_{2-x}$ catalyst supported by Co nanoparticles (Co NPs-MoS$_2$) based on the reducibility of defection-rich MoS$_{2-x}$ (Wu et al., 2020). The HRTEM and DFT results showed that Co NPs were energetically favored to adsorb on the defects to form a metal-vacancy interface. Also, the Co NPs promoted the formation of new sulfur vacancies at the proximal sites as evidenced by TPR results. More importantly, the DFT results showed that the adsorption energy of 4-methylphenol and the reaction energy barrier were significantly decreased on Co NPs-MoS$_2$, which endowed the catalyst exhibit the lowest reaction temperature (120°C) up to now.

Ni is also a commonly used promoter to improve the catalytic performance of MoS$_2$. However, Ni-promoted MoS$_2$ catalysts usually have high hydrogenation activity because Ni is more capable of adsorbing and activating H$_2$. Ni-Mo-S and NiS$_2$//MoS$_2$ catalysts with the same Ni/Mo molar ratio by one-step hydrothermal method and two-step hydrothermal method were prepared, respectively (Wang et al., 2015a). It was found that NiS$_2$//MoS$_2$ showed a much higher p-cresol conversion than Ni-Mo-S, which indicated that the synergistic effect between Ni

promoters and MoS$_2$ came from the spillover hydrogen rather than the Ni-Mo-S phase (Wang et al., 2016a). The optimized NiS$_2$//MoS$_2$ showed a p-cresol conversion of 95.8% and a methylcyclohexane selectivity of 55.6% at 275°C for 4 h. Although Fe is much cheaper than Co and Ni, Fe has attracted little research interest because of its poor performance in promoting MoS$_2$. Recently, Fe-promoted MoS$_2$ catalysts by one-step hydrothermal method, which exhibited separated FeS$_2$ and MoS$_2$ phases were prepared (Guo et al., 2019). However, the FeS$_2$ was transformed into FeS after a pretreatment in H$_2$ and the HDO activity was significantly enhanced. The authors concluded that FeS was a better promoter than FeS$_2$ for MoS$_2$, and acts as a donor of activated hydrogen in the HDO reaction.

According to a recent report, precious metals such as Pt can also play a synergistic role in promoting the HDO activity of unsupported MoS$_2$ catalysts. A metal insertion-deinsertion strategy was adopted to prepare Pt-MoS$_{2-x}$ catalysts in which Pt^{4+} initially substituted the Mo^{4+} on the basal planes and then Pt species was deinserted to be anchored on the adjacent sites (Wu et al., 2022). As a result, a large number of edge sites were created at the proximal sites of the Pt-edge interface within the basal planes which are originally inert. Thus, the optimized Pt-MoS$_{2-x}$ catalyst displayed extraordinary catalytic activity in the HDO of p-cresol, which achieved a conversion of 100% and a methylcyclohexane selectivity of 96.3% at 120°C. The DFT calculation results showed that the metal-edge interface was beneficial for lowering both the adsorption energy of reactants and the energy barrier of the HDO reaction. We have summarized the HDO performance of some unsupported MoS$_2$-based catalysts in the past decade utilizing p-cresol as a probe molecule (**Table 1**).

DEACTIVATION MECHANISM AND MEASURES TO INHIBIT DEACTIVATION

Deactivation is a serious problem when MoS$_2$-based catalysts are applied in the HDO reactions, which include two main causes such as sulfur loss and coking (**Figure 1D**). As the bio-oil does not contain sulfur, sulfur will be gradually lost due to S-O exchange, and the presence of H$_2$O product will aggravate this process. Therefore, the following strategies have been carried out in order to inhibit catalyst deactivation due to sulfur loss. The first type of method is the co-feeding of sulfur-containing compounds such as H$_2$S or benzothiophene. Adding an appropriate amount of H$_2$S to the reaction system could well maintain the activity and stability of NiMo and CoMo catalysts due to the increased concentration of -SH groups (Dabros et al., 2018). A small amount of benzothiophene in the feed is helpful to inhibit catalyst deactivation because the H$_2$S molecules produced by HDS of benzothiophene will adsorb on the active sites and weaken the negative effect of water (Wang et al., 2018). However, excessive benzothiophene introduction resulted in a decrease in HDO activity due to competitive adsorption between H$_2$S and p-cresol. More importantly, it should be noted that contamination of bio-oil products is inevitable by adding sulfiding agents. To overcome this shortcoming, a surface hydrophobic treatment strategy was proposed in which the generated water is removed from the surface immediately, thus improving the cyclic stability of MoS$_2$-based HDO catalysts. For example, the surface hydrophobicity of MoS$_2$ was enhanced significantly by silicomolybdic acid modification as revealed by the contact angle results (Wu et al., 2019). After recycling for three runs, the p-cresol conversion of the modified MoS$_2$ catalyst only showed a slight loss of 0.4%, which is much lower than that of the original MoS$_2$ (9.2%). Carbon coating is another surface hydrophobic modification method to prevent sulfur loss in the HDO process. Amorphous carbon-coated CoS$_2$-MoS$_2$ catalysts were prepared by adding polyvinylpyrrolidone (PVP) to the hydrothermal system (Wang et al., 2017). The hydrophobic carbon layer covered on the surface effectively prevented the oxidation caused by water, and the HDO activity of CoS$_2$-MoS$_2$ decreased by only 2.6% after recycling three times. Lowering the reaction temperature is also an effective way to inhibit sulfur loss. The Co-^{S}MoS$_2$ maintained excellent HDO activity and selectivity without sulfur loss after using seven cycles, which is attributed to the greatly decreased reaction temperature from 300°C of traditional CoMo/Al$_2$O$_3$ catalysts to 180°C (Liu et al., 2017). The Co NPs-MoS$_2$ and Pt-MoS$_{2-x}$ catalysts reported (Wu et al., 2020; Wu et al., 2022) also showed superior stability in the HDO of p-cresol due to the further lowered operating temperature of 120°C.

Coking is a general problem for catalyst deactivation by decreasing the surface area and blocking the active sites. The total pore volume of the Co-MoS$_2$/Al$_2$O$_3$ catalyst was reduced by 1/3 due to carbon deposition in the initial stage (Fonseca et al., 1996). In our previous works, the Raman characterization of spent Co/MoS$_2$ catalysts after running for 72 h at 220°C showed typical peaks at 1,350 and 1,586 cm^{-1} attributed to graphitic carbon species. In addition, the coke content was 4.4 wt.% determined by CHNS analysis, and the combination of carbon deposition and sulfur loss jointly resulted in the decrease of HDO conversion by 2.8% (Zhang C. et al., 2021). In order to reduce the formation of coking, some measures could be adopted such as reducing the acidity of catalysts or increasing the hydrogen pressure.

CONCLUSION AND FUTURE PERSPECTIVES

In this mini-review, we summarized the recent progress of unsupported MoS$_2$-based catalysts in the HDO of bio-oil. Reducing the layer number of MoS$_2$, especially to a single-layer could significantly improve the HDO activity. Creating defects within the basal planes is also an effective way to enhance the HDO activity, especially for metal-promoted MoS$_2$ catalysts because it provides additional anchoring sites. The regulation of HDO selectivity is easily realized by just adjusting the layer number of MoS$_2$. Co and Pt doping can both significantly improve the HDO activity and stability of MoS$_2$ catalysts, while Co-promoted catalysts are more potential due to the minimized H$_2$ consumption. Four different active phases including Co-Mo-S, CoS$_2$-MoS$_2$, Co-S-Mo, and Co NPs-MoS$_2$ have been proposed to construct highly efficient CoMo bimetallic catalysts. Sulfur loss and coking are the main factors to cause deactivation, which could be alleviated by co-feeding of sulfiding agents, surface hydrophobic treatment, and lowering the reaction temperature.

Although tremendous progress has been achieved in the construction of efficient MoS$_2$-based HDO catalysts, there are still some challenges to be solved in future research. 1) Simple synthesis of monolayer MoS$_2$ nanosheets with rich defects which are ideal supports to prepare CoMo bimetallic catalysts. 2) Experimental and theoretical comparison of the four different active phases of Co-promoted catalysts to figure out which model is best for designing highly efficient CoMo bimetallic catalysts. 3) Deactivation study by using real bio-oil as feedstock and determination of the sulfur loss and coke content.

AUTHOR CONTRIBUTIONS

JC and YZ drafted the manuscript. LW and CoZ participated in the manuscript revision. CeZ revised the manuscript and provided the funding support.

FUNDING

REFERENCES

Cao, J., Li, A., Zhang, Y., Mu, L., Huang, X., Li, Y., et al. (2021a). Highly Efficient Unsupported Co-doped Nano-MoS$_2$ Catalysts for P-Cresol Hydrodeoxygenation. *Mol. Catal.* 505, 111507. doi:10.1016/j.mcat.2021.111507

Cao, J., Xia, J., Zhang, Y., Liu, X., Bai, L., Xu, J., et al. (2021b). Influence of the Alumina Crystal Phase on the Performance of CoMo/Al$_2$O$_3$ Catalysts for the Selective Hydrodesulfurization of Fluid Catalytic Cracking Naphtha. *Fuel* 289, 119843. doi:10.1016/j.fuel.2020.119843

Cao, J., Zhang, Y., Zhang, C., Cai, L., Li, Z., and Zhou, C. (2021c). Construction of Defect-Rich 1T-MoS$_2$ towards Efficient Electrocatalytic Hydrogen Evolution: Recent Advances and Future Perspectives. *Surfaces Interfaces* 25, 101305. doi:10.1016/j.surfin.2021.101305

Daage, M., and Chianelli, R. R. (1994). Structure-function Relations in Molybdenum Sulfide Catalysts: The "Rim-Edge" Model. *J. Catal.* 149, 414–427. doi:10.1006/jcat.1994.1308

Dabros, T. M. H., Gaur, A., Pintos, D. G., Sprenger, P., Høj, M., Hansen, T. W., et al. (2018). Influence of H$_2$O and H$_2$S on the Composition, Activity, and Stability of Sulfided Mo, CoMo, and NiMo Supported on MgAl$_2$O$_4$ for Hydrodeoxygenation of Ethylene Glycol. *Appl. Catal. A General* 551, 106–121. doi:10.1016/j.apcata.2017.12.008

Fonseca, A., Zeuthen, P., and Nagy, J. B. (1996). 13C n.m.R. Quantitative Analysis of Catalyst Carbon Deposits. *Fuel* 75, 1363–1376. doi:10.1016/0016-2361(96)00106-8

Genuit, D., Afanasiev, P., and Vrinat, M. (2005). Solution Syntheses of Unsupported Co(Ni)-Mo-S Hydrotreating Catalysts. *J. Catal.* 235, 302–317. doi:10.1016/j.jcat.2005.08.016

Guo, X., Wang, W., Wu, K., Huang, Y., Shi, Q., and Yang, Y. (2019). Preparation of Fe Promoted MoS$_2$ Catalysts for the Hydrodeoxygenation of P-Cresol as a Model Compound of Lignin-Derived Bio-Oil. *Biomass Bioenergy* 125, 34–40. doi:10.1016/j.biombioe.2019.04.014

Jiang, S., Ji, N., Diao, X., Li, H., Rong, Y., Lei, Y., et al. (2021). Vacancy Engineering in Transition Metal Sulfide and Oxide Catalysts for Hydrodeoxygenation of Lignin-Derived Oxygenates. *ChemSusChem* 14, 4377–4396. doi:10.1002/cssc.202101362

Lai, W., Chen, Z., Zhu, J., Yang, L., Zheng, J., Yi, X., et al. (2016). A NiMoS Flower-like Structure with Self-Assembled Nanosheets as High-Performance Hydrodesulfurization Catalysts. *Nanoscale* 8, 3823–3833. doi:10.1039/c5nr08841k

Lauritsen, J. V., Nyberg, M., Nørskov, J. K., Clausen, B. S., Topsøe, H., Lægsgaard, E., et al. (2004). Hydrodesulfurization Reaction Pathways on MoS$_2$ Nanoclusters Revealed by Scanning Tunneling Microscopy. *J. Catal.* 224, 94–106. doi:10.1016/j.jcat.2004.02.009

Li, L., Qin, Z., Ries, L., Hong, S., Michel, T., Yang, J., et al. (2019). Role of Sulfur Vacancies and Undercoordinated Mo Regions in MoS$_2$ Nanosheets toward the Evolution of Hydrogen. *ACS Nano* 13, 6824–6834. doi:10.1021/acsnano.9b01583

Liu, G., Ma, H., Teixeira, I., Sun, Z., Xia, Q., Hong, X., et al. (2016). Hydrazine-Assisted Liquid Exfoliation of MoS$_2$ for Catalytic Hydrodeoxygenation of 4-Methylphenol. *Chem. Eur. J.* 22, 2910–2914. doi:10.1002/chem.201504009

Liu, G., Robertson, A. W., Li, M. M.-J., Kuo, W. C. H., Darby, M. T., Muhieddine, M. H., et al. (2017). MoS$_2$ Monolayer Catalyst Doped with Isolated Co Atoms for the Hydrodeoxygenation Reaction. *Nat. Chem.* 9, 810–816. doi:10.1038/nchem.2740

Liu, X., Hou, X., Zhang, Y., Yuan, H., Hong, X., and Liu, G. (2020). *In Situ* formation of CoMoS Interfaces for Selective Hydrodeoxygenation of P-Cresol to Toluene. *Ind. Eng. Chem. Res.* 59, 15921–15928. doi:10.1021/acs.iecr.0c03589

Mortensen, P. M., Grunwaldt, J.-D., Jensen, P. A., Knudsen, K. G., and Jensen, A. D. (2011). A Review of Catalytic Upgrading of Bio-Oil to Engine Fuels. *Appl. Catal. A General* 407, 1–19. doi:10.1016/j.apcata.2011.08.046

Qu, L., Jiang, X., Zhang, Z., Zhang, X.-g., Song, G.-y., Wang, H.-l., et al. (2021). A Review of Hydrodeoxygenation of Bio-Oil: Model Compounds, Catalysts, and Equipment. *Green Chem.* 23, 9348–9376. doi:10.1039/d1gc03183j

Song, W., Nie, T., Lai, W., Yang, W., and Jiang, X. (2018a). Tailoring the Morphology of Co-doped MoS$_2$ for Enhanced Hydrodeoxygenation Performance of P-Cresol. *CrystEngComm* 20, 4069–4074. doi:10.1039/c8ce00510a

Song, W., Zhou, S., Hu, S., Lai, W., Lian, Y., Wang, J., et al. (2018b). Surface Engineering of CoMoS Nanosulfide for Hydrodeoxygenation of Lignin-Derived Phenols to Arenes. *ACS Catal.* 9, 259–268. doi:10.1021/acscatal.8b03402

Tao, L., Duan, X., Wang, C., Duan, X., and Wang, S. (2015). Plasma-engineered MoS$_2$ Thin-Film as an Efficient Electrocatalyst for Hydrogen Evolution Reaction. *Chem. Commun.* 51, 7470–7473. doi:10.1039/C5CC01981H

Wandas, R., Surygala, J., and Śliwka, E. (1996). Conversion of Cresols and Naphthalene in the Hydroprocessing of Three-Component Model Mixtures Simulating Fast Pyrolysis Tars. *Fuel* 75, 687–694. doi:10.1016/0016-2361(96)00011-7

Wang, C., Wang, D., Wu, Z., Wang, Z., Tang, C., and Zhou, P. (2014a). Effect of W Addition on the Hydrodeoxygenation of 4-methylphenol over Unsupported NiMo Sulfide Catalysts. *Appl. Catal. A General* 476, 61–67. doi:10.1016/j.apcata.2014.02.010

Wang, L., Zhang, Y., Zhang, Y., Jiang, Z., and Li, C. (2009). Ultra-deep Hydrodesulfurization of Diesel Fuels on Trimetallic NiMoW Sulfide Catalysts. *Chem. Eur. J.* 15, 12571–12575. doi:10.1002/chem.200901997

Wang, W., Li, L., Tan, S., Wu, K., Zhu, G., Liu, Y., et al. (2016a). Preparation of NiS$_2$//MoS$_2$ Catalysts by Two-step Hydrothermal Method and Their Enhanced Activity for Hydrodeoxygenation of P-Cresol. *Fuel* 179, 1–9. doi:10.1016/j.fuel.2016.03.068

Wang, W., Li, L., Wu, K., Zhang, K., Jie, J., and Yang, Y. (2015a). Preparation of Ni-Mo-S Catalysts by Hydrothermal Method and Their Hydrodeoxygenation Properties. *Appl. Catal. A General* 495, 8–16. doi:10.1016/j.apcata.2015.01.041

Wang, W., Li, L., Wu, K., Zhu, G., Tan, S., Li, W., et al. (2015b). Hydrothermal Synthesis of Bimodal Mesoporous MoS$_2$ Nanosheets and Their Hydrodeoxygenation Properties. *RSC Adv.* 5, 61799–61807. doi:10.1039/c5ra09690a

Wang, W., Li, L., Wu, K., Zhu, G., Tan, S., Liu, Y., et al. (2016b). Highly Selective Catalytic Conversion of Phenols to Aromatic Hydrocarbons on CoS$_2$/MoS$_2$ Synthesized Using a Two Step Hydrothermal Method. *RSC Adv.* 6, 31265–31271. doi:10.1039/c5ra27066a

Wang, W., Tan, S., Wu, K., Zhu, G., Liu, Y., Tan, L., et al. (2018). Hydrodeoxygenation of P-Cresol as a Model Compound for Bio-Oil on MoS$_2$: Effects of Water and Benzothiophene on the Activity and Structure of Catalyst. *Fuel* 214, 480–488. doi:10.1016/j.fuel.2017.11.067

Wang, W., Wu, K., Tan, S., and Yang, Y. (2017). Hydrothermal Synthesis of Carbon-Coated CoS$_2$-MoS$_2$ Catalysts with Enhanced Hydrophobicity and Hydrodeoxygenation Activity. *ACS Sustain. Chem. Eng.* 5, 8602–8609. doi:10.1021/acssuschemeng.7b01087

Wang, W., Zhang, K., Li, L., Wu, K., Liu, P., and Yang, Y. (2014b). Synthesis of Highly Active Co-mo-S Unsupported Catalysts by a One-step Hydrothermal Method for P-Cresol Hydrodeoxygenation. *Ind. Eng. Chem. Res.* 53, 19001–19009. doi:10.1021/ie5032698

Wang, W., Zhang, K., Qiao, Z., Li, L., Liu, P., and Yang, Y. (2014c). Hydrodeoxygenation of P-Cresol on Unsupported Ni-W-Mo-S Catalysts Prepared by One Step Hydrothermal Method. *Catal. Commun.* 56, 17–22. doi:10.1016/j.catcom.2014.06.024

Wang, W., Zhang, K., Qiao, Z., Li, L., Liu, P., and Yang, Y. (2014d). Influence of Surfactants on the Synthesis of MoS$_2$ Catalysts and Their Activities in the Hydrodeoxygenation of 4-Methylphenol. *Ind. Eng. Chem. Res.* 53, 10301–10309. doi:10.1021/ie500830f

Wang, W., Zhu, G., Li, L., Tan, S., Wu, K., Zhang, X., et al. (2016c). Facile Hydrothermal Synthesis of Flower-like Co-mo-S Catalysts and Their High Activities in the Hydrodeoxygenation of P-Cresol and Hydrodesulfurization of Benzothiophene. *Fuel* 174, 1–8. doi:10.1016/j.fuel.2016.01.074

Wang, X., Zhang, Y., Si, H., Zhang, Q., Wu, J., Gao, L., et al. (2020). Single-Atom Vacancy Defect to Trigger High-Efficiency Hydrogen Evolution of MoS$_2$. *J. Am. Chem. Soc.* 142, 4298–4308. doi:10.1021/jacs.9b12113

Wu, K., Li, X., Wang, W., Huang, Y., Jiang, Q., Li, W., et al. (2022). Creating Edge Sites within the Basal Plane of a MoS$_2$ Catalyst for Substantially Enhanced Hydrodeoxygenation Activity. *ACS Catal.* 12, 8–17. doi:10.1021/acscatal.1c03669

Wu, K., Wang, C., Chen, X., Wang, W., and Yang, Y. (2019). Facile Synthesis of Hydrophobic MoS$_2$ and its Activity and Stability in the Hydrodeoxygenation Reaction. *New J. Chem.* 43, 2734–2739. doi:10.1039/C8NJ05980B

Wu, K., Wang, W., Guo, H., Yang, Y., Huang, Y., Li, W., et al. (2020). Engineering Co Nanoparticles Supported on Defect MoS$_2$-X for Mild Deoxygenation of

Lignin-Derived Phenols to Arenes. *ACS Energy Lett.* 5, 1330–1336. doi:10.1021/acsenergylett.0c00411

Yi, Y., Jin, X., Wang, L., Zhang, Q., Xiong, G., and Liang, C. (2011). Preparation of Unsupported Ni-Mo-S Catalysts for Hydrodesulfurization of Dibenzothiophene by Thermal Decomposition of Tetramethylammonium Thiomolybdates. *Catal. Today* 175, 460–466. doi:10.1016/j.cattod.2011.04.039

Yoosuk, B., Tumnantong, D., and Prasassarakich, P. (2012). Unsupported MoS₂ and CoMoS₂ Catalysts for Hydrodeoxygenation of Phenol. *Chem. Eng. Sci.* 79, 1–7. doi:10.1016/j.ces.2012.05.020

Zhang, C., Li, P., Liu, X., Liu, T., Jiang, Z., and Li, C. (2018a). Morphology-performance Relation of (Co)MoS₂ Catalysts in the Hydrodesulfurization of FCC Gasoline. *Appl. Catal. A General* 556, 20–28. doi:10.1016/j.apcata.2018.02.026

Zhang, C., Liu, K., Zhang, Y., Mu, L., Zhang, Z., Huang, J., et al. (2021a). Co-promoted Few-Layer and Defect-Rich MoS₂ for Enhanced Hydrodeoxygenation of P-Cresol. *Appl. Catal. A General* 621, 118175. doi:10.1016/j.apcata.2021.118175

Zhang, H., Lin, H., Zheng, Y., Hu, Y., and MacLennan, A. (2015). Understanding of the Effect of Synthesis Temperature on the Crystallization and Activity of Nano-MoS₂ Catalyst. *Appl. Catal. B Environ.* 165, 537–546. doi:10.1016/j.apcatb.2014.10.046

Zhang, W., Xie, Z., Wu, X., Sun, M., Deng, X., Liu, C., et al. (2018b). Acid-engineered Defective MoS₂ as an Efficient Electrocatalyst for Hydrogen Evolution Reaction. *Mater. Lett.* 230, 232–235. doi:10.1016/j.matlet.2018.07.108

Zhang, Y., Liu, T., Xia, Q., Jia, H., Hong, X., and Liu, G. (2021b). Tailoring of Surface Acidic Sites in Co-MoS₂ Catalysts for Hydrodeoxygenation Reaction. *J. Phys. Chem. Lett.* 12, 5668–5674. doi:10.1021/acs.jpclett.1c01201

Zhu, C., Gao, D., Ding, J., Chao, D., and Wang, J. (2018). TMD-based Highly Efficient Electrocatalysts Developed by Combined Computational and Experimental Approaches. *Chem. Soc. Rev.* 47, 4332–4356. doi:10.1039/c7cs00705a

Preparation of Activated Carbon-Based Solid Sulfonic Acid and Its Catalytic Performance in Biodiesel Preparation

Yuanzheng Pi[1], Wenzhu Liu[1,2]*, Jiani Wang[1], Guanmin Peng[1], Dabo Jiang[2], Ruike Guo[1]* and Dulin Yin[2]

[1]College of Chemistry and Materials Engineering, Huaihua University, Huaihua, China, [2]National and Local Joint Engineering Laboratory for New Petro-Chemical Materials and Fine Utilization of Resources, Hunan Normal University, Changsha, China

With activated carbon as raw material, AC-Ph-SO$_3$H was prepared after oxidation with nitric acid, modification with halogenated benzene and sulfonation with concentrated sulfuric acid. After modified by 10% bromobenzene with toluene as a solvent for 5 h, followed sulfonation with concentrated sulfuric acid at 150°C, the -SO$_3$H content of prepared AC-Ph-SO$_3$H was 0.64 mmol/g. Acid content test, infrared spectroscopy and Raman spectroscopy detection proved that the surface of AC-Ph-SO$_3$H was successfully grafted with -SO$_3$H group. When used as a catalyst for the methylation of palmitate acid, the catalytic performance of AC-Ph-SO$_3$H was explored. When the reaction time was 6 h, the amount of catalyst acid accounted for 2.5 wt% of palmitic acid, and the molar ratio of methanol/palmitic acid was 40, the esterification rate of palmitic acid was 95.2% and the yield of methyl palmitate was 94.2%, which was much better than those of its precursors AC, AC-O, and AC-Ph (both about 4.5%). AC-Ph-SO$_3$H exhibited certain stability in the esterification reaction system and the conversion rate of palmitic acid was still above 80% after three reuses.

Keywords: halogenated benzene, activated carbon, sulfonic acid catalyst, palmitic acid, biodiesel

1 INTRODUCTION

Fossil energy plays an extremely important role in the national economy and people's livelihood, and is a strong driving force for human progress and social development (Darda et al., 2019; Antar et al., 2021). With the rapid development of the global industry, the consumption of oil resources is increasing day by day, resulting in a decrease in oil reserves and serious environmental problems. More and more countries have begun to pay attention to new energy sources that can replace fossil energy. Biodiesel is considered to be an effective substitute for fossil energy with the advantages of high safety in use, excellent environmental protection properties, good ignition performance and good lubricity (Gebremariam and Marchetti, 2018a; Singh et al., 2020). Homogeneous acid catalysts such as sulfuric acid, nitric acid, and phosphoric acid are often used in the traditional production process of biodiesel (Su, 2013; Gebremariam and Marchetti, 2018b). However, homogeneous acid catalysts have some unavoidable defects, such as strong protonic acid catalysts that are easy to corrode production equipment during the reaction process, difficult to separate and recycle when mixed with products after the reaction, and generate waste acid and pollute the environment, etc. (Wancura et al., 2020) Therefore, in the pursuit of green and sustainable development, the application of homogeneous acid catalysts is becoming less and less popular.

Heterogeneous catalysts, which can perfectly avoid the above problems, have attracted more and more attention of researchers (Jayakumar et al., 2021; Esmi et al., 2022). However, many existing heterogeneous catalysts also have some shortcomings, such as high catalyst preparation cost, low catalytic activity, slightly poor reuse performance, long time and high temperature for catalytic reaction, etc. (Hsiao et al., 2020; Mukhtar et al., 2022) Therefore, the development and preparation of highly active, low-cost, and multi-functional heterogeneous catalysts used in catalyzing the synthesis of biodiesel, has far-reaching significance for realizing the effective replacement of fossil energy and promoting social development.

For the advantages of high acid density, good thermodynamic stability, excellent surface hydrophobicity, high chemical stability and other characteristics, carbon-based solid acids have gradually been developed into popular catalysts that attract the interest of many researchers (Vakros, 2018; Tang and Niu, 2019; Tobío-Pérez et al., 2022). In addition, carbon-based solid acid catalysts can be prepared using inexpensive and renewable biomass and its derivatives as raw materials (Rocha et al., 2019; Wilk et al., 2020), and the required production cost is low. Rocha (Rocha et al., 2019) prepared sulfonated activated carbon from corn cobs and used it as catalyst for biodiesel production using microwave-assisted transesterification of soybean oil with ethanol, and the yield of product was 88.7%. While there are some problems such as poor stability and easy shedding of acidic functional groups due to the leaching of–SO₃H groups or small molecular fragment on surface structure of amorphous carbon (Ma et al., 2020; Yusuff et al., 2022). Tang (Tang and Niu, 2019) synthesized a series of carbon-based solid acid catalysts from bamboo, which showed a strong acid density of 1.28 mmol g⁻¹ and excellent catalytic performance in esterification reaction, but the biodiesel yield declines to 83.7% after fourth reused cycle of the catalyst. Ma et al. (2020) produced microporous lignin-derived carbon-based solid acid with lignin as a carbon precursor, and used it in the esterification of oleic acid with methanol. The conversion of oleic acid reached 92.3% but reduced to 72.9% after recycling for five times. Using skeleton-stabilized activated carbon materials to prepare solid acids to avoid the shedding of surface functional groups is an effective way to prepare carbon-based solid acids. But due to the stable structure of the activated carbon surface, there are few sulfonable functional groups on the surface, and it is difficult to be grafted with strong acid functional groups directly with sulfonation. Therefore, the development of new methods to introduce sulfonable functional groups on the surface of activated carbon is of great significance for the preparation of activated carbon-based solid acids.

In this research, in view of the fact that there are basically no sulfonated sites on the surface of activated carbon (AC) materials, oxidation with nitric acid was used to destroyed the surface structure of activated carbon and lead to generate a certain amount of oxygen-containing functional groups, which can be coupled with halobenzenes to create sulfonated sites on the surface. Then activated carbon-based solid sulfonic acid (denoted as AC-Ph-SO₃H) was further prepared by using concentrated sulfuric acid as sulfonating agent. The effect of modification conditions on the content of sulfonic acid groups on AC surface was investigated, and its stability in different solvents was also investigated. The catalytic performance of the prepared AC-Ph-SO₃H in the preparation of biodiesel by methyl esterification of palmitic acid was investigated and discussed.

2 EXPERIMENTAL

2.1 Materials
Activated carbon (AR, Xilong Chemical Co., Ltd., China); concentrated hydrochloric acid (AR, Chongqing Chuandong Chemical Co., Ltd., China); concentrated sulfuric acid (98%) (AR, Chengdu Jinshan Chemical Reagent Co., Ltd., China); concentrated nitric acid (AR, Guangdong Guanghua Technology Co., Ltd.,China). Other reagents were all of analytical grade and purchased from Sinopharm Group Chemical Reagent Co., Ltd., China.

2.2 Preparation of AC-Ph-SO₃H
With AC as raw material, AC-Ph-SO₃H was prepared by sulfonation with concentrated sulfuric acid after oxidizing with nitric acid and modified by halogenated benzene. The general process of preparation was as follows: 2 g activated carbon and 20 ml 12 mol/L nitric acid was added into a three-necked flask equipped with a condenser and a thermometer and was reacted at 100°C for 8 h. After the reaction was completed, the oxidized activated carbon (denoted as AC-O) was prepared by washing with water and drying. Then 2 g AC-O was added into 50 ml of 0.1 mol/L NaOH aqueous solution, stirred for 12 h, filtered, washed and dried to obtain AC-ONa. 2 g AC-ONa was added into 20 ml halobenzene solution of a certain concentration, reacted at reflux temperature for a certain time, followed by being filtered, washed and dried to prepare halobenzene modified activated carbon (denoted as AC-Ph). 2 g of AC-Ph was added to 20 ml of concentrated sulfuric acid, and stirred at 150°C for 4 h. After the reaction was completed, AC-Ph-SO₃H was prepared after being filtered and washed until neutral.

2.3 Structural Analysis of AC-Ph-SO₃H
2.3.1 Determination of Acid Functional Group Content
The acid contents of samples were analyzed using Boehm titration (Scheibe et al., 2010). The specific methods include: 1) Determination of strong acid content: 50 mg of sample was added into 20 ml 2 mol/L NaCl and ultrasonically treated for 30 min, followed with filtered and washed with water. Then 0.01 mol/L NaOH was used to titrate the filtrate with phenolphthalein as an indicator to determine the content of strong acids such as -SO₃H; 2) Determination of the content of medium and strong acids: 50 mg of the sample was added into 20 ml of 0.01 mol/L NaHCO₃ and ultrasonically treated for 30 min, followed with filtered and washed with water. Then the filtrate was titrated with 0.01 mol/L HCl with bromocresol green-methyl red as an indicator to determine the contents of strong acids such as -SO₃H and medium-strong acids such as -COOH.

2.3.2 Stability Test of Acidic Functional Group
The stability of -COOH and -SO₃H in different solvents was tested as follows. 2 g carbon material and 20 ml different solvents were added to the reflux condensation device. After refluxing for a

certain time, the content of acidic functional groups of the material was measured after being filtrated, washed with ethanol and distilled water and dried.

2.3.3 Analysis of Surface Structure of AC-Ph-SO₃H

The functional groups on the surface of the samples were analyzed by infrared spectroscopy. The used infrared spectrometer was Perkin Elmer 283 with DTGS/KBr detector. The test conditions were: the measurement wavenumber range was 4,000–400 cm^{-1}, the resolution was 4 cm^{-1}, and the acquisition rate was 20 times/min. The carbon skeleton of activated carbon before and after modification was tested by DXR laser microscope Raman spectrometer (laser wavelength 780 nm), the wavelength range was 50–3,250 cm^{-1}, the exposure time was 5 s, the exposure times were 10 times, and the laser intensity was 5 mW.

2.4 Catalytic Performance of AC-Ph-SO₃H in the Methylation of Palmitate

The catalytic performance of AC-Ph-SO₃H in the preparation of biodiesel from methylation of palmitic acid was investigated. The conditions of reaction time, catalyst dosage and acid-alcohol molar ratio during the methylation reaction were studied. The typical catalytic process was as follows: 0.01 mol of palmitic acid, 0.4 mol of methanol and catalyst accounted for 2.5 wt% of palmitic acid was added into a three-necked flask equipped with a thermometer and a reflux condenser for 6 h at reflux temperature.

3 RESULTS AND DISCUSSION

3.1 Preparation of AC-Ph-SO₃H

The modification process of halogenated benzene coupled with -COOH mainly affected the content of sulfonatable groups on the surface of the materials, which had an important effect on the subsequent sulfonation process. Therefore, the effect of different halogenated benzenes (including iodized benzene, brominated benzene and chlorinated benzene) on the content of -COOH on AC-O surface at the reflux temperature of different solvents was investigated. In the catalytic process, the strong acid content in the acidic carbon-based solid acid will significantly affect the catalytic effect. Therefore, the influence of the concentration of halogenated benzene, the modification reaction time of halogenated benzene and the sulfonation temperature of concentrated sulfuric acid on the content of -SO₃H during the preparation of AC-Ph-SO₃H were investigated.

3.1.1 Coupling Effect of Halogenated Benzene With -COOH in Different Solvents

The effects of halogenated benzenes (PhX) coupling with carboxyl groups on the surface of AC-O at reflux temperatures of different solvents (including cyclohexane, toluene, and DMSO) were investigated. The results were shown in **Table 1**. According to the results, the content of carboxyl groups on the surface of AC-O after oxidation of AC was 0.78 mmol/g. After modification by halogenated benzene in different solvents, the content of carboxyl

TABLE 1 | Density of -COOH in AC-Ph modified with different halogenated benzene

Sample	PhX	solvent	Temp. (°C)	-COOH (mmol/g)
AC-O	/	/	/	0.78
AC-Ph	PhI	Cyclohexane	80	0.62
	PhI	Toluene	110	0.28
	PhI	DMSO	180	0.29
	PhBr	Cyclohexane	80	0.63
	PhBr	Toluene	110	0.30
	PhBr	DMSO	180	0.29
	PhCl	Cyclohexane	80	0.65
	PhCl	Toluene	110	0.53
	PhCl	DMSO	180	0.48

groups on the surface decreased to a certain extent, indicating that the carboxyl groups on the surface of activated carbon was successfully coupled with halogenated benzene during the modification process. When cyclohexane was used as the solvent at 80°C of the reflux temperature, the -COOH content of AC-Ph was 0.62–0.65 mmol/g, which was only about 0.15 mmol/g lower than that of AC-O. When toluene being used as solvent at reflux temperature 110°C and DMSO being used as solvent at reflux temperature 180°C, the -COOH content on the surface of AC-Ph had little difference when modified with the same halogenated benzene. Under these conditions, the minimum content of carboxyl groups on the surface of the modified activated carbon was 0.28 mmol/g, indicating that the carboxyl groups being coupled were about 0.5 mmol/g and most of the carboxyl groups on AC-O had been replaced by benzene rings which can be easily sulfonated by concentrated sulfuric acid. When toluene was used as solvent, the -COOH content on AC-Ph modified by iodobenzene, bromobenzene and chlorobenzene were 0.28, 0.30, and 0.53 mmol/g, respectively. Since iodobenzene and bromobenzene have almost no difference in the modification of AC-O under the reflux condition of toluene, bromobenzene (PhBr) were used as the modification reagent due to its low economic cost and relatively stable performance, and toluene was used as the solvent when modifying AC-O in the follow-up studies. Under the selected conditions, the content of carboxyl groups on the surface of AC-Ph was 0.30 mmol/g, and the content of benzene rings grafted on the surface of activated carbon was about 0.50 mmol/g according to the difference in carboxyl content between AC-O and AC-Ph.

3.1.2 Effect of Bromobenzene Concentration on -SO₃H Content

With bromobenzene as modification reagent and toluene as solvent, the effect of bromobenzene concentration on -SO₃H content of AC-Ph-SO₃H surface was studied. The results were shown in **Figure 1**. According to the results, as the concentration of bromobenzene increased, the content of -SO₃H gradually increased. The concentration of bromobenzene showed a great influence on the -SO₃H groups content on the surface of AC-Ph-SO₃H. When the concentration of bromobenzene was 3%, the content of -SO₃H was only 0.18 mmol/g. While when the concentration of bromobenzene was 10%, the content of -SO₃H on the surface of AC-Ph-SO₃H was 0.64 mmol/g. We
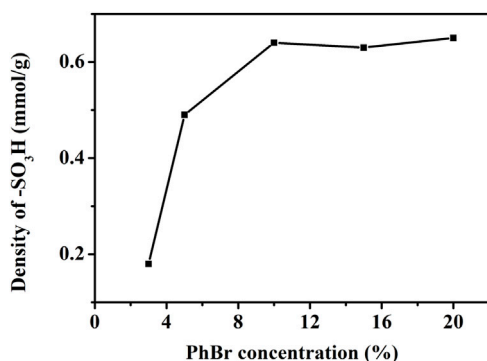
FIGURE 1 | Density of -SO₃H in AC-Ph-SO₃H prepared under different PhBr concentration.
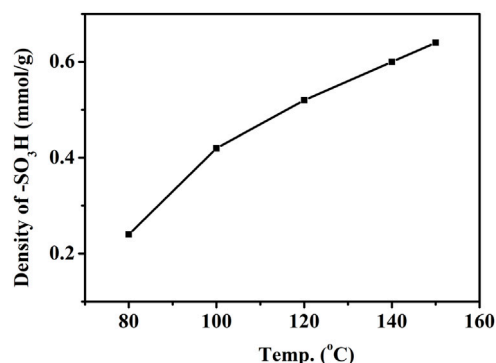

FIGURE 3 | Density of -SO₃H of AC-Ph-SO₃H under different sulfonation temperature.
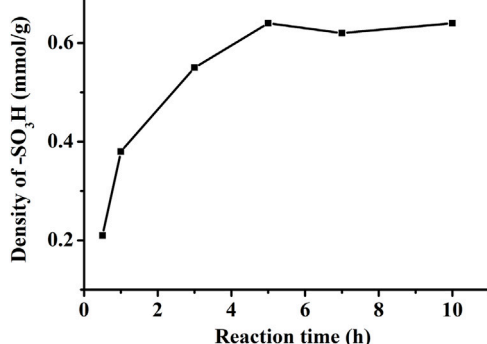

FIGURE 2 | Density of -SO₃H in AC-Ph-SO₃H prepared under different PhBr treated time.

TABLE 2 | Surface -COOH and -SO₃H contents of AC-Ph-SO₃H and its precursors

Sample	Density of -SO₃H (mmol/g)	Density of -COOH (mmol/g)
AC	/	0.03
AC-O	/	0.78
AC-Ph	/	0.30
[a]AC-SO₃H	0.03	0.28
[b]AC-O-SO₃H	0.15	0.69
AC-Ph-SO₃H	0.64	0.54

[a]Sulfonation of unoxidized AC.
[b]Sulfonation of AC-O, without bromobenzene treatment.

speculated that the reason for this result was that the effective collision rate of bromobenzene with AC-O particles in solution was lower at a lower bromobenzene concentrations.

3.1.3 Effect of Modification Time of Bromobenzene on -SO₃H Content

The effect of bromobenzene modification time on -SO₃H content of AC-Ph-SO₃H surface was shown in **Figure 2**. When the modification time was 0.5 h, the surface -SO₃H content of AC-Ph-SO₃H was 0.21 mmol/g and gradually increased with the prolongation of modification time. When the modification time reached 5 h, the content of -SO₃H groups was 0.64 mmol/g and did not change when the time continued to prolong.

3.1.4 Effect of Sulfonation Temperature on -SO₃H Content

The effect of temperature on the -SO₃H content of AC-Ph-SO₃H during sulfonation with concentrated sulfuric acid was shown in **Figure 3**. When the temperature was low, the effect of sulfonation process was poor, and the content of -SO₃H was only 0.24 mmol/g at 80°C. With the increasing of sulfonation temperature, the

content of sulfonic acid groups on the surface of AC-Ph-SO₃H gradually increased, which was 0.64 mmol/g when the temperature reached 150°C.

3.2 Structural Analysis
3.2.1 Surface -COOH and -SO₃H Contents of AC-Ph-SO₃H and Its Precursors

The content of -SO₃H and -COOH on AC-Ph-SO₃H and its precursors in the preparation process were studied. At the same time, in order to verify the effect of bromobenzene modification on the sulfonated sites on the surface of activated carbon, the AC-SO₃H and AC-O-SO₃H prepared from the precursors AC and AC-O under the same sulfonation conditions were compared. The test results were shown in **Table 2**. According to **Table 2**, there was absolutely no -SO₃H detected on the surface of AC-SO₃H prepared by the direct sulfonation of AC. The reason was that there was little sulfonation site because of the fused ring structure on the surface of AC. The AC surface structure was damaged and resulted in a certain amount sulfonatable sites after oxidation with HNO₃, which lead to generating a certain -SO₃H group after sulfonation treatment of AC-O, but the content of -SO₃H was only 0.15 mmol/g. While after being coupled with bromobenzene, the sulfonatable sites was increased on the surface of AC-Ph, so the amount of -SO₃H on AC-Ph-SO₃H surface

TABLE 3 | Stability of AC-Ph-SO₃H in different solvents

Solvent	Temp. (°C)	-SO₃H (mmol/g)		Lost (%)	
		10 h	20 h	10 h	20 h
Non	/	0.64	0.64	/	/
Cyclohexane	81	0.61	0.58	4.7	9.4
Ethanol	78	0.54	0.50	15.6	21.9
Water	100	0.49	0.48	23.4	25.0
Acetic acid	118	0.30	0.25	53.1	60.9

Note: Reaction conditions: 2 g AC-Ph-SO₃H, was added into 20 ml solvents and refluxed under refluxed temperature.

could reach up to 0.64 mmol/g. According to the changes of -COOH content on the surface of the material, it can be seen that a large number of carboxyl groups was generated on the surface of AC during oxidation process; while the content of carboxyl groups decreased after the modification of bromobenzene, and a large number of sulfonic acid groups were generated after sulfonation of AC-Ph, indicating that bromobenzene was successfully combined with the surface carboxyl groups to introduce a large number of sulfonatable sites on the surface. The content of -COOH on the surface of AC-O was 0.78 mmol/g, while that of AC-O-SO₃H obtained by treating AC-O with concentrated sulfuric acid was 0.69 mmol/g, which was slightly lower for the shedding of AC-O during the sulfonation process. After sulfonation of AC-Ph, the -COOH content on the surface of AC-Ph-SO₃H was 0.54 mmol/g, which was higher than 0.30 mmol/g on the surface of AC-Ph. That was because concentrated sulfuric acid had a certain oxidation effect in the process of sulfonation which leaded to generate a certain amount of -COOH.

3.2.2 Stability of AC-Ph-SO₃H in Different Solvents

The stability of the prepared AC-Ph-SO₃H was investigated at reflux temperatures of different polar solvents. The shedding of -SO₃H groups under reflux treatment for 10 and 20 h was investigated respectively, and the results were shown in **Table 3**. As shown, the stability of the -SO₃H group on the surface of AC-Ph-SO₃H gradually decreased with the enhancement of solvent polarity. After refluxing in cyclohexane for 20 h, the -SO₃H content of AC-Ph-SO₃H decreased from 0.64 mmol/g to 0.58 mmol/g with a loss of only 9.4%; while refluxing in acetic acid for 20 h, the -SO₃H content was only 0.25 mmol/g with the loss as high as 60.9%. The reason was that the -SO₃H groups on the surface of the prepared materials were bonded to the surface aromatic rings in the form of C-S bonds, and when the polarity of the solution increased, the small molecular aromatic rings were more likely to fall off on the surface of the materials, resulting in a decrease in the content of -SO₃H groups.

3.2.3 Raman Spectroscopy

The Raman spectra of AC-Ph-SO₃H and its precursors AC, AC-O, AC-Ph were characterized, and the carbon skeleton changes of activated carbon during oxidation, amination, and bromobenzene treatment were analyzed. The results were shown in **Figure 4**. According to **Figure 4**, there were mainly two broad peaks at 1,586 and 1,336 cm⁻¹ in all carbon materials, of which the peak at
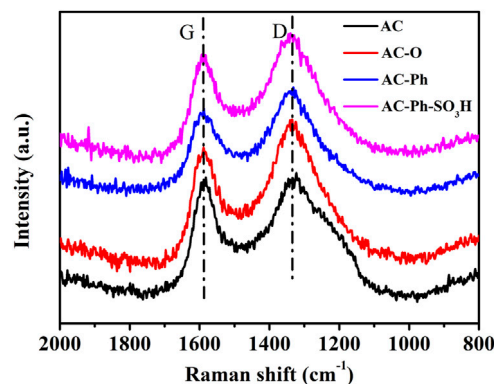
FIGURE 4 | Raman spectrum of AC, AC-O, AC-Ph and AC-Ph-SO₃H.

TABLE 4 | Raman spectrum I_D/I_G of AC, AC-O, AC-Ph and AC-Ph-SO₃H

Sample	AC	AC-O	AC-Ph	AC-Ph-SO₃H
I_D/I_G	1.029	1.256	1.191	1.174

1,586 cm⁻¹ was a G peak, representing the graphite structure of the carbon material framework; 1,336 cm⁻¹ was the D peak, which represented the non-graphitized amorphous structure. The intensity ratio I_D/I_G of the D peak and the G peak can represent the graphitization degree of the carbon material. The smaller the I_D/I_G, the higher the graphitization degree of the material. The I_D/I_G values of AC-Ph-SO₃H and its precursors were shown in **Table 4**. According to **Table 4**, the I_D/I_G value of AC was 1.029. After oxidation by nitric acid, the degree of graphitization of AC-O was reduced to 1.256, which indicated that the oxidation process had damaged the activated carbon structure to a certain extent, mainly by increasing the surface oxygen-containing functional groups. After further treatment with bromobenzene, the I_D/I_G value of AC-Ph was 1.191, and its graphitization degree was improved to a certain extent. After AC-Ph was sulfonated with concentrated sulfuric acid, the I_D/I_G value of AC-Ph-SO₃H was 1.174, and its graphitization degree was slightly increased compared with AC-Ph, which was because of the shedding of some disordered small-molecule aromatic ring species.

3.2.4 FT-IR

Functional groups on surface of AC-Ph-SO₃H and its precursors AC, AC-O, AC-Ph were characterized by infrared spectroscopy, the results were shown in **Figure 5**. The strong absorption peak near 3,400 cm⁻¹ was the O-H stretching vibration absorption peak. The absorption peak at 1,705 cm⁻¹ was the stretching vibration of -COOH, and the absorption peak at 1,570 cm⁻¹ was the stretching vibration of oxygen-containing functional groups such as quinoid structure. Except for AC, other samples all showed a certain absorption peak at 1,705 cm⁻¹, indicating that the content of carboxyl groups on the surface of AC before treatment was very low, and a certain amount of carboxyl functional groups were added onto the surface of AC-O after oxidation. There was a broad absorption peak near
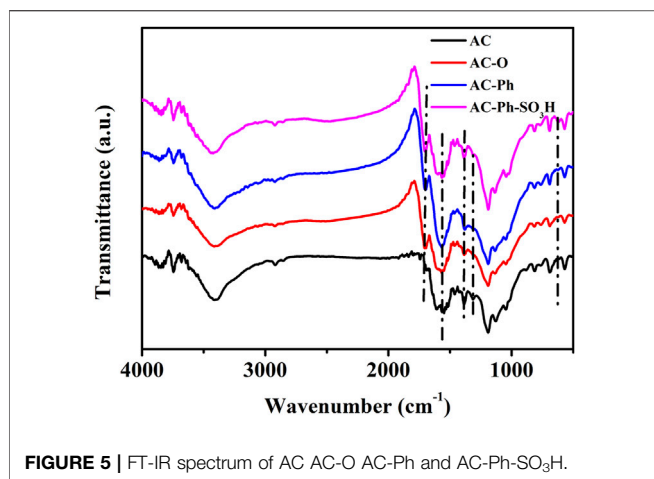
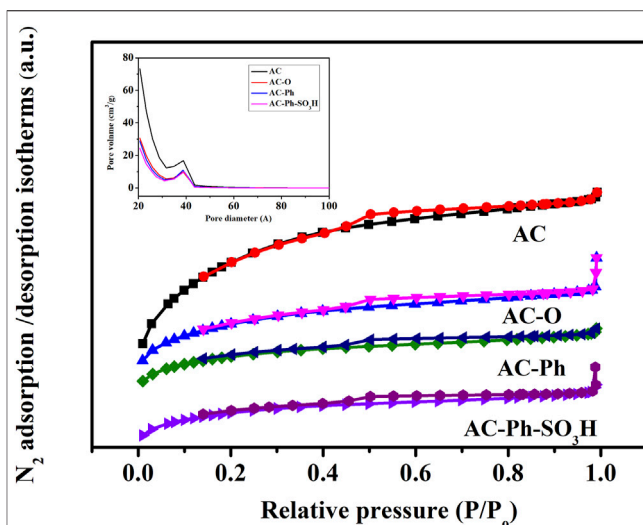**FIGURE 5 |** FT-IR spectrum of AC AC-O AC-Ph and AC-Ph-SO₃H.

FIGURE 6 | N₂ adsorption-desorption isotherms and pore size distribution for AC-Ph-SO₃H and its precursors.

$1,200\ cm^{-1}$, which was the stretching vibration of functional groups containing oxygen atoms such as S = O, phenolic hydroxyl group, ether bond, lactones, etc. In AC-Ph-SO₃H, in addition to the adsorption peak at $1,200\ cm^{-1}$, there was also an absorption peak at $1,030\ cm^{-1}$, both of which were S = O stretching vibration absorption peaks; an absorption peak was also found at $621\ cm^{-1}$, which was the characteristic absorption peak of C-S, so it could be proved that a certain amount of -SO₃H groups was generated on the surface of AC-Ph-SO₃H after sulfonation.

3.2.5 Specific Surface Area Analysis

The N₂ adsorption-desorption isotherms and pore size distribution of AC-Ph-SO₃H and its precursors were shown in **Figure 6**, which were all belonged to type IV class and showed mesoporous structure indicating that the presence of a uniform mesoporous structure for AC-Ph-SO₃H and its precursors. The surface areas were calculated with standard BET equation, which was shown in **Table 5**. According to **Table 5**, the BET surface area and pore volume changed greatly due to the destruction of the pore structure by the oxidation process, while the halogenated benzene modification and sulfonation process had relatively less effect on the pores. After modification, the obtained AC-Ph-SO₃H still had a high specific surface area, of which was up to $472\ m^2/g$, which provided the possibility of application in acidic catalytic systems combined with the high -SO₃H density.

3.3 Catalytic Performance of AC-Ph-SO₃H in the Methylation of Palmitate Acid

3.3.1 Effects of Reaction Conditions on Palmitic Acid Conversion and Methyl Palmitate Yield

The effects of reaction time, catalyst dosage and acid-alcohol molar ratio on the conversion of palmitic acid were investigated. The results were shown in **Figure 7**.

As shown in **Figure 7**, with the increase of the reaction time, the conversion rate of palmitic acid gradually increased. When the

catalyst dosage was lower than 2.5 wt%, the conversion rate of palmitic acid increased significantly with the increase of the catalyst dosage. The conversion of palmitic acid was less affected by the molar ratio of methanol/palmitic acid and decreased to a certain extent when the amount of methanol was too large, which was because of the concentration of palmitic acid in the system diluted to a certain extent. The effect of reaction conditions on methyl palmitate yield was similar to the effect on conversion rate of palmitic acid, and the selectivity of methyl palmitate remained basically around 99% under almost all conditions. When the reaction time was 6 h, the catalyst dosage was 2.5 wt%, and the molar ratio of methanol/palmitic acid was 40, the palmitic acid conversion rate was 95.2% and the yield of methyl palmitate was 94.2%. When the reaction time continued to prolong and the catalyst dosage continues increased to 3.5 wt%, the conversion rate and methyl palmitate yield was still increased but not obvious. When the molar ratio was 20, the conversion of palmitic acid was 94.3%, which was similar to that of 40 m ratio. But when the methanol/palmitic acid molar ratio was lower than 20, the palmitic acid was not easily to dissolve completely, which affected the progress of the reaction.

3.3.2 Catalytic Effects Comparation of AC-Ph-SO₃H and Its Precursors

In order to illustrate the modification effect more intuitively, the effects of AC, AC-O, AC-Ph, and AC-Ph-SO₃H in catalyzing the reaction of methylation of palmitate were investigated respectively. The test results were shown in **Figure 8**. The reaction conditions were: 0.01 mol palmitic acid, 0.4 mol methanol, 0.39 g catalyst, and the reaction was carried out at reflux temperature (65°C) for 6 h. According to **Figure 8**, AC, AC-O, AC-Ph basically had no catalytic effect on palmitic acid methylation reaction, the conversion rates of palmitate acid were 4.4, 4.7, and 4.3%, respectively. While the conversion rate of palmitic acid under the catalysis of AC-Ph-SO₃H was 95.2%, which indicated that the successful introduction

TABLE 5 | BET surface area of AC-N of AC-Ph-SO$_3$H and its precursors.

Samples	BET surface area (m^2/g)	Pore volume (cm^3/g)	Pore size (nm)
AC	1,286	0.77	2.4
AC-O	614	0.38	2.5
AC-Ph	528	0.31	2.5
AC-Ph-SO$_3$H	472	0.30	2.5
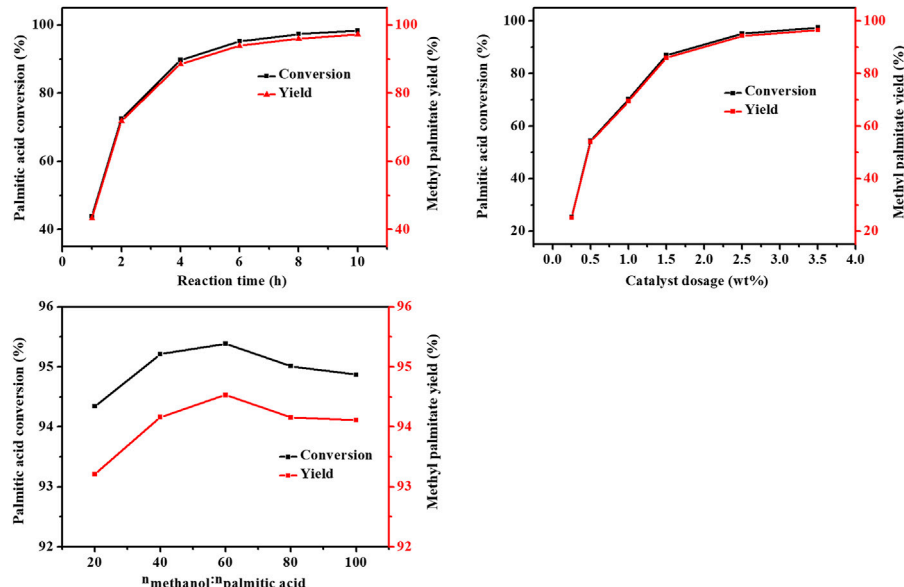
FIGURE 7 | Effect of reaction conditions on methylation of palmitic acid.
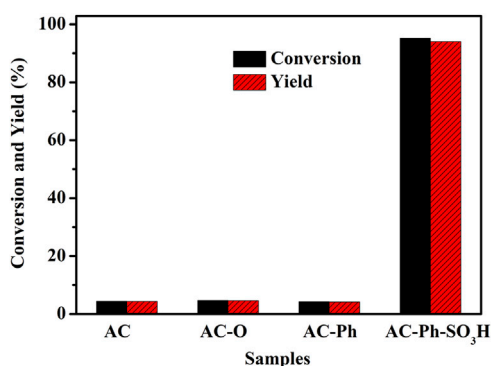
FIGURE 8 | Conversion of palmitic acid catalyzed by AC-Ph-SO$_3$H and its precursors.
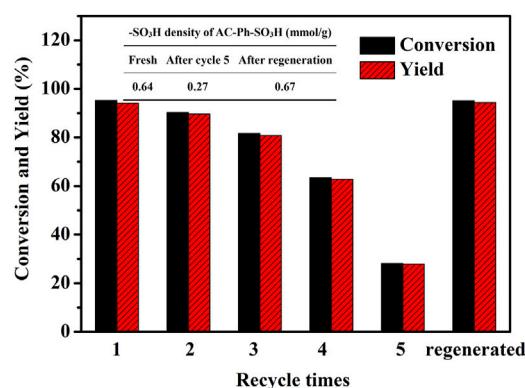
FIGURE 9 | Recycle performance of AC-Ph-SO$_3$H on methylation of palmitic acid.

of -SO$_3$H on the surface of activated carbon played an important role in catalyzing the methylation of palmitate acid.

3.3.3 Reusability of AC-Ph-SO$_3$H in the Methylation of Palmitate Acid

The reusability of AC-Ph-SO$_3$H in methylation of palmitic acid was investigated. In the study, the catalyst AC-Ph-SO$_3$H was washed with methanol after use and fed under the same conditions. The test results were shown in **Figure 9**. The reaction conditions were: 0.01 mol palmitic acid, 0.4 mol methanol, 0.39 g catalyst, and reacted at reflux temperature (65°C) for 6 h. According to **Figure 9**, the conversion of palmitic acid was 95.2% at the first use of the catalyst. The

TABLE 6 | Comparison of catalytic performance with the reported carbon-based solid acids.

Entry	Solid acid catalyst	Density of -SO₃H (mmol/g)	Catalyst amount (wt%)	Acid	Time (h)	Conv. in the first Cycle (%)	Reaction cycle	Conv. in the last cycle (%)	Ref.
1	AC-Ph-SO₃H	0.64	2.5	Palmitate acid	6	95.2	3	81.7/N	This study
2	MLC-S	0.91	5	Oleic acid	6	92.3	5	72.9/N	Ma et al. (2020)
3	CS-SAC	1.48	5	Oleic acid	24	93	3	56/N	Bureros et al. (2019)
4	CS-SAC	0.85	7.5	Oleic acid	24	76	5	78/Y	Mendaros et al. (2020)
5	AC108	0.93	10	Oleic acid	6	89	5	89/N	Wang et al. (2014)
6	Heterogeneous acid catalyst synthesized from bamboo-AC	1.17	12	Oleic acid	3	96	5	28/N; 94/Y	Niu et al. (2018)
7	SO₃H-KSC	—	2	palm fatty acid	1.5	98.7	6	60/N	Akinfalabi et al. (2019)
8	Bamboo-SO₃H	—	4	palm fatty acid	1	95.8	4	71/N	Farabi et al. (2019)
9	HTC-S	—	3	palm fatty acid	2	92	3	82/N	Ibrahim et al. (2020)
10	ASHC-SO₃H	1.4	10	Oleic acid	3	96.4	4	55.1/N; 95.4/Y	Cao et al. (2021)

Note: N represents no regeneration; Y represents regeneration.

conversion rate of palmitic acid was 90.4%, 81%, 7%, and 63.5% in the process of second to fourth reuse of the catalyst. In the fifth reuse, the conversion rate of palmitic acid was only 28.1%. The yield of methyl palmitate declined by a similar magnitude. The conversion rate and the yield gradually decreased with the increase of repeated times, but it showed good catalytic effect when it was reused three times. The reason for the gradual decrease of the catalytic effect was mainly including the formation of sulfonate and exfoliation of sulfonic acid groups on the surface of AC-Ph-SO₃H during the catalytic process (Zhang et al., 2021), which had an important relationship with the presence of methanol and the polar environment of the reaction system.

After the catalyst was used for five times, the AC-Ph-SO₃H was regenerated after being washed with methanol, dried, and sulfonated with concentrated sulfuric acid at 150°C for 4 h. As shown in **Figure 9**, the density of -SO₃H on the surface of AC-Ph-SO₃H was only 0.27 mmol/g after being used for five times, while reached 0.67 mmol/g after regeneration, which was even slightly higher than that of the fresh catalyst. At the same time, the conversion rate of palmitic acid also reached 95.1%. Which indicated that the structure of AC-Ph-SO₃H was not destroyed in the catalysis process, although there were problems such as functional group shedding or masking.

3.3.4 Comparison of Catalytic Performance With the Reported AC-Based Solid Acids

The catalytic performance of prepared AC-Ph-SO₃H and the reported carbon-based sulfonic acid-type catalysts in the esterification of long-chain fatty acids were compared, and the results were shown in **Table 6**. As shown, most of the catalysts had good catalytic performance in the esterification

reaction, but basically there was a problem that the catalytic efficiency decreased when they were recycled. The prepared AC-Ph-SO₃H showed comparable catalytic performance to those reported catalyst, and showed advantages in terms of catalyst dosage and catalytic efficiency. Some of the catalysts (Niu et al., 2018) presented in the table were regenerated and showed excellent catalytic performance again. As shown in Entry 6, the conversion rate of fatty acid was only 28% when it was reused for the fifth time. After regeneration, the conversion rate of fatty acid reached 94% like that of catalyzed with fresh catalyst. At the same time, the density of -SO₃H on the surface of the material also returned to the fresh level. Combined with these research results, carbon-based catalysts had great application potential in catalytic esterification to prepare biodiesel, while their stability and regeneration performance still need to be further explored.

4 CONCLUSION

Using activated carbon as raw material, AC-Ph-SO₃H was prepared by oxidation with nitric acid, modification with halogenated benzene and sulfonation with concentrated sulfuric acid. With toluene as solvent and bromobenzene as modification reagent, high density of acidic group -SO₃H were grafted on the surface of AC successfully. When the concentration of bromobenzene was 10%, the modification time of bromobenzene was 5 h, and the sulfonation temperature was 150°C, the surface -SO₃H content of AC-Ph-SO₃H was 0.64 mmol/g.

In the reaction of catalyzing the methylation of palmitate acid to prepare biodiesel, AC-Ph-SO₃H showed a good catalytic performance. When the reaction time was 6 h, the

amount of catalyst acid accounted for 2.5 wt% of palmitic acid, and the mole fraction of methanol/palmitic acid was 40, the conversion rate of palmitic acid was 95.2%. While the conversion rates of palmitate acid catalyzed by AC, AC-O, AC-Ph were only about 4.5%, which indicated the success of the modification process. In the study of the reusability of AC-Ph-SO₃H as catalyst in methyl esterification of palmitate acid, the conversion rate of palmitate acid was still above 80% after three times of use, which indicated an excellent reusability.

Because unmodified activated carbon materials are difficult to be sulfonated to obtain activated carbon-based solid acid materials, the results of this study provided certain scientific support for the preparation of activated carbon-based solid acid materials. We believe that activated carbon materials with strongly acidic group have very good application prospects in the field of catalysis combined with its rich pore structure. However, like the reported amorphous carbon-based acid catalyst, the group of -SO₃H on AC-Ph-SO₃H was also easy to fall off after several reaction cycles. The specific reasons for -SO₃H shedding and how to improve the stability of AC-Ph-SO₃H need to be researched further. The application of AC-Ph-SO₃H in the catalytic conversion of biomass also needs to be further developed.

DATA AVAILABILITY STATEMENT

The original contributions presented in the study are included in the article/Supplementary Material, further inquiries can be directed to the corresponding authors.

REFERENCES

Akinfalabi, S.-I., Rashid, U., Shean, T. Y. C., Nehdi, I. A., Sbihi, H. M., and Gewik, M. M. (2019). Esterification of Palm Fatty Acid Distillate for Biodiesel Production Catalyzed by Synthesized Kenaf Seed Cake-Based Sulfonated Catalyst. *Catalysts* 9 (5), 482. doi:10.3390/catal9050482

Antar, M., Lyu, D., Nazari, M., Shah, A., Zhou, X., and Smith, D. L. (2021). Biomass for a Sustainable Bioeconomy: An Overview of World Biomass Production and Utilization. *Renew. Sustain. Energy Rev.* 139, 110691. doi:10.1016/j.rser.2020.110691

Bureros, G. M. A., Tanjay, A. A., Cuizon, D. E. S., Go, A. W., Cabatingan, L. K., Agapay, R. C., et al. (2019). Cacao Shell-Derived Solid Acid Catalyst for Esterification of Oleic Acid with Methanol. *Renew. Energy* 138, 489–501. doi:10.1016/j.renene.2019.01.082

Cao, M., Peng, L., Xie, Q., Xing, K., Lu, M., and Ji, J. (2021). Sulfonated Sargassum Horneri Carbon as Solid Acid Catalyst to Produce Biodiesel via Esterification. *Bioresour. Technol.* 324, 124614. doi:10.1016/j.biortech.2020.124614

Darda, S., Papalas, T., and Zabaniotou, A. (2019). Biofuels Journey in Europe: Currently the Way to Low Carbon Economy Sustainability Is Still a Challenge. *J. Clean. Prod.* 208, 575–588. doi:10.1016/j.jclepro.2018.10.147

Esmi, F., Borugadda, V. B., and Dalai, A. K. (2022). Heteropoly Acids as Supported Solid Acid Catalysts for Sustainable Biodiesel Production Using Vegetable Oils: A Review. *Catal. Today* (In press). doi:10.1016/j.cattod.2022.01.019

Farabi, M. S. A., Ibrahim, M. L., Rashid, U., and Taufiq-Yap, Y. H. (2019). Esterification of Palm Fatty Acid Distillate Using Sulfonated Carbon-Based Catalyst Derived from Palm Kernel Shell and Bamboo. *Energy Convers. Manag.* 181, 562–570. doi:10.1016/j.enconman.2018.12.033

Gebremariam, S. N., and Marchetti, J. M. (2018). Economics of Biodiesel Production: Review. *Energy Convers. Manag.* 168, 74–84. doi:10.1016/j.enconman.2018.05.002

Gebremariam, S. N., and Marchetti, J. M. (2018). Biodiesel Production through Sulfuric Acid Catalyzed Transesterification of Acidic Oil: Techno Economic Feasibility of Different Process Alternatives. *Energy Convers. Manag.* 174, 639–648. doi:10.1016/j.enconman.2018.08.078

Hsiao, M.-C., Kuo, J.-Y., Hsieh, S.-A., Hsieh, P.-H., and Hou, S.-S. (2020). Optimized Conversion of Waste Cooking Oil to Biodiesel Using Modified Calcium Oxide as Catalyst via a Microwave Heating System. *Fuel* 266, 117114. doi:10.1016/j.fuel.2020.117114

Ibrahim, S. F., Asikin-Mijan, N., Ibrahim, M. L., Abdulkareem-Alsultan, G., Izham, S. M., and Taufiq-Yap, Y. H. (2020). Sulfonated Functionalization of Carbon Derived Corncob Residue via Hydrothermal Synthesis Route for Esterification of Palm Fatty Acid Distillate. *Energy Convers. Manag.* 210, 112698. doi:10.1016/j.enconman.2020.112698

Jayakumar, M., Karmegam, N., Gundupalli, M. P., Bizuneh Gebeyehu, K., Tessema Asfaw, B., Chang, S. W., et al. (2021). Heterogeneous Base Catalysts: Synthesis and Application for Biodiesel Production - A Review. *Bioresour. Technol.* 331, 125054. doi:10.1016/j.biortech.2021.125054

Ma, Z., Xing, X., Qu, Z., Sun, Y., Sun, G., Wang, X., et al. (2020). Activity of Microporous Lignin-Derived Carbon-Based Solid Catalysts Used in Biodiesel Production. *Int. J. Biol. Macromol.* 164, 1840–1846. doi:10.1016/j.ijbiomac.2020.08.002

Mendaros, C. M., Go, A. W., Nietes, W. J. T., Gollem, B. E. J. O., and Cabatingan, L. K. (2020). Direct Sulfonation of Cacao Shell to Synthesize a Solid Acid Catalyst for the Esterification of Oleic Acid with Methanol. *Renew. Energy* 152, 320–330. doi:10.1016/j.renene.2020.01.066

Mukhtar, A., Saqib, S., Lin, H., Hassan Shah, M. U., Ullah, S., Younas, M., et al. (2022). Current Status and Challenges in the Heterogeneous Catalysis for Biodiesel Production. *Renew. Sustain. Energy Rev.* 157, 112012. doi:10.1016/j.rser.2021.112012

Niu, S., Ning, Y., Lu, C., Han, K., Yu, H., and Zhou, Y. (2018). Esterification of Oleic Acid to Produce Biodiesel Catalyzed by Sulfonated Activated Carbon from

Bamboo. *Energy Convers. Manag.* 163, 59–65. doi:10.1016/j.enconman.2018.02.055

Rocha, P. D., Oliveira, L. S., and Franca, A. S. (2019). Sulfonated Activated Carbon from Corn Cobs as Heterogeneous Catalysts for Biodiesel Production Using Microwave-Assisted Transesterification. *Renew. energy* 143, 1710–1716. doi:10.1016/j.renene.2019.05.070

Scheibe, B., Borowiak-Palen, E., and Kalenczuk, R. J. (2010). Oxidation and Reduction of Multiwalled Carbon Nanotubes - Preparation and Characterization. *Mater. Charact.* 61 (2), 185–191. doi:10.1016/j.matchar.2009.11.008

Singh, D., Sharma, D., Soni, S. L., Sharma, S., Kumar Sharma, P., and Jhalani, A. (2020). A Review on Feedstocks, Production Processes, and Yield for Different Generations of Biodiesel. *Fuel* 262, 116553. doi:10.1016/j.fuel.2019.116553

Su, C.-H. (2013). Recoverable and Reusable Hydrochloric Acid Used as a Homogeneous Catalyst for Biodiesel Production. *Appl. Energy* 104, 503–509. doi:10.1016/j.apenergy.2012.11.026

Tang, X., and Niu, S. (2019). Preparation of Carbon-Based Solid Acid with Large Surface Area to Catalyze Esterification for Biodiesel Production. *J. industrial Eng. Chem.* 69, 187–195. doi:10.1016/j.jiec.2018.09.016

Tobío-Pérez, I., Domínguez, Y. D., Machín, L. R., Pohl, S., Lapuerta, M., and Piloto-Rodríguez, R. (2022). Biomass-based Heterogeneous Catalysts for Biodiesel Production: a Comprehensive Review. *Int. J. Energy Res.* 46 (4), 3782–3809. doi:10.1002/er.7436

Vakros, J. (2018). Biochars and Their Use as Transesterification Catalysts for Biodiesel Production: a Short Review. *Catalysts* 8 (11), 562. doi:10.3390/catal8110562

Wancura, J. H. C., Tres, M. V., Jahn, S. L., and Oliveira, J. V. (2020). Lipases in Liquid Formulation for Biodiesel Production: Current Status and Challenges. *Biotechnol. Appl. Biochem.* 67 (4), 648–667. doi:10.1002/bab.1835

Wang, C., Gui, X., and Yun, Z. (2014). Esterification of Lauric and Oleic Acids with Methanol over Oxidized and Sulfonated Activated Carbon Catalyst. *Reac Kinet. Mech. Cat.* 113 (1), 211–223. doi:10.1007/s11144-014-0720-4

Wilk, M., Magdziarz, A., Kalemba-Rec, I., and Szymańska-Chargot, M. (2020). Upgrading of Green Waste into Carbon-Rich Solid Biofuel by Hydrothermal Carbonization: The Effect of Process Parameters on Hydrochar Derived from acacia. *Energy* 202, 117717. doi:10.1016/j.energy.2020.117717

Yusuff, A. S., Thompson-Yusuff, K. A., and Porwal, J. (2022). Sulfonated Biochar Catalyst Derived from eucalyptus Tree Shed Bark: Synthesis, Characterization and its Evaluation in Oleic Acid Esterification. *RSC Adv.* 12 (17), 10237–10248. doi:10.1039/d1ra09179d

Zhang, B., Gao, M., Geng, J., Cheng, Y., Wang, X., Wu, C., et al. (2021). Catalytic Performance and Deactivation Mechanism of a One-step Sulfonated Carbon-Based Solid-Acid Catalyst in an Esterification Reaction. *Renew. Energy* 164, 824–832. doi:10.1016/j.renene.2020.09.076

Imidazolized Activated Carbon Anchoring Phosphotungstic Acid as a Recyclable Catalyst for Oxidation of Alcohols With Aqueous Hydrogen Peroxide

Min Zheng[1,2], Huiting He[3], Xiangzhou Li[1]* and Dulin Yin[3]

[1]College of Material Science and Engineering, Central South University of Forestry and Technology, Changsha, China, [2]College of Physics and Chemistry, Hunan First Normal University, Changsha, China, [3]National & Local Joint Engineering Laboratory for New Petro-chemical Materials and Fine Utilization of Resources, College of Chemistry and Chemical Engineering, Hunan Normal University, Changsha, China

Keggin-type phosphotungstic acid (HPW) supported on imidazolyl-activated carbon (AC-COIMI-HPW) catalysts was prepared, which was used to catalyze the oxidation of benzyl alcohol with aqueous H_2O_2. In the presence of AC-COIMI-HPW, the benzyl alcohol conversion of 90.2% with 91.8% selectivity of benzaldehyde was obtained at 90°C for 6 h in an acetonitrile aqueous solution. The catalyst exhibited an outstanding performance for the oxidation of various benzyl alcohols and aliphatic alcohols. In addition, the catalyst could be easily recovered and reused five times without significant deactivation. The characterization results showed that HPW was chemically bonded on the surface of the carbon material through an ionic bond. It is proposed that the combination of the imidazole cation with the HPW anion could not only tune the redox catalytic properties of the PW anion but also enhance the compatibility of the catalyst in the reaction medium, thereby improving the catalytic performance.

Keywords: phosphotungstic acid, 2-methylimidazole, activated carbon, oxidation, benzyl alcohol

1 INTRODUCTION

The oxidation of alcohols to aldehydes and ketones plays an important role in the synthesis of organic compounds such as agrochemicals, pharmaceuticals, and dyestuff in the industry and laboratory (Mandal et al., 2013). In the traditional chemical oxidation process, several common oxidants such as dichromate or permanganate were usually used and exhibited strong oxidative properties. However, these oxidants are often associated with poor selectivity, high toxicity, and harmful by-products of heavy metals, which result in serious environmental pollution, increasing the difficulty and cost of subsequent treatment. Aerobic oxidation is an attractive strategy for the oxidation of alcohols. Ten years ago, ruthenium hydroxide supported on silica was used as an efficient catalyst for the aerobic oxidation of monoterpene alcohols (Costa et al., 2011). Recently, layered double hydroxide-supported Cu^0 nanoparticles (Choudhary et al., 2019), Au nanoparticles (Karimi et al., 2020), and polymeric ionic liquid microspheres/Pd nanoparticles (Wu et al., 2020) have been designed for the oxidation of alcohols. It was presented that primary and secondary alcohols can be efficiently oxidized using $CoFe_2O_4$@HT@Imine-Cu II and TEMPO in the air atmosphere (Salimi et al., 2020). However, the above-mentioned catalysts were expensive and

generally require a longer reaction time at high temperatures to achieve good catalytic performance. Therefore, it is still a challenge to develop an oxidation system that is easily available, stable, inexpensive, environmentally acceptable, and promotes selective oxidation under mild reaction conditions.

The green chemical industry is aimed at reducing or eliminating the use and generation of hazardous substances. Hydrogen peroxide (H_2O_2) has been recognized as a green oxidant because of it being environmentally friendly, inexpensive, and easy to handle (Shi et al., 2021). In the past period, much research has been devoted to the selective oxidation of alcohols in the presence of H_2O_2. Tungstate ions supported on imidazolium framework (Hosseini et al., 2017) or magnetic mesoporous silica (Norouzi et al., 2019) and molybdate ions immobilized on ionic liquid–modified CMK-3 (Hosseini-Eshbala et al., 2020) were employed for the oxidation of benzyl alcohols. It is noteworthy that iron chloride ionic liquid immobilized on SBA-15 (Cang et al., 2015) and cheap iron (III) tosylate (Zhao et al., 2018) was applied for selective oxidation of alcohols, whereas a large amount of H_2O_2 was consumed in the presence of iron ion. Chromium borophosphate synthesized by the solution combustion method at 800°C was also tested for the oxidation of benzyl alcohol (Demet Ozer, 2020).

Polyoxometalates (POMs) are a category of transition metal oxide clusters with hollow structures and relatively large surface areas (Hao et al., 2018). Benefiting from the modifiable redox and acidic properties, POMs have received widespread attention in the catalytic oxidation of alcohols with H_2O_2. However, the direct use of pure POMs has some problems such as low activity and difficulty in recovering the catalyst due to its water solubility. In order to solve this problem in the oxidation of alcohols with H_2O_2, a lot of research has been devoted to fabricating insoluble POM catalytic composite materials, including macromolecular-like polyoxometalate-based ionic hybrid with a polyamine (Chen et al., 2014; Su et al., 2014), dendritic phosphotungstate structure (Chen et al., 2014; Sadjadi et al., 2019), squeezing POMs in ionic liquids (Li et al., 2015; Keshavarz et al., 2019), and immobilizing onto mesoporous molecular sieves (Tan et al., 2012; Dong et al., 2014). In order to promote selective oxidation of alcohols, some carbon materials such as multi-wall carbon nanotubes modified with ionic liquids (Hajian et al., 2017: Liu et al,2014) and ionic liquid–functionalized graphene oxide (Liu et al., 2013; Zheng et al., 2019) were also used as a support for POMs. It should be observed that there exist alkaline sites or ion exchangeable sites on supports that are used for immobilization of POMs.

Activated carbon (AC) is a large-tonnage industrial carbonaceous material, which might be produced from biomass formed by natural photosynthesis. AC has a high specific surface area, pore structure, and surface functional groups (Alslaibi et al., 2014). Therefore, it has a wide range of applications in the fields of adsorption of heavy metals (Koohzad et al., 2019), supercapacitor electrodes (Fan et al., 2011), decolorization (Shahbazi et al., 2020; Liu et al., 2021), and catalyst supports (Yao et al., 2020; Xu et al., 2021; Costa et al., 2021). However, it is generally believed that the most attractive feature of activated carbon materials is their specific and controllable surface reactivity. Usually, the oxidation of

activated carbon with nitric acid can increase carboxylic acid sites (Ternero-Hidalgo et al., 2016) or convert to basic sites by NaOH treatment (Cazettaa et al., 2011). Furthermore, imidazolyl-activated carbon has been recently prepared by ethylenediamine treatment (Liu et al., 2019). Based on the aforementioned facts, phosphotungstate catalytic active sites were constructed by chemically modifying the surface carboxylation and imidazolization of carbonic materials with 2-methylimidazole, and their catalytic performances in the oxidation of alcohols were investigated.

2 EXPERIMENT

2.1 Materials

Phosphotungstic acid was purchased from Aladdin. Benzyl alcohol was purchased from Xilong Science Co., Ltd., and 30% hydrogen peroxide solution was provided by Baling Branch, SINOPEC. Other reagents were purchased from Sinopharm Chemical Reagent Co., Ltd. (Shanghai, China). All chemicals were not further purified prior to use.

## 2.2 Catalyst Preparation

2.2.1 AC-COOH

The preparation process of the catalyst is shown in **Scheme 1**. Unlike the usual carboxylation of carbon materials with hazardous nitric acid, a green oxidation method of the activated carbon surface was developed. Generally, 10 g of activated carbon was added to a three-necked flask equipped with a condenser and a thermometer, 50 ml of 50% hydrogen peroxide and 5 ml of 12 mol L^{-1} H_2SO_4 aqueous solution were added, and then stirred at 80°C in an oil bath for 2 h, while which another 25 ml of 50% hydrogen peroxide was added drop by drop for 1 h. When the oxidative treatment was completed, the reaction mixture was then filtered and washed repeatedly with deionized water until no SO_4^{2-} ion could be detected in the barium chloride solution. The resulting solid was dried in an oven at 120°C for 6 h. The oxidized activated carbon was designated as AC-COOH.

2.2.2 AC-COIMI

Direct imidazolization of oxidized activated carbon was carried out. Generally, 50 g of 2-methylimidazole was first added in a three-necked flask; then, 10 g of AC-COOH was added, equipped with a condenser and connected to an anhydrous calcium chloride tube, a thermometer, and a silicone oil bath; the temperature was increased to 180°C at 3°C min^{-1} and maintained for 10 h. After the operation of amidation, the oil bath was removed, the flask was cooled to room temperature, and 70 ml of acetone was added. Once sealed overnight, it was filtered, and extraction of the residue was launched with acetone for 10 h until 2-methylimidazole did not exist in the Soxhlet apparatus monitored by a UV-vis spectrometer and dried in a vacuum to collect the acyl-imidazolized activated carbon AC-COIMI.

2.2.3 AC-COIMI-HPW

First, a certain amount of HPW was dissolved in ultrapure water to obtain a series of standard solution. Then, 1.00 g of AC-COIMI was added to the corresponding solution, standing for 24 h. The
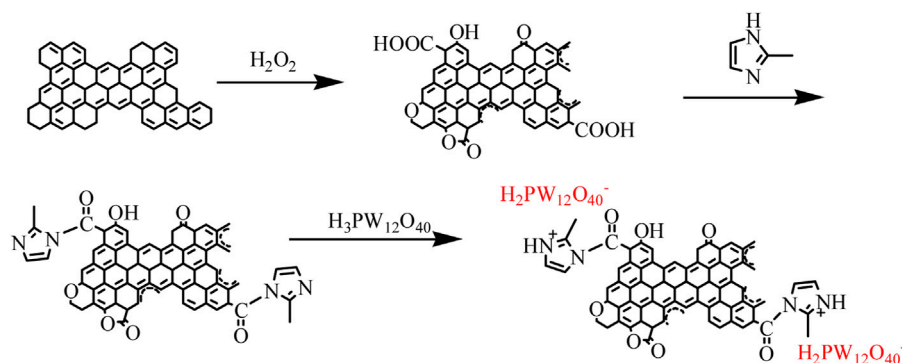
Scheme 1 | Preparation of AC-COIMI-HPW.

parent liquor was separated by centrifugation, washed with ultrapure water until no phosphotungstic acid exists in the liquid monitored by using a UV-vis spectrometer, and dried in vacuo overnight. The resultant material is designed as an AC-COIMI-HPW catalyst.

2.3 Adsorption Isotherm Determination

Accurately weighed AC-COIMI samples were put in a series solution in conical bottles with different concentrations of HPW and then fixed in a constant temperature shaker, shaken at 25°C for 5 h or more to adsorption equilibrium. Once equilibration was attained, the centrifuged mother liquor was taken out, and the concentration of HPW in the liquor was detected by UV-vis spectrophotometry from the absorbance at 258 nm. The adsorption quantity of HPW on an AC-COIMI catalyst was calculated by measuring the concentration difference of the initial and last solution.

2.4 Catalyst Characterizations

The Fourier transform infrared spectra (FT-IR) of the samples were collected by the KBr pellet technique on a Nicolet 370 infrared spectrophotometer in the range of 400–4,000 cm^{-1}. The X-ray diffraction (XRD) patterns of the sample were recorded by using a Bruker diffractometer with Cu Kα radiation and diffraction angle (2θ) ranging from 10° to 80°. A DXR laser Raman microscope (laser wavelength 780 nm) was used; the wavelength range was 50–3,250 cm^{-1}, the exposure time was 5 s, the number of exposures was 10, and the laser intensity was 5 mW. The Thermogravimetric and derivative thermogravimetric (TG-DTG) experimental results were obtained on a Netzsch Model STA 409PC instrument, from room temperature to 800°C at 10°C/min using α-Al$_2$O$_3$ as the standard material. The UV-Vis spectrum (190~900 nm) was measured by using a UV-2450 apparatus of Shimadzu. Chemical analysis of W in the reaction was carried out by inductively coupled plasma-emission spectrometry (ICAP 7200, Thermo Fisher Scientific Co., Ltd., United States)

2.5 Catalytic Reaction Tests

Benzyl alcohol and a certain amount of catalyst were added into a 25-ml round bottom flask. Then, a certain amount of solvent was

added, and the mixture was heated to the specified temperature. When the temperature was stable, a quantitative 30 wt% H$_2$O$_2$ was added, and timing was started. After the reaction was completed, the mixture was cooled to room temperature and centrifuged. Then, 100 µl of the reaction solution was sucked into the PV tube and diluted 10 times before passing through the ultrafiltration membrane. The conversion and selectivity were determined by GC using an internal standard method (Nexis GC-2030). In reuse experiments, the deposited catalyst was washed with the solvent three times for the next run.

3 RESULTS AND DISCUSSION

### 3.1 Catalyst Characterization
3.1.1 FTIR

It is shown, in **Figure 1**, that the carbonyl stretching vibration peak at 1722 cm^{-1} from the oxidized activated carbon can be seen as higher than the original activated carbon without oxidation. In addition, the absorption peaks at 1,609 and 1,533 cm^{-1} belong to the C=C stretching vibration zone of the fused ring aromatic hydrocarbon skeleton on the activated carbon. The peak at 1,190 cm^{-1} is attributed to the stretching vibration of the carboxyl group, lactone group, or the phenolic hydroxyl group on the activated carbon. This result proves the existence of abundant functional groups on activated carbon, which also provides basic conditions for us to modify activated carbon by chemical methods. As compared to AC-COIMI, AC-COIMI-HPW retains its 2-methylimidazole structure and therefore presents the characteristic peak of the imidazole skeleton. The peak at 3,125 cm^{-1} belongs to the C-H stretching vibration on the unsaturated carbon of fused ring aromatic hydrocarbons on imidazole or activated carbon. The peak at 2,919 cm^{-1} belongs to the C-H stretching vibration of the saturated carbon of the methyl group on 2-methylimidazole. The peak at 1,717 cm^{-1} belongs to the stretching vibration of the carbonyl group. Here, 1,650 cm^{-1} represents the -C=N stretching vibration on the imidazole skeleton, and 1,265 cm^{-1} is attributed to the C-N bending vibration peaks on the imidazole ring. The four main characteristic bands of pure phosphotungstic acid are located at 1,078 (P-O$_a$), 983 (W=O$_d$), 894 (W-O$_b$-W with co-angular

FIGURE 1 | FT-IR spectra of (a) AC, (b) AC-COOH, (c) AC-COIMI, (d) AC-COIMI-HPW and (e) HPW.

FIGURE 2 | Raman of (a) AC, (b) AC-COOH, (c) AC-COIMI and (d) AC-COIMI-HPW.
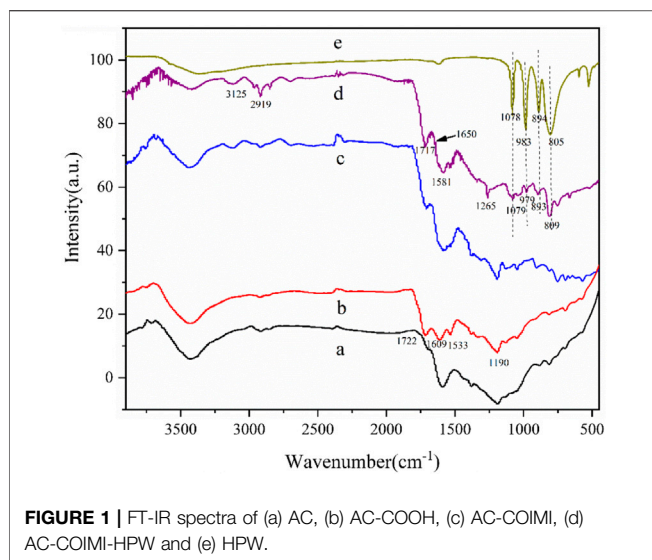
octahedron), and 805 cm^{-1} (W-O$_c$-W with co-lateral octahedral), and the corresponding peaks can be found in AC-COIMI-HPW. The characteristic peak of heteropoly acid has a slight deviation, which is mainly because the lone pair of electrons in the organic cation extends into the inorganic framework of the heteropoly anion, which makes the formation of a strong electronic force between the two so that the characteristics of both sides and the absorption peaks have shifted to a certain extent, and these shifts and changes indicate the interaction between the phosphotungstate anion and imidazolium cation (Mohamadi et al., 2020). The aforementioned results showed that the modification of activated carbon is successful. No obvious Keggin structure's absorption peak is observed in the catalyst, which confirms that the phosphotungstic acid species is highly dispersed, which is consistent with the following XRD results.

3.1.2 Raman Spectra

The Raman spectra of AC-COIMI-HPW and its precursors AC, AC-COOH, and AC-COIMI are presented in **Figure 2**, and the changes in the carbon skeleton of the activated carbon after each step of modification are presented. These carbon materials mainly have two broad peaks at 1,580 and 1,336 cm^{-1}. The peak at 1,580 cm^{-1} is the G peak, which represents the graphite-like structure of the central sp^2 carbon skeleton. Another peak at 1,336 cm^{-1} is D which represents the non-graphitized amorphous structure in the material (Shimodaira et al., 2002). The intensity ratio I$_D$/I$_G$ of peak D and peak G can represent the relative content of the graphene-like structure of the carbon material. Analyzing the I$_D$/I$_G$ value obtained by Gaussian fitting, the I$_D$/I$_G$ of the activated carbon after the nitric acid treatment becomes larger, indicating that the non-graphitized amorphous degree of the activated carbon is increased by oxidation treatment because the graphene-like fused-ring aromatic structure at each layer is destroyed to a certain extent. After the subsequent modification of 2-methylimidazole, it seems the degree of graphitization increased again. The main reason may be that the G peak represents C (sp^2), and the D peak represents the vibration of
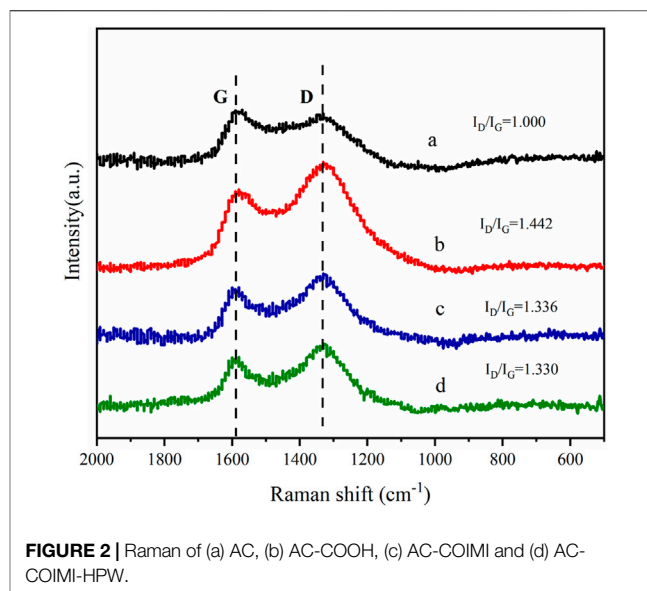
C (sp^3). The introduction of imidazole makes the sp^2 type carbon have a certain degree of increase so that the degree of G peak has a certain increase. The subsequent phosphotungstic acid modification shows that it has little effect on the Raman spectra of AC-COIMI because HPW cannot change the ratio of both sp^2 and sp^3 carbon in the carbon material.

3.1.3 XRD

Figure 3 shows the wide-angle X-ray diffraction curves of phosphotungstic acid, oxidized activated carbon, and phosphotungstic acid-loaded activated carbon. It shows the characteristic diffraction peaks of phosphotungstic acid crystals. The Keggin cubic structure diffraction peaks of HPW mainly appear at 10.3°, 18.0°, 20.6°, 23.1°, 25.2°, 29.3°, 34.6°, and 37.8°, which are consistent with the literature reports (JCPDS-#7521–25) (Atia et al., 2008; Costa et al., 2021). The diffraction curve of the oxidized activated carbon showed the dispersion peak of the amorphous phase. In the case of AC-COIMI-HPW, it was observed that it does not show an obvious phosphotungstic acid diffraction peak, and the 2θ value of the diffraction peak representing the (002) crystal plane of the graphite structure has shifted from 21.9° to 25.7°. From Bragg **Eq. 2** d$_{hkl}$ sin θ = n λ, it seems to indicate that the graphene-like structure in AC-COIMIHPW is compressed, and the particle size is smaller by the reaction of AC-COIMI with HPW. This may be because the subsequent modification operations have changed the degree of graphitization of carbon materials. The results are good and agree with the FTIR result, and it shows that the phosphotungstate species are highly self-dispersed on the activated carbon from the adsorption process, in other words, which also means that HPW is loaded uniformly on the imidazole site in the form of a single molecule.

3.1.4 TG-DTG

The TG-DTG profile of four samples is shown in **Figure 4**. The weight loss curve of HPW in **Figure 4d** indicates that the first

FIGURE 3 | XRD patterns of (a) HPW, (b) AC, (c) AC-COOH, (d) AC-COIMI and (e) AC-COIMI-HPW.

FIGURE 4 | TG and DTG of (a) AC-COOH, (b) AC-COIMI, (c) AC-COIMI-HPW and (d) HPW.
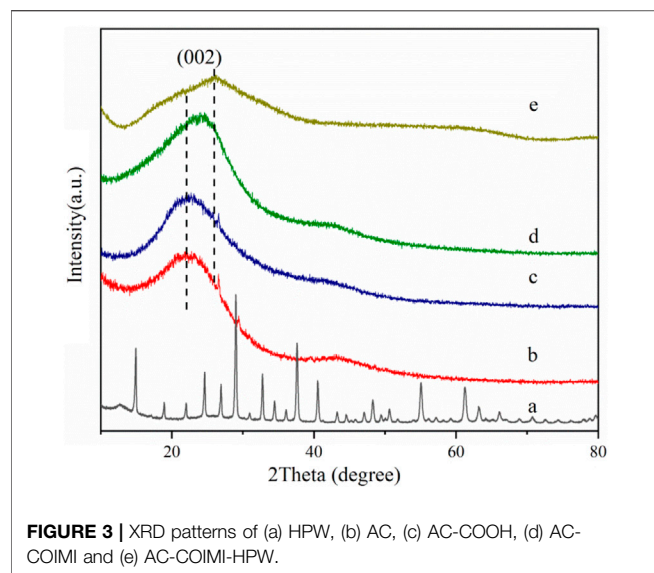
weight loss peak between 0°C and 100°C is the removal of phosphotungstic acid physical adsorption water in three carbon materials. The structural water of phosphotungstic acid forms $[H_2O{\cdots}H^{+}{\cdots}OH_2]$ ions by hydrogen bonding with acidic protons, and its water loss peak is located at 100°C–200°C, and only pure HPW loses weight at about 200°C. However, it is mainly due to a small amount of weight loss of the decomposition of phosphotungstic acid between 300–600°C, that is, the Keggin structure is destroyed (Tan et al., 2012). The total weight loss of HPW was ca. 5.5% ranging from 600°C to 800°C. In the weight loss curve of AC-COOH shown in **Figure 4a**, the weight loss peak of the adsorbed water on the surface of the carbon material below 100°C was observed. In addition, the weight loss (about 15%) between 150°C and 250°C is mainly the decomposition of the carboxyl group on the carbon material, which further verified the existence of the abundant carboxyl group on the oxidized modified carbon material. The TG curve of AC-COIMI-HPW is shown in **Figure 4b**. The first weight loss can be assigned to the physical adsorption of water. The second stage ranging from 150°C to 450°C corresponds to the decomposition of the oxygen-containing groups on the surface of the carbon material and the decomposition of the imidazole organic skeleton. The weight loss during this stage is about 38.3%. In the third stage up to 800°C, the weight loss can be considered as the decomposition of the residual oxygen-containing groups in the activated carbon. **Figure 4c** shows the weight loss curve of AC-COIMI-HPW, and the weight loss peak in the first stage is still the physical adsorption water lost by the catalyst. The corresponding weight loss can be found in the AC-COIMI ranging from 150°C to 450°C, it includes the decomposition of oxygen-containing groups and imidazole skeletons and water of the phosphotungstic acid structure. The increase in the decomposition temperature of bound water in phosphotungstic acid is also proof of our successful combination of imidazole and phosphotungstic acid, improving the stability of phosphotungstic acid on the activated carbon.
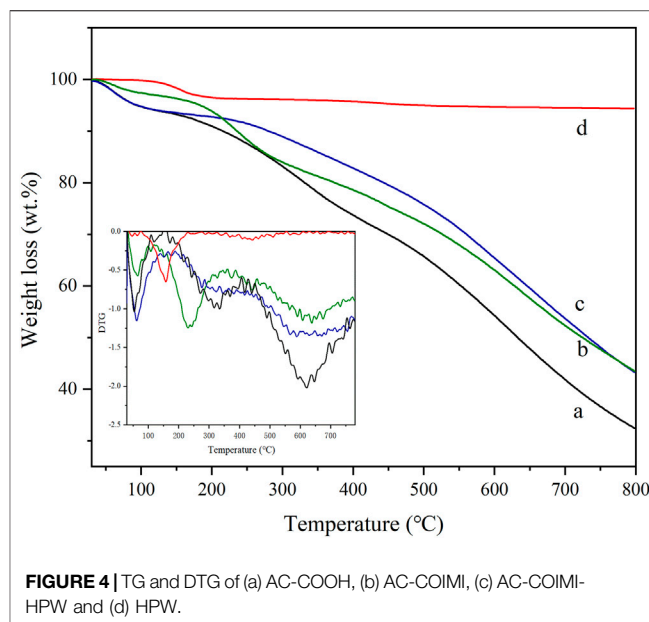
3.1.5 BET

The specific surface areas of AC, AC-COOH, AC-COIMI, and AC-COIMI-HPW are determined using the BET method, and the isotherms of nitrogen absorption and desorption are shown in **Figure 5A**. It can be seen that N_2 adsorption isotherms of four samples showed type IV adsorption isotherms, indicating the presence of the mesoporous structure (Park et al., 2014; Liu et al., 2019).

The pore size distribution of the sample is shown in **Figure 5B**. It was found that the pore size distribution of AC-COOH, AC-COIMI, and AC-COIMI-HPW was decreased obviously, indicating the mesoporous structure may be blocked or destroyed during the oxidation and subsequent modification process.

From **Table 1**, the specific surface area and pore volume of the carbon materials are gradually decreased with oxidation, imidazolization, and binding HPW. It was shown that the texture of the carbon materials has a certain degree of change after a series of chemical modifications. It could be found that the surface carboxyl density of the activated carbon was vastly increased after the oxidation. The imidazole group density (N-Base) is not equivalently matching with the carboxyl amount; this may be the existence of the decarboxylation of oxidized carbon during the amidation of the carboxyl imidazole salt in the alkaline 2-methylimidazole medium.

3.2 Catalytic Performance
3.2.1 Evaluation of the Catalysts

The catalytic performance of AC-COIMI and AC-COIMI-HPW was investigated in the benzyl alcohol oxidation reaction, and the results are shown in **Table 2**. It could be seen from **Table 2** that the conversion of benzyl alcohol was less than 5% in the presence of no catalyst or AC-COIMI (**Table 2**, entries 1 and 2), indicating that self-oxidation with H_2O_2 is very difficult in the reaction
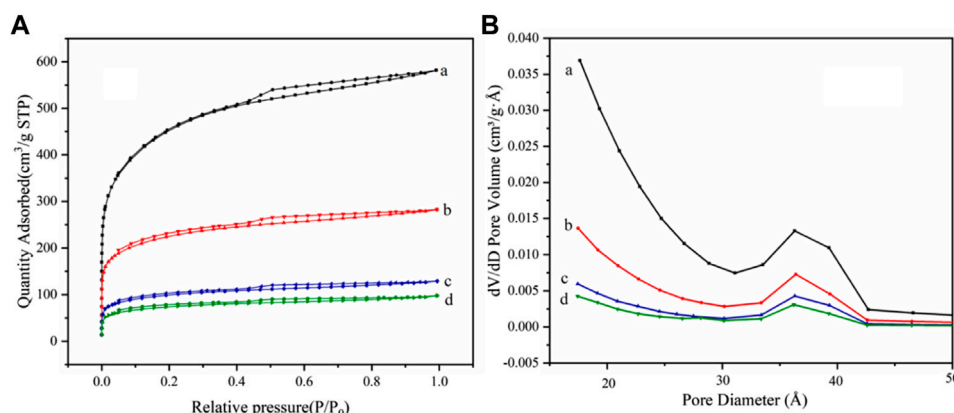
FIGURE 5 | **(A)** N_2 adsorption–desorption isotherms and **(B)** pore size distribution for (a) AC, (b) AC-COOH, (c) AC-COIMI and (d) AC-COIMI-HPW.

TABLE 1 | Surface area and pore properties of four carbonic material samples.

Sample	BET surface area (m^2/g)	Pore volume (cm^3/g)	Density ($\mu mol/g$)
AC	1,072	0.65	10 (-COOH)
AC-OOH	615	0.37	152 (-COOH)
AC-COIMI	316	0.19	103 (N-Base)
AC-COIMI-HPW	235	0.15	—

TABLE 2 | Effects of various catalysts on the oxidation reaction of benzyl alcohol.

Entry	Catalyst	HPW loading (mmol/g)	Conversion (%)	Selectivity[a] (%)
1	None	—	4.7	98.5
2	AC-COIMI	—	2.0	99.2
3	HPW	0.075	58.6	70.1
4	AC-HPW	0.075	70.4	91.8
5	AC-COIMI-HPW (1)	0.031	43.9	97.3
6	AC-COIMI-HPW (2)	0.061	66.8	96.7
7	AC-COIMI-HPW (3)	0.075	82.4	96.0
8	AC-COIMI-HPW (4)	0.087	90.2	91.5
9	AC-COIMI-HPW (5)	0.090	91.3	90.4

Reaction conditions: 4 mmol alcohol, 16 mmol H_2O_2, 30 mg catalyst, 90℃, 6 h, and 15 ml solvent (CH_3CN: H_2O, 1:3).
[a]Selectivity for benzaldehyde.

conditions. It is noteworthy that the catalytic performance was improved by HPW supported on AC (**Table 2**, entries 3 and 4), which brought an increase of 12 percentage points in the conversion and more than twenty in benzaldehyde selectivity. When HPW was supported on AC-COIMI (entry 7), the catalytic performance was further improved. The conversion raised 12 percentage points, and the benzaldehyde selectivity slightly increased in comparison with AC-HPW.

As the loading of phosphotungstic acid increased, the conversion of benzyl alcohol gradually is increased (**Table 2**, entries 6–10) due to the increase in the catalytic sites. However, the selectivity of benzaldehyde is decreased on the contrary, which was caused by the consecutive oxidation of benzaldehyde to benzoic acid. It is very interesting that the conversion of benzyl alcohol on AC-COIMI-HPW (3) is

higher than that of AC-COIMI and HPW (**Table 2**, entries 2 and 3), which means the catalytic properties of HPW adsorbed on AC-COIMI were modified by the interaction of the phosphotungstic acid molecule with the imidazole site through adsorption on the AC-COIMI surface.

3.2.2 Influence of the Reaction Medium
The solvent has an important influence on the oxidation of benzyl alcohol to benzaldehyde when heteropoly acid was used as a catalyst because solvent molecules can occupy the lower energy LUMO in the heteropoly acid (Majid et al., 2007). The effect of the reaction medium on the catalytic performance of AC-COIMI-HPW (4) was investigated, and the results are shown in **Table 3**. The oxidation of benzyl alcohol with H_2O_2 occurred on the catalyst with no additional

TABLE 3 | Catalytic oxidation of benzyl alcohol in various solvents.

Entry	Solvent	Temp. (°C)	Conversion (%)	Selectivity (%)[a]
1	—	90	52.3	88.5
2	Acetone	60	6.8	98.5
3	Ethyl acetate	80	13.5	88.9
4	Toluene	100	40.4	90.8
5	H_2O	90	75.0	92.0
6	CH_3CN	90	8.6	97.7
7	CH_3CN: H_2O(3: 1)	90	13.8	98.6
8	CH_3CN: H_2O(1: 1)	90	42.2	97.6
9	CH_3CN: H_2O(1: 3)	90	90.2	91.5
10	CH_3CN: H_2O(0.5: 3.5)	90	88.5	90.5

Reaction conditions: 4 mmol alcohol, 16 mmol H_2O_2, 30 mg catalyst, 90°C, 6°h, and 15 ml solvent.
[a]Selectivity of benzaldehyde.
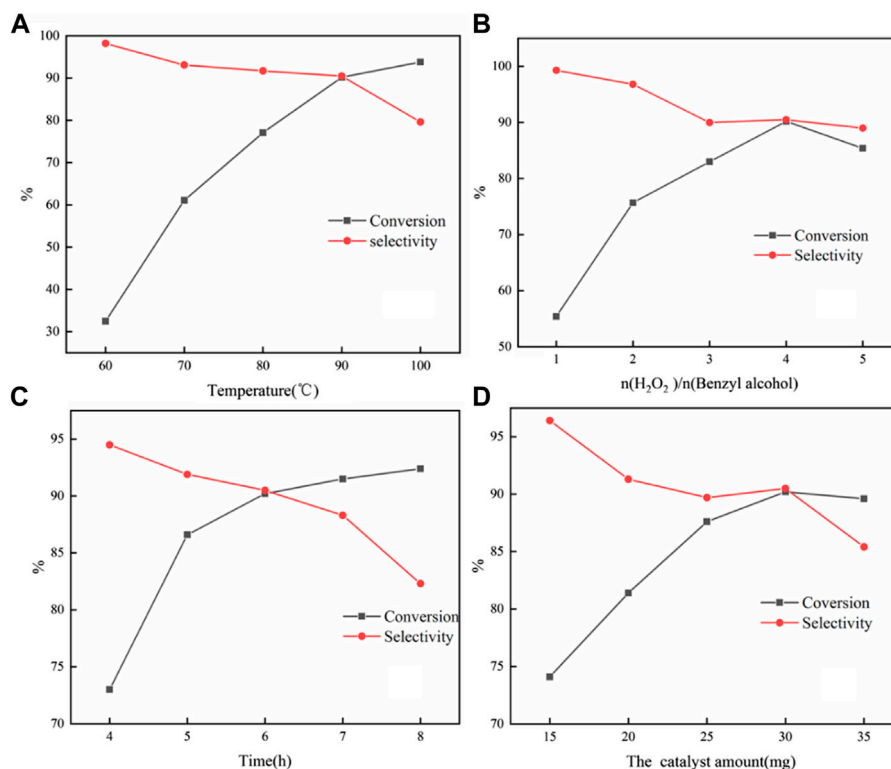
FIGURE 6 | Influences of reaction conditions on the selective oxidation of benzyl alcohol with H_2O_2: temperature **(A)**; molar ratio of H_2O_2 to benzyl alcohol **(B)**; time; and **(C)** catalyst amount **(D)**. Reaction condition: 4 mmol benzyl alcohol, 16 mmol H_2O_2, 30 mg catalyst, 90°C, 6 h, and 15 ml solvent (CH_3CN: H_2O, 1: 3); for each figure, there is a specific parameter changed.

solvent, but the catalytic performance is not attractive (entry 1).
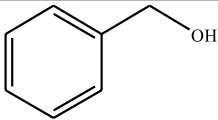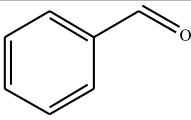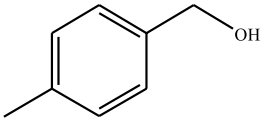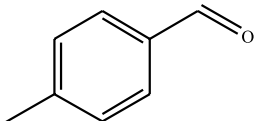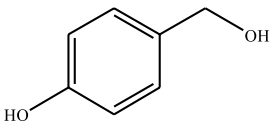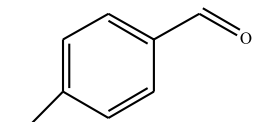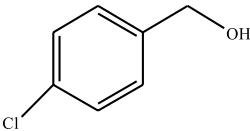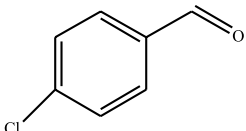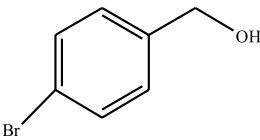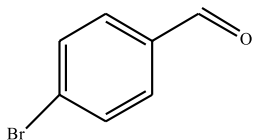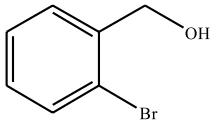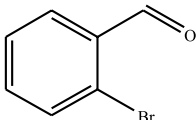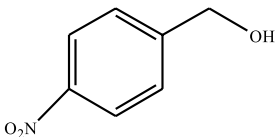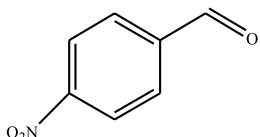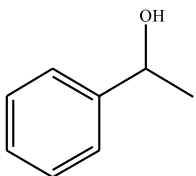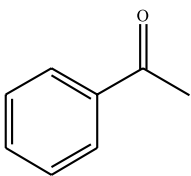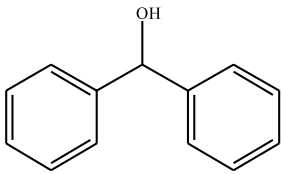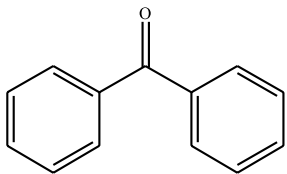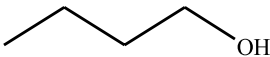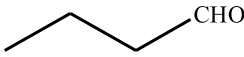
For aprotic polar organic solvents, such as acetone and acetonitrile were added, the catalytic activity was ineffective (Entries 2 and 6). On the contrary, a relatively high conversion for benzyl alcohol was obtained in the presence of ethyl acetate and toluene, respectively. However, the selectivity of benzaldehyde was decreased close to 90% (entries 3 and 4). An interesting phenomenon occurred when the mixtures of acetonitrile and pure water were used in the reaction medium,

in which the activity and selectivity were both improved (Entries 7–10). By adjusting the ratio of the mixed solvent, an optimal conversion was obtained at a 1: 3 volume ratio of acetonitrile with water.

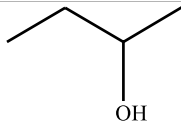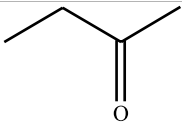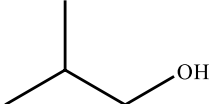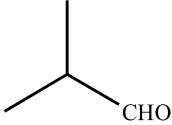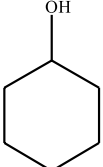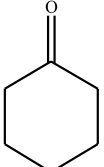### 3.2.3 Influence of Reaction Conditions

From **Figure 6A**, it was found that high selectivity could be obtained at 60°C; however, the conversion was very low. As the temperature further increased and the conversion increased, the selectivity declined sharply at 100°C. This

TABLE 4 | Selective oxidation of various alcohols over the catalyst.

| Entry	Substrate	Product	T (h)	Conversion (%)>	Selectivity[a] (%)
1			6	90.2	95.5
2			6	86.5	97.5
3			6	98.9	93.2
4			6	77.7	94.6
5			6	61.7	>99
6			6	34.2	>99
7			6	55.0	96.5
8			6	98.4	>99
9			6	57.4	>99
10			6	86.0	94.8
11			6	93.6	>99

(Continued on following page)

TABLE 4 | (*Continued*) Selective oxidation of various alcohols over the catalyst.

Entry	Substrate	Product	T (h)	Conversion (%)>	Selectivity[a] (%)
12	(isobutyl alcohol structure, OH)	(isobutyraldehyde structure, CHO)	6	97.3	96.2
13	(cyclohexanol, OH)	(cyclohexanone, O)	12	98.6	>99
14	(hexanol, OH)	(hexanal, CHO)	12	39.5	55.7

Reaction conditions: 4 mmol alcohol, 16 mmol H$_2$O$_2$, 30 mg catalyst, 90°C, 6 h, and 15 ml solvent (CH$_3$CN: H$_2$O, 1: 3).
[a]*Selectivity of aldehydes or ketones.*

FIGURE 7 | (A) Recycling experiment and **(B)** leaching experiment.
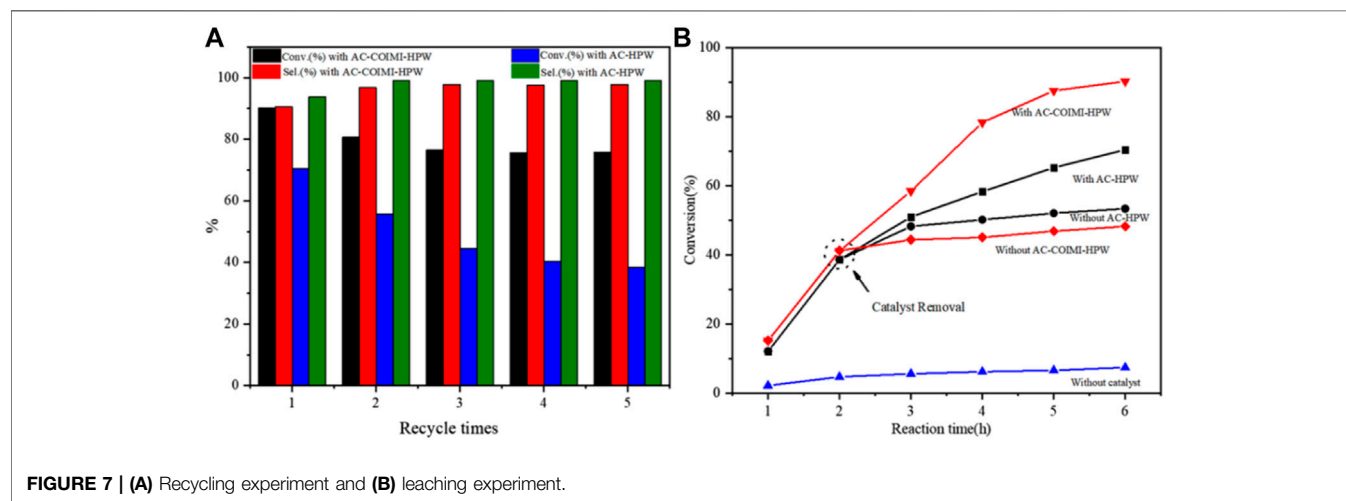
TABLE 5 | ICP results of the W element for the samples of the reaction mixture after tests.

Catalyst	First[a]	Third[a]	Fifth[a]
AC-COIMI-HPW	0.017	Not detected	Not detected
AC-HPW	0.026	0.004	0.004

[a]*W content in the reaction mixture (μg·ml^{-1}).*

might be due to high temperature conditions, which were more conducive to the conversion to the direction of benzoic acid. Therefore, 90°C was selected as the optimal reaction temperature.
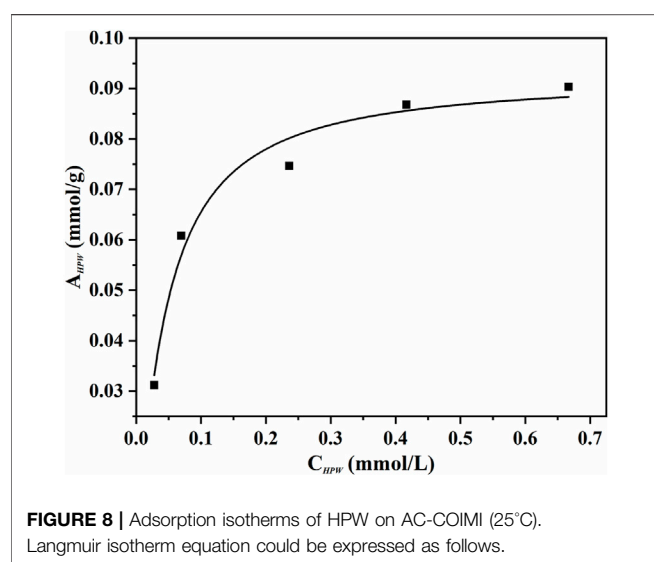
It was found that the reaction conversion increases with the increase in the amount of H$_2$O$_2$ (**Figure 6B**). However, when the amount of H$_2$O$_2$ reached 5 eq., the conversion and selectivity dropped slightly. The reason for the slight decrease in the conversion rate could be understood as the increase in the concentration of hydrogen peroxide in the entire reaction system, which reduced the stability of hydrogen peroxide at this temperature, leading to an increase in self-decomposition. Therefore, the molar ratio of H$_2$O$_2$ to benzyl alcohol was four for the investigation of catalytic performance.

Figure 6C showed the effect of reaction time on the selective oxidation of benzyl alcohol. It can be found that the conversion

TABLE 6 | Comparison of the reported catalytic oxidation of benzyl alcohol with H_2O_2.

Catalyst	Temperature (°C)	Time (h)	Conversion (%)	Selectivity (%)	Times[a]	Reference
AC-COIMI-HPW	90	6	90.2	91.5	5	This work
[TMGHA]$_{2.4}$H$_{0.6}$PW	90	6	69.8	91.8	1	Chen et al. (2014)
GO–N–PW	100	6	80	95	3	Liu et al. (2014)
PAMAM dendritic phosphotungstate hybrids	100	6	89	91	5	Chen et al. (2014)
Long-chain multi-SO$_3$H heteropolyanion	70	4	100	92	5	Li et al. (2015)
HPW/PEHA/ZrSBA-15	80	4	61.5	89.0	1	Zhang et al. (2015)
Polyoxometalate-based gemini ionic liquid	95	6	96	86	7	Hao et al. (2018)
Iron (III) tosylate	60	10	91.7	71.3	1	Zhao et al. (2018)
[PipBs$_2$]$_3$-(PW)$_2$	90	3	96	93	5	Keshavarz et al. (2019)
Chromium borophosphate	80	8	58	95	1	Demet Ozer, (2020)
PW@IL-GO	100	5	93	91	5	Zheng et al. (2020)
Iron chloride–immobilized ionic liquid	90	6	61.8	73.6	7	Cang et al. (2020)

[a]The numeral referring to total times in recycling use of typical catalyst.

FIGURE 8 | Adsorption isotherms of HPW on AC-COIMI (25°C). Langmuir isotherm equation could be expressed as follows.

could rise continuously with the extension of time. The selectivity could basically remain stable having a linear descent with the reaction time less than 7 h, after that sharp decline, which

confirmed the consecutive oxidation of benzaldehyde to benzoic acid.

It could be seen from **Figure 6D** that the increase in the amount of catalyst could effectively increase the conversion. The increasing catalyst dosage can provide more catalytic sites. The collision probability of the substrate and the catalyst per unit time increased, so the oxidation reaction rate was effectively improved. At the same time, the generation of consecutive by-products would also be increased, so the selectivity of the catalyst decreased. With further increase to 35 mg, it speeded up the decomposition of hydrogen peroxide due to the excessive catalyst. The strong adsorption performance of the substrate prevents a part of the substrate from forming peroxide intermediates with phosphotungstic acid peroxide, which led to a decrease in conversion. This showed that an excess amount of the catalyst may be due to an inhibition effect during the reaction process.

3.2.4 Substrate Adaptability

From the results of the substrate scope experiment with AC-COIMI-HPW in **Table 4**, it could be found that the regularity of the catalytic oxidation reaction of aromatic alcohols was that aromatic alcohols with electron-donating groups at the para
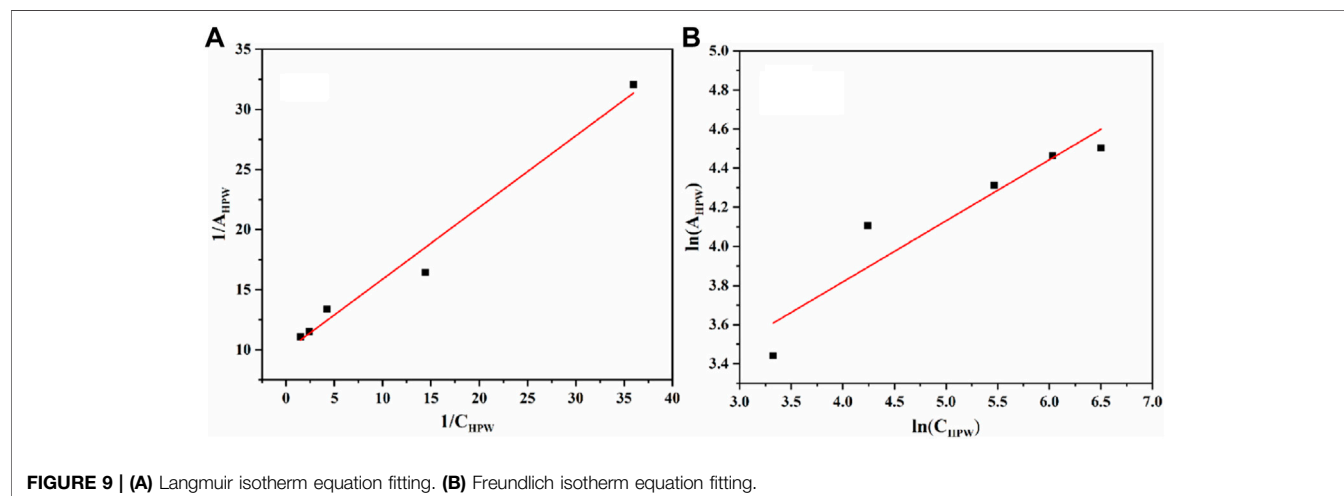

FIGURE 9 | (A) Langmuir isotherm equation fitting. **(B)** Freundlich isotherm equation fitting.

TABLE 7 | Effects of various catalysts on the oxidation reaction of benzyl alcohol.

Entry	2-Methylimidazole: HPW	Conversion (%)	Selectivity[a] (%)
1	0:1	58.6	70.1
2	1:1	69.0	96.8

Reaction conditions: 4 mmol benzyl alcohol, 16 mmol H_2O_2, 0.075 mmol HPW t, 90°C, 6 h, and 15 ml solvent (CH_3CN: H_2O, 1: 3).
[a]Selectivity for benzaldehyde.

position were more reactive than with electron-withdrawing groups. This may be attributed to the electron-donating group transferring electrons to the benzene ring, which increased the electron density of the benzene ring and activates the benzene ring, which made the aromatic alcohol more susceptible to oxidation. On the contrary, the presence of electron-withdrawing groups would reduce the conversion of benzyl alcohol. The activity of 2-bromobenzyl alcohol was further reduced compared with 4-bromobenzyl alcohol because of the existence of steric hindrance.

The reason for the conversion rate of 1-phenylethanol better than benzyl alcohol might be the difference in bond energy values for the oxidation of C-H, the secondary C-H which in 1-phenylethanol is weaker than the primary C-H in benzyl alcohol (entries 1 and 8). This was confirmed by comparing the selective oxidation results of sec-butanol and n-butanol. Similarly, comparing cyclohexanol and n-hexanol, it was also found that the catalytic oxidation activity of cyclohexanol was much better than that of n-hexanol. Moreover, due to the large steric hindrance of the two benzene rings, the oxidized activity of benzhydrol was much low. Without exception, all secondary alcohols were metrologically oxidized to the corresponding ketone with H_2O_2; it was shown that the insertion of active oxygen species to the C–C bond in the ketone very difficultly occurred on the catalytic site of AC-COIMI-HPW; however, the active oxygen species on the catalytic site could generally insert to the C-H bond of the aldehyde group resulting in the formation of the corresponding acid. It is noted that modification is a very important strategy to inhibit or reduce the catalytic activity for the consecutive oxidation of the aldehyde group.

3.3 Catalytic Reusability

To understand the recyclability of AC-COIMI-HPW, the catalyst was usually separated, washed, and dried and then used for the next run. Technically, the drying operation is a consumption process for the recovery and is not suitable for industrial applications. In this work, the recycled catalyst was directly put into reuse in the next run, after centrifugal separation and transferring to the reaction flask with the solvent in the oxidation. Through the recycling experiment (**Figure 7A**), it could be seen that AC-COIMI-HPW could remain extremely stable when it was used three times. This indicated that the imidazole-modified activated carbon not only had higher catalytic activity than the unmodified activated carbon-supported phosphotungstic acid catalyst but also had better stability.

A leaching experiment was carried out in order to verify the decrease in the catalyst effect, and the results are displayed in

Figure 7B. When the reaction reached 2 h, the reaction mixture in the flask was drawn out and centrifuged to separate the catalyst. The collected reaction liquid was allowed to react further without any catalyst. It could be seen that when the AC-COIMI-HPW catalyst was taken out, the conversion of benzyl alcohol was similar to that without a catalyst. Moreover, it could be found that the catalytic activity of AC-HPW was higher than that of AC-COIMI-HPW under the same reaction conditions. On the other hand, it is shown that benzyl alcohol conversion was slightly decreased, and the selectivity of benzaldehyde was elevated on both catalysts in the second run in **Figure 7A**. In order to clarify whether the leaching of phosphotungstic acid was responsible for the decrease in the catalytic activity, an ICP experiment was operated for the detection of the W element in the reaction mixture. As expected, it was found that a trace of phosphotungstic acid was dissolved in the first operation, and the detected amount from the reaction liquids on AC-HPW was more than on AC-COIMI-HPW (**Table 5**). It was observed that no W element was found in the AC-COIMI-HPW system after three recycling phases. This indicated that the activated carbon modified by imidazole anchored phosphotungstic acid through ionic bonds, which not only had better catalytic activity but also greatly improved its stability.

In addition, it is clear seen that AC-COIMI-HPW worked as an oxidative catalyst, exhibiting excellent catalytic performance for the oxidation of benzyl alcohol to benzaldehyde as compared to other systems (**Table 6**).

3.4 Adsorption and Catalytic Mechanism

An adsorption experiment was carried out for discriminating the distribution characteristics of phosphotungstic acid on the innovative catalyst AC-COIMI-HPW at 25°C. The AC-COIMI-HPW samples were added to a series of concentration gradient phosphotungstic acid solutions, and the actual HPW load relative to the equilibrium concentration was obtained by measuring the initial and final absorbance value with the UV-Vis spectrum. The adsorption isotherm is depicted in **Figure 8**. The Langmuir model or Freundlich adsorption model was used to compare the adaptability, respectively.

$$\frac{A_{HPW}}{A_{m,HPM}} = \frac{b_{HPW}C_{HPW}}{1 + b_{HPW}C_{HPW}}. \tag{1}$$

In **Eq. 1**, C_{HPW} is the equilibrium concentration of HPW (mmol/L), A_{HPW} is the corresponding adsorption amount (mmol/g), $A_{m,HPW}$ is the maximal adsorption amount or saturated adsorption capacity (mmol/g) in the Langmuir adsorption model, and b_{HPW} is the Langmuir adsorption equilibrium constant or adsorption coefficient.

Equation 1 could easily be converted to **Eq. 2**:

$$\frac{1}{A_{HPW}} = \frac{1}{A_{m,HPW}} + \frac{1}{A_{m,HPW}b_{HPW}}\frac{1}{C_{HPW}}. \tag{2}$$

Freundlich isotherm equation could be expressed as **Eq. 3**:

$$A_{HPW} = K_F C_{HPW}^{\frac{1}{n}}. \tag{3}$$

Equation 4 could be obtained by taking the natural logarithm to **Eq. 3**.

$$\ln A_{HPW} = \ln K_F + \frac{1}{n} \ln C_{HPW}. \tag{4}$$

K_F and n, respectively, are the constants in the Freundlich adsorption model.

As seen in **Figure 9**, it is found that the Langmuir adsorption model was more suitable, according to the comparison of the linear correlation of **Eq. 2** ($R^2 = 0.975$) with **Eq. 4** ($R^2 = 0.851$). The maximum adsorption capacity per unit mass of AC-COIMI-HPW, $A_{m, HPW} = 97.6$ μmol/g could be obtained. Surprisingly, the value of $A_{m, HPW}$ was very consistent with the N-Base density of 103 μmol/g. It is revealed that HPW could be fixed on the surface of AC-COIMI by an acid-base ionic bond combination. Therefore, the catalytic stability of AC-COIMI-HPW was better than AC-HPW (**Figure 7A**).

In order to explain the differences in the catalytic activity of AC-COIMI-HPW (3), AC-COIMI, and HPW for benzyl alcohol conversion (**Table 2**, entries 2 and 3), a comparative experiment was performed, and the results are listed in **Table 7**. The catalytic results showed that at the same HPW loading, after the addition of 2-methylimidazole at 1:1 concentration, the catalytic performance was markedly modified for the oxidation of benzyl alcohol with H_2O_2. It should be noted that the effective catalytic species is 2-methyl imidazolium dihydrogen phosphotungstate, in which the acid strength of dihydrogen phosphotungstate anion is lower than phosphotungstic acid, so the redox potential of the catalytic species was adjusted to the synergetic activation of the substrates. In another consideration, the lipophilicity of 2-methyl imidazolium is beneficial for grasping benzyl alcohol and further sending the alcohol into the catalytic sphere of the dihydrogen phosphotungstate anion by π–π conjugation of a benzene ring and imidazole ring so that the activity and selectivity of AC-COIMI-HPW both improved the single phosphotungstic acid molecule adsorbed on the imidazole site of the AC-COIMI-activated carbon carrier.

4 CONCLUSION

Keggin-type phosphotungstic acid was successfully hybridized with 2-methylimidazole-modified activated carbon through ionic interactions and hydrogen bonds, showing excellent characteristics of environmental friendliness, high efficiency, and easy reusability in the selective oxidation of alcohols using aqueous H_2O_2. The imidazole-functionalized activated carbon material in this work makes it not only easy to obtain the carrier from the activated carbon but also the modification method is also convenient for operation with aqueous H_2O_2 instead of nitric acid. It provides a practical innovative way for designing efficient heteropoly-based acid catalysts and possesses the potential for industrial application prospects.

DATA AVAILABILITY STATEMENT

The original contributions presented in the study are included in the article/Supplementary Material; further inquiries can be directed to the corresponding author.

AUTHOR CONTRIBUTIONS

MZ: methodology and investigation. HH: conceptualization and methodology. XL: conceptualization, methodology, investigation, resources, and supervision. DY: conceptualization and methodology.

FUNDING

REFERENCES

Alslaibi, T. M., Abustan, I., Ahmad, M. A., and Foul, A. A. (2014). Microwave Irradiated and Thermally Heated Olive Stone Activated Carbon for Nickel Adsorption from Synthetic Wastewater: A Comparative Study. *AIChE J.* 60 (1), 237–250. doi:10.1002/aic.14236

Atia, H., Armbruster, U., and Martin, A. (2008). Dehydration of Glycerol in Gas Phase Using Heteropolyacid Catalysts as Active Compounds. *J. Catal.* 258 (1), 71–82. doi:10.1016/j.jcat.2008.05.027

Cang, R., Lu, B., Li, X., Niu, R., Zhao, J., and Cai, Q. (2015). Iron-chloride Ionic Liquid Immobilized on SBA-15 for Solvent-free Oxidation of Benzyl Alcohol to Benzaldehyde with H_2O_2. *Chem. Eng. Sci.* 137, 268–275. doi:10.1016/j.ces.2015.06.044

Cazetta, A. L., Vargas, A. M. M., Nogami, E. M., Kunita, M. H., Guilherme, M. R., Martins, A. C., et al. (2011). NaOH-activated Carbon of High Surface Area Produced from Coconut Shell: Kinetics and Equilibrium Studies from the Methylene Blue Adsorption. *Chem. Eng. J.* 174, 117–125. doi:10.1016/j.cej.2011.08.05810.1016/j.cej.2011.08.058

Chen, G., Zhou, Y., Long, Z., Wang, X., Li, J., and Wang, J. (2014). Mesoporous Polyoxometalate-Based Ionic Hybrid as a Triphasic Catalyst for Oxidation of

Benzyl Alcohol with H_2O_2 on Water. *ACS Appl. Mat. Interfaces* 6 (6), 4438–4446. doi:10.1021/am5001757

Chen, Y., Tan, R., Zheng, W., Zhang, Y., Zhao, G., and Yin, D. (2014). Dendritic Phosphotungstate Hybrids Efficiently Catalyze the Selective Oxidation of Alcohols with H_2O_2. *Catal. Sci. Technol.* 4 (11), 4084–4092. doi:10.1039/c4cy00675e

Choudhary, A., Sharma, N., Sharma, C., JamwalPaul, B. S., and Paul, S. (2019). Synergistic Effect of Cr^{3+} on Layered Double Hydroxide Supported Cu 0 Nanoparticles for the Oxidation of Alcohols and Hydrocarbons. *ChemistrySelect* 4, 5276–5283. doi:10.1002/slct.20180382910.1002/slct.201803829

Costa, V. V., Jacinto, M. J., Rossi, L. M., Landers, R., and Gusevskaya, E. V. (2011). Aerobic Oxidation of Monoterpenic Alcohols Catalyzed by Ruthenium Hydroxide Supported on Silica-Coated Magnetic Nanoparticles. *J. Catal.* 282 (1), 209–214. doi:10.1016/j.jcat.2011.06.014

Dong, X., Wang, D., Li, K., Zhen, Y., Hu, H., and Xue, G. (2014). Vanadium-substituted Heteropolyacids Immobilized on Amine- Functionalized Mesoporous MCM-41: A Recyclable Catalyst for Selective Oxidation of Alcohols with H_2O_2. *Mater. Res. Bull.* 57, 210–220. doi:10.1016/j.materresbull.2014.05.041

Fan, Z., Yan, J., Wei, T., Zhi, L., Ning, G., Li, T., et al. (2011). Asymmetric Supercapacitors Based on Graphene/MnO_2 and Activated Carbon Nanofiber

Electrodes with High Power and Energy Density. *Adv. Funct. Mat.* 21, 2366–2375. doi:10.1002/adfm.201100058

Hajian, R., and Alghour, Z. (2016). Selective Oxidation of Alcohols with H_2O_2 Catalyzed by Zinc Polyoxometalate Immobilized on Multi-Wall Carbon Nanotubes Modified with Ionic Liquid. *Chi. Chem. Lett.* 28 (5), 971–975. doi:10.1016/j.cclet.2016.12.003

Hao, P., Zhang, M., Zhang, W., Tang, Z., Luo, N., Tan, R., et al. (2018). Polyoxometalate-based Gemini Ionic Catalysts for Selective Oxidation of Benzyl Alcohol with Hydrogen Peroxide in Water. *Catal. Sci. Technol.* 8 (17), 4463–4473. doi:10.1039/C8CY01191E

Hosseini Eshbala, F., Mohanazadeh, F., and Sedrpoushan, A. (2016). Tungstate Ions ($WO_4 =$) Supported on Imidazolium Framework as Novel and Recyclable Catalyst for Rapid and Selective Oxidation of Benzyl Alcohols in the Presence of Hydrogen Peroxide. *Appl. Organometal. Chem.* 31 (5), e3597. doi:10.1002/aoc.3597

Hosseini-Eshbala, F., Sedrpoushan, A., Breit, B., Mohanazadeh, F., and Veisi, H. (2020). Ionic-liquid-modified CMK-3 as a Support for the Immobilization of Molybdate Ions (MoO_4^{2-}): Heterogeneous Nanocatalyst for Selective Oxidation of Sulfides and Benzylic Alcohols. *Mater. Sci. Eng. C* 110, 110577. doi:10.1016/j.msec.2019.110577

Karimi, B., Bigdeli, A., Safari, A. A., Khorasani, M., ValiKhodadadi, H. K. S., and Khodadadi Karimvand, S. (2020). Aerobic Oxidation of Alcohols Catalyzed by In Situ Generated Gold Nanoparticles inside the Channels of Periodic Mesoporous Organosilica with Ionic Liquid Framework. *ACS Comb. Sci.* 22 (2), 70–79. doi:10.1021/acscombsci.9b00160

Keshavarz, M., Tabatabaee, M., and Shahabi, M. (2019). Novel Piperazinium Polyoxo Metalate-Based Acidic Ionic Liquids as Highly Efficient Catalysts for the Selective Oxidation of Alcohols. *Catal. Commun.* 131, 105748. doi:10.1016/j.catcom.2019.105748

Koohzad, E., Jafari, D., and Esmaeili, H. (2019). Adsorption of Lead and Arsenic Ions from Aqueous Solution by Activated Carbon Prepared from Tamarix Leaves. *ChemistrySelect* 4, 12356–12367. doi:10.1002/slct.201903167

Li, X., Cao, R., and Lin, Q. (2015). Selective Oxidation of Alcohols with H_2O_2 Catalyzed by Long Chain Multi-So3h Functionalized Heteropolyanion-Based Ionic Liquids under Solvent-free Conditions. *Catal. Commun.* 69, 5–10. doi:10.1016/j.catcom.2015.05.011

Liu, H., Su, Y., Liu, C., Zhou, A., Chu, X., Liu, S., et al. (2021). Practical and Sustainable Modification Method on Activated Carbon to Improve the Decolorization Process in the Acetaminophen Pharmaceutical Industry. *ACS Omega* 6 (8), 65451–65462. doi:10.1021/acsomega.0c05637

Liu, K., Chen, T., Hou, Z., Wang, Y., and Dai, L. (2014). Graphene Oxide as Support for the Immobilization of Phosphotungstic Acid: Application in the Selective Oxidation of Benzyl Alcohol. *Catal. Lett.* 144 (2), 314–319. doi:10.1007/s10562-013-1121-410.1007/s10562-013-11214

Liu, W., Xiao, J., Xu, Q., Liu, X., Zhong, S., Huang, H., et al. (2019). Imidazolyl Activated Carbon Refluxed with Ethanediamine as Reusable Heterogeneous Catalysts for Michael Addition. *RSC Adv.* 9 (1), 185–191. doi:10.1039/C8RA09457H

Lopes da Costa, N., Guedes Pereira, L., Mendes Resende, J. V., Diaz Mendoza, C. A., Kaiser Ferreira, K., Detoni, C., et al. (2021). Phosphotungstic Acid on Activated Carbon: A Remarkable Catalyst for 5-hydroxymethylfurfural Production. *Mol. Catal.* 500, 111334. doi:10.1016/j.mcat.2020.11133410.1016/j.mcat.2020.111334

Majid, M. H., Benmorad, T., Bakhtiari, K., Bamoharram, F. F., and Oskooie, H. (2007). $H_{3+x}PMo_{12-x}V_xO_{40}$ (Heteropolyacids)-catalyzed Regioselective Nitration of Phenol to O-Nitrophenol in Heterogeneous System. *J. Mol. Catal. A Chem.* 264, 318–321. doi:10.1016/j.molcata.2006.09.014

Mandal, S., Bando, K. K., Santra, C., Maity, S., James, O. O., Mehta, D., et al. (2013). Sm-CeO$_2$ Supported Gold Nanoparticle Catalyst for Benzyl Alcohol Oxidation Using Molecular O$_2$. *Appl. Catal. A General* 452, 94–104. doi:10.1016/j.apcata.2012.11.03010.1016/j.apcata.2012.11.030

Mohamadi, M., Kowsari, E., haddadi-Asl, V., Yousefzadeh, M., Chinnappan, A., and Ramakrishna, S. (2020). Highly-efficient Microwave Absorptivity in Reduced Graphene Oxide Modified with PTA@ Imidazolium Based Dicationic Ionic Liquid and Fluorine Atom. *Compos. Sci. Technol.* 188, 107960. doi:10.1016/j.compscitech.2019.10796010.1016/j.compscitech.2019.107960

Norouzi, M., and Elhamifar, D. (2019). Ionic Liquid-Modified Magnetic Mesoporous Silica Supported Tungstate: A Powerful and Magnetically Recoverable Nanocatalyst. *Compos. Part B Eng.* 176, 107308. doi:10.1016/j.compositesb.2019.10730810.1016/j.compositesb.2019.107308

Ozer, D. (2020). Liquid Phase Oxidation of Benzyl Alcohol to Benzaldehyde over Chromium Borophosphate Catalyst Synthesized by Solution Combustion Method Using Different Types of Fuel. *Res. Chem. Intermed.* 46, 3449–3458. doi:10.1007/s11164-020-04155-2

Park, J., Nabae, Y., Hayakawa, T., and Kakimoto, M.-a. (20142014). Highly Selective Two-Electron Oxygen Reduction Catalyzed by Mesoporous Nitrogen-Doped Carbon. *ACS Catal.* 4, 3749–3754. doi:10.1021/cs5008206

Sadjadi, S., Malmir, M., and Heravi, M. M. (2019). A Novel Magnetic Heterogeneous Catalyst Based on Decoration of Halloysite with Ionic Liquid-Containing Dendrimer. *Appl. Clay Sci.* 168, 184–195. doi:10.1016/j.clay.2018.11.012

Salimi, M., Esmaili, F., and Sandaroos, R. (2020). Effective and Selective Aerobic Oxidation of Primary and Secondary Alcohols Using CoFe$_2$O$_4$ @HT@Imine-Cu II and TEMPO in the Air Atmosphere. *Appl. Org. Met. Chem.* 35. doi:10.1002/aoc.6074

Shahbazi, D., Mousavi, S. A., and Nayeri, D. (2020). Low-cost Activated Carbon: Characterization, Decolorization, Modeling, Optimization and Kinetics. *Int. J. Environ. Sci. Technol.* 17 (9), 3935–3946. doi:10.1007/s13762-020-02698-w

Shi, Y., Xia, Y., Xu, G., Wen, L., Gao, G., and Zong, B. (2022). Hydrogen Peroxide and Applications in Green Hydrocarbon Nitridation and Oxidation. *Chin. J. Chem. Eng.* 41, 145–161. doi:10.1016/j.cjche.2021.09.030

Shimodaira, N., and Masui, A. (2002). Raman Spectroscopic Investigations of Activated Carbon Materials. *J. Appl. Phys.* 92, 902–909. doi:10.1063/1.148743410.1063/1.1487434

Su, H., and Yang, C. (2014). Selective Oxidation of Benzyl Alcohol Catalyzed by (TEAH)nH3-nPW12O40 and its Reaction Mechanism. *Chin. J. Catal.* 35, 1224–1234. doi:10.1016/S1872-2067(14)60097-8

Tan, R., Liu, C., Feng, N., Xiao, J., Zheng, W., Zheng, A., et al. (2012). Phosphotungstic Acid Loaded on Hydrophilic Ionic Liquid Modified SBA-15 for Selective Oxidation of Alcohols with Aqueous H$_2$O$_2$. *Microporous Mesoporous Mater.* 158, 77–87. doi:10.1016/j.micromeso.2012.03.023

Ternero-Hidalgo, J. J., Rosas, J. M., Palomo, J., Valero-Romero, M. J., Rodríguez-Mirasol, J., and Cordero, T. (2016). Functionalization of Activated Carbons by HNO$_3$ Treatment: Influence of Phosphorus Surface Groups. *Carbon* 101, 409–419. doi:10.1016/j.carbon.2016.02.01510.1016/j.carbon.2016.02.015

Wu, Y., Zhang, Y., Lv, X., Mao, C., Zhou, Y., Wu, W., et al. (2020). Synthesis of Polymeric Ionic Liquids mircrospheres/Pd nanoparticles/CeO$_2$ Core-Shell Structure Catalyst for Catalytic Oxidation of Benzyl Alcohol. *J. Taiwan Inst. Chem. Eng.* 107, 161–170. doi:10.1016/j.jtice.2019.11.006

Xu, Z., Zhou, S., and Zhu, M. (2021). Ni Catalyst Supported on Nitrogen-Doped Activated Carbon for Selective Hydrogenation of Acetylene with High Concentration. *Catal. Commun.* 149, 106241. doi:10.1016/j.catcom.2020.106241

Yao, M., Liang, W., Chen, H., and Zhang, X. (2020). Efficient Hydrogen Production from Formic Acid Using Nitrogen-Doped Activated Carbon Supported Pd. *Catal. Lett.* 150, 2377–2384. doi:10.1020.03141.y10.1007/s10562.020.03141.y

Zhao, Y., Yu, C., Wu, S., Zhang, W., Xue, W., and Zeng, Z. (2018). Synthesis of Benzaldehyde and Benzoic Acid by Selective Oxidation of Benzyl Alcohol with Iron(III) Tosylate and Hydrogen Peroxide: A Solvent-Controlled Reaction. *Catal. Lett.* 148, 3082–3092. doi:10.1007/s10562.018.2515.0

Zheng, W., Wu, M., Yang, C., Chen, Y., Tan, R., and Yin, D. (2020). Alcohols Selective Oxidation with H$_2$O$_2$ Catalyzed by Robust Heteropolyanions Intercalated in Ionic Liquid-Functionalized Graphene Oxide. *Mater. Chem. Phys.* 256, 123681. doi:10.1016/y2020.12368.1

Check for updates

*CORRESPONDENCE
Qiong Xu,
xuqiong@hunnu.edu.cn
Dulin Yin,
dulinyin@126.com

Recent advances on bifunctional catalysts for one-pot conversion of furfural to γ-valerolactone

Jianhua Wang, Zhiyan Xiang, Zexing Huang, Qiong Xu* and Dulin Yin*

National and Local Joint Engineering Laboratory for New Petrochemical Materials and Fine Utilization of Resources, Key Laboratory of Chemical Biology and Traditional Chinese Medicine, Ministry of Education, Hunan Normal University, Changsha, China

γ-Valerolactone (GVL) is one of the most valuable compounds derived from furfural (FAL), which has been industrially produced from agricultural byproducts like corn cobs. It is extremely challenging to synthesize GVL from FAL efficiently *via* a one-pot cascade reaction due to the need for multiple active sites in a single pot. By focusing on the aspects of one-pot synthesis of GVL from FAL, the authors aim to shed light on the rational design and utilization of environmentally friendly bifunctional catalysts with high efficiency in this reaction. Perspectives regarding future research opportunities in bi- or multi-functional catalysts for one-pot GVL synthesis are also discussed.

Introduction

In the 21st century, transition from a fossil-fuel industry to one based on renewable resources is a great challenge in the process of sustainable development (Jakob and Hilaire, 2015). Biomass is the only renewable carbon resource with a wide range of sources, abundant reserves, short formation cycles, and low prices, which can be used as an alternative resource for fuel and chemical production (Chua et al., 2019; Liu et al., 2020; Clauser et al., 2021). γ-Valerolactone (GVL) is an important intermediate compound derived from biomass. The unique physicochemical properties of GVL enables it to have a wide range of applications as fuel, fuel additive, polymeric material precursor, and green solvent (Alonso et al., 2013; Xu et al., 2020). Figure 1 shows the production routes of GVL from lignocelluloses (Raj et al., 2021). Lignocellulosic biomass, whose main components are cellulose/hemicellulose or derived platform compounds like 5-hydroxymethyl furfural (HMF)/furfural (FAL), can be converted into GVL smoothly.

Among these routes, the approach to producing GVL from FAL has attracted much attention. That is because first, it is a carbon-balanced process and has a good carbon-atom economy. In addition, FAL is non-edible, inexpensive, and can be produced from agricultural waste corn cobs industrially (Cui et al., 2016). This makes it possible to produce GVL on a large scale by a two-step reaction from lignocellulose to FAL and then
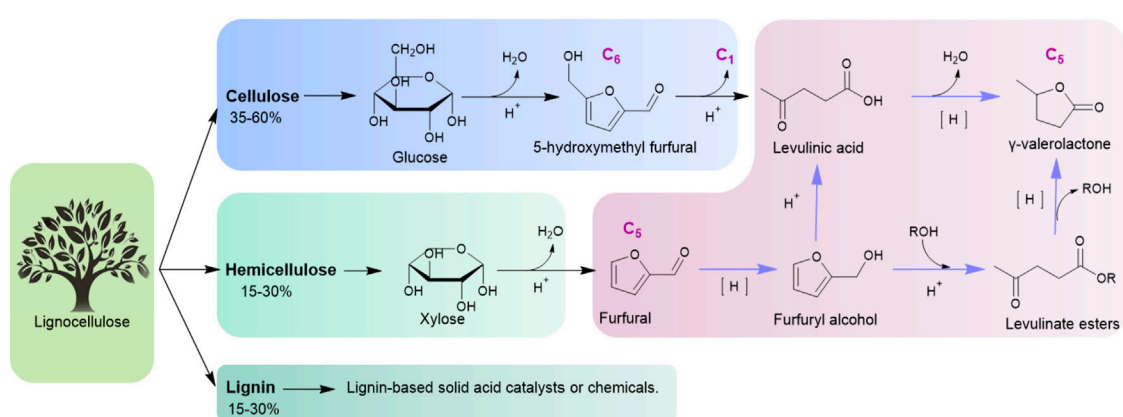
FIGURE 1
Production routes of GVL from lignocellulose.

TABLE 1 Overview of important bifunctional catalysts for one-pot synthesis of GVL from FAL.

Entry	Catalyst	B/L acid ratio	Dosing ratio[a]	Optimum condition	GVL yield/%	Reference
1	Zr-HY + Al-HY	2[c]	2	120°C, 5 h, and 2-pentanol	85	Zhang T et al. (2019)
2	Chitosan-Ru/PPh$_3$+HZSM-5	—	—	160°C, 30 h, and ethanol/formic acid = 95/5	79	Wang Y et al. (2020)
3	CuAl + HZSM-5	1[c]	0.5	160°C, 2 h, ethanol, and 5 MPa H$_2$	90.5	Shao et al. (2021)
4	Zr-Al-beta (Al/Zr[b] = 0.2)	0.05	1.2	170°C, 4 h, and 2-propanol	70.0	Melero et al. (2018)
5	Meso-Zr-Al-beta (Al/Zr[b] = 0.77)	0.5	0.4	120°C, 24 h, 2-propanol, and 5% water	95.0	Song et al. (2017)
6	Hf-Al-USY	0.43	1.0	140°C, 12 h, and 2-propanol	64.9	Tang et al. (2021)
7	HPW/Zr-beta	0.31	2.5	160°C, 24 h, and 2-propanol	70.0	Winoto et al. (2019)
8	ZrO$_2$-HPW-beta	0.65	1.3	170°C, 10 h, and 2-propanol	90.0	Rao et al. (2019)
9	ZrO$_2$-Al-MFI-ns	0.035	2.5	170°C, 36 h, and 2-propanol	82.8	Kim et al. (2020)
10	Zr-CN/H-bate	—	2.2	160°C, 18 h, and 2-propanol	76.5	Zhang H et al. (2019)
11	HPW/ZrO$_2$-SBA-15	0.49	1.31	170°C, 11 h, and 2-propanol	81.0	Rao et al. (2021)
12	Fe$_3$O$_4$/ZrO$_2$@MCM-4	—	0.12	130°C, 30 h, and 2-propanol	85.7	Gao et al. (2021)
13	Sulfated DUT-67(Hf)MOF	—	0.4	180°C, 24 h, and 2-propanol	87.1	Li et al. (2019)
14	Meso-Al$_2$O$_3$-SO$_3$H+0.1 g LiCl	4.35	1.33	120°C, 4 h, 2-butanol, ultrasonic power 90W, and duty cycle 60%	85.6	Karnjanakom et al. (2021)
15	FM-Zr-ARS	1.89	0.48	160°C, 8 h, and 2-propanol	72.4	Peng et al. (2021)
16	VPA-Hf	0.19	0.5	180°C, 14 h, and 2-propanol	81.0	Tan et al. (2022)
17	ZrP/HZSM-5	0.15	—	180°C, 10 h, 2-propanol, and 0.5 MPa N$_2$	64.2	Ye et al. (2020)
18	Zr-P/SAPO-34	0.12	0.5	150°C, 18 h, and 2-propanol	80.0	Li et al. (2021)

[a]Furfural to catalyst mass ratio.
[b]Al/Zr molar ratio.
[c]Ratio of the two mixing catalysts.

to GVL. Therefore, great efforts have been made to one-pot conversion of FAL to GVL (Osatiashtiani et al., 2017; Yu et al., 2019).

There is a series of cascading reactions involving hydrogenation, ring-opening reaction, and lactonization in this reaction. Regarding the hydrogenation process for γ-

valerolactone synthesis, metal catalysts such as Ru, Pt, and Ni (Nemanashi et al., 2018; Wang Y et al., 2020; Maumela et al., 2021) are efficient for direct hydrogenation using gaseous H_2 as an H-donor in FAL hydrogenation and LA/levulinate ester lactonization. Compared with the use of H_2 reduction, reaction systems using alcohol as an H-donor for one-pot production of GVL from FAL *via* a Meerwein–Ponndorf–Verley (MPV) reduction can be effectively catalyzed by acid catalysts (He et al., 2020; Antunes et al., 2022). As the ring-opening reaction of furfuryl alcohol (FOL) is also an acidic catalytic reaction, bifunctional catalysts with Brönsted/Lewis acid active sites have been greatly developed for the GVL synthesis *via* a MPV reaction (Osatiashtiani et al., 2017).

In this mini-review, the authors summarize the efficient bifunctional catalysts with metal/acid or Brönsted/Lewis acid active sites for one-pot conversion of FAL to GVL reported in the last 5 years. Table 1 lists the most efficient catalytic systems among them. Construction of acid centers as well as the supports' structure are discussed, and catalytic reaction conditions are compared. It is hoped to provide insights into designing and developing efficient new sustainable catalysts for one-pot synthesis of GVL.

Efficient bifunctional catalysts

Molecular sieve catalysts

Molecular sieves have regular pore structure, strong acidity, and high hydrothermal stability, which have been perceived as the most popular catalysts reported in the synthesis of GVL so far. Both physically mixed molecular sieve co-catalysts and modified bifunctional molecular sieve catalysts have been developed in one-pot synthesis of GVL from FAL. A physical mixture of Zr-HY and Al-HY zeolites was reported as a highly efficient catalyst system for the one-pot transformation of FAL to GVL using 2-pentanol as the hydrogen donor (Zhang H et al., 2019; Table 1, entry 1). GVL yields reached 85% only after 5 h of reaction at 120 C. The excellent activity of Zr-HY zeolites for the Meerwein–Ponndorf–Verley (MPV) reduction of FAL and levulinate ester was attributed to the larger pore size of HY-zeolites and stronger Lewis acidic sites. Also, Al-HY zeolites provided Brönsted acids, thus promoting furfuryl ether conversion to levulinate ester. Physically mixing H-ZSM-5 and metal catalysts was also reported as efficient metal/acid bifunctional catalytic systems in this reaction. Wang T et al. (2020) mixed chitosan-Ru/PPh₃ and HZSM-5 in an ethanol/formic acid (95/5) solvent to catalyze the FAL one-pot cascade reaction (Table 1, entry 2). GVL yield was 79% after 30 h at 160 C. The unprecedented GVL yield of 90.5% has been reported in a dual catalyst system including CuAl and H-ZSM-

5 in ethanol solvent and 5 MPa H_2 (Shao et al., 2021; Table 1, entry 3). The relative abundance of the hydrogenation sites provided by CuAl and acidic sites provided by HZSM-5 determines the main products from furfuryl alcohol (FA) to ethyl levulinate (EL) or GVL. The biggest advantage of physically mixed catalysts is that the proportion and strength of acid sites can be independently optimized conveniently, thus avoiding complicated catalyst preparation. However, the physically mixed approach does not perform well when reusability and selectivity are concerned.

Since an appropriate proportion of Lewis and Brönsted acid plays a key role in the activity of the catalyst, molecular sieves with tunable Lewis and Brönsted acid sites prepared by doping metal ions or loading Brönsted acids have been widely reported (Li et al., 2020; Sun et al., 2022). Beta zeolite was treated in nitric acid solution and calcination was performed to remove Al, which can lead to more vacancies for the introduction of other metal species by post-impregnation (Melero, et al., 2018, Table 1, entry 4) or solid-state ion-exchange method (Song et al., 2017; Table 1, entry 5; Tang et al., 2021; Table 1, entry 6). The Zr(Hf)-modified molecular sieve catalysts showed superior catalytic activities in this reaction (Table 1, entries 4–10). In this type of dual acid site catalysts, Brönsted acidity is obtained from the Al sites and Lewis acidity is obtained from Zr or Hf sites. From the aspect of increasing catalysts' Brönsted acid centers, phosphotungstic acid (HPW) has received attention for its strong Brönsted acidity (Frattini et al., 2017). HPW/Zr-beta and ZrO_2-HPW-beta were prepared and applied in one-pot conversion of FAL in 2-propanol to give high GVL yields (Winoto et al., 2019; Table 1, entry 7; Rao et al.; Table 1, entry 8).

In addition to the effect brought by active sites, structure and morphology of the molecular sieve are also important for its catalytic efficiency. Taking ZrO_2-[Al]MFI-ns 30 as an example, the MFI molecular sieve has a nano-sponge (NS) morphology, and its unique mesoporous structure allows the ZrO_2 clusters (Lewis acid sites) to be confined within a few unit cell-thin porous silica-aluminate molecular sieve walls (Brönsted acid sites) (Kim et al., 2020; Table 1, entry 9). The generation of separate Brönsted and Lewis acid sites on the internal and external molecular sieves resulted in a significant enhancement of GVL yield (82.8%).

Mesoporous silica catalysts

Mesoporous silica materials are good catalytic supports for their well-defined pore channels, large surface area, and tunable physical/chemical properties (Singh et al., 2018). ZrO_2/SBA-15 and Zr-KIT were prepared by loading ZrO_2 onto SBA-15 (Iglesias et al., 2018) and incorporating Zr into KIT-5 (He et al., 2019) and applied for GVL production by MPV reduction. A medium GVL yield of about 40% from FAL was reported. It may be because the acid strength and density of the catalyst is not enough.

Rao et al. (2021) reported a more efficient bifunctional mesoporous silica catalyst containing Zr and tungstophosphoric acid (TPA/ZrO$_2$-SBA-15), which can completely convert furfural and give a GVL yield of 81%. (Table 1, entry 11). This research indicated that the acid–base properties of the catalyst were directed by the location of ZrO$_2$ or TPA in the support, and that the catalyst with ZrO$_2$ present inside the SBA-15 pores and TPA dispersed on the support showed the highest activity.

A magnetically recoverable multifunctional catalyst (Fe$_3$O$_4$/ZrO$_2$@MCM-41) was tailored by the impregnation of ZrO$_2$ supported on mesoporous MCM-41 coated with Fe$_3$O$_4$ nanoparticles for the cascade conversion of furfural (FAL) giving high yield of GVL. According to the literature, incorporation of Fe$_3$O$_4$ could not only impart the catalyst with a strong magnetism but also tune its acidity to promote GVL production (Gao et al., 2021; Table 1, entry 12).

Other bifunctional catalysts

Among the most active bifunctional catalytic systems reported in the last 5 years, metal–organic frameworks (MOFs), porous Al$_2$O$_3$, and inorganic–organic framework catalysts are notable. As MOFs have a well-defined three-dimensional crystal structure, uniform active centers, high surface area, and porosity, they can be used as both catalysts and catalyst carriers. As shown in Table 1 entry 13, sulfated DUT-67(Hf) bifunctional metal–organic framework catalyst was prepared for the preparation of GVL reaching a yield of 87.1% (Li et al., 2019). The amount of Brönsted acid centers is regulated by adjusting the concentration of the aqueous sulfuric acid solution. But this catalyst cannot be recycled due to a dramatic loss of Brönsted acid sites in the reaction. A complex acid regeneration process was required before reuse.

A mesoporous Al$_2$O$_3$-SO$_3$H catalyst was prepared by grafting sulfonic acid groups onto mesoporous Al$_2$O$_3$ (Karnjanakom et al., 2021, Table 1 entry 14). The mesoporous structure allows the Lewis and Brönsted acid sites in the catalyst to easily transfer intermediates and thus produces the desired GVL. The addition of salt (LiCl) increased the miscibility of the substrate and intermediates in the solvent phase and therefore increased the diffusion rate of the reacting molecules in the organic phase. It was also shown that ultrasonic assistance and the presence of O$_2$ could inhibit the formation of humus and could maintain the stability of the catalyst. The catalyst could be reused for up to twenty runs without significant change. This catalytic system replaces the high-pressure hydrothermal system with a safer and greener ultrasonic/oxygen molecular system, which provides a new idea for the future one-pot method to produce GVL.

Peng et al. (2021) (Table 1 entry 15) reported a multifunctional Zr-containing catalyst (FM-Zr-ARS) with a stable porous inorganic–organic framework that showed high catalytic activity for GVL production (72.4% yield of GVL) from FAL (Table 1, entry 14). The -O-Zr-O- network in the FM-Zr-ARS structure formed a rich content of Lewis acid–base sites. The inherent sulfonic groups in ARS gave the FM-Zr-ARS hybrid an unsaturated acid site.

In addition, coordination organophosphate-Hf polymers (VPA-Hf) were prepared and found to exhibit superior performance in the one-step conversion of furfural to γ-valerolactone with a high yield of 81.0%, with a turnover frequency of 5.0 h^{-1} (Ye et al., 2020, Table 1 entry 16). The environmentally friendly material zirconium phosphate (ZrP) was also used as bifunctional catalysts in this reaction and showed good catalytic activity (Ye et al., 2020, Table 1 entry 17; Li et al., 2021, Table 1 entry 18).

It is noteworthy that ZrOCl$_2$ as an acid/base bifunctional catalyst showed remarkable catalytic activity in the production of GVL (He et al., 2020). A maximum GVL yield of 63.3 and 52.1% was achieved from furfuryl alcohol and furfural at 200°C, respectively. [ZrO(OH)$_2$]n• xH$_2$O species and Brönsted acid species H$^+$ were derived from *in situ* hydrolysis of ZrOCl$_2$•8H$_2$O. This research may provide a new idea for the construction of bifunctional catalysts.

Conclusion and outlook

At present, researchers continue to explore various bifunctional or multifunctional high-efficiency catalysts for the one-pot production of GVL from FAL. To avoid the high pressure and high cost associated with direct hydrogenation (H$_2$), alcohols, especially 2-propanol, are considered hydrogen donors for the production of GVL *via* MPV reduction reactions. In terms of bifunctional catalysts, molecular sieve catalysts with Brönsted/Lewis acid active sites are in mainstream GVL production. The highly active Lewis acid centers are mainly Zr or its cognate main group of Hf-based genera. Acting as Brönsted acids are Al-beta molecular sieves, H-ZSM-5 molecular sieves, HPW, zirconium phosphate, and sulfonic acid groups. The supports with a well-defined structure, well-developed pores, and an easily adjustable acid center will be more favorable for this reaction.

Though rapid development in developing efficient catalytic systems for one-pot conversion of FAL to GVL has been made, there are still some challenges. For example, humins are a big problem in the one-pot reaction, which decrease GVL yields and deactivate catalysts by deposition. Future research should also vigorously focus on exploring new bifunctional catalysts with high efficiency, low cost, energy saving, and environmental protection. Synergistic acid–base bifunctional catalysts can be developed to explore new catalytic systems. The plausible catalytic mechanism is worthy to be understood. Finally,

one-pot synthesis of GVL from more upstream raw materials (e.g., lignocellulose, hemicellulose, or xylose) by using synergistic catalysis of Brönsted acid and Lewis acid is highly expected.

Author contributions

JW: investigation, methodology, writing—original draft preparation, data curation, and formal analysis. ZX: methodology and formal analysis. ZH: validation and discussion. QX: writing—review and editing, conceptualization, project administration, funding acquisition, and supervision. DY: conceptualization, project administration, funding acquisition, and supervision.

Conflict of interest

The authors declare that the research was conducted in the absence of any commercial or financial relationships that could be construed as a potential conflict of interest.

Publisher's note

All claims expressed in this article are solely those of the authors and do not necessarily represent those of their affiliated organizations, or those of the publisher, the editors, and the reviewers. Any product that may be evaluated in this article, or claim that may be made by its manufacturer, is not guaranteed or endorsed by the publisher.

References

Alonso, D. M., Wettstein, S. G., and Dumesic, J. A. (2013). Gamma-valerolactone, a sustainable platform molecule derived from lignocellulosic biomass. *Green Chem.* 15 (3), 584. doi:10.1039/c3gc37065h

Antunes, M. M., Silva, A. F., Fernandes, A., Pillinger, M., Ribeiro, F., Valente, A. A., et al. (2022). Renewable bio-based routes to gamma-valerolactone in the presence of hafnium nanocrystalline or hierarchical microcrystalline zeotype catalysts. *J. Catal.* 4, 56–71. doi:10.1016/j.jcat.2021.12.022

Chua, S. Y., A/P Periasamy, L., Goh, C. M. H., Tan, Y. H., Mujawar, M. N., Kansedo, J., et al. (2019). Biodiesel synthesis using natural solid catalyst derived from biomass waste - a review. *J. Ind. Eng. Chem.* 81, 41–60. doi:10.1016/j.jiec.2019.09.022

Clauser, N. M., González, G., Mendieta, C. M., Kruyeniski, J., Area, M. C., andVallejos, M. E., et al. (2021). Biomass waste as sustainable raw material for energy and fuels, *Sustainability*, 13, 794–814. doi:10.3390/su13020794

Cui, C. X., Zhang, X. M., Bi, Y. Y., Wang, Y. J., Wang, L., Wang, H. Y., et al. (2016). Estimation of corn cob resources and their development and utilization in China. *Chin.agr. Res. Reg. Plan.* 37 (1), 1–8. doi:10.7621/cjarrp.1005-9121.20160101

Frattini, L., Isaacs, M. A., Parlett, C. M. A., Wilson, K., Kyriakou, G., Lee, A. F., et al. (2017). Support enhanced alpha-pinene isomerization over HPW/SBA-15. *Appl. Catal. B Environ.* 200, 10–18. doi:10.1016/j.apcatb.2016.06.064

Gao, X. Y., Yu, X., Peng, L. C., He, L., and Zhang, J. H. (2021). Magnetic Fe$_3$O$_4$ nanoparticles and ZrO$_2$-doped mesoporous MCM-41 as a monolithic multifunctional for gamma-valerolactone production directly from furfural. *Fuel* 300, 120996. doi:10.1016/j.fuel.2021.120996

He, J., Li, H., Xu, Y., and Yang, S. (2019). Dual acidic mesoporous KIT silicates enable one-pot production of γ-valerolactone from biomass derivatives via cascade reactions, *Renew. Energy*, (146), 359–370. doi:10.1016/j.renene.2019.06.105

He, J., Xu, Y. F., Yu, Z. Z., Li, H., Zhao, W. F., Wu, H. G., et al. (2020). ZrOCl$_2$ as a bifunctional and *in situ* precursor material for catalytic hydrogen transfer of bio-based carboxides. *Sustain. Energy Fuels* 4, 3102–3114. doi:10.1039/c9se01313j

Iglesias, J., Melero, J. A., Morales, G., Paniagua, M., Hernández, B., Osatiashtiani, A., et al. (2018). ZrO$_2$-SBA-15 catalysts for the one-pot cascade synthesis of GVL from furfural. *Catal. Sci. Technol.* 17 (8), 4485–4493. doi:10.1039/C8CY01121D

Jakob, M., and Hilaire, J. (2015). Climate science: Unburnable fossil-fuel reserves. *Nature* 517, 150–151. doi:10.1038/517150a

Karnjanakom, S., Bayu, A., Maneechakr, P., Samart, C., Kongparakul, S., Guan, G. Q., et al. (2021). Simultaneous assistance of molecular oxygen and mesoporous SO$_3$H-alumina for a selective conversion of biomass-derived furfural to gamma-valerolactone without an external addition of H-2. *Sustain. Energy Fuels* 5 (16), 4041–4052. doi:10.1039/d1se00817j

Kim, K. D., Kim, J., Teoh, W. Y., Kim, J. C., Huang, J., Ryoo, R., et al. (2020). Cascade reaction engineering on zirconia-supported mesoporous MFI zeolites with tunable lewis-bronsted acid sites: A case of the one-pot conversion of furfural to gamma-valerolactone. *RSC Adv.* 10 (58), 35318–35328. doi:10.1039/d0ra06915a

Li, W. K., Cai, Z., Li, H., Shen, Y., Zhu, Y. Q., Li, H. C., et al. (2019). Hf-based metal organic frameworks as bifunctional catalysts for the one-pot conversion of furfural to gamma-valerolactone. *Mol. Catal.* 472, 17–26. doi:10.1016/j.mcat.2019.04.010

Li, W. L., Li, M. Z., Liu, H., Jia, W. L., Yu, X., Wang, S., et al. (2021). Domino transformation of furfural to γ-valerolactone over SAPO-34 zeolite supported zirconium phosphate catalysts with tunable Lewis and Bronsted acid sites. *Mol. Catal.* 506, 111538. doi:10.1016/j.mcat.2021.111538

Li, X. C., Yuan, X. H., Xia, G. P., Liang, J., Liu, C., Wang, Z. D., et al. (2020). Catalytic production of gamma-valerolactone from xylose over delaminated Zr-Al-SCM-1 zeolite via a cascade process. *J. Catal.* 392, 175–185. doi:10.1016/j.jcat.2020.10.004

Liu, X., Yang, W., Zhang, Q., Li, C., and Wu, H. (2020). Current approaches to alkyl levulinates via efficient valorization of biomass derivatives. *Front. Chem.* 8, 794. doi:10.3389/fchem.2020.00794

Maumela, M., Marx, S., and Meijboom, R. (2021). Heterogeneous Ru catalysts as the emerging potential superior catalysts in the selective hydrogenation of bio-derived levulinic acid to γ-valerolactone: Effect of particle size, solvent, and support on activity, stability, and selectivity. *Catalysts* 11, 292. doi:10.3390/catal.11020292

Melero, J. A., Morales, G., Iglesias, J., Paniagua, M., and Lopez-Aguado, C. (2018). Rational optimization of reaction conditions for the one-pot transformation of furfural to γ-valerolactone over Zr–Al-beta zeolite: Toward the efficient utilization of biomass. *Ind. Eng. Chem. Res.* 57 (34), 11592–11599. doi:10.1021/acs.iecr.8b02475

Nemanashi, M., Noh, J. H., and Meijboom, R. (2018). Hydrogenation of biomass-derived levulinic acid to γ-valerolactone catalyzed by mesoporous supported dendrimer-derived Ru and Pt catalysts: An alternative method for the production of renewable biofuels. *Appl. Catal. A General* 550, 77–89. doi:10.1016/j.apcata.2017.10.015

Osatiashtiani, A., Lee, A. F., and Wilson, K. (2017). Recent advances in the production of gamma-valerolactone from biomass-derived feedstocks via heterogeneous catalytic transfer hydrogenation. *J. Chem. Technol. Biotechnol.* 92 (6), 1125–1135. doi:10.1002/jctb.5213

Peng, Q. R., Wang, H. J., Xia, Y. M., and Liu, X. (2021). One-pot conversion of furfural to gamma-valerolactone in the presence of multifunctional zirconium alizarin red S hybrid. *Appl. Catal. A General* 621, 118203. doi:10.1016/j.apcata.2021.118203

Raj, T., Chandrasekhar, K., Banu, R., Yoon, J., Kumar, G., Kim, S., et al. (2021). Synthesis of γ-valerolactone (GVL) and their applications for lignocellulosic deconstruction for sustainable green biorefineries. *Fuel.* 303; 121333. doi:10.1016/j.fuel.2021.121333

Rao, B. S., Kumari, P. K., Koley, P., Tardio, J., and Lingaiah, N. (2019). One pot selective conversion of furfural to gamma-valerolactone over zirconia containing heteropoly tungstate supported on beta-zeolite catalyst. *Mol. Catal.* 466, 52–59. doi:10.1016/j.mcat.2018.12.024

Rao, B. S., YogitaLakshmi, D. D., Kumari, P. K., and Lingaiah, N. (2021). Influence of metal oxide and heteropoly tungstate location in mesoporous silica towards catalytic transfer hydrogenation of furfural to gamma-valerolactone. *Sustain. Energy Fuels* 5 (14), 3719–3728. doi:10.1039/d1se00340b

Shao, Y. W., Li, Q. Y., Dong, X. Y., Wang, J. Z., Sun, K., Zhang, L. J., et al. (2021). Cooperation between hydrogenation and acidic sites in Cu-based catalyst for

selective conversion of furfural to gamma-valerolactone. *Fuel* 293, 120457. doi:10.1016/j.fuel.2021.120457

Singh, S., Kumar, R., Setiabudi, H. D., Nanda, S., and Vo, D. V. N. (2018). Advanced synthesis strategies of mesoporous SBA-15 supported catalysts for catalytic reforming applications: A state-of-the-art review. *Appl. Catal. A General* 559, 57–74. doi:10.1016/j.apcata.2018.04.015

Song, S., Di, L., Wu, G. J., Dai, W. L., Guan, N. J., Li, L. D., et al. (2017). Meso-Zr-Al-beta zeolite as a robust catalyst for cascade reactions in biomass valorization. *Appl. Catal. B Environ.* 205, 393–403. doi:10.1016/j.apcatb.2016.12.056

Sun, W. J., Li, H. F., Wang, X. C., and Liu, A. Q. (2022). Cascade upgrading of biomass-derived furfural to γ-valerolactone over Zr/Hf-based catalysts. *Front. Chem.* 10, 863674–863679. doi:10.3389/fchem.2022.863674

Tan, J. Y., Liu, Y. X., Li, M. R., Li, H., and Yang, S. (2022). One-step catalytic upgrading of bio-based furfural to gamma-valerolactone actuated by coordination organophosphate-Hf polymers. *Sustain. Energy Fuels* 6 (4), 484–501. doi:10.1039/d1se01476e

Tang, B., Li, S., Song, W. C., Li, Y., and Yang, E. C. (2021). One-pot transformation of furfural into gamma-valerolactone catalyzed by a hierarchical Hf-Al-USY zeolite with balanced Lewis and Bronsted acid sites. *Sustain. Energy Fuels* 5 (18), 4724–4735. doi:10.1039/d1se00942g

Wang T, T. L., He, J. H., and Zhang, Y. T. (2020). Production of gamma-Valerolactone from one-pot transformation of biomass-derived carbohydrates over chitosan-supported Ruthenium catalyst combined with zeolite ZSM-5. *Eur. J. Org. Chem.* 2020 (11), 1611–1619. doi:10.1002/ejoc.201901704

Wang Y, Y. X., Lu, Y. W., Cao, Q. E., and Fang, W. H. (2020). A magnetic CoRu-CoO$_X$ nanocomposite efficiently hydrogenates furfural to furfuryl alcohol at ambient H-2 pressure in water. *Chem. Commun.* 56 (26), 3765–3768. doi:10.1039/d0cc01039a

Winoto, H. P., Fikri, Z. A., Ha, J. M., Park, Y. K., Lee, H., Suh, D. J., et al. (2019). Heteropolyacid supported on Zr-Beta zeolite as an active catalyst for one-pot transformation of furfural to gamma-valerolactone. *Appl. Catal. B Environ.* 241, 588–597. doi:10.1016/j.apcatb.2018.09.031

Xu, R., Liu, K., Du, H. S., Liu, H. Y., Cao, X. F., Zhao, X. Y., et al. (2020). Falling leaves return to their roots: A review on the preparation of γ-valerolactone from lignocellulose and its application in the conversion of lignocellulose. *ChemSusChem* 13, 6461–6476. doi:10.1002/cssc.202002008

Ye, L., Han, Y. W., Bai, H., and Lu, X. B. (2020). HZ-ZrP catalysts with adjustable ratio of bronsted and Lewis acids for the one-pot value-added conversion of biomass-derived furfural. *ACS Sustain. Chem. Eng.* 8 (19), 7403–7413. doi:10.1021/acssuschemeng.0c01259

Yu, Z. H., Lu, X. B., Liu, C., Han, Y. W., and Ji, N. (2019). Synthesis of γ-valerolactone from different biomass-derived feedstocks: Recent advances on reaction mechanisms and catalytic systems, *Renew. Sustain. Energy Rev.*, 112, 140–157. doi:10.1016/j.rser.2019.05.039

Zhang H, H. W., Yang, W. J., Roslan, I. I., Jaenicke, S., and Chuah, G. K. (2019). A combo Zr-HY and Al-HY zeolite catalysts for the one-pot cascade transformation of biomass-derived furfural to gamma-valerolactone. *J. Catal.* 375, 56–67. doi:10.1016/j.jcat.2019.05.020

Zhang T, T. W., Lu, Y. J., Li, W. Z., Su, M. X., Yang, T., Ogunbiyi, A., et al. (2019). One-pot production of gamma-valerolactone from furfural using Zr-graphitic carbon nitride/H-beta composite. *Int. J. Hydrogen Energy* 44 (29), 14527–14535. doi:10.1016/j.ijhydene.2019.04.059

Check for updates

Catalytic hydrogenolysis of lignin to phenolic monomers over Ru supported N,S-co-doped biochar: The importance of doping atmosphere

Wenran Gao[1], Ke Wang[1], Yishuang Wu[1], Xun Zhu[2], Yinlong Wu[3], Shoujun Zhang[3], Bin Li[4], Yong Huang[1]*, Shu Zhang[1]* and Hong Zhang[1]

[1]Joint International Research Laboratory of Biomass Energy and Materials, Jiangsu Co-Innovation Center of Efficient Processing and Utilization of Forest Resources, College of Materials Science and Engineering, Nanjing Forestry University, Nanjing, Jiangsu, China, [2]Department of Chemistry, Shantou University Medical College, Shantou, Guangdong, China, [3]Hefei Debo Bioenergy Science & Technology Co., Ltd., Hefei, Anhui, China, [4]School of Energy and Power Engineering, Jiangsu University, Zhenjiang, China

Doping of heteroatoms into carbon materials is a popular method to modify their physicochemical structures and has been widely used in the fields of energy conversion and storage. This study aims to investigate the effect of doping atmosphere on the catalytic performance of nitrogen and sulfur co-doped biochar supported Ru in the production of phenolic monomers from lignin hydrogenolysis. The results showed that the catalyst prepared under CO_2 atmosphere (Ru@CNS-CO_2) was able to produce phenolic monomers from corncob lignin with a yield up to 36.41 wt%, which was significantly higher than that from the run over N_2-prepared catalyst (Ru@CNS-N_2). The characterization of the catalysts demonstrated that the CNS-CO_2 support had a larger specific surface area, richer C=S and C-S groups, and higher oxygen content than CNS-N_2, resulting in finer Ru particles and more Ru^0 content on the CNS-CO_2 support. The Ru@CNS-CO_2 catalyst exhibited high activity in hydrogenation and fragmentation of β-O-4 linkages.

KEYWORDS

lignin, phenolic monomers, N,S-co-doping, biochar, hydrogenolysis

Introduction

With the exhaustion of fossil energy and the emission of carbon dioxide during its utilization, biomass conversion has become a hot topic because of its renewability and carbon neutrality or even negativity. Lignin, which accounts for 15–30 wt% of biomass, consists of coniferyl alcohol (G), sinapyl alcohol (S), and *p*-coumaryl alcohol (H) phenylpropane units connected by C-O/C bonds, and is usually considered to be the largest source of renewable aromatic-containing compounds in nature (Zakzeski et al.,

2010; Shuai et al., 2016). The main method for lignin valorization is to break the linkages among structural units to form small molecular phenolic compounds, which has great potentials in important platforms to produce fuels, phenolic resin, and other chemicals (Ragauskas et al., 2014; Schutyser et al., 2018; Zevallos Torres et al., 2020). Lignin depolymerization into chemicals and fuels, however, remains a challenge due to the stability and complexity of its structure.

Many strategies, such as catalytic pyrolysis, oxidation, hydrogenolysis, have been developed to break the C-O/C bonds among structural units (Li et al., 2015; Chen et al., 2021). Among them, catalytic hydrogenolysis is considered as one of the most promising methods because of the high selectivity to break specific bonds (Ye et al., 2021). Transition metals loaded on various supports are commonly employed as effective catalysts for the hydrogenolysis of lignin, which has led to two research directions: 1) exploration of the types of metals and/or the synergistic effect of multiple metals. For example, Cheng et al. compared the effects of Ni/C, Cu/C, and NiCu/C catalysts on depolymerization of organosolv poplar lignin, and NiCu/C was found to have the best catalytic performance among them (Cheng et al., 2020). Also, Li et al. investigated the activity of M/NiAl$_2$O$_4$ (M = Pt, Pd, Ru) catalysts in lignin hydrogenolysis, and Ru/NiAl$_2$O$_4$ showed the highest activity due to the rapid recovery of active sites (Li et al., 2021). 2) modification of the structures of supports to adjust the interactions between metals and supports, including the control of support composition and/ or morphology, skeleton doping, and surface functionalization (van Deelen et al., 2019).

Among various support materials, biomass-derived biochar has attracted extensive attention because of the structural controllability, environmental friendliness, and low cost (Liu et al., 2015; Xiong et al., 2017). Since biochar is mainly composed of carbon atoms, doping heteroatoms (e.g., oxygen, nitrogen, sulfur, phosphorus, etc.) into biochar structure (including skeleton doping and surface functionalization) will inevitably affect the electron cloud density distribution of biochar, thus leading to change in interactions between metals and biochar. Recently, Luo et al. used nitrogen-doped biochar to load Ru particles as a catalyst and a high yield of phenolic monomer with 31.2 wt% was obtained by cornstalk lignin hydrogenolysis at 260°C (Luo et al., 2022). They claimed that the doping of nitrogen led to the formation of micro-mesoporous structure and promoted the electron transfer between the loaded Ru and biochar. Our previous study also investigated lignin hydrogenolysis over Ru supported on various (non)-functionalized graphitized carbon nanotubes (CNT, CNT-OH, CNT-COOH, and CNT-NH$_2$), and Ru@CNT-NH$_2$ provided the highest yield of phenolic monomers due to the prominent partial hydrogenation of C (sp^2)-O/C bonds to C (sp^3)-O/C bonds in lignin (Wu et al., 2021).

It should be noted that the doping of heteroatoms into biochar was usually conducted under an inert atmosphere

(e.g., N$_2$ and Ar), indicating that the insertion of heteroatoms into biochar was highly temperature-dependent. This often results in an inefficient doping process and non-uniform distribution of heteroatoms, which further affects the distribution of metals. It can be known from gasification of coal/biochar that carbon is easy to react with some active atmospheres (such as O$_2$, CO$_2$, and H$_2$O), thus forming defects in carbon skeleton. Particularly for CO$_2$, it can selectively react with the small aromatic rings in the carbon structure (Zhang et al., 2022). Inspired by this, doping of heteroatoms under an active atmosphere is expected to create more sites for doping and help the insertion of heteroatoms into carbon skeleton.

In this study, nitrogen and sulfur co-doped biochars in N$_2$ and CO$_2$ atmospheres were prepared as supports. After loading Ru onto the prepared supports, various characterizations were conducted to understand the differences in the physiochemical structures of the catalysts. Finally, catalytic hydrogenolysis of a technical lignin was performed to investigate the effect of doping atmosphere, with an emphasis on the production of phenolic monomers.

Experiments

Materials

Technical lignin (40–200 mesh) was purchased from Shandong Longlive Biotechnology Co., Ltd., China. Ruthenium chloride hydrate (RuCl$_3$•xH$_2$O) with Ru content 35–42% was purchased from Aladdin Technical Corporation, China. Methanol (>99.5%) was purchased from Nanjing Chemical Reagent Co., Ltd., China. Thiourea (≥99.0%) was purchased from Sinopharm Chemical Reagent Co., Ltd. Deionized water was used throughout the experiment.

Catalysts preparation

The biochar support was obtained from poplar pyrolysis under a N$_2$ atmosphere at 450°C for 3 h. Nitrogen and sulfur co-doped supports were prepared by carbonizing a mixture of char and thiourea at a 1:2 mass ratio under a N$_2$ or CO$_2$ atmosphere at 800°C for 1 h, which were noted as CNS-N$_2$ and CNS-CO$_2$ later. To understand the effect of nitrogen and sulfur co-doping, a sole biochar sample was also carbonized at 800°C under N$_2$ atmosphere to prepare a undoped support (marked as C). Then, the supports were volume-impregnated by a mixed solution of RuCl$_3$•xH$_2$O dissolved by ethanol and water (1: 1 volume ratio) to load Ru, the amount of which was precalculated of 5 wt%. The dried samples were reduced at 400°C for 3 h with a mixed atmosphere flow of 5% H$_2$ and 95% Ar (total 1 L/min) to finally obtain the Ru@C, Ru@CNS-N$_2$ and Ru@CNS-CO$_2$ catalysts⁰.

Catalytic performance tests

For each hydrogenolysis reaction, 1 g of dried technical lignin, 0.2 g catalyst and 30 ml methanol were put into a 100 ml mechanical stirring autoclave. Residual air in the sealed autoclave was purged with nitrogen and hydrogen for five times successively, and then 1 MPa H_2 was pressurized. The reaction was maintained at 250°C for 2 h. After that, the reactor was cooled down to room temperature and the liquid products were collected for qualitative and quantitative analysis.

The obtained organic soluble oil was analyzed by gas chromatography/mass spectrometry (GC/MS) equipped with column Agilent J&W VF-1701ms (30 m × 250 μm × 0.5 μ m). The column was heated to 200°C at the rate of 5°C/min from the initial temperature of 40°C, and then raised to 280°C at the rate of 10°C/min and held for 3 min. The external standard sample concentrations of five concentrations were used for the standard curve, and then the concentration of the compound was calculated according to the peak area. The yield of phenolic monomer was calculated according to the following formula:

$$Y_{monomer} = \frac{C_{monomer} \times V}{1000 \times m_{lignin}} \qquad (1)$$

where $Y_{monomer}$ (%) was the monomer yield based on the weight of technical lignin; $C_{monomer}$ (g/L) represented the concentration calculated by the peak area; V (ml) was the total volume of liquid sample taken for GC/MS analysis; and m_{lignin} (g) was the mass of technical lignin.

Catalyst characterization

Elemental analysis to determine the contents of C, S, N and H of ash-free base of the catalysts was conducted on a Vario ELIII elemental analyzer (Elementar Company, Gernany). The Brunauer–Emmett–Teller method (BET) with a nitrogen adsorption/desorption isotherm was conducted on BSD-PM4 analyzer from BSD INSTRUMENT (Beijing) to obtain the specific surface area. The degassing temperature was 300°C, and the degassing time was 510 min. The prepared catalysts were also analyzed by FTIR (Bruker Vertex 80V, Germany) using the potassium bromide pellet technique, in which a KBr:char ratio of 100:1 (w:w) was used. The FTIR spectral region was from 400 to 4,000 cm^{-1}. The carbon structures of the catalysts were measured by a Raman technique spectrometer (ThermoFisher DXR532). The excitation laser wavelength used in the equipment was 780 nm, while the laser power was 24 mW. Based on previous study (Zhang et al., 2011; Wang et al., 2017), the original Raman spectra were curve-fitted into 10 Gaussian bands, in which the ratio of D to (G_R + V_L + V_R) band areas would suggest the ratio of the large to small aromatic ring systems. Temperature-programmed desorption (TPD) was conducted on a PCA-1200 BUILDER chemical adsorption

analyzer (China) to analyze the surface acid sites. The samples were first saturated using 10 vol% NH_3 (30 ml/min) at 50°C for 30 min. After purging by N_2 (30 ml/min) at 50°C for 1 h, the NH_3-TPD was conducted by raising temperature from 50 to 650°C at a rate of 10°C/min and keeping it at 650°C for 1 h. X-ray photoelectron spectroscopy (XPS) was measured to investigate the chemical states of elements, such as Ru, C, N and S, relying on AXIS UltraDLD (Shimadzu, Japan) instrument equipped with Al Kα radiation (150 W), whose wide pass energy was 160 eV and narrow pass energy was 40 eV. Before testing, pure silica was mixed up with the catalysts as an internal standard to calibrate the binding energies. High-resolution transmission electron microscopy (HRTEM) was carried out to analyze the Ru particle size and observe the dispersion, of which the average particle diameter (d) was calculated according to the following formula:

$$d = \frac{\sum n_i d_i^3}{\sum n_i d_i^2} \qquad (2)$$

where n_i was the count of particles and d_i was each characteristic diameter of particles.

Results and discussion

Characteristics of Ru@C, Ru@CNS-N$_2$ and Ru@CNS-CO$_2$

The three prepared catalysts were analyzed by various methods to understand the differences in their physicochemical structures caused by N,S co-doping and/or doping atmosphere. TEM analysis was conducted to measure the morphology and distribution of metal Ru particles on the three supports. It can be observed from Figure 1 that the Ru particles on the undoped char were agglomerated with an average size of 5.42 nm, while the Ru particles were well dispersed on the N,S-co-doped char with smaller sizes. Surprisingly, the particles size of Ru on CNS-CO$_2$ was as small as 1.41 nm. This is consistent with the results of the study from Li et al., in which they found that the strong chemical interaction between metal and the doped sulfur atoms can greatly suppress the aggregation of metal species (Li et al., 2020). It has also been reported that smaller metal particles showed better catalytic performance during reactions (Che et al., 1989; Isaifan et al., 2013). Thus, Ru@CNS-CO$_2$ was expected to have a good catalytic effect on lignin depolymerization.

CO_2 is a typical agent for activation of carbon material, and the specific surface area of the carbon material can be significantly improved. Figure 2A shows the nitrogen adsorption and desorption isotherms of the three catalysts, among which Ru@C belonged to a typical type IV isotherm, while Ru@CNS-N$_2$ and Ru@CNS-CO$_2$ were typical type I isotherm. The change of the isotherm type of the catalyst
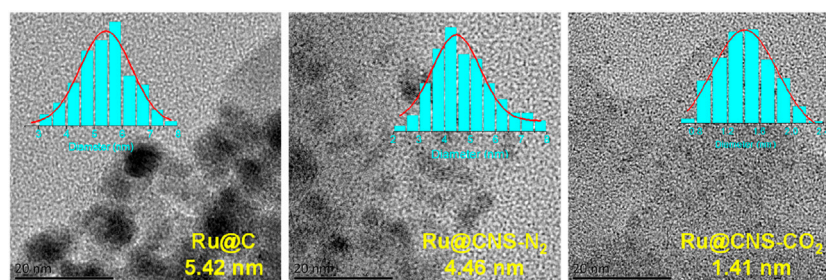
FIGURE 1
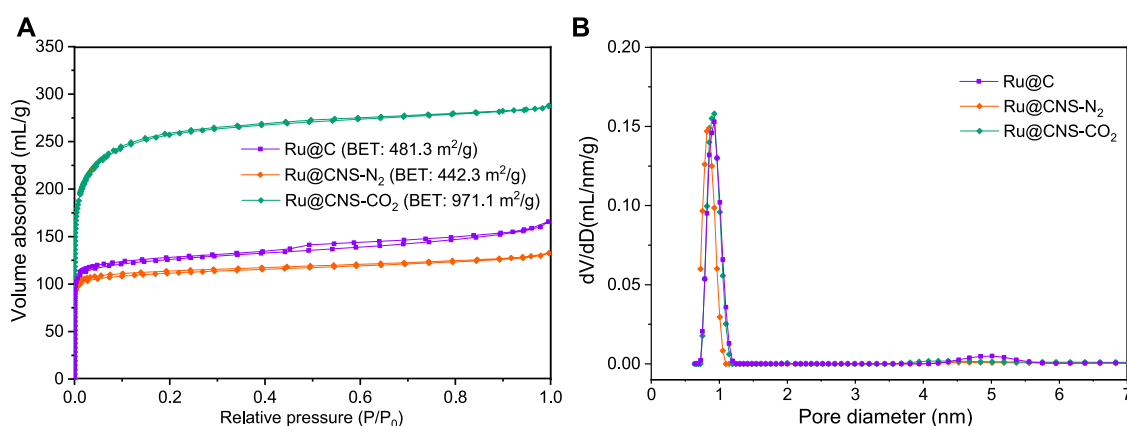TEM images and histograms of particle size for the catalysts.

FIGURE 2
Nitrogen physical sorption isotherms **(A)** and pore size distribution **(B)** of the catalysts.

from type IV to type I indicated that the mesopores in the catalyst were consumed during the N,S-co-doping process, which was also proved by the pore size distribution shown in Figure 2B. Although the three catalysts were predominant in micropores, a small peak at around 5 nm for Ru@C could be observed. Compared with Ru@C, the specific surface area of Ru@CNS-N_2 slightly reduced from 481.3 to 442.3 m^2/g, indicating that the doping of nitrogen and sulfur into char under N_2 atmosphere also consumed a portion of micropores. Conversely, the specific surface area of Ru@CNS-CO_2 significantly increased to 971.1 m^2/g due to the reaction of CO_2 with carbon to generate micropores.

Table 1 lists the elemental composition of the three catalysts. The content of Ru was stabilized at 4.5–4.8 wt% for all prepared catalysts. Since the biochar support has experienced the temperature as high as 800°C, the carbon content in Ru@C reached 83.2 wt% and the oxygen content reduced to 11.3 wt %. After the biochar support was doped by nitrogen and sulfur,

the carbon content in Ru@CNS-N_2 reduced to 74.2 wt%. However, the reduction in carbon content did not necessarily mean that carbon was successfully replaced by heteroatoms, which could also be present as surface functional groups. Reasonably, the contents of nitrogen and sulfur, which were negligible in Ru@C, respectively increased to 6.3 and 2.8 wt% in Ru@CNS-N_2. The doping process insignificantly affect the oxygen content. When the doping atmosphere changed from N_2 to CO_2, the carbon content obviously decreased to 58.5 wt%, mainly caused by the reaction between carbon and CO_2. It is well known that CO_2 atmosphere favors the formation of oxygen-containing functional groups on biochar surface under high temperature (Liu et al., 2020), which led to an oxygen content up to 25.0 wt% in Ru@CNS-CO_2. It has been reported that the carbon atoms close to oxygen-containing functional groups had unique electron cloud densities and thus exhibited special interactions with Ru nanoparticles and/or lignin molecules (Li et al., 2019).

TABLE 1 Elemental and Raman analyses of the three catalysts.

Sample	C (%)	H (%)	N (%)	S (%)	Ru^a (%)	O^b (%)	I $(G_R + V_L + V_R)/I_D$
Ru@C	83.2	0.7	0.2	<0.1	4.5	11.3	0.81
Ru@CNS-N_2	74.2	1.1	6.3	2.8	4.8	10.8	1.08
Ru@CNS-CO_2	58.5	1.3	5.6	4.9	4.7	25.0	0.93

[a]Quantified by ICP-OES.
[b]By difference.
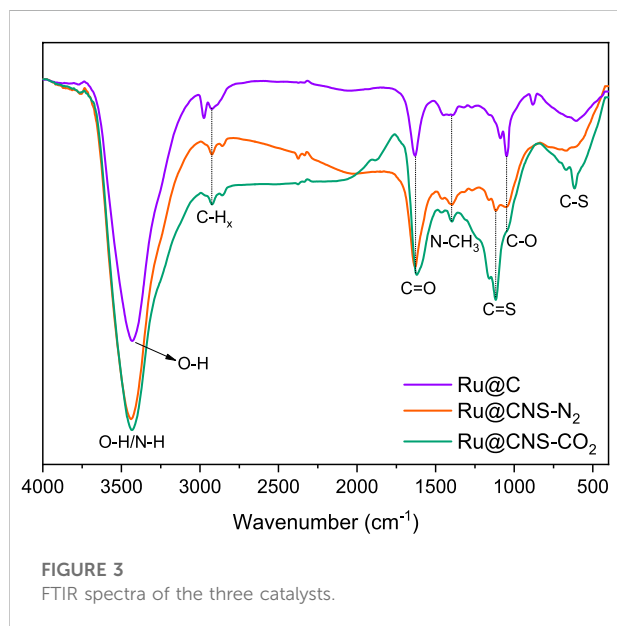
FIGURE 3
FTIR spectra of the three catalysts.

Figure 3 shows the FTIR spectra of the three catalysts. Compared with Ru@C, the band at around 3,435 cm^{-1} from Ru@CNS-CO_2 and Ru@CNS-N_2, which is assigned to O-H and/ or N-H, became significantly higher because of the presence of N-H groups derived from nitrogen doping. The band at 1,620 cm^{-1} is assigned to C=O group. It is interesting to find that the doping of nitrogen and sulfur under both N_2 and CO_2 atmospheres favored the formation of C=O group. More importantly, the CO_2 atmosphere was obviously beneficial to the doping of sulfur into the char carbon skeleton, since the signals of C=S and C-S groups from Ru@CNS-CO_2 were much stronger than those from the others (Taheri-Torbati et al., 2017; Cui et al., 2018). Similar to oxygen doping, since sulfur has a larger electronegativity than carbon, the successful doping of sulfur into carbon skeleton can also cause changes in the electron cloud density of the char, which is expected to improve the catalytic performance of Ru@CNS-CO_2.

The chemical states of Ru, C, N, and S elements in the three catalysts were studied by XPS measurements. The XPS spectra of Ru 3p 3/2 can be deconvoluted into Ru^0 and Ru^{n+} species, in which the Ru^0 species had been recognized as the active sites for hydrogenolysis of lignin (Wu et al., 2021; Ding et al., 2022). As shown in Figure 4A, the content of Ru^0 species slightly increased from 75.45% (Ru@C) to 78.14% (Ru@CNS-N_2), suggesting that the co-doping of nitrogen and sulfur could facilitate the formation of Ru^0 species. When the doping atmosphere changed from N_2 to CO_2, the content of Ru^0 species in Ru@CNS-CO_2 significantly increased to 87.51%. This can be explained by the better doping of sulfur into the carbon skeleton under CO_2 atmosphere and the greater electronegativity of sulfur in comparison to carbon, thus promoting the electron transfer from CNS-CO_2 support to Ru particles. The interactions between the doped chars and Ru particles were also demonstrated by the shift of the binding energy of metallic Ru (462.9 vs 461.4 eV). Figure 4B showed the XPS spectra of C 1s. Except for the overlapping peak of Ru 3d 3/2, the C 1s XPS spectra can be deconvoluted into C-C/C=C at 284.8 eV, C-O at 285.9 eV, C-O-C at 286.9 eV, and π-π bond at 289.4 eV. The content of C-C/C=C reduced from 46.9% (Ru@C) to 42.3% (Ru@CNS-N_2), indicating that the doping of nitrogen and sulfur in N_2 reduced the graphitization degree of the char to a certain degree. However, that number increased to 58.5% in the case of Ru@CNS-CO_2, resulting from the selective consumption of small aromatic rings in carbon structure by CO_2. This conclusion was also proved by the Raman analysis of the catalysts. The value of $(G_R + V_L + V_R)/D$, which represents the ratio of the small to large aromatic ring systems in carbon materials (Huang et al., 2020), increased from 0.81 (Ru@C) to 1.08 (Ru@CNS-N_2) and then decreased to 0.93 (Ru@CNS-CO_2), as listed in Table 1. The N 1s XPS spectra, as exhibited in Figure 4C, were deconvoluted into pyridinic-N (398.6 eV), pyrrolic-N (400.5 eV), graphitic-N (402.0 eV), and nitrogen oxide (405 eV). The high contents of pyridinic-N and pyrrolic-N suggested the doping of nitrogen into carbon skeleton of char. Since the CO_2 atmosphere would introduce oxygen-containing functional groups to the char surface, the content of the O-N species in Ru@CNS-CO_2 was significantly higher than that in Ru@CNS-N_2. Figure 4D shows the S 2p XPS spectra, which were deconvoluted into C-S-C species of S 2p 1/2 and S 2p 3/2 as well as C-SO_x. The higher contents of C-S-C species in Ru@CNS-CO_2 also
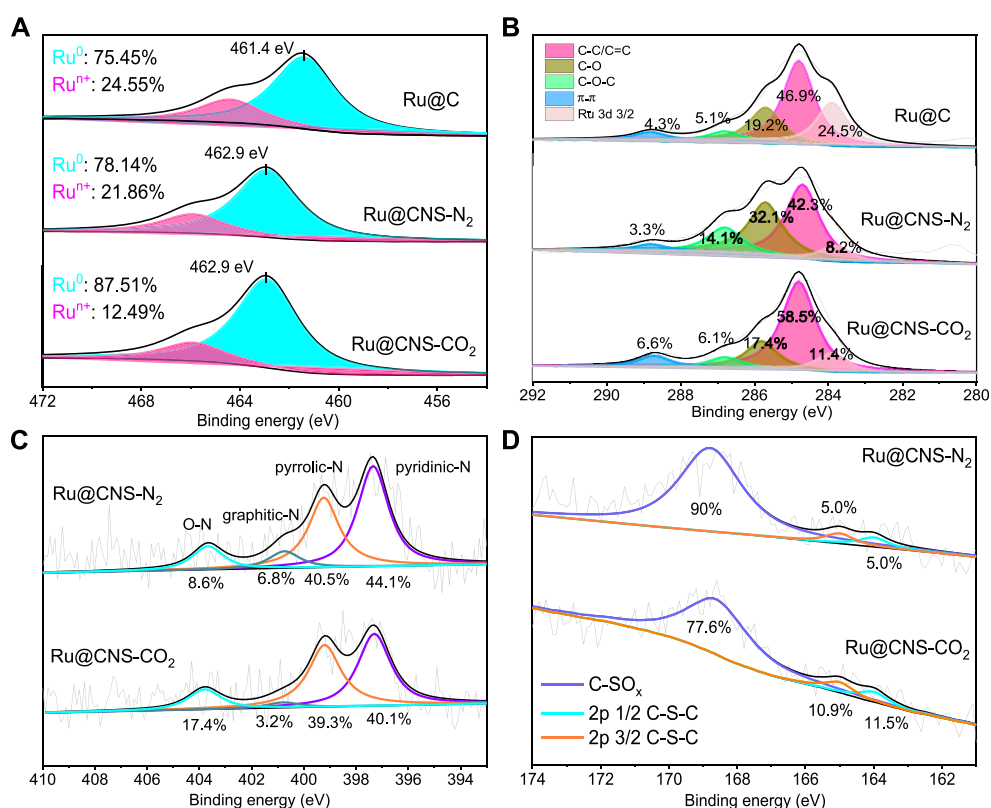
FIGURE 4
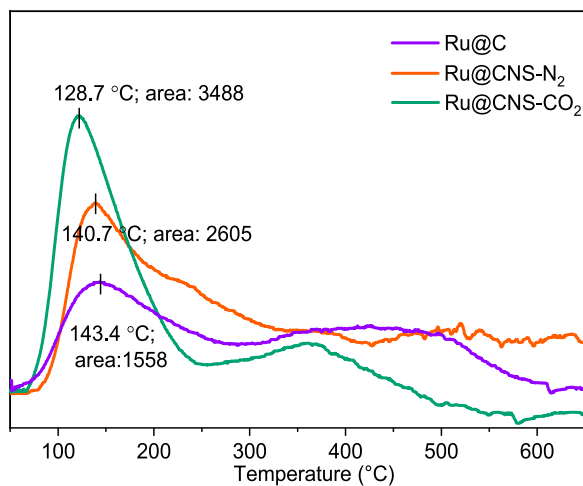XPS spectra of **(A)** Ru 3p 3/2, **(B)** C 1s, **(C)** N 1s and **(D)** S 2p of the catalysts.

**FIGURE 5**
NH_3-TPD patterns of the three catalysts.
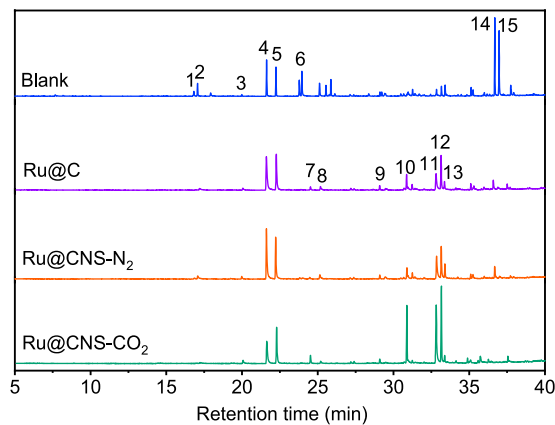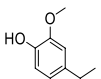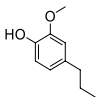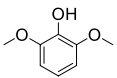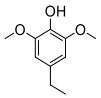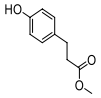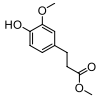
FIGURE 6
TICs of the products from lignin depolymerization over different catalysts.

indicated the successfully doping of sulfur into the carbon skeleton of char, which was in good agreement with the FTIR analysis.

The introduction of oxygen-, nitrogen-, and/or sulfur-containing functional groups into carbon materials significantly affects their acidity, NH_3-TPD analysis was thus

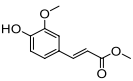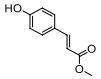TABLE 2 Yields of phenolic monomers from catalytic depolymerization of lignin over different catalysts.

Entry	Name	Structure	Yield (wt%)			
			Blank	Ru@C	Ru@CNS-N$_2$	Ru@CNS-CO$_2$
1	Phenol		0.25	0.20	0.23	0.21
2	2-Methoxyphenol		0.37	0.25	0.37	0.29
3	2-Methoxy-4-methylphenol		0.28	0.23	0.31	0.47
4	4-Ethylphenol		1.01	4.03	5.31	3.77
5	4-Ethyl-2-methoxyphenol		0.49	4.47	5.23	5.31
6	4-Vinylphenol		0.82	0.16	0.12	0.13
7	2-Methoxy-4-propylphenol		0	0.27	0.21	0.44
8	2,6-Dimethoxyphenol		0.61	0.68	0.36	0.31
9	4-Ethyl-2,6-dimethoxyphenol		0.15	0.40	0.21	0.22
10	2,6-Dimethoxy-4-propylphenol		0.20	0.81	1.61	6.74
11	Methyl 3-(4-hydroxyphenyl)propanoate		0.30	1.89	2.31	4.53
12	Methyl 3-(4-hydroxy-3-methoxyphenyl)propanoate		0.49	5.14	5.32	13.29
13	4-Allyl-2,6-dimethoxyphenol		0.17	0.32	0.41	0.38
14	Methyl ferulate		2.38	1.49	0.88	0.11
15	Methyl coumarate		2.74	0.13	0.07	0.21
16	Total		10.25	20.47	22.95	36.41

FIGURE 7
Schematic diagram of lignin depolymerization to the main compounds.
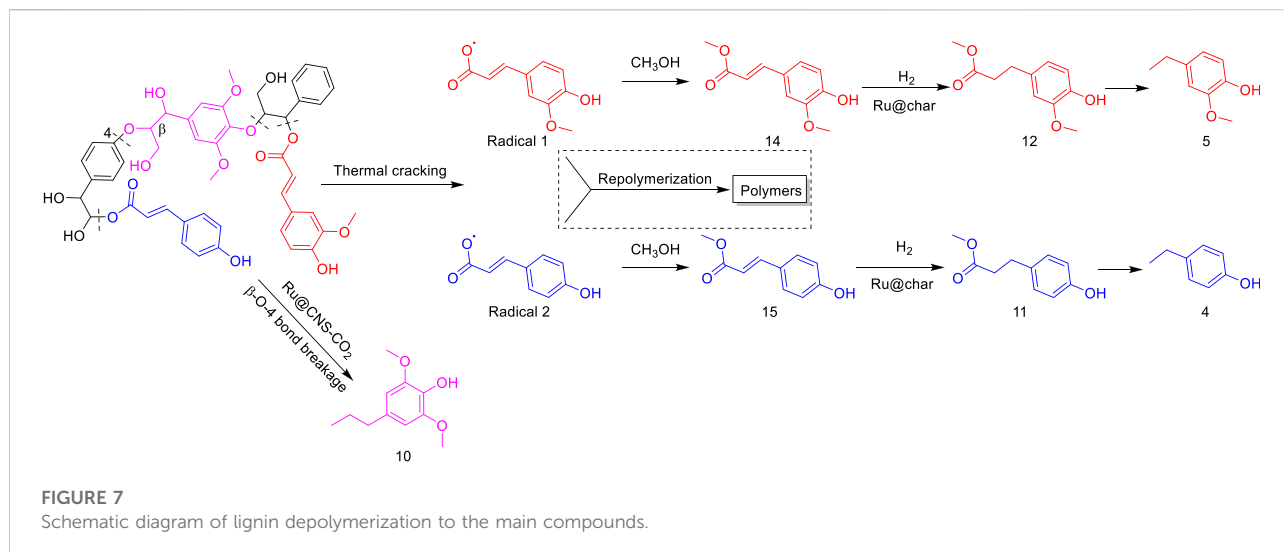
conducted to determine the acidic sites of the prepared catalysts. As shown in Figure 5, a small peak at 143.4°C with an area of 1,558 was found for Ru@C, suggesting the presence of very few weakly acidic sites. When the nitrogen and sulfur were doped into the char, the peak was slightly shifted to 140.7°C with an area of 2,605 (Ru@CNS-N_2) and 128.7°C with an area of 3,488 (Ru@CNS-CO_2), indicating that the acidity of the catalyst became weaker but the acid sites were more abundant, particularly under the CO_2 atmosphere.

Production of phenolic monomers from lignin depolymerization over the three catalysts

On the basis of understanding the properties of the three catalysts, a technical lignin derived from corncob was selected to test their catalytic performances on the production of phenolic monomers. The liquid products from the lignin depolymerization were qualitatively and quantitatively analyzed by GC/MS, and the total ion chromatograms (TICs) of the products as well as the yield of each compound are shown in Figure 6 and Table 2, respectively. For comparison, a run without catalyst was also conducted, in which the total yield of all identified phenolic monomers was only 10.25 wt% (entry 16, Table 2). The most abundant compounds from the blank run, compounds **14** (methyl ferulate, 2.38 wt%) and **15** (methyl coumarate, 2.74 wt%), were not the products from the typical β-O-4 subunits. When the non-doped catalyst (Ru@C) was employed, the richest product shifted to compound **12** (methyl 3-(4-hydroxy-3-methoxyphenyl)propanoate, 5.14 wt %), followed by compounds **5** (4-ethyl-2-methoxyphenol, 4.47 wt%) and **4** (4-ethylphenol, 4.03 wt%). It should be noted that compound **12** was a hydrogenation product of compound

14. Based on our previous study, the saturation of the double bond ($C\beta = C_\gamma$) in compounds **14** and **15** reduced the bond dissociation energies of C_β-C_γ, thus contributing to the production of compounds **five** and **four** by decarboxylation, respectively (Wu et al., 2021). With the help of Ru@C, the total yield of phenolic monomers of corncob lignin depolymerization increased to 20.47 wt%. Repolymerization of lignin-derived intermediates to macromolecules has been recognized as common reactions during lignin conversion, which led to the low yield of total phenolic monomers from the blank run (Deuss et al., 2015). Since the compounds **12**, **4**, and **five** could be derived from the products **14** and **15**, the improved yield of total phenolic monomers from the Ru@C run meant that the catalyst not only facilitated the depolymerization of lignin to compounds **14** and **15** but also hindered their repolymerization. Unfortunately, the yield of total phenolic monomers and the main composition of the lignin oil from the run over Ru@CNS-N_2 were very close to those from the Ru@C run. This could be explained by the similar properties between Ru@C and Ru@CNS-N_2, such as Ru particle sizes, specific surface areas, and contents of Ru^0 species, also reflected the inapplicability of N_2 atmosphere in doping of heteroatoms into carbon materials to prepare catalyst. On the other hand, as discussed in Section 3.1, the CO_2 atmosphere not only obviously improved the specific surface area but also helped the doping of sulfur into the carbon skeleton of char, thus leading to finer Ru particle size, more Ru^0 content, and more weak acid sites. Unsurprisingly, the yield of total phenolic monomers significantly increased to 36.41 wt% in the case of Ru@CNS-CO_2 (see Table 2), demonstrating the importance of CO_2 for the doping process. This yield was even higher than the data from our previous study by a factor of 1.34, in which Ru supported on aminated carbon nanotubes was employed as the catalyst (Wu et al., 2021). The most abundant compound from the Ru@CNS-CO_2 run was still compound **12** with a yield as high as 13.29 wt%,

suggesting a promising hydrogenation ability of Ru@CNS-CO_2. Different with the runs over Ru@C and Ru@CNS-N_2, the second richest compound here was compound **10** (2,6-dimethoxy-4-propylphenol) rather than compounds **four** or **5**, implying that Ru@CNS-CO_2 also had high activity in fragmentation of typical β-O-4 bonds (Wang et al., 2018; Wang et al., 2019). Based on the experimental results, a schematic diagram of lignin depolymerization to the main compounds can be proposed in Figure 7.

Conclusion

Ru supported on nitrogen and sulfur co-doped biochar catalysts were prepared for hydrogenolysis of technical lignin to phenolic monomers. The effect of atmosphere for the doping process on catalytic performance was studied by using N_2 and CO_2. The following conclusions can be drawn based on the experimental results:

1) The physicochemical structures of CNS-N_2 and CNS-CO_2 supports were significantly different. Compared with CNS-N_2, CNS-CO_2 was characterized by larger specific surface area, richer C=S and C-S groups, and higher oxygen content.
2) The unique structure of CNS-CO_2 support can prevent the agglomeration of Ru particles. The particle size of Ru from Ru@CNS-CO_2 was as small as 1.41 nm, which was significantly smaller than that from Ru@CNS-N_2 (4.46 nm). Furthermore, the Ru^0 species in Ru@CNS-CO_2 as well as its acid sites were much richer than those in Ru@CNS-N_2.
3) The yield of phenolic monomers from corncob-derived lignin hydrogenolysis over Ru@CNS-CO2 was as high as 36.41 wt%, which was higher than that over Ru@CNS-N_2 by a factor of 1.6.

Data availability statement

The original contributions presented in the study are included in the article/Supplementary Material, further inquiries can be directed to the corresponding authors.

Author contributions

WG: Conceptualization, Funding acquisition, Writing—Reviewing and Editing. KW: Investigation, Data curation, Writing—original draft preparation. YhW: Investigation, Data curation. XZ: Investigation. YlW: Reviewing and Editing. SoZ: Investigation. BL: Reviewing and Editing. YH: Funding acquisition, Investigation, Writing— review and editing, Supervision. SuZ: Funding acquisition, Investigation, Writing—review and editing, Supervision. HZ: Investigation.

Funding

Conflicts of interest

YlW and SoZ are employed by the Hefei Debo Bioenergy Science & Technology Co., Ltd., China.

The remaining authors declare that the research was conducted in the absence of any commercial or financial relationships that could be construed as a potential conflict of interest.

Publisher's note

All claims expressed in this article are solely those of the authors and do not necessarily represent those of their affiliated organizations, or those of the publisher, the editors and the reviewers. Any product that may be evaluated in this article, or claim that may be made by its manufacturer, is not guaranteed or endorsed by the publisher.

References

Che, M., and Bennett, C. O. (1989). "The influence of particle size on the catalytic properties of supported metals," Editors D. D. Eley, H. Pines, and P. B. Weisz (Academic Press), 36, 55–172. *Adv. Catal.*

Chen, S., Lu, Q., Han, W., Yan, P., Wang, H., and Zhu, W. (2021). Insights into the oxidation–reduction strategy for lignin conversion to high-value aromatics. *Fuel* 283, 119333. doi:10.1016/j.fuel.2020.119333

Cheng, C., Li, P., Yu, W., Shen, D., Jiang, X., and Gu, S. (2020). Nonprecious metal/bimetallic catalytic hydrogenolysis of lignin in a mixed-solvent system. *ACS Sustain. Chem. Eng.* 8 (43), 16217–16228. doi:10.1021/acssuschemeng.0c05362

Cui, Y., Li, M., Wang, H., Yang, C., Meng, S., and Chen, F. (2018). *In-situ* synthesis of sulfur doped carbon nitride microsphere for outstanding visible light

photocatalytic Cr(VI) reduction. *Sep. Purif. Technol.* 199, 251–259. doi:10.1016/j.seppur.2018.01.037

Deuss, P. J., Scott, M., Tran, F., Westwood, N. J., de Vries, J. G., and Barta, K. (2015). Aromatic monomers by *in situ* conversion of reactive intermediates in the acid-catalyzed depolymerization of lignin. *J. Am. Chem. Soc.* 137 (23), 7456–7467. doi:10.1021/jacs.5b03693

Ding, T., Wu, Y., Zhu, X., Lin, G., Hu, X., Sun, H., et al. (2022). Promoted production of phenolic monomers from lignin-first depolymerization of lignocellulose over Ru supported on biochar by N, P-co-Doping. *ACS Sustain. Chem. Eng.* 10 (7), 2343–2354. doi:10.1021/acssuschemeng.1c06335

Huang, Y., Liu, S., Akhtar, M. A., Li, B., Zhou, J., Zhang, S., et al. (2020). Volatile–char interactions during biomass pyrolysis: Understanding the potential origin of char activity. *Bioresour. Technol.* 316, 123938. doi:10.1016/j.biortech.2020.123938

Isaifan, R. J., Ntais, S., and Baranova, E. A. (2013). Particle size effect on catalytic activity of carbon-supported Pt nanoparticles for complete ethylene oxidation. *Appl. Catal. A General* 464-465, 87–94. doi:10.1016/j.apcata.2013.05.027

Li, C., Zhao, X., Wang, A., Huber, G. W., and Zhang, T. (2015). Catalytic transformation of lignin for the production of chemicals and fuels. *Chem. Rev.* 115 (21), 11559–11624. doi:10.1021/acs.chemrev.5b00155

Li, J., Fan, J., Ali, S., Lan, G., Tang, H., Han, W., et al. (2019). The origin of the extraordinary stability of mercury catalysts on the carbon support: The synergy effects between oxygen groups and defects revealed from a combined experimental and DFT study. *Chin. J. Catal.* 40 (2), 141–146. doi:10.1016/s1872-2067(19)63271-7

Li, L-Z., Xu, S-L., Shen, S-C., Wang, L., Zuo, M., Chen, P., et al. (2020). A sulfur-fixing strategy toward carbon-supported Ru-based bimetallic nanocluster catalysts. *ChemNanoMat* 6 (6), 969–975. doi:10.1002/cnma.202000054

Li, L., Zhang, T., Guo, Z., Liu, X., Guo, Y., Huang, Y., et al. (2021). Unraveling the role of metal in M/NiAl2O4 (M = Pt, Pd, Ru) catalyst for the self-reforming-driven hydrogenolysis of lignin. *Ind. Eng. Chem. Res.* 60 (31), 11699–11706. doi:10.1021/acs.iecr.1c01572

Liu, W-J., Jiang, H., and Yu, H-Q. (2015). Development of biochar-based functional materials: Toward a sustainable platform carbon material. *Chem. Rev.* 115 (22), 12251–12285. doi:10.1021/acs.chemrev.5b00195

Liu, Y., Paskevicius, M., Wang, H., Fushimi, C., Parkinson, G., and Li, C-Z. (2020). Difference in tar reforming activities between biochar catalysts activated in H2O and CO2. *Fuel* 271, 117636. doi:10.1016/j.fuel.2020.117636

Luo, B., Zhou, L., Tian, Z., He, Y., and Shu, R. (2022). Hydrogenolysis of cornstalk lignin in supercritical ethanol over N-doped micro-mesoporous biochar supported Ru catalyst. *Fuel Process. Technol.* 231, 107218. doi:10.1016/j.fuproc.2022.107218

Ragauskas, A. J., Beckham, G. T., Biddy, M. J., Chandra, R., Chen, F., Davis, M. F., et al. (2014). Lignin valorization: Improving lignin processing in the biorefinery. *Science* 344 (6185), 1246843. doi:10.1126/science.1246843

Schutyser, W., Renders, T., Van den Bosch, S., Koelewijn, S. F., Beckham, G. T., and Sels, B. F. (2018). Chemicals from lignin: An interplay of lignocellulose fractionation, depolymerisation, and upgrading. *Chem. Soc. Rev.* 47 (3), 852–908. doi:10.1039/c7cs00566k

Shuai, L., Amiri, M. T., Questell-Santiago, Y. M., Héroguel, F., Li, Y., Kim, H., et al. (2016). Formaldehyde stabilization facilitates lignin monomer production during biomass depolymerization. *Science* 354 (6310), 329–333. doi:10.1126/science.aaf7810

Taheri-Torbati, M., Eshghi, H., Rounaghi, S. A., Shiri, A., and Mirzaei, M. (2017). Synthesis, characterization and application of nitrogen–sulfur-doped carbon

spheres as an efficient catalyst for the preparation of novel α-aminophosphonates. *J. Iran. Chem. Soc.* 14 (9), 1971–1982. doi:10.1007/s13738-017-1135-8

van Deelen, T. W., Hernández Mejía, C., and de Jong, K. P. (2019). Control of metal-support interactions in heterogeneous catalysts to enhance activity and selectivity. *Nat. Catal.* 2 (11), 955–970. doi:10.1038/s41929-019-0364-x

Wang, Y., Jiang, L., Hu, S., Su, S., Zhou, Y., Xiang, J., et al. (2017). Evolution of structure and activity of char-supported iron catalysts prepared for steam reforming of bio-oil. *Fuel Process. Technol.* 158, 180–190. doi:10.1016/j.fuproc.2017.01.002

Wang, S., Gao, W., Li, H., Xiao, L-P., Sun, R-C., and Song, G. (2018). Selective fragmentation of biorefinery corncob lignin into p-hydroxycinnamic esters with a supported zinc molybdate catalyst. *ChemSusChem* 11 (13), 2114–2123. doi:10.1002/cssc.201800455

Wang, S., Gao, W., Xiao, L-P., Shi, J., Sun, R-C., and Song, G. (2019). Hydrogenolysis of biorefinery corncob lignin into aromatic phenols over activated carbon-supported nickel. *Sustain. Energy Fuels* 3 (2), 401–408. doi:10.1039/c8se00359a

Wu, Y., Lin, Z., Zhu, X., Hu, X., Gholizadeh, M., Sun, H., et al. (2021). Hydrogenolysis of lignin to phenolic monomers over Ru based catalysts with different metal-support interactions: Effect of partial hydrogenation of C(sp2)-O/C. *Fuel (Lond)* 302, 121184. doi:10.1016/j.fuel.2021.121184

Xiong, X., Yu, I. K. M., Cao, L., Tsang, D. C. W., Zhang, S., and Ok, Y. S. (2017). A review of biochar-based catalysts for chemical synthesis, biofuel production, and pollution control. *Bioresour. Technol.* 246, 254–270. doi:10.1016/j.biortech.2017.06.163

Ye, K., Liu, Y., Wu, S., and Zhuang, J. (2021). A review for lignin valorization: Challenges and perspectives in catalytic hydrogenolysis. *Industrial Crops Prod.* 172, 114008. doi:10.1016/j.indcrop.2021.114008

Zakzeski, J., Bruijnincx, P. C. A., Jongerius, A. L., and Weckhuysen, B. M. (2010). The catalytic valorization of lignin for the production of renewable chemicals. *Chem. Rev.* 110 (6), 3552–3599. doi:10.1021/cr900354u

Zevallos Torres, L. A., Lorenci Woiciechowski, A., de Andrade Tanobe, V. O., Karp, S. G., Guimarães Lorenci, L. C., Faulds, C., et al. (2020). Lignin as a potential source of high-added value compounds: A review. *J. Clean. Prod.* 263, 121499. doi:10.1016/j.jclepro.2020.121499

Zhang, S., Min, Z., Tay, H-L., Asadullah, M., and Li, C-Z. (2011). Effects of volatile–char interactions on the evolution of char structure during the gasification of Victorian Brown coal in steam. *Fuel* 90 (4), 1529–1535. doi:10.1016/j.fuel.2010.11.010

Zhang, S., Yu, S., Li, Q., Mohamed, B. A., Zhang, Y., and Zhou, H. (2022). Insight into the relationship between CO2 gasification characteristics and char structure of biomass. *Biomass Bioenergy* 163, 106537. doi:10.1016/j.biombioe.2022.106537

Frontiers in
Chemistry

Explores all fields of chemical science across the periodic table

Advances our understanding of how atoms, ions, and molecules come together and come apart. It explores the role of chemistry in our everyday lives - from electronic devices to health and wellbeing.

Discover the latest Research Topics

See more →

Frontiers

Avenue du Tribunal-Fédéral 34
1005 Lausanne, Switzerland
frontiersin.org

Contact us

+41 (0)21 510 17 00
frontiersin.org/about/contact

frontiers

Frontiers in
Chemistry

frontiers | Research Topics